Acoustical Physics, Vol. 51, No. 6, 2005, pp. 609–618. From Akusticheskiĭ Zhurnal, Vol. 51, No. 6, 2005, pp. 709–720.

Active Noise Cancellation of a Spherical Multipole Source Using a Radially Vibrating Spherical Baffled Piston[1]

M. Azarpeyvand

Institute of Sound and Vibration Research, Southampton University, Highfield, Southampton SO17 1BJ, UK

e-mail: ma@isvr.soton.ac.uk

Received May 17, 2004

Abstract—The creation of quiet zones in a diffuse sound field due to a multipole spherical primary source by means of a radially vibrating surface set in the side of a rigid sphere (secondary source) is investigated in this article. The formulation utilizes the appropriate wave field expansions along with the translational addition theorems for spherical wave functions to develop a closed-form solution in the form of an infinite series. The numerical results reveal that using a baffled spherical piston model as a secondary source instead of a monopole control source will obviously improve the sound minimization efficiency of such noise-control systems in all cases, especially for a dipolar primary source. © *2005 Pleiades Publishing, Inc.*

1. INTRODUCTION

Active noise control (ANC) of a spherical source using a secondary control source to cancel the pressure at a particular location or to reduce the output acoustic power is an old concept [1–10]. Local active cancellation of acoustic pressure using a closed control source was originally studied by Olson and May [1]. Fedoryuk [2] considered the problem of active sound suppression by means of continuous arrays of monopoles. In this research, two receiving and two radiating surfaces filled continuously with point monopole receivers and radiators are assumed to simulate a sound-control system. Later, active suppression of sound fields by the method of spatial harmonics was examined by Mazanikov *et al.* [3]. In this problem, monopole sources and sensors distributed on the surface of a concentric sphere were brought into play to show an ANC system. In the same way, Nelson *et al.* [4, 5] studied the minimum power output of a pair of free-field monopole sources. It has been demonstrated that, for the numbers and arrangements of the secondary sources considered, significant reductions in power output may only be achieved if, in general, secondary sources are placed within a distance of half of the wavelength of the primary source. Later, Joseph *et al.* [6] investigated the near-field zone of quiet created when the total pressure is driven to zero at a field point on the axis of a flat piston source. By assuming a uniform pure tone sound field and a feedforward control arrangement, they found that the near-field characteristics of the secondary source are very important in determining the resulting on-axis pressure distribution. David and Elliott [7] performed a computer simulation to estimate both the on-axis and off-axis extent of the near-field zone of quiet created by a local active control system in which the secondary source is modeled as a flat piston in an infinite baffle. It was shown that the zone of quiet becomes larger as the control microphone is moved further away from the control source, until, for large separations, the 10-dB zone of quiet, defined as the spatial zone in which the sound pressure level of the controlled acoustic field is at least 10 dB below that of the primary field, approaches the limiting case of a sphere with a diameter that is one-tenth of a wavelength, as predicted by Elliott *et al.* [8]. Active cancellation of pressure and the pressure gradient in a pure diffuse sound field with a remote control source is studied by Elliott and Garcia-Bonito [9]. Analytical expressions for the extension of the zones of quiet generated when the cancellation point is closed or on the surface of the rigid sphere, a wall, a two-wall edge, and a corner have been reported by Garcia-Bonito *et al.* [10]. In a more related work, Bolton *et al.* [11] discussed global free-field cancellation in the region exterior to a monopole primary source by the use of a single multipole secondary source. It was found that improved attenuation could be achieved by choosing the secondary multipole-component source strength to minimize the total sound power radiated by the combination of the primary and secondary sources rather than by using a direct multipole expansion of the primary sound field. Also, it was shown that it is more efficient in some instances to use a single multipole rather than an array of monopoles for global cancellation. Martin and Roure [12] used a spherical harmonic expansion to simulate a primary sound field, and it was shown that, by using such an expansion, a method can be developed for optimizing the transducer locations for the case of free-field radiation of a period general (multipole) primary source. Soon after, active noise cancellation of a dipolar source using the previous method was studied and checked experimentally [13]. In a similar problem, an active spherical volume was used to absorb the energy

[1] The text was submitted by the author in English.

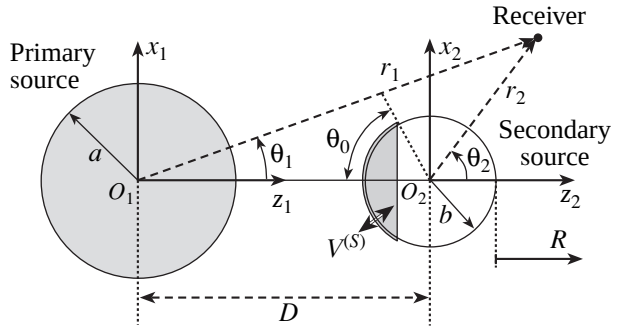

Fig. 1. Illustration of the geometrical configuration of the problem.

of an incident wave [14], and it was shown that using a spherical active absorber instead of a similar passive model would improve the efficiency of the control system.

On the other hand, acoustic radiation of pistons placed on baffles has been extensively considered in the literature for various piston and baffle geometries (i.e., planes, spheres, cylinders, and spheroids [15–21]). The self-radiation impedance for the classic problem of a radially (axially) vibrating piston set in a rigid sphere is presented in [15]. The mutual acoustic impedance of pistons on a sphere and a cylinder are analyzed in [16] and [17], respectively. Likewise, the acoustic radiation impedance of curved vibrating caps and rings located on the hard baffles of an oblate spheroidal obstacle is formulated in [18]. The self- and mutual radiation impedances for rectangular piston sources vibrating on a rigid prolate spheroidal baffle were investigated in [19]. More recently, Hasheminejad and Azarpeyvand examined acoustic radiation from a pulsating spherical cap set on a spherical baffle near a hard/soft flat surface [20]. Sound radiation from a liquid-filled underwater spherical acoustic lens with an internal eccentric baffled spherical piston is also studied by the same authors [21].

Taking into consideration the fact that the attenuation of sound in an active noise-control system is not only highly dependent on the secondary source number and location but also on its type [22], the principal objective of the present work is to study active noise cancellation of a finite general primary disquieting source by using a single partially vibrating control source. Thus, the present work is intended to extend the previous research carried out in [4, 5]. It is worth mentioning here that, in the low-frequency range, each multipole can be represented by a set of point sources, and vice versa (see Figs. 1 and 2 in [12]). The organization of the work is described next. Following the Introduction, the second section presents a general solution of the wave equation in terms of scalar generating functions. The solution to the boundary-value problem is obtained in terms of spherical Bessel and Hankel functions with unknown (modal) coefficients for the radiated waves. The unknown coefficients are determined incorporating the appropriate translational addition theorem and imposing the proper boundary conditions at the surfaces. For the given properties of the problem, namely, the primary source type (i.e., monopole, dipole, and general case), the excitation frequency, and the separation distance, the resultant set of coupled linear algebraic equations is solved numerically. Subsequently, the appropriate secondary-source velocity components (strength and phase) are found to diminish the sound pressure at a particular point. Later, important acoustic-field quantities such as sound attenuation and acoustic pressure levels after sound reduction are evaluated and discussed in Section 3.

2. THEORETICAL DEVELOPMENT

The problem can be analyzed by means of the standard methods of theoretical acoustics. The fluid is assumed to be inviscid and ideally compressible; it is assumed that it cannot support shear stresses, making the state of stress in the fluid purely hydrostatic. In view of the fact that the spherical cap is supposed to undergo time-harmonic surface pulsations, the field equations may conveniently be expressed in terms of a scalar velocity potential as [23]

$$\mathbf{u} = -\nabla\Phi, \quad p = -i\omega\rho\Phi, \quad \nabla^2\Phi + k^2\Phi = 0, \quad (1)$$

where $\omega = 2\pi f$ is the angular frequency of the harmonic fluctuations (rad/s) with frequency f, k is the wavenumber, $k = \omega/c = 2\pi/\lambda$, λ is the wavelength, ρ is the ambient fluid density, c is the ideal speed of sound, $\mathbf{u}$ is the fluid particle velocity vector, p is the acoustic pressure in the inviscid fluid, and where we have assumed harmonic time variations throughout, with the $e^{-i\omega t}$ dependence suppressed for simplicity.

Undoubtedly, the sound field radiated by a source may often be appreciably affected by a neighboring surface. In fact, the presence of a radiating and reflecting surface (i.e., a finite control source) near a primary source can affect not only the directional properties of the source but also the total radiated sound power by the first source [24, 25]. Consider a spherical piston set on a rigid spherical baffle positioned at a finite distance from a primary multipole source (Fig. 1). It is clear that the proximity of the second vibrating obstacle makes the problem more difficult to solve. The problem geometry is depicted in Fig. 1. The centers of the two spheres are separated by a distance D, and the cap angle of the secondary source is θ_0. The origins O_1 and O_2 of the two spherical coordinate systems $(r_1, \theta_1, \vartheta_1)$ and $(r_2, \theta_2, \vartheta_2)$ coincide with the centers of the primary and secondary sources, respectively. The direct distance between the center of the primary source and the receiver (field point) is r_1; the direct distance between the center of the control source and the receiver (field point) is r_2. The dynamics of the present multiscattering problem may be expressed in terms of two scalar potentials: one cor-

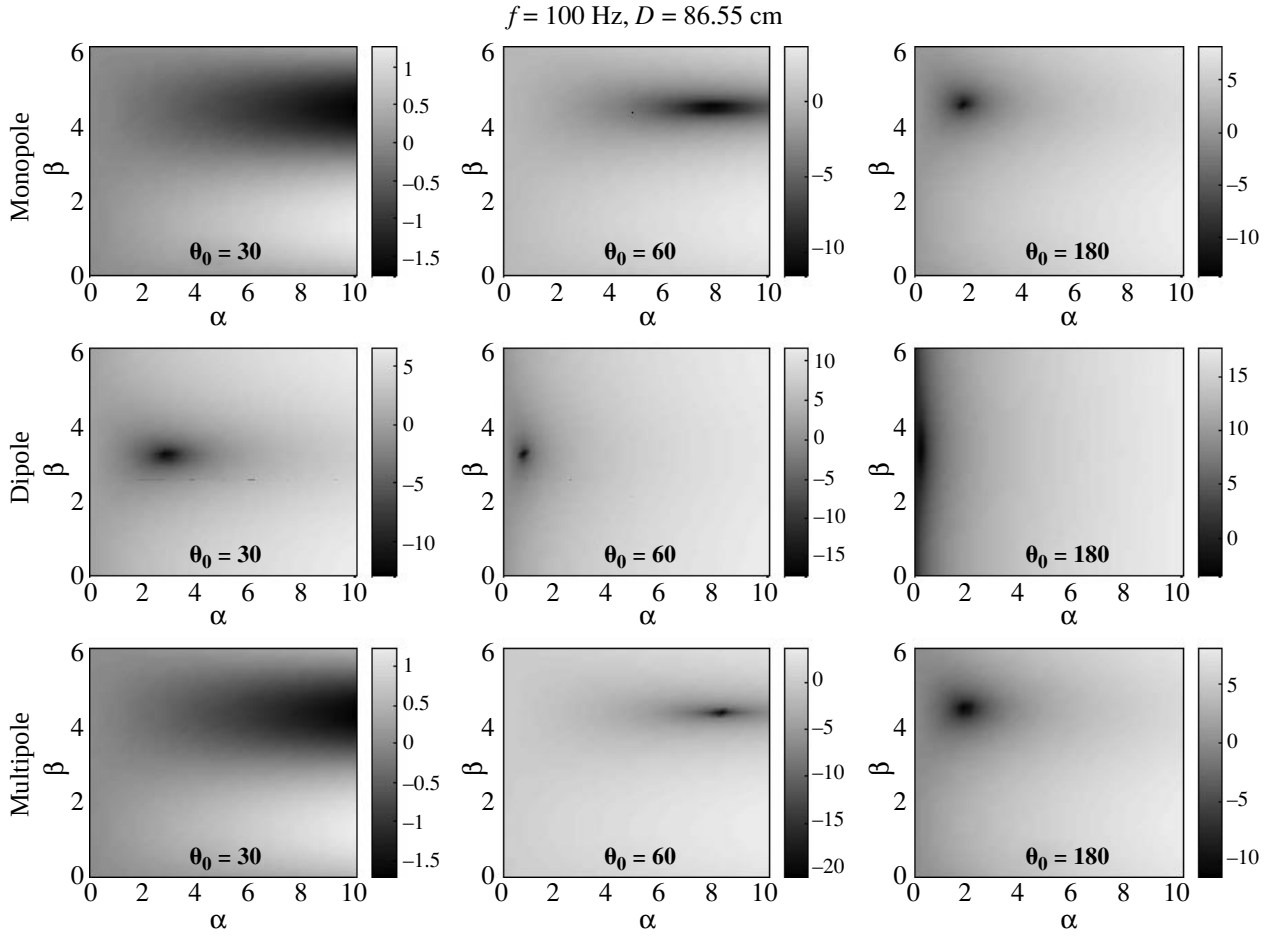

Fig. 2. Sound attenuation due to the presence of the secondary partially vibrating source versus velocity strength α and velocity phase β (rad), $f = 100$ Hz, $D = \lambda/4 = 86.55$ cm.

responding to the waves disseminating from the disquieting source, and the other relating to the waves from the control source. Each of these waves can be represented in the form of an infinite (generalized Fourier) series whose unknown modal coefficients are to be determined by imposing the proper boundary conditions. Accordingly, for axisymmetric motion in bispherical coordinates, we set

$$\Phi^{(P)}(r_1, \theta_1, \omega) = \sum_{n=0}^{\infty} a_n h_n(kr_1) P_n(\eta_1),$$
$$\Phi^{(S)}(r_2, \theta_2, \omega) = \sum_{n=0}^{\infty} b_n h_n(kr_2) P_n(\eta_2), \quad (2)$$

where $h_n(\ ) = j_n(\ ) + iy_n(\ )$ is a spherical Hankel function [26], n is the circumferential wave number, $P_n(\eta_i)$ is a Legendre function ($\eta_i = \cos\theta_i$, $i = 1, 2$), and $a_n(\omega)$ and $b_n(\omega)$ are unknown modal coefficients.

The general expressions for the normal surface velocity of the primary multipole spherical radiators is written as

$$v^{(P)}(\theta_1, \omega) = \sum_{n=0}^{\infty} V_n^{(P)} P_n(\eta_1). \quad (3)$$

Similarly, the piston set in the surface of the secondary rigid sphere pulsates in the region $\pi - \theta_0 \le \theta_2 \le \pi$ with a prescribed complex velocity $V^{(S)}$. The velocity of the piston can be expressed as a linear combination of spherical modes in the form of an infinite series:

$$v^{(S)}(\theta_2, \omega) = \sum_{n=0}^{\infty} V_n^{(S)} P_n(\eta_2)$$
$$= \begin{cases} 0 & 0 \le \theta_2 \le \pi - \theta_0 \\ V^{(S)} & \pi - \theta_0 \le \theta_2 \le \pi, \end{cases} \quad (4)$$

where $V_n^{(S)}$ $(n = 0, 1, 2, \ldots)$ are the complex modal coefficients of surface velocity distributions. These coefficients can be readily determined after multiplying both sides of (4) by $P_m(\eta_2)$, $(m = 0, 1, 2, \ldots)$, integrating over

$d\eta_2$, and applying the orthogonality property of the Legendre functions:

$$V_n^{(S)} = \left(n+\frac{1}{2}\right)V^{(S)}\int_{-1}^{-\eta_0} P_n(\eta_2)d\eta_2 = \frac{V^{(S)}(-1)^n}{2}[P_{n-1}(\eta_0)-P_{n+1}(\eta_0)], \quad (5)$$

where the integrations are performed using the following well-known relation [15]:

$$(2n+1)\int_{\eta_0}^{1} P_n(\eta)d\eta = P_{n-1}(\eta_0)-P_{n+1}(\eta_0). \quad (6)$$

Many radiation and scattering problems involve waves of one characteristic shape (coordinate system) that are incident upon a boundary of some other shape (coordinate system). Thus, it is difficult to satisfy the boundary conditions on that surface. There exists, however, a class of mathematical relationships called wave transformations that circumvent this difficulty in many cases by allowing one to express the incident wave in terms of wave functions for some other coordinate system that is more appropriate for the boundary; i.e., they simply permit the study of the fields scattered by various bodies by referring them all to a common origin ([24, 25]). This transformation (shift of origin) of the wave functions greatly simplifies the task of satisfying the specified boundary conditions on the various surfaces. In particular, to satisfy orthogonality in the current problem (Fig. 1), we need to express the spherical wave functions of the (r_1, θ_1) coordinate system in terms of spherical wave functions of the (r_2, θ_2) coordinate system and, vice versa, through application of the classical form of the translational addition theorem for bispherical coordinates [27]:

$$h_n(kr_s)P_n(\cos\theta_s) = \begin{cases} \sum_{m=0}^{\infty} Q_{mn}(kr_{sl},\theta_{sl})j_m(kr_l)P_m(\cos\theta_l), & r_l < r_{sl} \\ \sum_{m=0}^{\infty} R_{mn}(kr_{sl},\theta_{sl})h_m(kr_l)P_m(\cos\theta_l), & r_l > r_{sl}, \end{cases} \quad (7)$$

where s, $l = 1, 2$ $(s \neq l)$, $j_n(\ )$ is the spherical Bessel function of order n [26], θ_{sl} is the angle between the z_s axis and the O_sO_l line (i.e., such that $\theta_{12} = 0$ or $\theta_{21} = \pi$), $r_{12} = r_{21} = D$ is the center–center distance (Fig. 1), and

$$Q_{mn}(kr_{sl},\theta_{sl}) = i^{m-n}(2m+1)\times\sum_{\sigma=|m-n|}^{m+n} i^{\sigma}b_{\sigma}^{nm}h_{\sigma}(kr_{sl})P_{\sigma}(\cos\theta_{sl}),$$
$$R_{mn}(kr_{sl},\theta_{sl}) = i^{m-n}\times\sum_{\sigma=|m-n|}^{m+n} i^{\sigma}(2\sigma+1)b_{\sigma}^{nm}j_{\sigma}(kr_{sl})P_{\sigma}(\cos\theta_{sl}), \quad (8)$$

where $b_{\mu}^{nm} = (nm00|\mu0)^2$, in which the Clebsch–Gordan coefficients are defined, with $q = (\mu + n + m)/2$ and $2q$ being even, as [26]

$$(nm00|\mu0) = \frac{(-1)^{\mu+q}q!}{(q-n)!(q-m)!(q-\mu)!}\times\sqrt{\frac{(2\mu+1)}{(2q+1)!}(2q-2n)!(2q-2m)!(2q-2\mu)!}, \quad (9)$$

and, when $2q$ is odd, $(nm00|\mu0) = 0$.

Incorporation of the above addition theorem in (2) allows us to translate the wave components of the first coordinate system in terms of spherical wave functions of the second coordinate system and vice versa, i.e.,

$$\Phi^{(P)}(r_2,\theta_2,\omega) = \sum_{n=0}^{\infty}\left[\sum_{m=0}^{\infty} a_m Q_{mn}(kD,0)\right]j_n(kr_2)P_n(\eta_2),$$
$$\Phi^{(S)}(r_1,\theta_1,\omega) = \sum_{n=0}^{\infty}\left[\sum_{m=0}^{\infty} b_m Q_{mn}(kD,\pi)\right]j_n(kr_1)P_n(\eta_1). \quad (10)$$

The modal coefficients $a_m(\omega)$ and $b_m(\omega)$ must be determined by imposing suitable boundary conditions. The continuity of radial velocity components at the surface of each sphere implies that

$$-\frac{\partial\Phi^{(T)}(r_1,\theta_1,\omega)}{\partial r_1}\Big]_{r_1=a} = \sum_{n=0}^{\infty} V_n^{(P)}P_n(\eta_1),$$
$$-\frac{\partial\Phi^{(T)}(r_2,\theta_2,\omega)}{\partial r_2}\Big]_{r_2=b} = \sum_{n=0}^{\infty} V_n^{(S)}P_n(\eta_2), \quad (11)$$

where $\Phi^T(r_i, \theta_i, \omega) = \Phi^{(P)}(r_i, \theta_i, \omega) + \Phi^{(S)}(r_i, \theta_i, \omega)$, $(i = 1, 2)$. Substitution of velocity potential expansions (2), (5), and (10) into the above boundary conditions leads to

$$-k\left[h_n'(ka)a_n + j_n'(ka)\sum_{n=0}^{\infty} b_m(\omega)Q_{mn}(kD,\pi)\right] = V_n^{(P)},$$
$$2k(-1)^{n+1}\left[j_n'(kb)\sum_{n=0}^{\infty} a_m(\omega)Q_{mn}(kD,0)\right. \quad (12)$$

$$+ h_n'(kb)b_n \Big] = [P_{n-1}(\eta_0) - P_{n+1}(\eta_0)]V^{(S)}, \tag{12}$$

where the prime symbol indicates the derivative with respect to the argument. Subsequently, the unknown coefficients $a_n(\omega)$ and $b_n(\omega)$ may be readily computed by solving the linear system of equations (12). Now, from the second of (1), (2), and (10), the radiated acoustic pressure may be written as

$$p(r_1, \theta_1, \omega) = -i\omega\rho\Bigg\{\sum_{n=0}^{\infty}\Bigg[a_n h_n(kr_1)P_n(\cos\theta_1) + \sum_{m=0}^{\infty} b_m Q_{mn}(kD, \pi) j_n(kr_1)P_n(\eta_1)\Bigg]\Bigg\}. \tag{13}$$

As a final point, the acoustic sound attenuation (*SA*) due to the presence of the partially vibrating canceller can be obtained:

$$SA(\omega, V^{(S)}) = 10\log\left(\frac{\left|\sum_{n=0}^{\infty} a_n h_n(kr_1)P_n(\cos\theta_1) + \sum_{n=0}^{\infty}\sum_{m=0}^{\infty} b_m Q_{mn}(kD, \pi) j_n(kr_1)P_n(\eta_1)\right|}{\left|\sum_{n=0}^{\infty} \frac{V_n^{(P)}}{kh_n'(ka)} h_n(kr_1)P_n(\cos\theta_1)\right|}\right). \tag{14}$$

3. NUMERICAL RESULTS AND DISCUSSIONS

In order to illustrate the nature and general performance of the solution, a number of particular numerical examples are considered in this section. There are many conditions under which the active control system works effectively. In the present paper, among all of the factors, special attention is given to the following subjects: primary-source surface vibration type (i.e., monopole, dipole, and general source), separation distance, and effective vibrating area of the secondary source. Subsequently, a MATLAB program was constructed for treating the boundary conditions, to determine the unknown modal coefficients, and to compute the sound attenuation (*SA*) of the system as functions of $V^{(S)}$ for various cap angles ($\theta_0 = 30°$, 60°, and 180°) at two excitation frequencies ($f = 100$, 250 Hz) when the primary source may vibrate in the monopole ($n = 0$), dipole ($n = 1$), or any of the higher multipole-like ($n = 1, 2, 3, 4, \ldots$) modes. It is noteworthy that the first two modes (i.e., the pulsating ($n = 0$) and the oscillating ($n = 1$) sources) are of most practical interest, as they are known to best represent the "expander" and "shaker" type acoustic transducers, respectively ([24], [25], and [28]). In order to produce a monopole (dipole) primary source in the computation process, it is sufficient to assume $V_0^{(P)} = 1$ ($V_1^{(P)} = 1$); also, for a multipole primary source, i.e., a general source, it should be assumed that $V_0^{(P)} = V_1^{(P)} = V_2^{(P)} = \ldots = 1$. In this example, the ambient fluid is assumed to be air at atmospheric pressure and room temperature, and the primary (secondary) finite source is presumed to be of dimension $a = 10$ cm ($b = 5$ cm). The computations were performed on a Pentium III personal computer with a truncation constant of $N = 20$ to assure convergence in the high-frequency range, and also in the case of close proximity of the secondary source to the primary source.

An important question in the practical application of a noise-control system is finding the necessary velocity of the secondary source (the phase and strength) to achieve maximum sound attenuation. In order to elucidate this point, Figs. 2–5 are displayed: they show the effect of varying the secondary-source velocity characteristics, namely, strength and phase, on the sound attenuation of the sound-control system presented here. It is assumed that the secondary control source is pulsating with a different amplitude and phase in comparison with the primary source, in order to minimize the sound pressure at a point within a region downstream of the secondary source ($R = 70$ cm, $\theta_1 = 0$). Hence, the secondary-source velocity can be written as $V^{(S)} = \alpha\exp(i\beta)$, where

$$\alpha = \sqrt{\Re(V^{(S)})^2 + \Im(V^{(S)})^2}, \quad \tan\beta = \Im(V^{(S)})/\Re(V^{(S)}), \quad (0 \le \beta \le 2\pi).$$

Figures 2 and 3 show the sound attenuation, $SA(\omega, V^{(S)})$, of the active noise-control system when the sources are vibrating at a selected frequency of $f = 100$ Hz and when the selected separation distances are $D = \lambda/4 = 86.55$ cm and $D = \lambda = 346.20$ cm, respectively [5]. A comparison of these figures leads to the following remarks. Using a baffled piston source instead of a wholly vibrating source ($\theta_0 = 180°$) as a sound controller will generally increase the efficiency of the control system, particularly when the primary source vibrates as a dipolar or a generally vibrating source (multipole source). Additionally, Fig. 2 shows that, for a dipolar disturbing source when the control source is positioned in close proximity to it ($D = \lambda/4$), a secondary source is needed to vibrate in antiphase ($\beta \approx \pi$) and with a weak strength $\alpha = 0.769$ in comparison with the primary

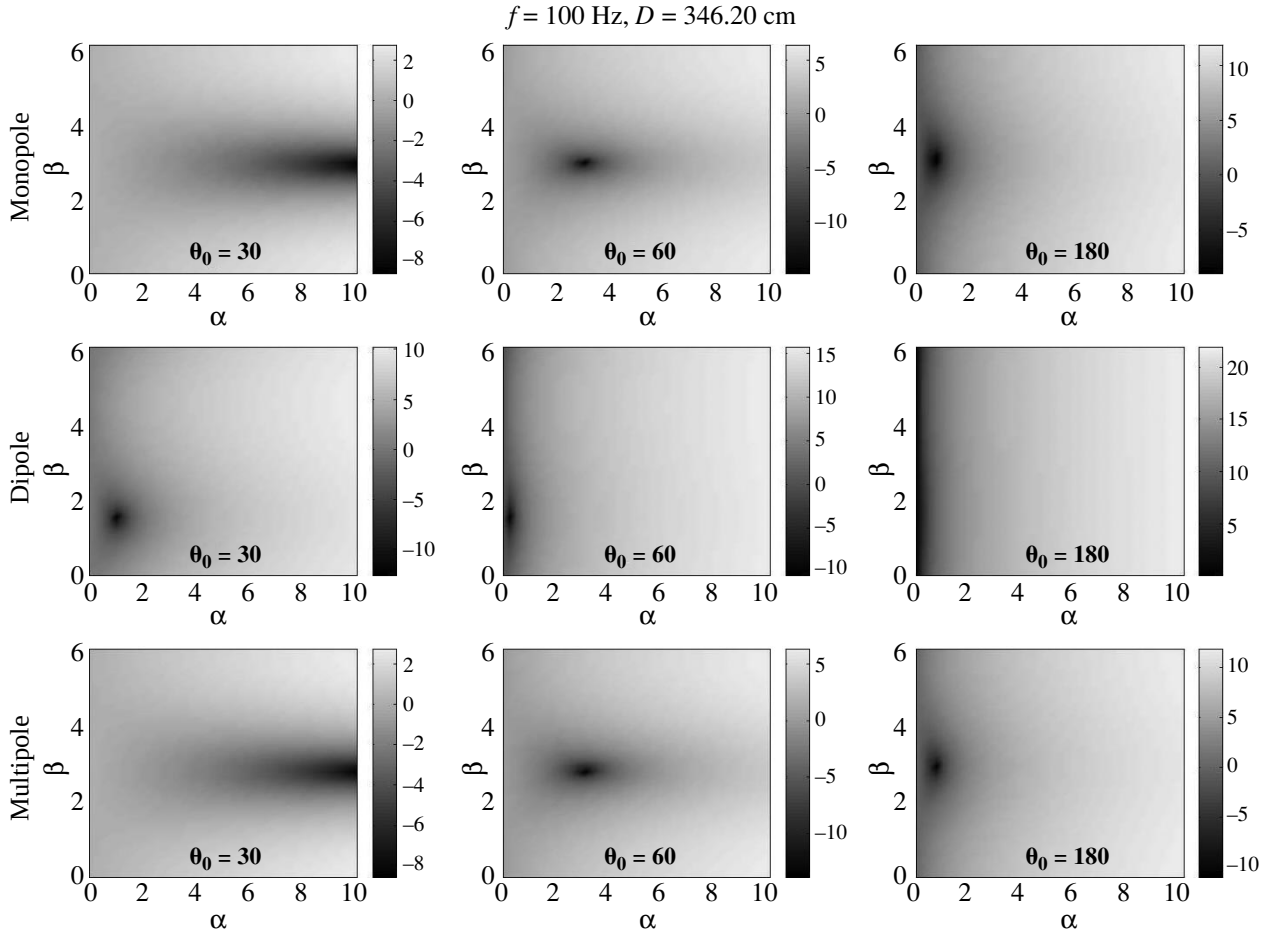

Fig. 3. Sound attenuation due to the presence of the secondary partially vibrating source versus velocity strength α and velocity phase β (rad), f = 100 Hz, $D = \lambda$ = 346.20 cm.

source to gain maximum sound attenuation. Furthermore, achieving an acceptable attenuation level (SA = –10 dB) for a monopole primary source by means of a baffled piston ($\theta_0 = 30°$ or 60°) located $\lambda/4$ away from the primary source requires a more forceful secondary source ($\alpha \geq 7.5$), but the same required attenuation level can be achieved with a weaker wholly vibrating source (α = 1.8). To have an all-encompassing study, it is required to scrutinize the shadow effect of the secondary source on the sound reduction at the selected point (microphone point). The shadow effect of the secondary source can be seen from the figures when $\alpha = 0$ (i.e., a rigid sphere). The numerical results reveal that the presence of a finite secondary source does not have any apparent effect on the sound attenuation of the system, so the active noise-cancellation process is the most important reason for sound attenuation. Moreover, the figures show that, as the value of the cap angle is increased, the adequate velocity strength of the secondary source is decreased but the velocity phase of the canceller source remains unchanged; alternatively, increasing the separation distance D will decrease the required phase of the secondary source.

Figures 4 and 5 show the sound reduction in a control system when the separation distances are $D = \lambda/4$ = 34.62 cm and $D = \lambda$ = 138.48 cm respectively, and the system is excited at a frequency of f = 250 Hz. A comparison of Figs. 4 and 5, in addition to the results noted in the previous paragraph, leads to the following observations. Although using a secondary source with a small cap ($\theta_0 = 30°$) when the dipole primary source is located at distance $D = \lambda/4$ = 34.62 cm away from the control source leads to maximum sound attenuation (SA = –15), the $\theta_0 = 60°$ case will attain the required sound attenuation level of 10 dB with a lower velocity strength (α = 2.56). Finally, the velocity power and phase angle of the selected secondary source, $\theta_0 = 60°$, as seen from Figs. 2–5, are summarized in the table.

In Figs. 6 and 7, we show the acoustic field computed all around the primary source (360° azimuthal angle), $10\log[|p(\theta_1, \omega)|]$, versus the angular parameter θ_1 for prescribed values of α, β from the table. These

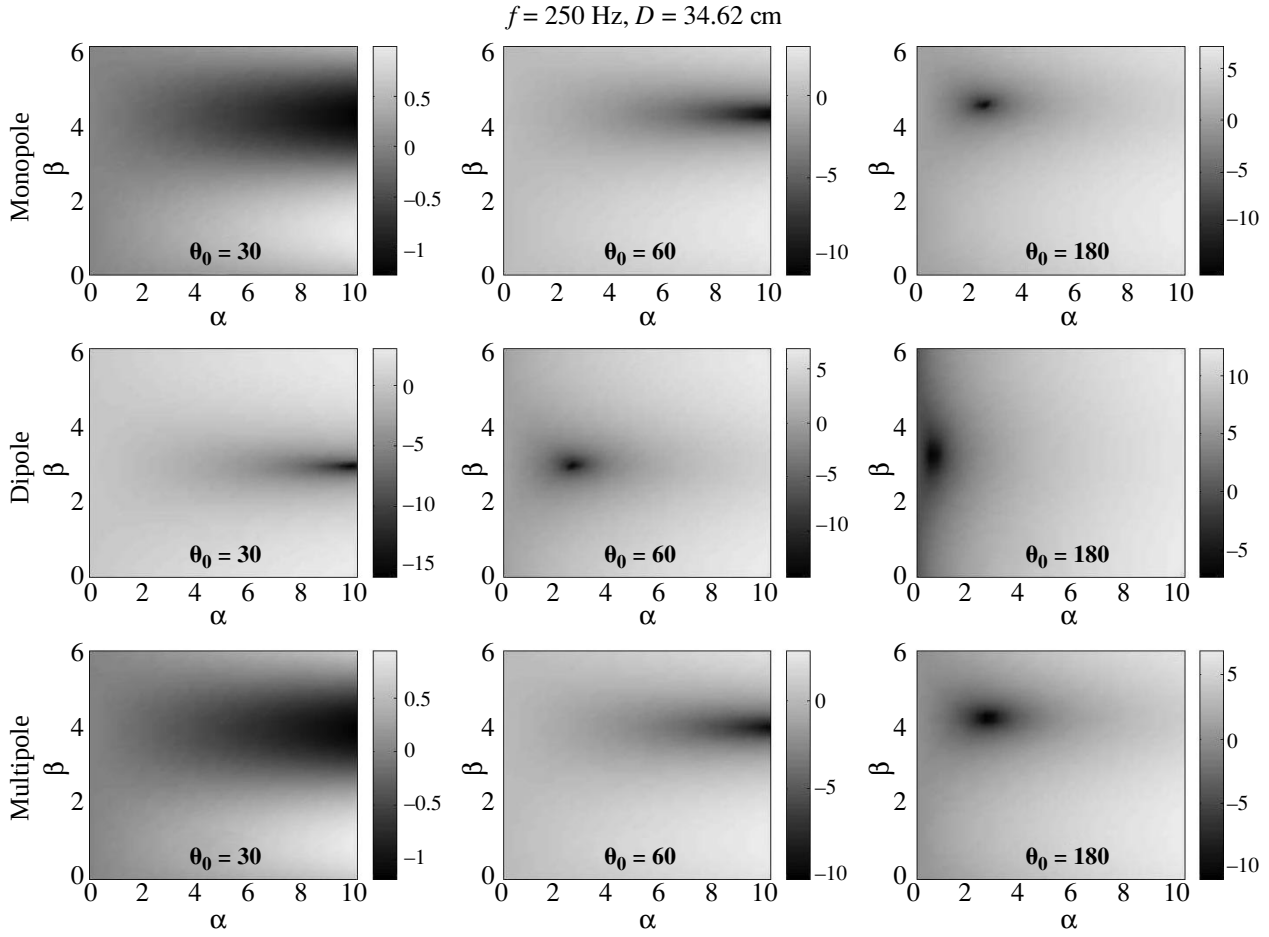

Fig. 4. Sound attenuation due to the presence of the secondary partially vibrating source versus velocity strength α and velocity phase β (rad), $f = 250$ Hz, $D = \lambda/4 = 34.62$ cm.

figures illustrate that, for a dipole and multipole primary source, using a baffled piston ($\theta_0 = 60°$) not only decreases the sound pressure at $\theta_1 = 0°$ (the main objective of the previous sections) but also allows all-around sound reduction to be achieved (i.e., this means that, in addition to minimization of pressure at a single point, the total output energy from the system is decreased as well). Also, the figures make clear that, although in all of the cases noise cancellation at a particular point, namely, ($R = 0.7$ m, $\theta_1 = 0°$), is achieved with an acceptable attenuation (10 dB), a single secondary source is not able to cancel the sound pressure of a monopole primary source all around it. These results demonstrate that the acceptable zone of quiet, $SA = -10$ dB, for a monopole primary source after the sound-cancellation operation is the region $-8° \le \theta_1 \le 8°$($-4.5° \le \theta_1 \le 4.5°$) when $f = 100$ Hz ($f = 250$ Hz). The presented results are comparable with those found in [29] using a wall of secondary monopole sources. It is worth mentioning here that the reason for the creation of this quiet region

Secondary-source velocity strength (α) and phase (β) required to minimize the sound pressure at $R = 0.7$ m, $\theta_1 = 0$

	$f = 100$ Hz, $D = \lambda/4$		$f = 100$ Hz, $D = \lambda$		$f = 250$ Hz, $D = \lambda/4$		$f = 250$ Hz, $D = \lambda$	
	α	β	α	β	α	β	α	β
Monopole	7.9487	4.6721	3.0769	3.0610	10.000	4.3499	5.6410	2.8999
Dipole	0.7692	3.3833	0.2564	1.6111	2.5641	3.0610	1.2821	1.4500
Multipole	8.2051	4.5110	3.0769	2.8999	10.000	4.1888	5.8974	2.5777

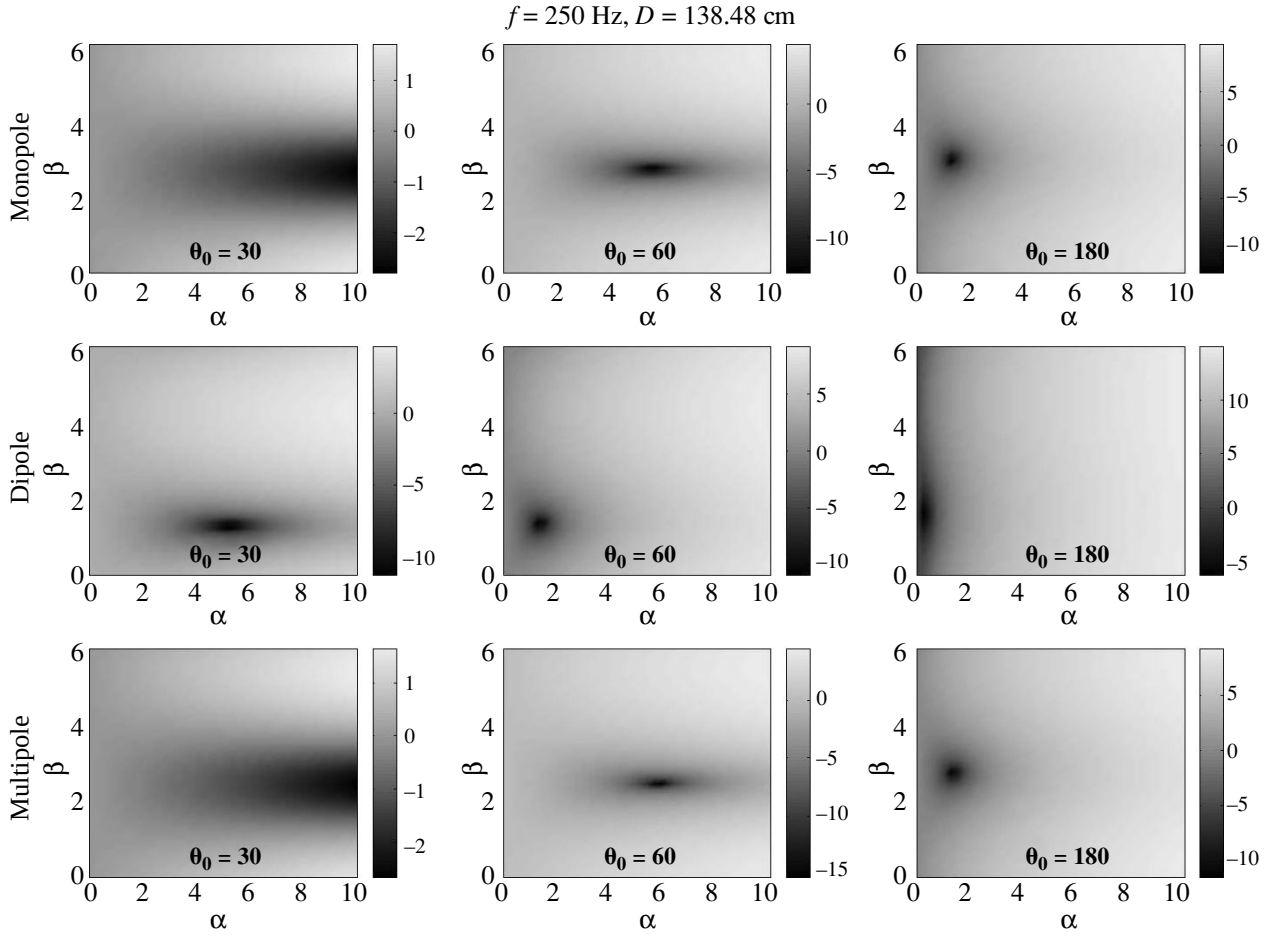

Fig. 5. Sound attenuation due to the presence of the secondary partially vibrating source versus velocity strength α and velocity phase β (rad), $f = 250$ Hz, $D = \lambda = 138.48$ cm.

is "active noise control," not the shadow effect due to the presence of the secondary finite source, but, on the other hand, the presence of a vibrating obstacle near a primary source leads to an increase in the number of lobes after the noise-cancellation process.

Finally, in order to check the overall validity of the work, the code was used to compute the normalized average radiation impedance load per unit area for the case of two vibrating spherical surfaces. The fluctuating fluid pressure on the surface of a vibrating source constitutes its radiation loading. The normalized average acoustic radiation impedance load per unit area on the vibrating piston may be computed by making use of Foldy's definition of the radiated power ([15, 30])

$$Z = R - iX = \frac{1}{4\pi\rho c (V^{(S)} b_e)^2} \times \int_{-1}^{-\eta_0} p(r_2 = b, \eta_2, \omega)(v^{(S)})^* d\eta_2,$$

where $b_e = b\sin(\theta_0/2)$ is the effective piston radius (i.e., the radius of the sphere that has the same area as the piston), ρc is the characteristic impedance, the asterisk indicates the complex conjugate, and R and X are the average acoustic resistance and reactance, respectively. Moreover, $p(b, \eta_2, \omega)$ is the acoustic pressure on the surface of the secondary sphere, which can be readily obtained by incorporating (2) and (10) in the second equation of (1):

$$p(r_2, \theta_2, \omega)]_{r_2 = b} = -i\omega\rho\Phi^T(r_2, \theta_2, \omega)]_{r_2 = b} = -i\omega\rho\sum_{n=0}^{\infty}\Psi_n(b, \omega)P_n(\eta_2),$$

where

$$\Psi_n(b, \omega) = j_n(ka)\sum_{m=0}^{\infty} a_m(\omega)Q_{mn}(kD, 0) + h_n(ka)b_n.$$

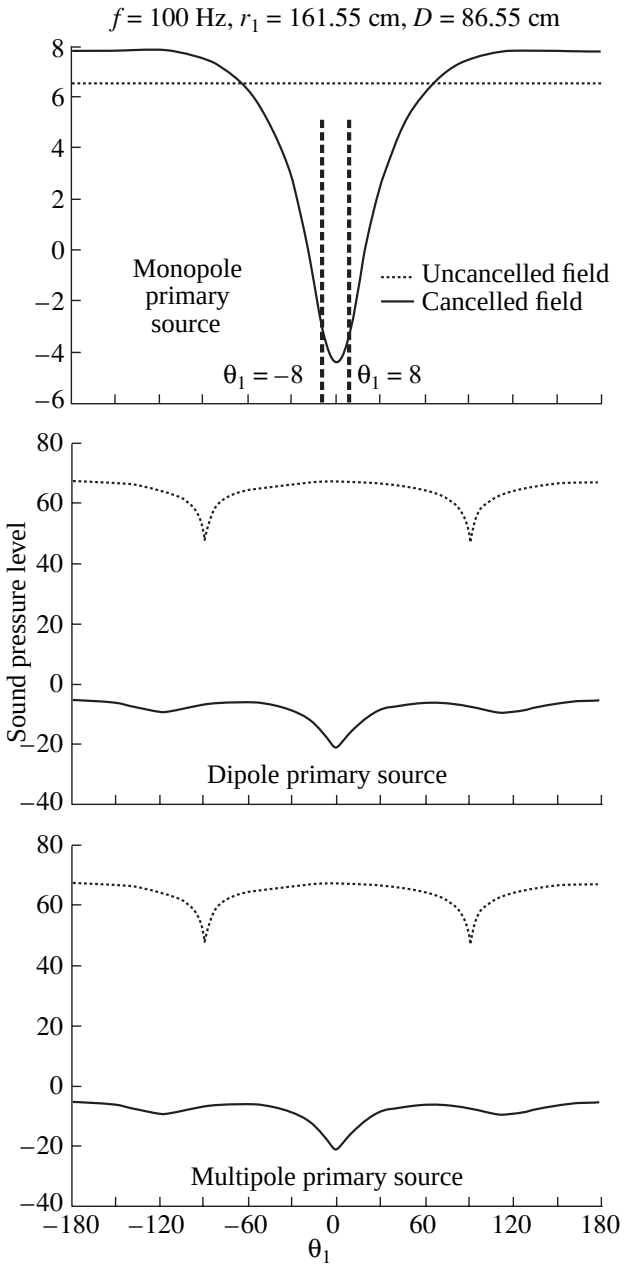

Fig. 6. Sound pressure levels versus the angular parameter θ_1 for prescribed values of α, β from the table, $f = 100$ Hz, $D = \lambda/4 = 86.55$ cm.

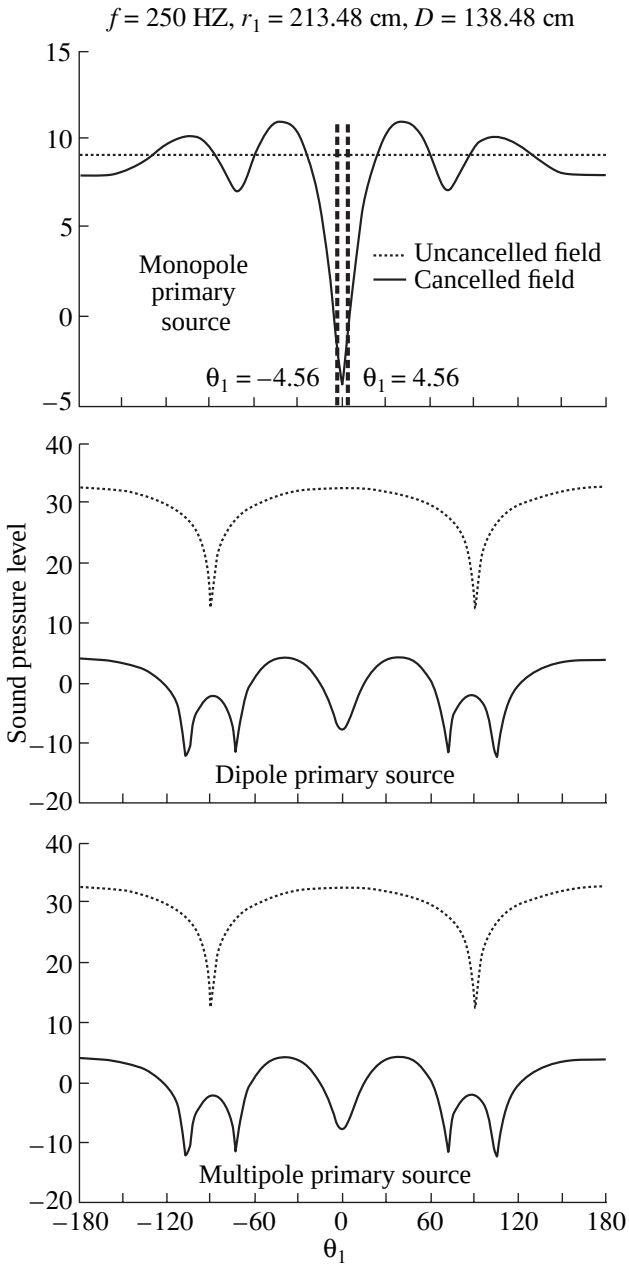

Fig. 7. Sound pressure levels versus the angular parameter θ_1 for prescribed values of α, β from the table, $f = 250$ Hz, $D = \lambda = 138.48$ cm.

After incorporating these two equations in Foldy's definition and integrating over $d\eta_2$, the modal acoustic impedance can be found. Numerical verifications are made by executing the general code for the case of a spherical cap positioned very far ($D = 200b$) from the primary sphere, and the corresponding radiation impedance components precisely reduce to the curves appearing in Fig. 20.4, page 308 in [15] (for brevity, the corresponding validation plots are not included). Subsequently, further verifications were made for the wholly vibrating cap ($\theta_0 = 180°$) positioned close to a pulsating spherical source. Figure 8 shows that the acoustic impedance components corresponding to the wholly radially vibrating sphere ($\theta_0 = 180°$, $V^{(S)} = 1$) near a monopole source ($V_0^{(P)} = 1$) agree very well with the results presented in Figs. 1 and 2 of Thompson's work [25]. Note that each curve is normalized to its corresponding value when the source is in an unbounded medium.

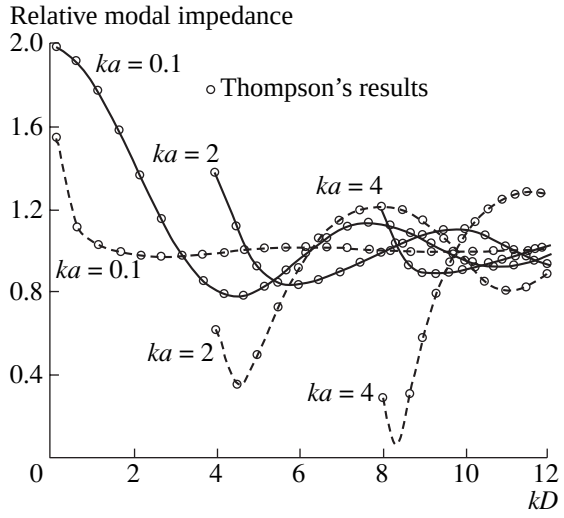

Fig. 8. Modal impedance curves of a pair of pulsating spheres in an infinite medium. Solid line: relative modal resistance; dotted line: relative modal reactance.

4. CONCLUSIONS

Active noise control of a generally vibrating spherical source with a single baffled piston was investigated in this paper. The presented results are the product of an exact multiscattering treatment that involves utilization of the translational addition theorem for spherical wave functions. Examples are presented for a primary source acting in the low-frequency range, $f = 100$, 250 Hz. The numerical results reveal that the shadow effect of the secondary finite source is negligible in comparison with the effect of the sound-cancellation mechanism. Furthermore, using a baffled piston instead of a wholly pulsating sphere increases the efficiency of the control system, especially for a dipole or multipole unwanted source, but the prescribed system is not acceptable for a monopole primary source and the system presented in [4] (i.e., using a monopole control source) is more efficient. The offered work is an idealized model for active noise control of a spherical multipole source, which can be of interest in noise-control engineering, room acoustics, and outdoor acoustics. The calculated results may also possibly be used to validate those found by experiment.

REFERENCES

1. H. F. Olson and E. G. May, J. Acoust. Soc. Am. **25**, 1130 (1953).
2. M. V. Fedoryuk, Acoust. Phys. **25**, 61 (1979).
3. A. A. Mazanikov, V. V. Tyutekin, and M. V. Fedoryuk, Acoust. Phys. **26**, 428 (1980).
4. P. A. Nelson and S. J. Elliott, J. Sound Vib. **105**, 173 (1986).
5. P. A. Nelson, R. D. Curtis, S. J. Elliott, and A. J. Bullmore, J. Sound Vib. **116**, 397 (1987).
6. P. Joseph, S. J. Elliott, and P. A. Nelson, J. Sound Vib. **172**, 605 (1994).
7. A. David and S. J. Elliott, Appl. Acoust. **41**, 63 (1994).
8. S. J. Elliott, P. Joseph, A. J. Bullmore, and P. A. Nelson, J. Sound Vib. **120**, 183 (1988).
9. S. J. Elliott and J. Garcia-Bonito, J. Sound Vib. **186**, 696 (1995).
10. J. Garcia-Bonito, S. J. Elliott, and M. Bonilha, J. Sound Vib. **201**, 43 (1997).
11. J. S. Bolton, B. K. Gardner, and T. A. Beauvilain, J. Acoust. Soc. Am. **98**, 2343 (1995).
12. T. Martin and A. Roure, J. Sound Vib. **201**, 577 (1997).
13. T. Martin and A. Roure, J. Sound Vib. **212**, 511 (1998).
14. A. A. Mazanikov, Akust. Zh. **46**, 89 (2000) [Acoust. Phys. **46**, 76 (2000)].
15. E. Skudrzyk, *The Foundations of Acoustics: Basic Mathematics and Basic Acoustics* (Springer, New York, 1971; Mir, Moscow, 1976).
16. C. H. Sherman, J. Acoust. Soc. Am. **31**, 947 (1959).
17. J. E. Greenspon and C. H. Sherman, J. Acoust. Soc. Am. **36**, 149 (1964).
18. B. Baier, J. Acoust. Soc. Am. **51**, 1705 (1972).
19. J. E. Boisvert and A. L. Van Buren, J. Acoust. Soc. Am. **111**, 867 (2002).
20. S. M. Hasheminejad and M. Azarpeyvand, IEEE J. Ocean. Eng. **29**, 110 (2004).
21. S. M. Hasheminejad and M. Azarpeyvand, IEEE J. Ocean. Eng. **31** (8–9), 1129 (2004).
22. X. Qiu and C. H. Hanson, J. Sound Vib. **232**, 1005 (2000).
23. A. D. Pierce, *Acoustics: An Introduction to Its Physical Principles and Applications* (Am. Inst. Phys., New York, 1991).
24. W. Thompson, Jr., J. Acoust. Soc. Am. **60**, 781 (1976).
25. W. Thompson, Jr., J. Acoust. Soc. Am. **62**, 8 (1977).
26. *Handbook of Mathematical Functions*, Ed. by M. Abramowitz and I. A. Stegun (National Bureau of Standards, Washington, 1964; Nauka, Moscow, 1979).
27. Y. A. Ivanov, *Diffraction of Electromagnetic Waves on Two Bodies* (Nauka Tekh., Minsk, 1968; NASA, Washington, 1970).
28. S. M. Hasheminejad and M. Azarpeyvand, Acta Acust. **89**, 998 (2003).
29. S. E. Wright and B. Vuksanovic, J. Sound Vib. **190**, 565 (1996).
30. W. Thompson, Jr., J. Acoust. Soc. Am. **54**, 1694 (1973).

Acoustical Physics, Vol. 51, No. 6, 2005, pp. 619–628. Translated from Akusticheskiĭ Zhurnal, Vol. 51, No. 6, 2005, pp. 721–731.

Hydroacoustic Coordinate-Measuring System of the NT-200 Baikal Neutrino Telescope

V. M. Aĭnutdinov[1], V. A. Balkanov[1], I. A. Belolaptikov[7], L. B. Bezrukov[1], N. M. Budnev[2], R. V. Vasil'ev[7], R. Wischnewski[8], E. A. Vyatchin[1], O. N. Gaponenko[1], O. A. Gress[2], T. I. Gress[2], I. A. Danil'chenko[1], Zh-A. M. Dzhilkibaev[1], A. A. Doroshenko[1], A. N. D'yachok[2], G. V. Domogatskiĭ[1], V. A. Zhukov[1], V. L. Zurbanov[2], A. M. Klabukov[1], A. I. Klimov[6], S. I. Klimushin[1], E. O. Kozakov[2], K. V. Konishchev[7], A. P. Koshechkin[1], V. E. Kuznetsov[1], V. F. Kulepov[4], L. A. Kuz'michev[3], Yu. B. Lanin[2], S. V. Lovtsov[2], B. K. Lubsandorzhiev[1], T. Mikolajski[8], M. B. Milenin[4], R. R. Mirgazov[2], S. P. Mikheev[1], A. V. Moroz[2], N. I. Moseĭko[3], S. A. Nikiforov[2], É. A. Osipova[3], A. I. Panfilov[1], A. A. Pavlov[2], G. L. Pan'kov[2], L. V. Pan'kov[2], Yu. V. Parfenov[2†], E. N. Pliskovskiĭ[7], V. A. Poleshchuk[1], S. I. Polityko[2†], E. G. Popova[3], P. G. Pokhil[1], V. A. Primin[2], V. V. Prosin[3], A. V. Rzhetsichkiĭ[2], M. I. Rozanov[5], V. Yu. Rubtsov[2], Yu. A. Semeneĭ[2], B. A. Tarashchanskiĭ[2], S. V. Fialkovskiĭ[4], A. G. Chenskiĭ[2], D. V. Chernov[3], B. A. Shaĭbonov[1], Ch. Spiering[8], and I. V. Yashin[3]

[1] Institute of Nuclear Research, Russian Academy of Sciences, pr. 60-letiya Oktyabrya 7a, Moscow, 119312 Russia

[2] Irkutsk State University, ul. K. Marksa 1, Irkutsk, 664003 Russia

[3] Moscow State University, Vorob'evy gory, Moscow, 119992 Russia

[4] Nizhni Novgorod State Technical University, ul. Minina 24, Nizhni Novgorod, 603600 Russia

[5] St. Petersburg State Marine Technical University, ul. Lotsmanskaya 3, St. Petersburg, 190008 Russia

[6] Kurchatov Institute Russian Research Center, pl. Kurchatova 1, Moscow, 123182 Russia

[7] Joint Institute for Nuclear Research, ul. Zholio-Kyuri 6, Dubna, Moscow oblast, 141980 Russia

[8] DESY-Zeuthen, Platanenallee 6, D-15738, Zeuthen, Germany

e-mail: nbudnev@api.isu.ru

Received June 16, 2004

Abstract—The hydroacoustic coordinate-measuring system of the NT-200 Baikal neutrino telescope is described. It is a ranging long-base hydroacoustic system constantly operating in an automated or interactive mode and capable of measuring the coordinates of the detecting modules of the NT-200 to within 20 cm. Special attention is given to the justification of the estimate of the coordinate measurement errors. As an illustration, some results of measuring the coordinates of the elements of the NT-200 and the hydrophysical characteristics of lake Baikal are presented. © *2005 Pleiades Publishing, Inc.*

1. INTRODUCTION

The idea of developing large deep-water systems for detecting elementary particles in natural water basins was put forward by M.A. Markov 40 years ago [1]. The essence of the idea consists in using an array of photodetectors deployed in a deep natural water basin to detect the Cherenkov radiation of relativistic particles moving in water, specifically, the particles produced by the interaction of high-energy neutrinos with the medium. Such systems were expected to allow the scientists to solve a variety of problems of high-energy neutrino astrophysics, high-energy physics, and elementary particle physics [2].

The first deep-water neutrino detector was the NT-200 Baikal neutrino telescope, which was put into full operation in April 1998 [3]. Today, the ANTARES neutrino detector is at the stage of realization in the Tulon bay [4] and two more deep-water neutrino detectors, NEMO [5] and NESTOR [6], are under development in the Mediterranean Sea. All of these systems are intended for the detection of Cherenkov radiation of the relativistic charged particles produced by the interaction of neutrinos with the medium. Today, the possibility to study high-energy neutrinos by detecting the acoustic signals from cascade showers [7] is at the initial stage of investigation.

In all the deep-water neutrino detector projects, the detecting modules are mounted on submerged buoy stations of different configurations with the distances between them being much smaller than their lengths. However, the buoy stations, whose lower ends are anchored to the bottom, move in space under the effect

† Deceased.

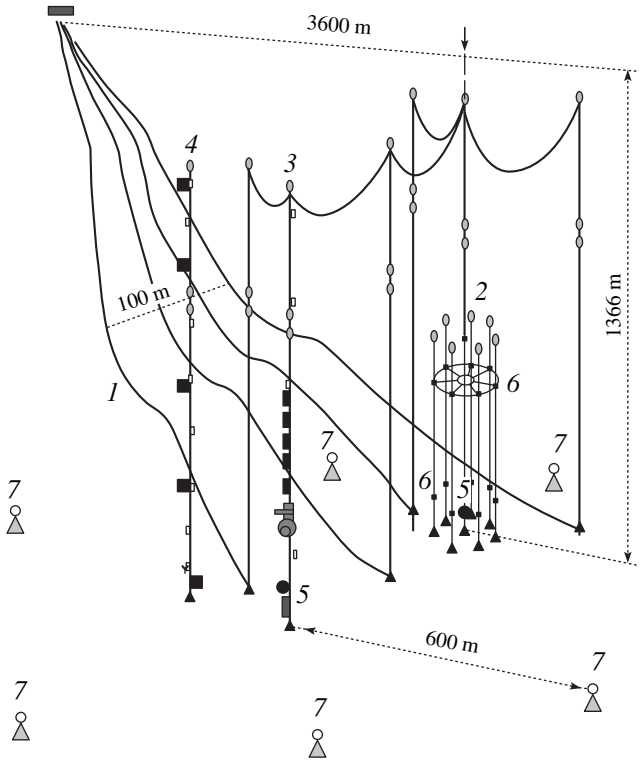

Fig. 1. The NT-200 deep-water Baikal neutrino telescope system: (*1*) cable communication lines, (*2*) NT-200 neutrino telescope, (*3*) hydrological string, (*4*) sedimentological string, (*5*) master modules, (*6*) acoustic receivers, and (*7*) acoustic beacons.

of currents, which occur in large natural water basins at any depth. Therefore, two problems arise:

(i) the determination of the possible evolution of the buoy stations forming the deep-water system of the detector and the consideration of the probability of their confusion due to the inhomogeneity of currents and the differences in buoy-station configurations;

(ii) the determination of the actual spatial positions of all detecting modules of the neutrino detector after their placement and the realization of the long-term monitoring of their coordinates to provide an adequate reconstruction of the events.

The problem of determining the spatial position of an object in the water medium is a common problem of practical oceanology. As a rule, it is solved using acoustic systems that determine the coordinates of objects with respect to a certain number of reference points—acoustic beacons [8, 9]. A specific feature of the case of a deep-water neutrino telescope is the necessity to provide long-term permanent measurement of the coordinates of many objects distributed over a large water volume (about one cubic kilometer).

In this paper, we describe the hydroacoustic coordinate-measuring system (HCMS) of the NT-200 neutrino telescope. This system is capable of permanent operation in an automated or interactive mode; it has a long base and allows one to measure the coordinates of the detecting modules of the NT-200 with an accuracy of 20 cm or better. We give special attention to the evaluation of the coordinate measurement errors. We also present some results obtained by measuring the coordinates of the modules of NT-200 and the results of measuring the velocity of sound in the Baikal water.

In the HCMS of NT-200, acoustic signals propagate over several tens of trajectories in a volume on the order of one cubic kilometer, which makes it possible to use this system for studying hydrophysical processes. In particular, it is possible to monitor the variations of the mean water temperature in different layers of the lake over a long period of time. This is an important alternative method for studying the variations in the heat store of the lake, the water-exchange processes, and other phenomena characterized by different space and time scales.

2. STRUCTURE OF THE HYDROACOUSTIC COORDINATE-MEASURING SYSTEM OF NT-200

The general view of the NT-200 deep-water neutrino telescope and its HCMS is shown in Fig. 1. The HCMS includes:

—a shore station consisting of a control computer, a communication modem, and a power supply unit;

—a cable communication line about 7 km in length;

—transceivers (master modules) and ultrasonic receivers (acoustic receivers);

—self-contained transponders—bottom beacons.

2.1. Master Modules and Acoustic Receivers

Durable cylindrical casings of the master modules and acoustic receivers are made of the AMG-6 aluminum alloy. Crates with electronics are fixed to the upper covers of the instruments. A cover has two holes for the modular parts of pressure-seal connectors. One of the connectors is used for the power supply and for communication with the shore station, and the other, for the connection to the hydrophone. As electroacoustic transducers the HCMS uses hydrophones made on the basis of piezoceramic spheres 50 mm in diameter. Their maximum sensitivity at a frequency of 30 kHz is 250–300 μV/Pa.

The HCMS contains more than twenty acoustic receivers and master modules placed on nine buoy stations, and all of them are connected in parallel to one conductor of the KG7-70-90 geophysical cable, which serves for the power supply and communication with the shore station. To ensure the performance of the system in the case of a leak or shortage in one of the instruments, each of the casings contains a sealed optronic switch through which high voltage arrives at the power supply unit. In the initial state, all switches are in the open-circuit position. At the initiation of the system,

according to the commands from the shore station, all the optronic switches are sequentially closed by individual codes. If the current consumption in one of the instruments exceeds the allowed limit, this instrument is excluded from the configuration and is not turned on at the next initiation. The electronics of an acoustic receiver is assembled on the basis of low-consumption components and includes a power-supply unit, which transforms the input dc voltage of 300 V to low voltages, and a receiving channel, which contains a selective amplifier, an envelope detector, a threshold device, and a signal duration check circuit. A master module additionally contains an ultrasonic signal generator.

The control over the measurement process and the communication of the acoustic receivers and master modules with the shore station occur through K1821BM85-microprocessor-based controllers. The latter provide for

—the execution of measurements according to a preset program,

—the preliminary data processing and the compaction of data,

—the data communication through the cable, and, finally,

—the data being saved in the internal solid memory.

2.2. Hydroacoustic Beacons

Six beacons of the HCMS are uniformly distributed over a circle with a radius of 600 m and with the center at the point of the hydrological string location (Fig. 1). This number of beacons makes it possible to enhance the robustness of the system and to improve the measurement accuracy, as well as to obtain additional information on the hydrophysical parameters of the water medium. Figure 2 shows the general view of a short buoy station with an acoustic beacon. On platform *7* made of pieces of rails welded together, a durable sealed casing *6* with electronics and power cells and a rigid arc with a rod *5* are mounted. At the upper end of the rod, a hydrophone *4* is fixed in the middle of a safety frame. The distance from the hydrophone to the bottom is 4 m (here, the fact that the lower layer of the rails is immersed in bottom sediments is taken into account). A kapron cord *3* with a length of 30–40 m is tied to the rod. The cord is held in the vertical position by a bundle of 20 aluminum floats *1*. One meter away from the floats, the so-called collar *2* is fixed, which serves for lifting the beacon: in this case, the collar is hooked by the crabs of a device [10] rotating in the course of its motion in water because of asymmetry. The instants when the beacon is hooked and when the bottom is touched in the process of beacon placement are determined from the dynamometer readings. The weight of the beacon in water is about 100 kg.

The electronics of a beacon consists of analog channels for reception and transmission, a decoder for coded signals, and a device analyzing the received code and generating the beacon response. The beacons are powered by galvanic cells, whose service life is 2–3 years.

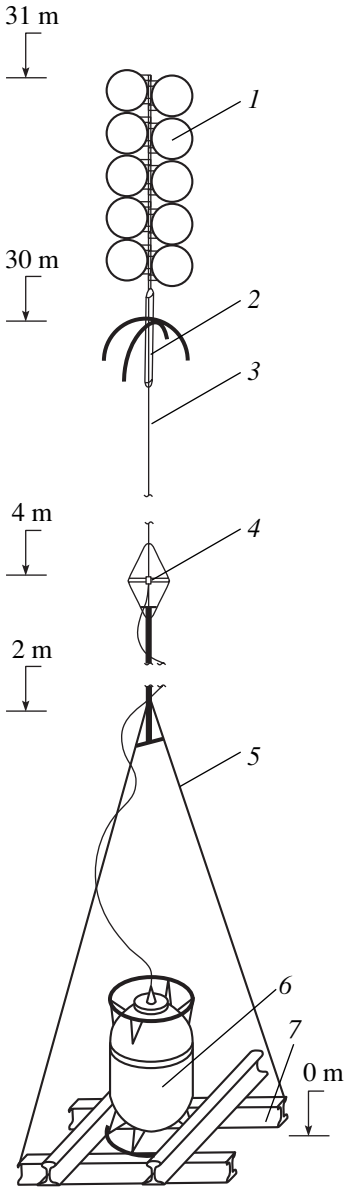

Fig. 2. Deep-water buoy station with an acoustic beacon: (*1*) aluminum floats, (*2*) collar, (*3*) kapron cord, (*4*) hydrophone, (*5*) rod, (*6*) casing, and (*7*) platform.

2.3. The Shore Station

The shore station includes a computer, a communication modem providing the communication between the shore computer and the underwater equipment of the HCMS, and a high-voltage source. The output voltage of the power source is automatically controlled with allowance for the value of the consumption current so that, independently of the voltage drop in the 7-km-

long cable line, the input voltage of the underwater instruments of the HCMS is 300 V.

The software makes it possible to measure the coordinates of the buoy stations in both automated and hand-operated modes of the sequential beacon data acquisition and data selection from certain master modules and acoustic receivers or from their group. The software supports the communication line protocol, remote program loading, and running the program. It is possible to set the necessary gating times for the input receivers of instruments positioned at different sites and to change the thresholds of comparators in the receiving channels of the master modules and acoustic receivers.

2.4. The Coordinate Measurement Cycle of the Neutrino Telescope

The coordinate measurement cycle is initiated by the shore control computer, which sends a sync pulse (a group start) via cable communication lines to the controllers of all or selected groups of master modules and acoustic receivers. The controllers of the instruments execute the preset programs. One of the master modules sequentially transmits coded interrogation signals to each of the beacons. The HCMS uses a time–pulse coding of beacon interrogation at a frequency of 28 kHz. All the necessary carrier frequencies and signal durations are obtained from a single quartz oscillator, which is included in the controller.

The beacon acquisition code contains a 2-ms-long pulse, which is common to all beacons, and a three-position code of the beacon number with a bit duration of 1 ms. The interval between the wave trains is equal to 2 ms. Thus, the length of the whole ultrasonic transmission packet is 10 ms.

To save battery power, all the electronics of a beacon, except for the receiving amplifier, comparator, and range meter, is usually in "sleep" mode. If a train of received signals arrives without discontinuities longer than one period of the carrier frequency and with a train length exceeding 1.75 ms, the timer unit of the beacon is turned on. Then, the beacon interrogation code fills the sequential register of the comparison circuit, and, at the coincidence of the proper code of the beacon with the code arriving to the comparison circuit, the beacon response signal is generated with a duration of 1 ms and a carrier frequency of 32768 Hz. The controllers of the acoustic receivers and master modules measure the travel times of an ultrasonic signal from the instant of interrogation to the instant of reception of the beacon response signal. The counters of the master modules fix the time of sound propagation from the master module to the beacon and back to the master module. The acoustic receivers are able to measure the time of sound propagation along the master module–beacon–acoustic receiver path and also (by measuring the gating time, see below) the time of sound propagation from the master module to the acoustic receiver. To increase the noise robustness, a discriminator is used to test the duration of each packet of the pulse transmission. An additional measure for increasing the noise robustness is the gating circuit, which opens the receiving channels in a master module and an acoustic receiver 20 ms before the expected arrival time of the response pulse.

Thus, the following times of sound propagation can be measured: $\tau_k^k(i)$, from the kth master module to the ith beacon and back; $\tau_k^j(i)$, along the master module (k)–beacon (i)–acoustic receiver (j) path; and $\tau_k^j(0)$, from the master module (k) to the acoustic receiver (j).

The distance from the point at which the hydrophone of the acoustic receiver(j) is located to the hydrophone of the beacon(i), i.e., the slant range R_{ij}, is calculated by the formula

$$R_{ij} = (\tau_k^j(i) - \tau_k^k(i)/2)C^s(z),$$

where $C^s(z) = z/\int_0^z dz/C(z)$ is the harmonic mean velocity of sound and $C(z)$ is the velocity of sound at a depth z.

The spatial position of the hydrophone of the acoustic receiver is determined as the point of intersection of the spheres whose centers are at the points of the beacon locations and radii are equal to the slant ranges from the beacons to the given hydrophone.

3. ERRORS IN MEASURING THE COORDINATES OF THE DETECTING MODULES

The error in the determination of the coordinates of the detecting modules depends on the accuracy achieved in measuring the slant ranges and the beacon coordinates.

3.1. Instrument Errors

Primarily, these are errors in measuring the travel times of acoustic signals. They consist of the following components:

—the error due to the asynchronous arrival of the initiation pulse from the shore station to the instruments distributed over the buoy stations;

—errors due to the threshold variations in the comparators included in the ultrasonic receiving circuits of the beacons and acoustic receivers; and

—errors due to the discreteness of the coded signal detection channel of a beacon.

The estimates of the maximum values of these errors yield 20, 18, and 36 μs, respectively. To determine the actual accuracy of the time interval measurements by the HCMS, the distribution of the experimental errors in measuring the signal travel times (1200 measurements) along one of the master module–beacon–acoustic receiver paths was obtained. The dis-

tribution half-width proved to be about 10 μs, which makes a contribution of about 2 cm to the error in the determination of the coordinates of a detecting module.

3.2. Errors Due to the Uncertainty in the Parameters of the Medium

The main source of errors associated with the properties of the medium is the inaccuracy in the determination of the absolute value of the sound velocity along the signal propagation paths [11]. An analysis has shown that, to measure the coordinates of the detecting modules with a required accuracy of 20 cm, the absolute value of sound velocity should in our case be determined to within 50 cm/s.

The value of the sound velocity can be measured directly [12, 13] or calculated from the data on the temperature T, salinity S, and pressure P with the use of empirical formulas [14–17]. Although the authors in some publications believe that the systematic errors in their formulas are small (e.g., 4 cm/s in [13]), the difference between the values obtained with these formulas for the sound velocity in the Baikal water at the telescope depth reaches 2 m/s.

To perform a direct experimental measurement of sound velocity and to test different empirical formulas for calculating C, we measured the time of sound propagation with an acoustic base 100 m in length, which was determined to within ±2 cm (with allowance for the extension of the cable in water). In this experiment, we measured the integral sound velocity over the base length, but the linearity of the depth dependence of C (see below) allowed us to determine the sound velocity at given depths by shifting the measuring system in depth within the interval from 800 to 1300 m. Simultaneously, we performed temperature and pressure measurements with an SBE 25-01 probe. As a result, we found that the data of the direct measurements performed as described above with an error no greater than 30 cm/s agree well with the results of calculation by the formulas taken from [13] with the use of the temperature data obtained from the SBE 25-01 probe, which were accurate to within 0.002 deg (the corresponding contribution to the error in calculating $C(z)$ is 1 cm/s). Figure 3 shows the results of calculating the vertical distribution of sound velocity according to [13] and according to the temperature data from [18] for the region where NT-200 was deployed; the distributions are given for different seasons. The greatest sound velocity variations associated with temperature variations are observed near the surface of the lake and reach 40 m/s. At large depths, where the temperature variations are very small, the depth dependence of sound velocity is mainly determined by pressure and can be approximated by the formula

$$C(z) = 1418.96 + 0.0153645z \text{ m s}^{-1},$$

where z is the depth in meters.

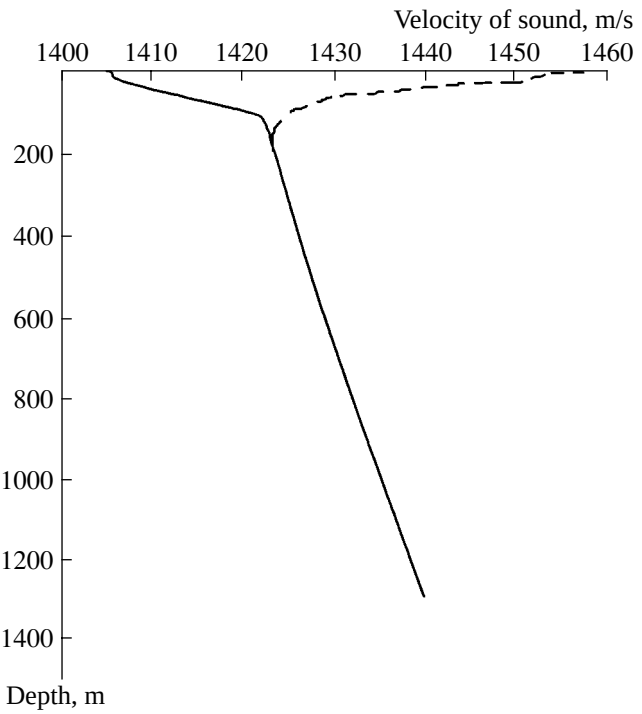

Fig. 3. Vertical sound velocity distribution in Baikal in March (the solid line) and in August (the dashed line).

According to long-term temperature observations [19], at the telescope depth, only slight temperature variations within several hundredths of a degree are possible. Therefore, we can use the sound-velocity profile shown in Fig. 3 as a reference in the HCMS data processing. At the same time, we observe relatively short temperature variations (Figs. 7 and 8) that should be taken into account in calculating the harmonic-mean sound velocity used in the computations. For this purpose, the temperature variations were monitored over a period of one year with the use of a series of TR-1000 termistors spaced at 100 m in depth and placed at the hydrological and neighboring sedimentological buoy stations (Fig. 1).

The average mineralization of Baikal water is about 96 mg/l [20], and its variations do not exceed 30%, which makes a contribution to sound velocity on the order of 12 cm/s with possible variations of about 4 cm/s. Thus, in our case, salinity variations can be ignored.

The currents that occur at the telescope depth in the southern part of Baikal usually do not exceed 20 cm/s [21] and practically do not affect the accuracy of coordinate measurements.

3.3. Errors in the Determination of the Beacon Positions

The beacons are placed at the sites of their operation in winter, by lowering them from the ice cover of the lake. The positions of the points of beacon submer-

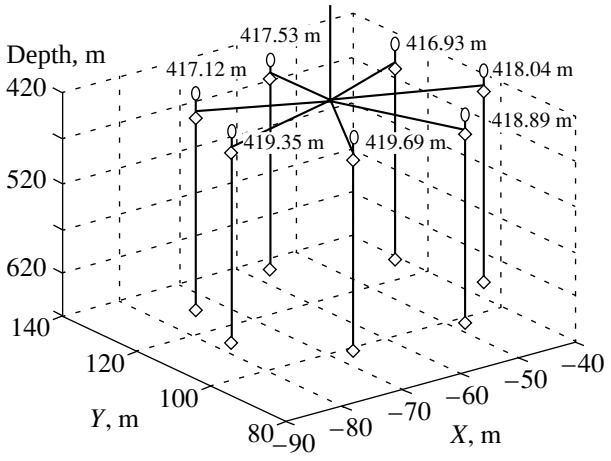

Fig. 4. Positions of the buoy stations of the NT-200 neutrino telescope in the course of their lowering. The numbers near the buoy stations indicate the depths of the upper acoustic receivers.

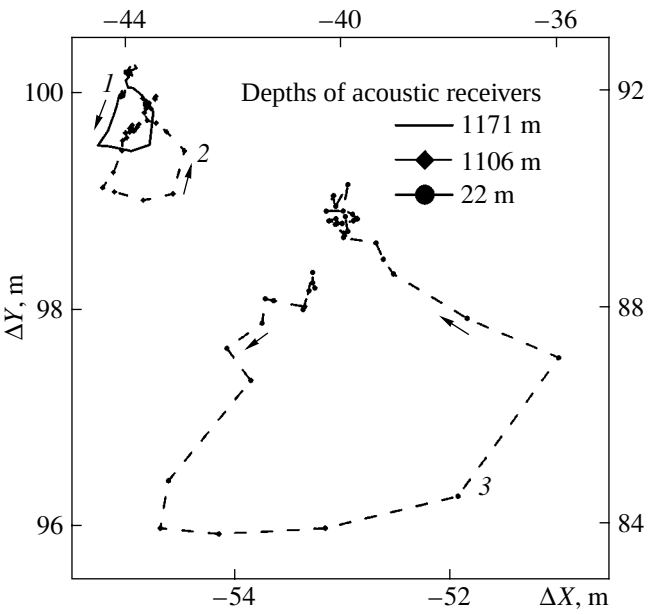

Fig. 5. Fragment of motion of a buoy station of the NT-200 neutrino telescope between June 28, 1994, and July 18, 1994: (*1, 2*) acoustic receivers at depth of 1171 and 1106 m (the left and bottom axes); (*3*) an acoustic receiver at a depth of 22 m (right and top axes).

gence are determined by a laser ranger and a theodolite to within 0.2 m. In winter, when the system is deployed, the currents in the upper layer of Baikal usually do not exceed 2 cm/s and logarithmically decrease with depth [21]. According to our estimates, in the presence of these currents, the points where beacons of the given configuration are placed on the bottom deviate from the corresponding points on the surface by no more than several tens of centimeters.

An independent determination of the beacon positions was performed with the use of an acoustic array consisting of four master modules, whose hydrophones were fixed on two vertical cables at distances of 4 and 104 m from the bottom. The distance between the cables was 336 m. An analysis has shown that the accuracy achieved by us in these measurements was 40 cm, and the average values of the beacon coordinates agreed well with the results of geodetic measurements.

The relative depths of the beacon placement were measured using a contact switch, which was closed at the instant of touching the bottom. This closure was detected by the ohmmeter positioned on the lake surface. The measurement accuracy was 1 cm. The scatter in the sea depths at the beacon sites was 5.69 m. With allowance for the uncertainty in the depth of anchor submergence in the silty bottom, the error in the relative depths does not exceed 5 cm.

3.4. Conclusions

—The main sources of errors in the HCMS are the errors in the determination of the sound velocity profile and the beacon coordinates.

—The HCMS provides the possibility to carry out long-term measurements of the coordinates of the detecting modules of the NT-200 to an accuracy of 20 cm or better.

4. RESULTS OF MEASURING THE COORDINATES OF THE NEUTRINO TELESCOPE

The first measurements of the coordinates of the detecting modules by the HCMS were performed in 1994. These measurements are in progress at the present time. As a rule, they are carried out in four cycles with a periodicity of 10–12 h (or more often, if necessary). The HCMS also allows one to observe the variations that occur in the positions of the telescope strings as the telescope is submerged and placed on the bottom (Fig. 4). It is of interest that, from year to year, after the placement of the system, the strings prove to be almost at the same points. The distances between the hydrophones of the lower and upper acoustic receivers that are fixed on the same string are also retained. They usually differ by no more than 10 cm from the distances measured with a measuring reel before the placement.

During the year, the coordinate motion of the NT-200 as a whole was observed (Fig. 5). The maximum deviations of the buoy stations are observed in the period of autumn storms, in September and October. For the upper buoy (a depth of about 20 m), they exceed 50 m (Fig. 6), while the upper detecting modules deviate by no more than 1.3 m and the lower modules, by 1 m. In all cases, the telescope deviates from the vertical posi-

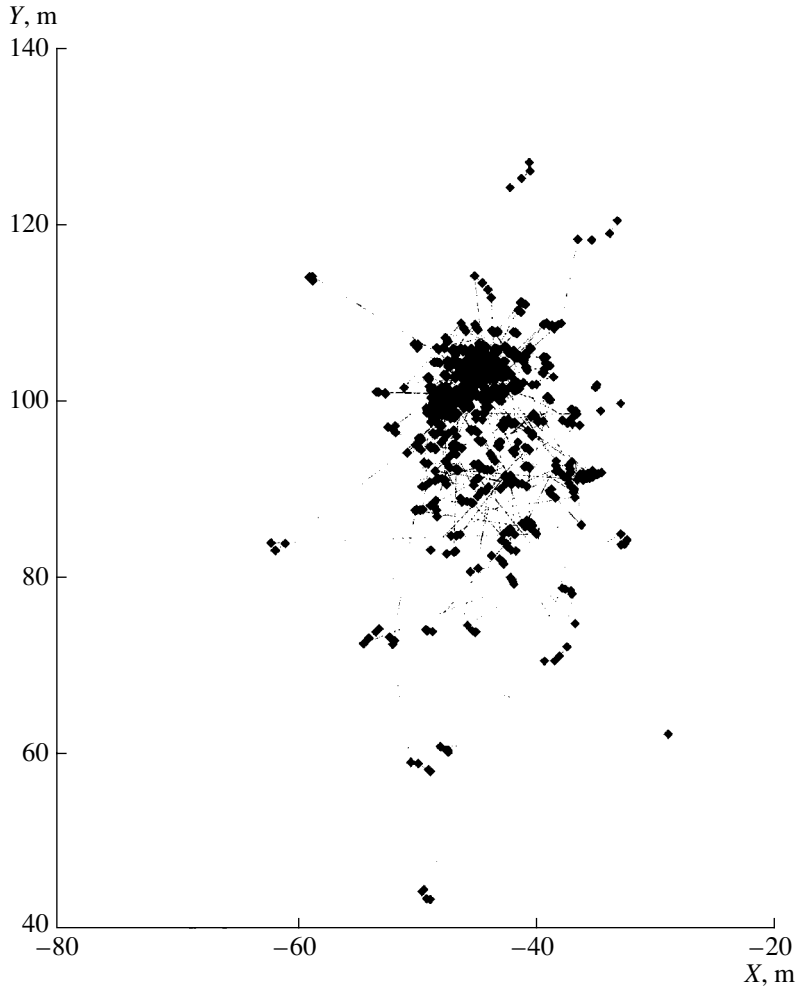

Fig. 6. Motion of an acoustic receiver located at a depth of 22 m under the upper float at a buoy station of NT-200 in 1994. The *Y* axis is directed along the coast to the west.

tion by no more than 1 deg, and the relative coordinates of the detecting modules vary by no more than 10 cm.

5. INVESTIGATION OF THE WATER MEDIUM BY THE HYDROACOUSTIC SYSTEM OF NT-200

The data obtained from the HCMS can also be used to study the hydrophysical processes in the lake. The simplest information of this kind is obtained by observing the behavior of the buoy stations of the telescope. The predominant displacement of the submerged buoy stations to the west confirms the concept concerning the global water circulation in the Southern trench of the lake [21]. Fourier analysis of the buoy station deviations revealed, e.g., the presence of oscillations with periods close to the periods of seiche oscillations in Lake Baikal [22, 23].

A much greater amount of information on the hydrophysical fields can be obtained by analyzing the data on the times of sound propagation between different points in the water medium. For this purpose, it is especially convenient to use paths with a fixed length. Such paths primarily are the paths along the bottom, from the master module to each of the beacons. With the accuracy of time measurements in the HCMS being $\Delta\tau = 10$ μs, the resolution of the observation of mean temperature variations on a path of length L is

$$\Delta T\ (\text{deg}) = \frac{\Delta\tau C^2}{\alpha L} = 0.004/L\ (\text{km}), \qquad (1)$$

where $\alpha = 5.0371$ is the proportionality coefficient in the formula determining the relation between the sound velocity and temperature [13].

The accuracy achieved in measuring the absolute value of the mean temperature also depends on the accuracy of determining the distance ΔL between the transmitting and receiving hydrophones. For the master module–beacon–master module path with $\Delta L = 40$ cm and $L = 1.2$ km, this accuracy is not high (about 0.1 deg), and, therefore, we compare the results with the absolute reference measurements by a TR-1000 termistor. Figure 7 compares the results of temperature

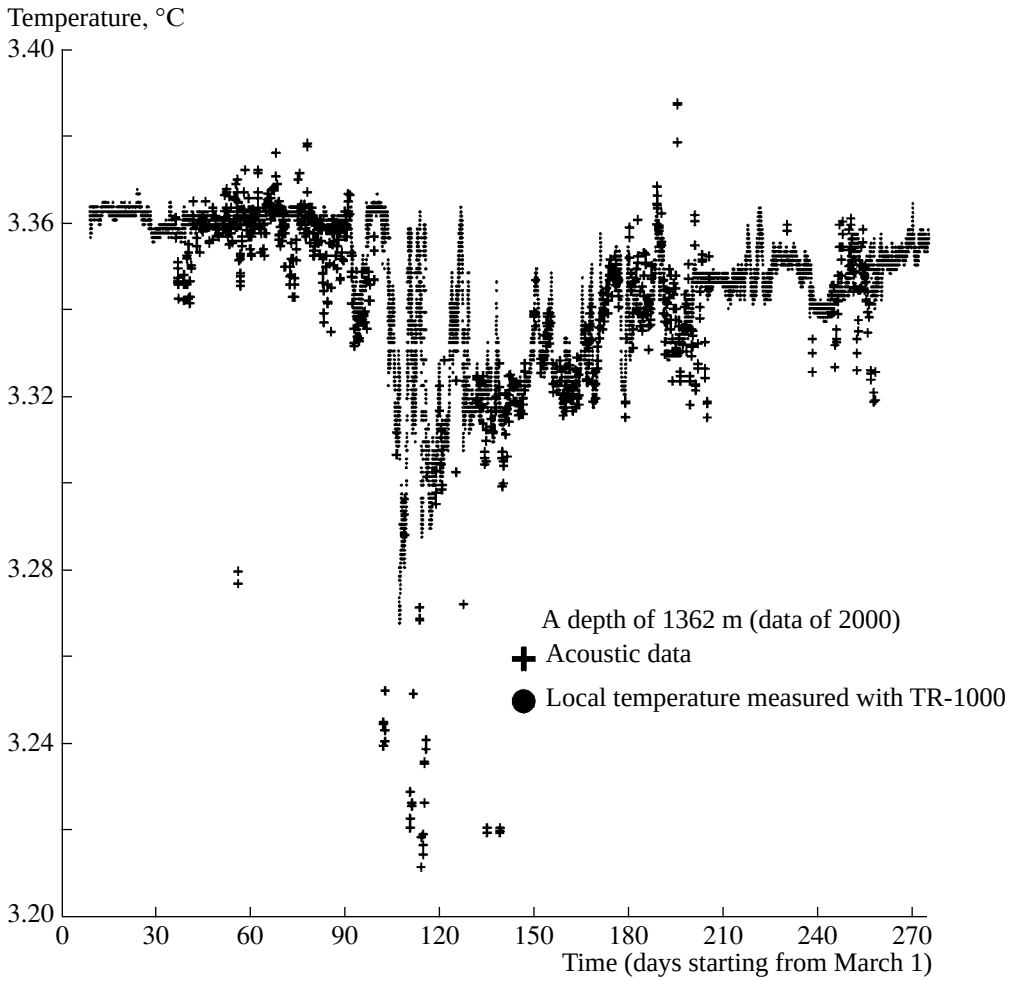

Fig. 7. Results of temperature measurements carried out in 2000 on the master module–beacon path by the HCMS (crosses) and by a TR-1000 termistor positioned 4 m above the bottom (full circles). The errors are not shown in the plot.

measurements on the master module–beacon path with the help of the HCMS and a TR-1000 termistor placed at a distance of 4 m from the bottom. On the whole, a qualitative agreement is observed between the temperature behavior at a point (the TR-1000 data) and the mean temperature of the layer (the HCMS data). After the period characterized by an almost constant temperature in March–May, both methods reliably detected a considerable temperature decrease in mid June and the subsequent decaying temperature variations, which testify to a considerable intrusion of cold waters into the near-bottom region in the homothermal period [18]. For clarity, the errors are not shown in Fig. 7. For the data obtained with TR-1000, the errors are on the order of the dots, and for the HCMS data, according to Eq. (1), they are about ±0.004°C in the given case. The spikes in the HCMS data may presumably be related to failures in the system's operation, for example, because of acoustic noise.

For tracing the hydrophysical characteristics of the water mass, in addition to the horizontal paths along the lake bottom, it is possible to use the vertical paths of sound propagation between the instruments positioned on the hydrological buoy station. As an example, in Fig. 8, we show the temperature variation in the deep 300-m-thick near-bottom layer with time starting from October 13, 1995. In the first part of the period of measurements, the data were taken at a step of 20 s. The large temperature variations (up to 0.4°C, the measurement error is about ±0.015°C), which are observed at large depths in the southern part of Lake Baikal, where, as a rule, a stable stratification of water temperature is observed in the layer from 300 to 1300 m during the whole year [19], may be related to the incursion of warmer near-surface waters due to the storm that occurred at the beginning of this period. Observations of this kind are very important for the understanding of the water-exchange processes in Lake Baikal and testify to the fact that the role of dynamic factors (such as atmospheric pressure variations or wind) should be taken into account in studying the hydrophysical processes in the lake.

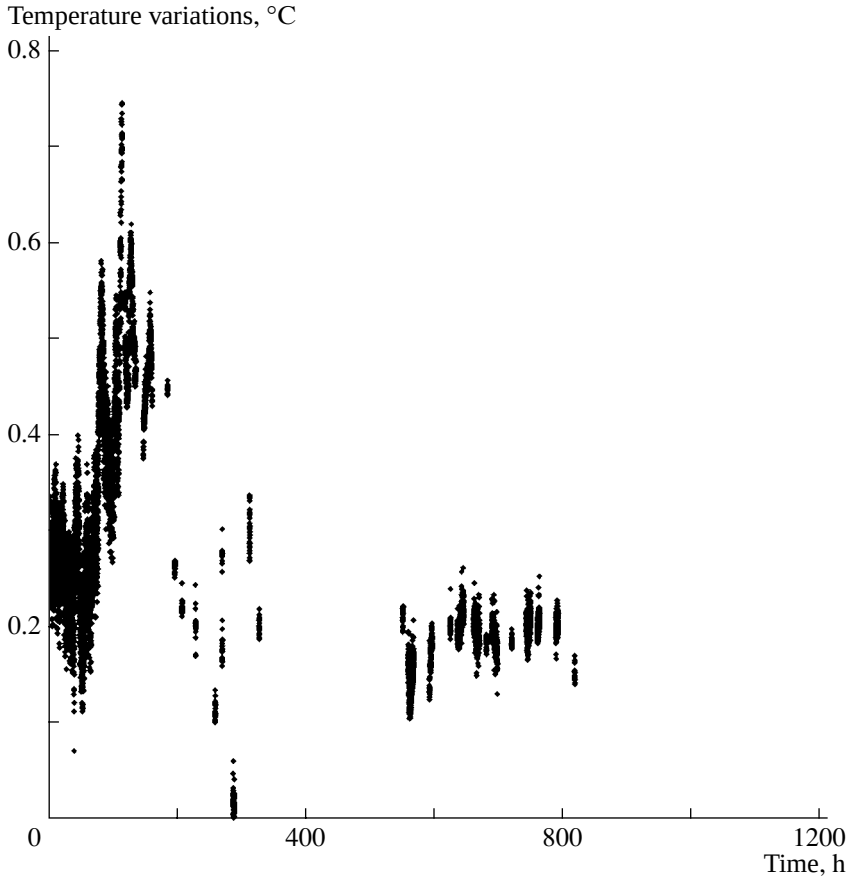

Fig. 8. Measurements of the mean temperature of water in the 300-m-thick near-bottom layer starting from October 13, 1995. Each of the points is a result of a cycle of measurements. The errors are not shown.

6. CONCLUSIONS

The HCMS of the NT-200 makes it possible to monitor the spatial positions of the elements of the neutrino telescope during a long period of time with an accuracy of 20 cm (or better). The architecture of the HCMS allows its further development with the expansion of the NT-200. The methodical and engineering solutions found in developing the HCMS of NT-200 can be used for designing other distributed acoustic systems intended for positioning various objects and for studying the hydrophysical processes in the water medium.

ACKNOWLEDGMENTS

This work was supported by the Ministry of Science of the Russian Federation, the Ministry of Science and Education of Germany, the Russian Foundation for Basic Research (project nos. 02-02-17031, 02-02-17427, 02-07-90293, and 04-02-31006), Russian Presidential Grant no. NSh-1828.2003.2, the Federal Target Program "Integratsiya" (project no. 0248), the Program "Universities of Russia (grant no. UR.02.01.004), and the Department of Water Resources of UNESCO.

REFERENCES

1. M. A. Markov, in *Proceedings of International Conference on High-Energy Physics, Rochester, 1960* (Rochester, 1960), p. 578.
2. V. S. Berezinskiĭ and G. T. Zatsepin, Usp. Fiz. Nauk **122**, 3 (1977) [Sov. Phys. Usp. **20** (5), 361 (1977)].
3. I. A. Belolaptikov, L. B. Bezrukov, B. A. Borisovets, *et al.*, Astroparticle Phys. **7**, 263 (1997).
4. *ANTARES Collaboration. ANTARES, Towards a Large-Scale High-Energy Cosmic Neutrino Undersea Detector: Proposal* (May, 1997).
5. A. Capone *et al.*, in *Proceedings of the XXVI International Cosmic Ray Conference, Salt Lake City, 1999* (Salt Lake City, 1999).
6. L. K. Resvanis, in *Proceedings of the 3rd Nestor International Workshop, Pylos, Greece, 1993* (Pylos, 1993).
7. L. M. Lyamshev, Akust. Zh. **38**, 197 (1992) [Sov. Phys. Acoust. **38**, 105 (1992)].
8. *Hydroacoustic Technology for Ocean Studies and Exploitation*, Ed. by V. V. Bogorodskiĭ (Gidrometeoizdat, Leningrad, 1984) [in Russian].
9. P. H. Milne, *Underwater Acoustic Positioning Systems* (Gulf, Houston, 1983; Sudostroenie, Leningrad, 1989).
10. A. I. Panfilov, Yu. V. Parfenov, N. M. Budnev, and M. I. Rozanov, in *Proceedings of All-Union Scientific-*

Engineering Conference on Scientific and Engineering Problems of Designing the Means for Hoisting and Utilization of Sunken Objects, St. Petersburg, 1994 (St. Petersburg, 1994), p. 11.

11. *Ocean Acoustics*, Ed. by L. M. Brekhovskikh (Nauka, Moscow, 1974) [in Russian].
12. G. N. Seravin, *Sound Speed Measurements in the Ocean* (Gidrometeoizdat, Leningrad, 1979) [in Russian].
13. E. D. Popov, É. Kh. Abzalilova, and M. V. Matveev, *Some Results of Experimental Works with Pulsed Cyclic Sound Velocity Meters for Single-Use Probes*, Available from VINITI, No. 4739-B86 (Moscow, 1986).
14. C. T. Chen and F. J. Millero, J. Acoust. Soc. Am. **62**, 1129 (1977).
15. C. T. Chen and F. J. Millero, Limnol. Oceanogr. **31**, 657 (1986).
16. C. C. Leroy, J. Acoust. Soc. Am. **46**, 216 (1969).
17. W. D. Wilson, J. Acoust. Soc. Am. **34**, 866 (1962).
18. M. N. Shimaraev and N. G. Granin, Dokl. Akad. Nauk SSSR **321** (2), 381 (1991).
19. M. N. Shimaraev, *Elements of the Thermal Conditions of Baikal Lake* (Nauka, Sib. Otdel., Novosibirsk, 1977) [in Russian].
20. K. K. Votintsev, *Hydrochemistry of Baikal Lake* (Akad. Nauk SSSR, Moscow, 1961) [in Russian].
21. A. N. Afanas'ev and V. I. Verbolov, *Currents in Baikal* (Nauka, Sib. Otdel., Novosibirsk, 1977) [in Russian].
22. V. I. Verbolov, *Seiche on the Lakes, Surface and Internal One* (Nauka, Leningrad, 1970), p. 50 [in Russian].
23. N. G. Granin, *Hydrology of Baikal and Other Water Basins* (Nauka, Novosibirsk, 1984), p. 67 [in Russian].

Translated by E. Golyamina

Acoustical Physics, Vol. 51, No. 6, 2005, pp. 629–637. Translated from Akusticheskiĭ Zhurnal, Vol. 51, No. 6, 2005, pp. 732–741.

Long-Range Sound Propagation in the Northeastern Atlantic

R. A. Vadov

Andreev Acoustics Institute, Russian Academy of Sciences, ul. Shvernika 4, Moscow, 117036 Russia
e-mail: vadov@akin.ru

Received July 20, 2004

Abstract—Experimental data on the long-range propagation of explosion-generated signals are analyzed. The experiments were performed in the northeastern Atlantic under the conditions of a two-axis underwater sound channel. The sound field in the upper channel was governed by the vertical redistribution of the ray structure and sound energy under the influence of a smooth increase in the depth of the channel's axis along the propagation path. The explosions were produced in the upper sound channel at a depth of 200 m, which was constant along the path. The time structure of the sound field is analyzed for the upper channel (a reception depth of 200 m) and for deeper layers lying somewhat below the boundary between the upper and lower sound channels (a reception depth of 1200 m). The deviation of the decay law obtained for the sound field level in the upper channel from the cylindrical law is used to estimate the attenuation coefficient. The low-frequency (several hundreds of hertz) attenuation coefficients experimentally determined with allowance for the sound field redistribution agree well with the calculated sound absorption in seawater. The attenuation coefficients determined by the differential method also agree well with the absorption calculated by the formulas proposed earlier. The analysis of the time structure of the sound field near the boundary between the upper and lower channels reveals a permanent insonification of this horizon by weak water-path signals propagating with the velocity typical of the signals traveling in the upper channel. © *2005 Pleiades Publishing, Inc.*

The Acoustics Institute has repeatedly performed experiments on long-range sound propagation in the northeastern part of the Atlantic Ocean. The characteristics of the sound field were studied on different propagation paths, in the regions that differed in their oceanographic properties. Tonal, pulsed, and explosion-generated signals were used in the experiments. The results of the measurements were published in *Akusticheskiĭ Zhurnal* (*Acoustical Physics*) [1–4] and reported at different scientific seminars.

In this paper, the experimental data on long-range propagation of explosion-generated signals are presented for the Iberian and West-European Basins. In these regions, the water bulk is formed by the Mediterranean waters passing into the Atlantic Ocean through the Strait of Gibraltar. Therefore, a two-axis underwater sound channel is characteristic of these regions.

Experimental conditions. The experiment was carried out in June. The propagation path was oriented in a direction close to the meridian. The path originated and terminated at the points 47° 00′ N, 13° 30′ W and 37° 40′ N, 15° 15′ W, respectively. The path length was 1160 km. The explosions were produced at a depth of 200 m. Charges were dropped and exploded at the full speed of the transmitting vessel that went off the reception point. In total, 145 charges with pressure-sensitive detonators were dropped. The omnidirectional receiving systems were at depths of 200 and 1200 m. The receiver positioned at a depth of 200 m was near the axis of the upper sound channel (Ch1). The main minimum in the sound speed profile, which corresponded to the axis of the lower sound channel (Ch2), was at a depth of about 1600 m.

The ISTOK-3 instrument was used to measure the vertical distributions of temperature and conductivity of water. The maximum depth of profiling was 1800–2000 m. These data were recalculated to the sound speed by using the Wilson formula [5]. The data on the sound speed at deep (near-bottom) horizons were obtained by bathometric measurements. Some of the data obtained are shown in Fig. 1. The profile measured at the beginning of the path (Fig. 1a) gives an overview of the propagation conditions in the region under study, namely, the distribution of the sound speed over the entire water column, from the surface to the bottom. The $c(z)$ profiles shown in Fig. 1b are measured at different distances from the reception point; they characterize the changes in the propagation conditions for the upper sound channel along the path.

The upper layer of the ocean, down to depths of 130–170 m, was formed by the Canary waters, which are characterized by rather low temperatures (13–14°C) and high salinity (35.7–36.7‰). The spring–summer warming covered a layer of 30–40 m. The temperature discontinuity was weakly pronounced. The unstable surface channel was observed only in the southern part of the path, at depths of 10–25 m. The near-surface sound speed increased in the north–south direction, from 1505 m/s (at the beginning of the path) to 1515 m/s (at the end of the path).

The water layer occupying the depths between 150 and 600 m was formed by the well-mixed subtrop-

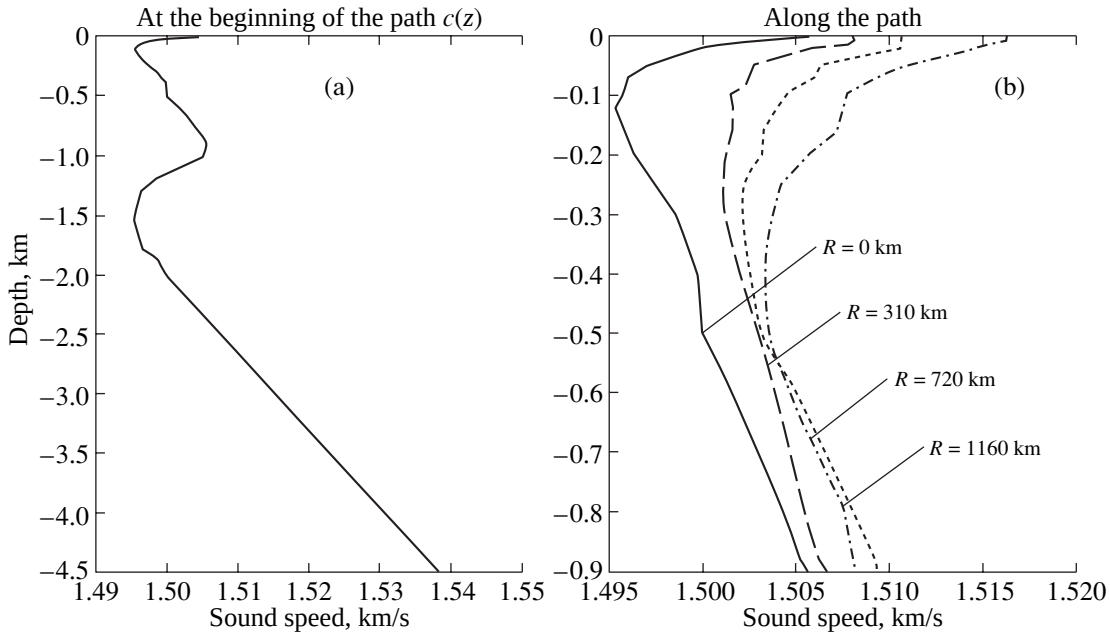

Fig. 1. Sound speed profiles $c(z)$ measured at different distances from the source.

ical masses with small positive gradients of temperature and salinity. As a consequence, a positive gradient of the sound speed was present, and the underwater sound channel had an axis that became deeper along the path: its depth varied from 110 m at the initial point of the path to 350–400 m at the terminal point. The sound speed at the axis varied from 1495 to 1503 m/s in the southward direction.

The water layer occupying the depths from 600 to 1300 m was represented by the water mass produced by mixing of three types of waters: deep Mediterranean waters, North Atlantic ones, and the waters embedded in the Newfoundland convergence zone [6]. This water layer had a temperature of 11–12°C, which was rather high for such depths, and a salinity of 35.5–36.0‰. The intense mixing led to a decrease in the vertical temperature gradient. The maximum in the sound speed was at 1000 m in this layer, and, at this depth, the sound speed increased in the southern direction from 1506 to 1510 m/s. In lower layers, the temperature rapidly decreased to 3.5–4°C.

The deep waters were comparatively homogeneous, with a temperature of 2.5–3.0°C and a salinity of 34.9‰. The gradient of the sound speed was close to the hydrostatic one in these waters. The near-bottom sound speed reached 1550 m/s. The minimum in the sound speed occurred at depths of 1500–1600 m.

The hydrological environment at the experimental site was characterized by the presence of a two-axis sound channel. The difference between the sound speeds at the surface and at the axis of the upper channel reached 8–12 m/s, and the corresponding difference between the surface and the axis of the lower channel was 12–15 m/s. The difference in the sound speed at the intermediate maximum (between Ch1 and Ch2) and at the axis of the upper channel was 4–10 m/s. With the source positioned at the axis of Ch1, the angles of the rays captured by this channel were within ±4°–5.5° along the entire path. With such a position of the sound source, the sound field at a depth of 1200 m was formed by both purely water-path rays (that are common for Ch1 and Ch2) and the rays reflected from the surface and the bottom.

Figure 2a shows the field of the sound speed at depths shallower than 800 m. These data are obtained from the hydrological survey of the path. The data clearly exhibit a smooth increase in the depth of the Ch1 axis in the southward direction. The sound speed at the axis increases monotonically. Figure 3 shows the ray pattern that illustrates the sound propagation in Ch1 with the sound source at a depth of 200 m (the departure angles of the rays are limited by ±4.2°). It is quite evident that the channeled rays become deeper because of the smooth changes in the parameters of Ch1 along the path.

The path passed over the West-European and Iberian Basins with mean depths of 4400–4800 and 5200–5300 m, respectively. The sea-floor relief plotted using echo-sounding data is presented in Fig. 2b. At four points along the path, samples of the bottom material were picked up. All the samples contained lime silt with a density of 1.51–1.58 g/cm^3.

In the experiment (carried out over three days), the wind speed varied within 4.5–12 m/s and the sea state was Beoufort 5. In the first day, a swell with a period of 8 s and a height of 2 m was predominant. In the second

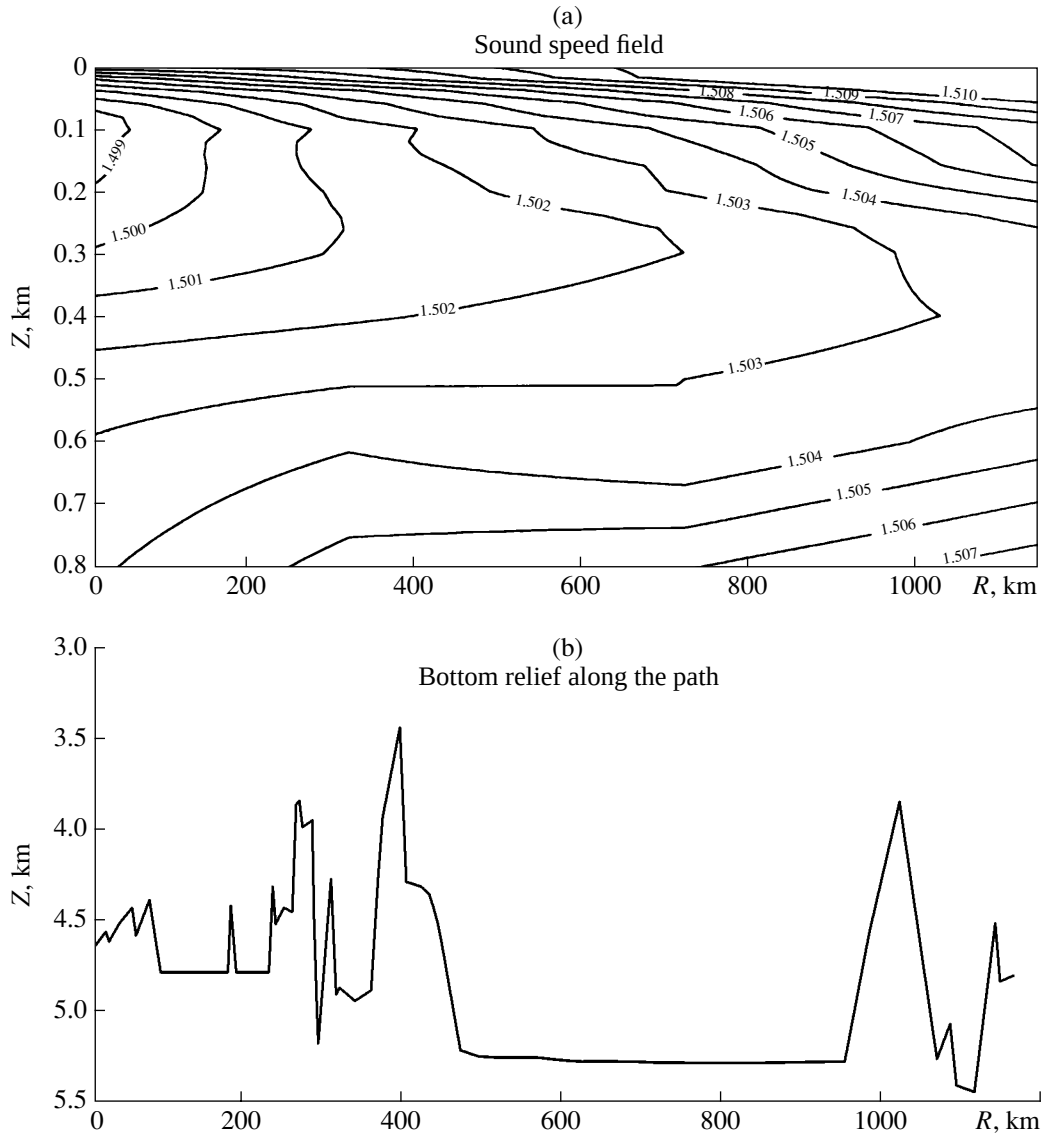

Fig. 2. Data of the hydrological and echo-sounder surveys of the path: (a) the sound speed field down to a depth of 800 m and (b) the bottom relief.

and third days, wind waves were the main cause of surface roughness.

Time structure of the sound field. In the case of single-ray propagation, the explosion-generated signal received in the bandwidth from 40–60 Hz to 1–2 kHz at a distance of 10–20 km and more has the following form in the time domain: it consists of two short pulses with a duration smaller than 1 ms, with equal amplitudes, and with the same sign (the shock wave and the first oscillation of the gas bubble). The pulses are separated in time by an interval equal to the period of the gas-bubble oscillation (about 35 ms in our case). In the case of multipath propagation, a pair of such pulses corresponds to each ray in the time structure of the explosion-generated signal.

To illustrate the range-dependent duration of the multipath signal and its time structure, Fig. 4 presents the signals received by a 200-m receiving system at distances of 100 to 1000 km from the source, at a 100-km step in distance. All the signals presented in this and the following figures are normalized to their maximal values.

Note that there are no well-resolved "classical" quartets that usually advance the most intense main group of signals. The shape of the total (multipath) water-path signal is also rather peculiar: neither the leading nor trailing edges of the signal are clearly defined. A gradual increase in the signal level is followed by an equally gradual (or even slower) decrease. If one neglects the elementary signals reflected by the bottom, the duration of such a multipath signal will be

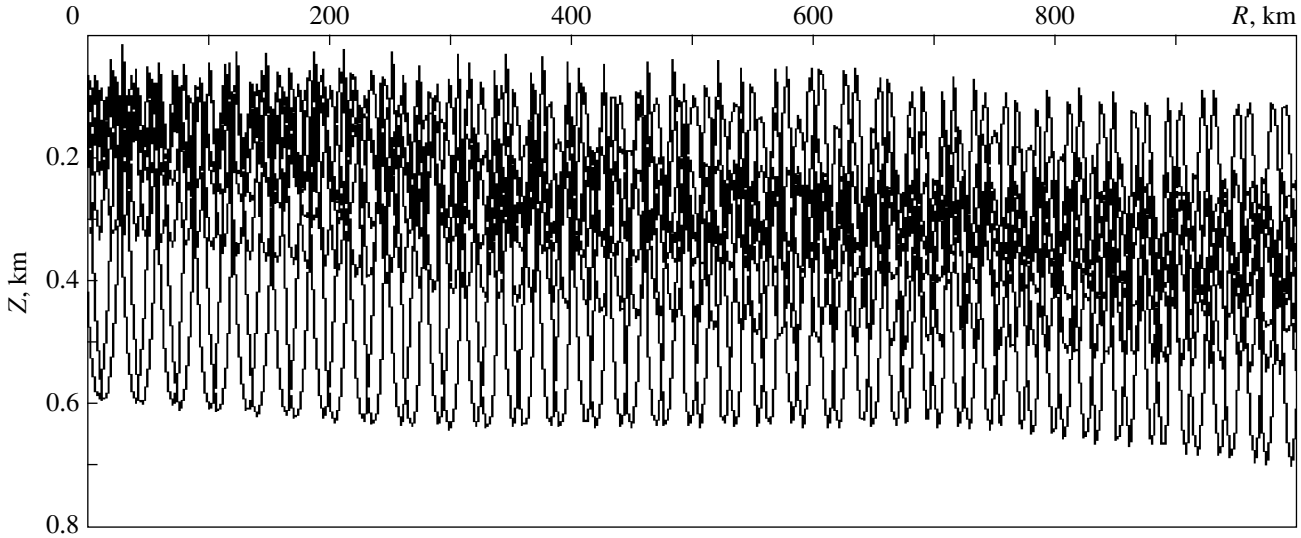

Fig. 3. Ray pattern in the upper channel with the source at a depth of 200 m. The departure angles are within ±4.2°.

proportional to the distance with a proportionality coefficient of approximately 0.0013 s/km.

The 100-km step in distance, which was chosen to illustrate the general changes in the multipath signal, is apparently insufficient to reveal the laws that govern the signal structure variation with distance. Figure 5 shows the signals received and recorded at distances from 25 to 100 km from the source at a step of about 5 km. Such steps allow one to analyze some features of the fine structure formation in the explosion-generated signal. Up to a distance of 100 km, the total multipath signal produced by the shock wave and the signal produced by the first gas-bubble oscillation are clearly separated. In addition to the group of signals propagating in the upper channel, another comparatively strong signal appears at a distance of 56 km from the source. This signal, being refracted at the lower boundary of Ch2, has a delay of 110–120 ms relative to the leading edge of the main signal and an amplitude that is a factor of 2–3 higher than that of the main signal.

After the main group of signals (to the right), the quartets of signals that are reflected by the bottom (and the surface) are observed. These signals arrive at the receiver with a time delay. The amplitudes of these signals are much lower than those of the main water signals. Their delay relative to the main group monotonically decreases as the distance increases. The quartet of the signals singly reflected by the bottom is followed by the quartets of signals with two, three, or more bottom reflections. In the experiment at hand, multiply reflected signals were observed at all distances from the source, up to the ultimate one (1160 km).

For the sake of comparison, Fig. 6 presents the same signals received at a depth of 1200 m. For signals received at this depth, the time scale is matched to the arrival of the first, relatively compact group of signals. After this group, two more groups of elementary signals arrive. They are coupled with each other, correspond to equal numbers of bottom reflections, and have delays that decrease with distance. Each group consists of two elementary (single-ray) signals of the same quartet, this feature being confirmed by the calculations. If the source and the receiver are at different depths, the quartet splits into two pairs of signals. The greater the depth separation of the source and the receiver, the higher the time interval between the pairs. In our case, the time interval between the initial pairs was about 400 ms (with a depth separation of 1000 m). The amplitudes of the bottom-reflected signals are quite comparable with those in the compact group of signals that are first to arrive at the receiver.

The calculations performed with the use of Tebyakin's computer code [7] (ray approximation and a horizontally layered medium) for distances shorter than 100 km agree well with the experiment in the time delays between the pairs of the bottom-reflected signals within the corresponding quartets. The observed delays of these signals relative to the first compact group satisfactorily agree with the computed delays relative to the water signals propagating in the upper channel. However, according to the calculations, the water signals propagating in the upper waveguide do not arrive at the depth of 1200 m at all. With the computer code by Avilov [8, 9] used to calculate the vertical structure of the sound field at distances from 20 to 40 km, the conclusion was drawn that a diffraction-induced insonification of the 1200-m horizon takes place. The level of the insonification proved to be 20–30 dB lower than the level of the sound field in the Ch1. This result agrees well with the experiment.

Attenuation and absorption of sound. One of the main objectives of the experiment on the long-range propagation of explosion-generated signals in the

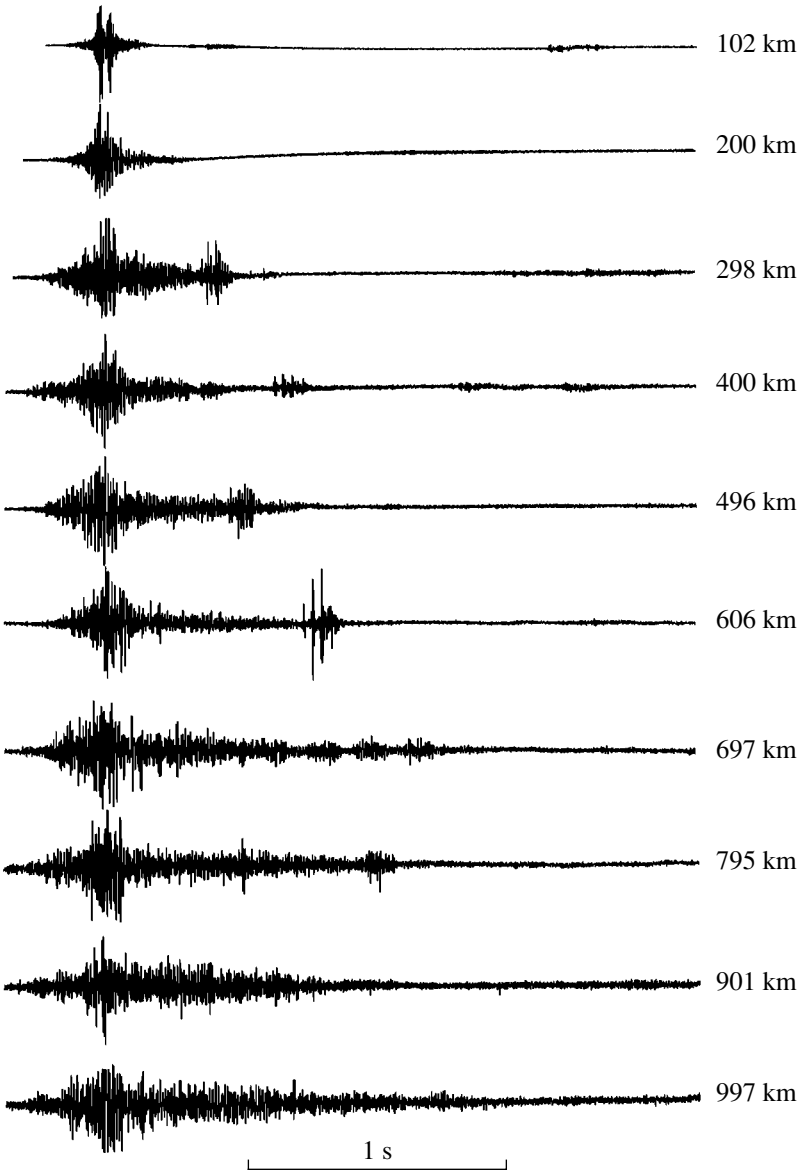

Fig. 4. Time structure of the signals received at a depth of 200 m at different distances. The distance from the source varies from 100 to 1000 km at a step of 100 km. Here and in the following figures, the signals are normalized to their maximal values.

northeastern Atlantic consisted in studying the frequency dependence of sound attenuation. The attenuation coefficient is usually determined from the deviation of the experimental decay of the sound-field level in the underwater channel from the cylindrical law of the geometrical spread (strictly speaking, such an approach is valid only for the channeled signals in a horizontally layered medium).

For explosive sources of sound, the following quantity is taken to be equivalent to the signal energy within the frequency band Δf:

$$E_f = \int_0^T p_f^2(t)dt,$$

where T is the duration of the explosion-generated signal and $p_f(t)$ is the acoustic pressure normalized to the frequency band Δf. Although the quartets of bottom-reflected signals were much lower than the main groups of the near-axis signals in their amplitudes, these quartets were artificially eliminated from the signal processing, so that their contribution to the sound field in the channel was minimal.

The results of the analysis performed for the signals received at a depth of 200 m are summarized in the table. The attenuation coefficients at frequencies lower than 630 Hz were determined from the deviation of the decay law observed for the sound field at distances of 50–1160 km from the cylindrical law. At 630 Hz and higher, the path fraction used for estimating the attenu-

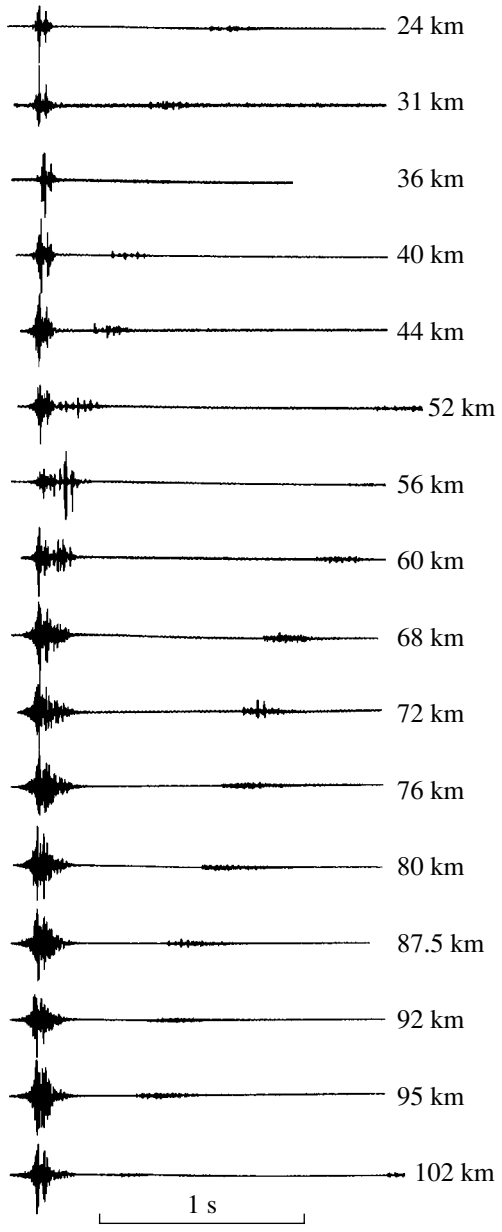

Fig. 5. Time structure of the signals received at a depth of 200 m at different distances. The distance from the source varies from 25 to 100 km at a step of 5 km.

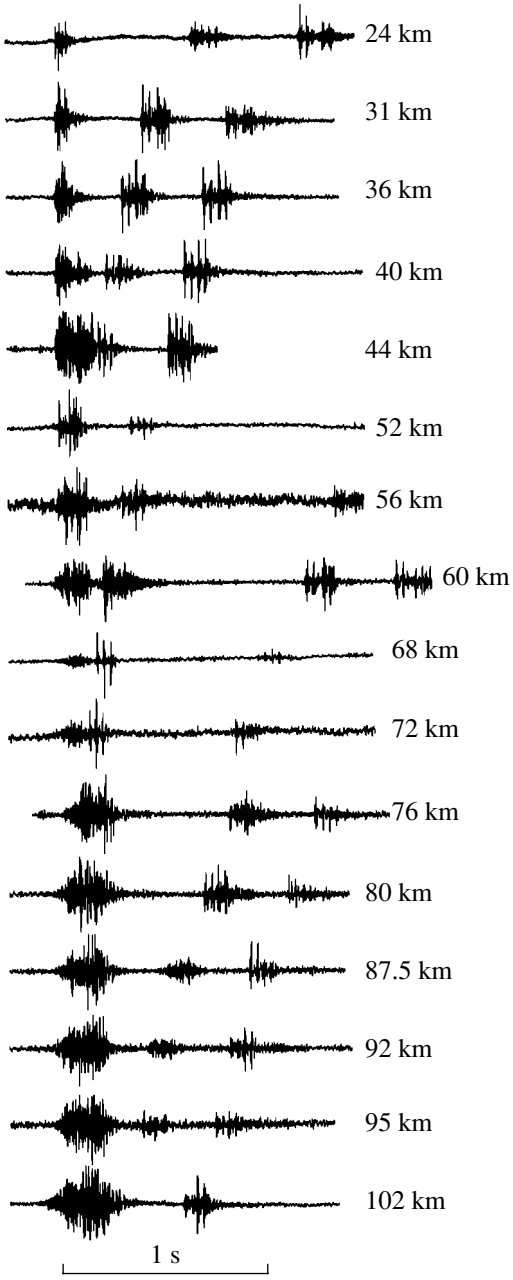

Fig. 6. Time structure of the signals received at a depth of 1200 m at different distances. The distance from the source varies from 25 to 100 km at a step of 5 km.

ation coefficient was shorter (50–850 km at 630 Hz and 50–350 km at 1600 Hz) because of the lower signal-to-noise ratio at higher frequencies.

In the third and fourth columns of the table, the calculated absorption coefficients are presented for the frequency band at hand. The calculations were based on the semiempirical equations derived from the analysis of the experimental data on long-range sound propagation in a number of ocean regions that noticeably differed in water temperature (– 2 to 13.5°C) and salinity (18 to 38‰) [10]:

$$\alpha = \frac{A_B f}{f/f_B + f_B/f} + \frac{A_{\mathrm{MgSO_4}} f}{f/f_{\mathrm{MgSO_4}} + f_{\mathrm{MgSO_4}}/f} + K f^2. \quad (1)$$

Here, f is the frequency (kHz), $K = 1.42 \times 10^{-8} \times 10^{1240/T}$ (dB/km × kHz^2), $f_{\mathrm{MgSO_4}} = 1.125 \times 10^{(9 - 2038/T)}$ (kHz), $A_{\mathrm{MgSO_4}} = 62.5ST \times 10^{-6}$ (dB/km × kHz), $f_B = 37.9S^{0.8} \times 10^{-780/T}$ (kHz), $A_B = 1.65S \times 10^{(4 + 0.78pH - 3696/T)}$ (dB/km × kHz), S is the salinity (‰), T is the temperature (K), and pH is the effective pH value.

The first term on the right-hand side of Eq. (1) characterizes the relaxation absorption caused by boron, the second term corresponds to the relaxation absorption caused by magnesium sulfate, and the third term determines the sound attenuation in seawater.

In accordance with the measured characteristics of Ch1 with the axis at a depth of 200–400 m, the temperature and salinity were specified as 11.5°C and 36‰, respectively. Unfortunately, no data were found on the vertical distributions of the pH value in the archives available to the author. In view of the general information given in [11] for this region of the Atlantic Ocean, the pH values were specified as 8.05 and 8.1 in the calculations.

The fifth column of the table contains the values of the excess of the experimental attenuation coefficients over the calculated coefficients of sound absorption. The differences are within –0.008 to +0.008 dB/km. At frequencies of 100–500 Hz, the values of the excess fall within a narrower range, 0.005 to 0.008 dB/km; that is, they are nearly independent of frequency. At these frequencies, the attenuation was determined from the decay of the sound field over nearly the entire path (50–1160 km). At frequencies higher than 800 Hz, the decay over a shorter path fraction (50–500 km or less that is, about half of the path length) was used in calculating the attenuation.

In view of the aforementioned changes in the hydrological parameters along the path, namely, the gradual increase in the depth of the Ch1 axis, the estimation was performed for the deviation of the geometrical-spread decay of the sound field from the cylindrical law. The calculations were based on the wave-field computer code by Avilov with a zero-valued sound absorption in seawater and a perfectly absorbing bottom. The resulting curves of the sound field decay at the distances of 50–1100 km were approximated by the cylindrical decay law with an exponential attenuation. The best agreement between the calculated and approximating curves was obtained for an exponent equal to 0.006-0.007 dB/km. The calculated exponent in the exponential attenuation caused by the variation of the hydrological parameters along the path agrees well with the excess Δ of the experimental attenuation coefficients over the ones calculated according to [10] for frequencies up to 800 Hz. Thus, the decay of the sound field at the 200-m horizon is fully determined by the sound absorption in seawater and by the geometrical spread that differs from the cylindrical law under the influence of the monotonic increase in the depth of the CH1 axis along the path with increasing distance from the reception point. Therefore, the decay law proved to be quite predictable in our case.

In the case under study, the predictability of the geometrical spread law is the consequence of the gradual changes in the characteristics of Ch1 along the propagation path. However, one cannot predict the changes in the hydrological parameters for the ocean regions where various disturbing factors (strong currents, frontal zones, and others) exist. To estimate the frequency dependence of the attenuation coefficient in such zones, we have repeatedly used the so-called differential method ([12, 13], for instance) proposed by Sheehy and Hally [14] in the mid-fifties. This method is based on two assumptions. The first one states that the law of the geometrical spread is unknown but is the same for the entire frequency band. The second assumption implies that the frequency dependence of the attenuation coefficient is described by a power-law function with a zero-valued constant component. The decays of the sound field at individual frequencies are normalized to the decay at a single frequency treated as a reference. Thus, the unknown law of the geometrical spread is eliminated. From the normalized spread at each of the frequencies, the differential attenuation coefficient is determined, which can be shown to be equal to the difference between the total attenuation coefficients at two frequencies: the frequency to be analyzed and the reference frequency. By approximating the frequency dependence of the differential attenuation coefficient with the power law and neglecting the absolute term, we obtain the following explicit form for the conventionally used attenuation coefficient: $\beta = kf^n$.

The differential method of estimating the attenuation was applied to the data of the experiment at hand. The resulting estimates for a frequency band of 100–800 Hz with a reference frequency of 250 Hz are

Comparison of the experimental data on sound attenuation (for the 200-m reception depth) with the frequency dependence of the absorption coefficient calculated by the formulas given in [10]

Frequency, Hz	β, dB/km	α, dB/km (t = 11.5°C, S = 36‰)		Δ, dB/km	β, dB/km (differential method)
		pH = 8.05	pH = 8.1		
100	0.008	0.001	0.001	0.007	0.0029
125	0.008	0.0016	0.0018	0.0063	0.0016
160	0.010	0.0027	0.0029	0.0072	0.0039
200	0.012	0.0041	0.0045	0.0077	0.0058
250	0.015	0.0063	0.0069	0.0084	0.0088
315	0.018	0.0098	0.0107	0.0078	0.012
400	0.023	0.0153	0.0166	0.0075	0.017
500	0.029	0.0228	0.0247	0.0053	0.022
630*	0.040	0.0336	0.0364	0.0050	0.034
800*	0.057	0.0486	0.0526	0.0064	0.048
1000*	0.070	0.0661	0.0715	0.0012	–
1250*	0.084	0.0865	0.0934	–0.006	–
1600*	0.108	0.112	0.120	–0.008	–

Note: Frequencies at which the sound attenuation was determined from the decay of the sound field within a fraction of the path.

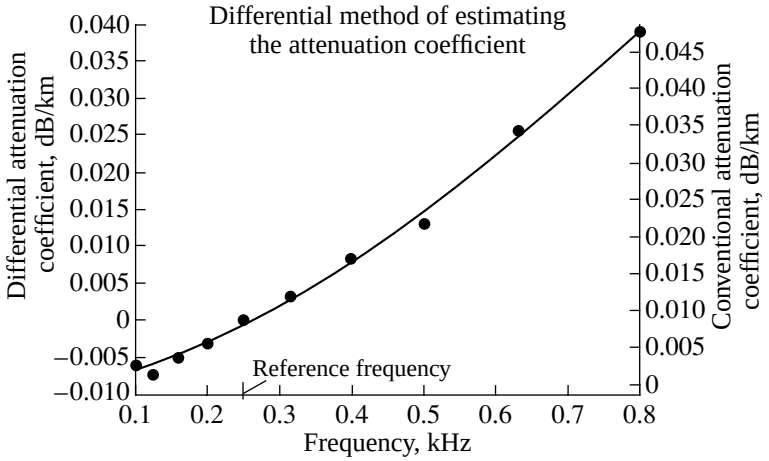

Fig. 7. Experimental values of the differential attenuation coefficient and the scheme of transforming it into the conventional attenuation coefficient.

0.0674 and 1.52 for k and n, respectively. Figure 7 shows the results of applying the differential method to our experimental data and illustrates the scheme of transforming the differential values into the conventional attenuation coefficients. The transformation consists in nothing but a shift of the scale by the constant component of the power-law dependence that approximates the frequency dependence of the differential attenuation coefficient. The last column of the table contains the conventional attenuation coefficients obtained with the use of the differential method. One can state that the application of this method confirms the main conclusion of this work: with the unknown law of the geometrical spread being eliminated, the attenuation is fully determined by the sound absorption in the sea medium. The attenuation coefficient estimated by the differential method agrees well with the calculated values: the deviations are lower than 0.001–0.002 dB/km.

In conclusion, let us formulate the main results obtained from analyzing the data of the experiment on long-range propagation of explosion-generated signals in a two-axis underwater sound channel in the northeastern Atlantic.

—The experiment was performed in a fully developed two-axis underwater sound channel with a monotonic increase in the depth of the axis of the upper channel from 100–140 m at the beginning to 350–400 m at the end of the 1160-km-long propagation path. The axis of the lower channel was at a depth of 1500–1600 m. The signals were received at depths of 200 and 1200 m. The charges used as the sound sources exploded at a depth of 200 m along the entire path.

—The time structure of the sound field in the upper channel is characterized by the absence of the "classical" signal quartets advancing the main group of waterpath signals. At distances that are multiples of 55–65 km, water signals that arrive with delays relative to the main group of signals and propagate in both the upper and lower channels were observed. Signals multiply reflected by the surface and the bottom were observed at all distances, up to the longest one. The shape of the signals in the main group, which are not separated in time, is worth noting: the leading and trailing edges are not clearly defined, and the total duration of this group is proportional to the distance with a proportionality factor of about 0.0013 s/km.

—The time structure of the sound field below the boundary between the upper and lower channels (at a reception depth of 1200 m) is characterized by a pronounced set of signals multiply reflected from the bottom and the surface. The structure of this set agrees well with the calculations. In addition to this set, compact groups of signals are steadily observed with the propagation velocity equal to that of the water signals propagating in the upper channel. The existence of this group can be explained by the calculations based on the wave-field computer code by Avilov.

—On the basis of the analysis of the explosion-generated signals received and recorded at 200 m, the frequency dependence of attenuation is estimated. Two methods of determining the attenuation coefficient are used: with the method of estimating the deviation of the decay of the sound field level from the cylindrical law and with the differential method that eliminates the unknown geometrical spread law (the latter being other than the cylindrical one). The attenuation coefficients obtained with these two methods differ from each other by 0.006–0.008 dB/km. This value is virtually independent of frequency and is determined by the variation of the hydrological parameters along the propagation path. For the experiment under study, this value agrees well with the calculations based on the computer code by Avilov. The attenuation coefficients obtained with the differential method agree well with the values obtained for the absorption coefficients in the sea medium from the formulas proposed in [10].

ACKNOWLEDGMENTS

I am grateful to V.V. Nemchenko for his active participation in the experiment and in the preliminarily processing of experimental data. This work was supported by the Russian Foundation for Basic Research, project nos. 04-02-16959 and 04-05-64557.

REFERENCES

1. R. A. Vadov, Akust. Zh. **40**, 992 (1994) [Acoust. Phys. **40**, 880 (1994)].
2. R. A. Vadov, Akust. Zh. **41**, 202 (1995) [Acoust. Phys. **41**, 172 (1995)].
3. R. A. Vadov, Akust. Zh. **42**, 269 (1996) [Acoust. Phys. **42**, 236 (1996)].
4. R. A. Vadov, Akust. Zh. **43**, 470 (1997) [Acoust. Phys. **43**, 401 (1997)].
5. W. D. Wilson, J. Acoust. Soc. Am. **32**, 1357 (1960).
6. R. P. Bulatov, M. S. Barash, V. N. Ivanenkov, and Yu. Yu. Marti, *Atlantic Ocean* (Mysl', Moscow, 1977) [in Russian].
7. V. P. Tebyakin *et al.*, *A Report of the Acoustics Institute* (Moscow, 1990).
8. K. V. Avilov, Akust. Zh. **41**, 5 (1995) [Acoust. Phys. **41**, 1 (1995)].
9. K. V. Avilov, N. A. Dobryakov, and O. E. Popov, in *Proceedings of X Workshop by Acad. L. M. Brekhovskikh* (GEOS, Moscow, 2004), p. 2.
10. R. A. Vadov, Akust. Zh. **46**, 624 (2000) [Acoust. Phys. **46**, 544 (2000)].
11. *Atlas of the Oceans. Atlantic and Indian Oceans. Navy of the USSR*, Ed. by S. G. Gorshkov (Min. Oborony SSSR, Moscow, 1977) [in Russian].
12. R. A. Vadov, Akust. Zh. **46**, 47 (2000) [Acoust. Phys. **46**, 37 (2000)].
13. R. A. Vadov, Akust. Zh. **48**, 751 (2002) [Acoust. Phys. **48**, 665 (2002)].
14. M. J. Sheehy and R. Halley, J. Acoust. Soc. Am. **29**, 464 (1957).

Translated by E. Kopyl

Acoustical Physics, Vol. 51, No. 6, 2005, pp. 638–643. Translated from Akusticheskiĭ Zhurnal, Vol. 51, No. 6, 2005, pp. 742–748.

Reconstruction of a Dynamic Load Acting on a Viscoelastic Layer

A. O. Vatul'yan*, V. M. Dragilev, and L. L. Dragileva*****

**Rostov State University, ul. Zorge 5, Rostov-on-Don, 344090 Russia*
e-mail: vatylian@mail.lp.ru
***Don State Technical University, pl. Gagarina 1, Rostov-on-Don, 344010 Russia*
e-mail: vdragil@mail.ru
****Rostov State Pedagogical University, ul. Bol'shaya Sadovaya 33, Rostov-on-Don, 344082 Russia*
e-mail: vdragil@rnd.runnet.ru
Received April 23, 2004

Abstract—An inverse boundary-value problem, namely, the reconstruction of the spatial distribution of a contact load from the displacements given on a part of a free surface, is considered. The model is formulated as the generalization of results obtained earlier for an elastic layer. It is found that viscosity produces no special effects that may hamper the reconstruction, except for the attenuation of quasi-homogeneous modes at long distances. At the same time, it is shown that a successful reconstruction requires a consideration of viscosity. The latter statement is illustrated by a numerical example calculated at a frequency equal to the inverse relaxation time; the corresponding dissipation factor is about 0.05. © *2005 Pleiades Publishing, Inc.*

Inverse boundary-value problems of the theory of elasticity form a topical branch of the mechanics of deformable solids [1–12]. The formulation of these problems is characterized by nonclassical boundary conditions that are specified on certain parts of a body's surface rather than on the whole surface. The interest in such problems follows from the engineering problems of strength analysis, nondestructive testing, structural intensimetry, and vibration resistance of structures. In the dynamical theory of elasticity, inverse boundary-value problems were studied for stationary wave fields [4–12]; these problems were discussed for isotropic [4–6, 10] and anisotropic [7–9] elastic media, as well as for viscoelastic materials [11, 12]. Mathematical methods used for solving inverse problems depend on their ill-posed nature and include analytical methods of boundary integral equations, finite-difference schemes with the Tikhonov regularization [13, 14], and (see [1–6, 9, 10]) different versions of the projection method [15] with a discrete regularization. The ill-posed character of inverse boundary-value problems makes it necessary to focus special attention on the analysis of model examples that give an idea about the actual possibilities of the wave field reconstruction. No such analysis was carried out in the context of models with allowance for the wave absorption. Here, we extend the inverse boundary-value problem considered earlier [10] to the case of a viscoelastic medium [16, 17]. The goal of this work consists in the determination of the extent to which the reconstruction efficiency depends on viscosity and the extent to which the consideration of viscosity is needed for a successful reconstruction of the field of a contact load.

Consider a homogeneous layer of a viscoelastic isotropic material occupying the region $[-\infty < x, z < \infty, 0 \le y \le h]$ in the Cartesian coordinates (x, y, z). The lower boundary of the layer ($y = 0$) is rigidly fixed, and the upper boundary ($y = h$) is loaded by an external normal load

$$q_y(x, t) = \mathrm{Re}\{\exp(-i\omega t)q(x)\}, \tag{1}$$

distributed over a certain region $x \in [X_1, X_2]$. We assume that the load brings the layer in the state of forced stationary vibrations under the conditions of planar deformation (under these conditions, the wave field components are independent of the z coordinate and the displacement vector $\mathbf{u}$ is parallel to the (x, y) coordinate plane). In the steady-state regime, the generalized Hooke's law [16, 17] holds:

$$\sigma_{ij} = \lambda(-i\omega)\delta_{ij}\varepsilon_{kk} + 2\mu(-i\omega)\varepsilon_{ij}, \tag{2}$$

where σ_{ij} and ε_{ij} are the stress and strain tensors, respectively; $\lambda(-i\omega)$ and $\mu(-i\omega)$ are the complex moduli that grade into the Lamé coefficients in the case of an elastic layer; here and below, symbols of all dynamical variables, such as $\mathbf{u}$ and ε_{ij}, denote the corresponding complex amplitudes. According to Eq. (2), the amplitude of displacements satisfies the equation

$$\rho\omega^2\mathbf{u} + [\lambda(-i\omega) + \mu(-i\omega)]\vec{\nabla}(\vec{\nabla}\mathbf{u}) + \mu(-i\omega)\Delta\mathbf{u} = 0, \tag{3}$$

where $\vec{\nabla}$ is the gradient operator, $\Delta = \vec{\nabla}^2$, and ρ is the density. At the layer boundaries, the following boundary conditions hold:

$$\begin{cases} (\hat{M}\mathbf{u})_x = (\hat{M}\mathbf{u})_y = 0, \\ (y = h, x \notin [X_1, X_2]), \\ (\hat{M}\mathbf{u})_x = 0, \quad (\hat{M}\mathbf{u})_y = q(x), \\ (y = h, x \in [X_1, X_2]), \\ \mathbf{u} = 0, \quad (y = 0), \end{cases} \tag{4}$$

where $\hat{M}\mathbf{u}$ is the vector operator of boundary stress with the components

$$\begin{cases} (\hat{M}\mathbf{u})_x = \mu(-i\omega)(u_{y,x} + u_{x,y}), \\ (\hat{M}\mathbf{u})_y = \lambda(-i\omega)u_{x,x} + [\lambda(-i\omega) + 2\mu(-i\omega)]u_{y,y}. \end{cases} \tag{5}$$

Boundary conditions (4) generate a mixed boundary-value problem whose solution describes forced vibrations of the layer under the action of source (1). We consider this problem to be the direct one.

Let us now formulate the inverse problem that consists in the reconstruction of the load field $q(x)$ from the normal displacements of the free surface of the layer, $u_y(x)$, that are given on a surface part $x \in [X_3, X_4]$, where $[X_3, X_4] \cap [X_1, X_2] = \varnothing$. In the inverse problem, the boundary conditions for Eq. (3) have the form

$$\begin{cases} \hat{M}\mathbf{u} = 0, \ (y = h, x \notin [X_1, X_2]), \\ u_y = u(x), \quad (y = h, x \in [X_3, X_4]), \\ \mathbf{u} = 0, \quad (y = 0), \end{cases} \tag{6}$$

where the function $u(x)$ is assumed to be known approximately (for example, from measurements) and the components of vector $\hat{M}\mathbf{u}$ are given by Eqs. (5).

Now, we have to complement the inverse problem formulation with formulas for the complex moduli. In the framework of the conventional theory of a viscoelastic solid [16, 17], for definiteness, we use the four-parameter model that implies the following expressions for the moduli:

$$\begin{aligned} \mu(-i\omega) &= \frac{1}{2}G_1(0) - \frac{1}{2}C\frac{1 + i\omega\tau}{1 + \omega^2\tau^2}, \\ \lambda(-i\omega) + 2\mu(-i\omega) &= K + \frac{2}{3}G_1(0) - \frac{2}{3}C\frac{1 + i\omega\tau}{1 + \omega^2\tau^2}; \end{aligned} \tag{7}$$

where $G_1(0)$, C, K, and τ are real constants. The constant K is the bulk modulus and $G_1(0)$, C, and τ are the parameters of the relaxation function for shear strains [16] (τ is the relaxation time).

We introduce the scale of stress as $\lambda_\infty + 2\mu_\infty$:

$$\lambda_\infty + 2\mu_\infty = \lim_{\omega \to \infty}[\lambda(-i\omega) + 2\mu(-i\omega)] = K + \frac{2}{3}G_1(0).$$

The formulated model can be parameterized using the following set of dimensionless physical constants:

$$\kappa = \omega h\sqrt{\rho/(\lambda_\infty + 2\mu_\infty)} \tag{8}$$

is the dimensionless frequency,

$$\tau_* = \tau h^{-1}\sqrt{(\lambda_\infty + 2\mu_\infty)/\rho} \tag{9}$$

is the dimensionless relaxation time, and

$$\chi_\infty = \frac{1}{2}G_1(0)/(\lambda_\infty + 2\mu_\infty), \quad C_* = C/(\lambda_\infty + 2\mu_\infty). \tag{10}$$

The layer thickness h will be used below as the unit of length.

By analogy with [10], the inverse problem can be reduced to a Fredholm integral equation of the first kind:

$$\int_{X_1}^{X_2} k(x - x')q(x')dx' = u(x), \quad x \in [X_3, X_4], \tag{11}$$

where $k(x - x')$ is Green's function (the solution to the direct problem for a point source). In the case of an elastic layer, Green's matrix was constructed using the method of integral transformations [18]. The corresponding extension to the case of a viscoelastic layer can be obtained using the conformity principle [16, 17] by replacing the Lamé coefficients with the complex moduli. As a result, we obtain Green's function in the integral representation:

$$k(\zeta) = \frac{1}{2\pi}\int_{-\infty}^{\infty} K(p)e^{-ip\zeta}dp, \tag{12}$$

where $\zeta = x - x'$,

$$K(p) = (\lambda_\infty + 2\mu_\infty)^{-1}\Delta_{yy}(p)/\Delta(p) \tag{13}$$

(the subscript yy corresponds to the tensor component of Green's matrix),

$$\begin{aligned} \Delta(p) &= (4\Omega_1^2\Omega_2^2\chi_1^2p^2 + 4\chi_1^2p^6 - 4\chi_1\kappa^2p^4 + \kappa^4p^2) \\ &\times \frac{\sin\Omega_1\sin\Omega_2}{\Omega_1\Omega_2} + (-8\chi_1^2p^4 + 4\chi_1\kappa^2p^2 - \kappa^4) \\ &\times \cos\Omega_1\cos\Omega_2 + 8\chi_1^2p^4 - 4\chi_1\kappa^2p^2, \end{aligned}$$

$$\Delta_{yy}(p) = \kappa^2\left(\cos\Omega_1\Omega_2\sin\Omega_2 + p^2\frac{\sin\Omega_1}{\Omega_1}\cos\Omega_2\right),$$

$$\chi_n \equiv \chi_n(\omega), \quad \Omega_n = \sqrt{\kappa^2/\chi_n(\omega) - p^2}, \quad (n = 1; 2),$$

$$\chi_1(\omega) = \frac{\mu(-i\omega)}{\lambda_\infty + 2\mu_\infty}, \quad \chi_2(\omega) = \frac{\lambda(-i\omega) + 2\mu(-i\omega)}{\lambda_\infty + 2\mu_\infty}.$$

Using Eqs. (7), one can easily express Eqs. (11)–(13) in terms of the dimensionless variables (8)–(10).

Wave numbers of homogeneous and quasi-homogeneous modes

Model	P_1	P_2	P_3
Elastic layer	1.1007	3.7744	6.8141
Viscoelastic layer	1.1007 + 0.0002 *i*	3.7744 + 0.0010 *i*	6.8141 + 0.00085 *i*

Note the fundamental properties of kernel (12) and its Fourier transform (13). Function $K(p)$ in Eq. (13) is an even meromorphic function. In the model of an elastic layer, at high frequencies, this function has real poles, which correspond to homogeneous wave modes [18] (the integration contour in Eq. (12) must bypass these poles according to the rules dictated by the principle of limiting absorption [18]). In a viscoelastic layer, homogeneous modes are generally absent. We can suppose that homogeneous modes may appear for specially adjusted parameters; however, we do not investigate here the possibility of such special cases and exclude them from consideration. For low and high frequencies, or, equivalently, for short and long relaxation times ($k\tau_* \ll 1$ and $k\tau_* \gg 1$), the limiting conformity with the model of an elastic layer [10] takes place. In these cases, the spectrum may contain weakly attenuating modes that pass into the homogeneous modes in the absence of viscosity. Such quasi-homogeneous modes appear for $\kappa > \bar{\kappa}$, where $\bar{\kappa}$ is the critical dimensionless frequency [18]; in the approximation of long relaxation times ($\kappa\tau_* \gg 1$), it is given by the expression

$$\bar{\kappa} = \pi\sqrt{\chi_\infty}/2. \tag{14}$$

For small arguments, function (12) can be described by the following asymptotic formula:

$$k(\zeta) = -\frac{(\lambda_\infty + 2\mu_\infty)^{-1}}{2\pi\chi_1(\omega)[\chi(\omega) - 1]}\ln|\zeta| + O(1), \quad \zeta \longrightarrow 0, \tag{15}$$

where $\chi(\omega) = \chi_1(\omega)/\chi_2(\omega)$. Formula (15) clearly shows that, irrespective of the presence of quasi-homogeneous modes, the kernel $k(\zeta)$ has a nonzero imaginary component (it disappears in the case of an elastic layer) that causes the vibrations to be shifted in phase; this phase shift can be interpreted as the viscosity-induced effect of retardation. For large arguments, kernel (12) degenerates, because the corresponding asymptotics is governed by the contribution of the pole nearest to the real axis:

$$k(\zeta) = iR\exp(ip|\zeta|)\{1 + O[\exp(-c|\zeta|)]\}, \quad (|\zeta| \longrightarrow \infty). \tag{16}$$

Here, R, p, and c are complex constants, $\mathrm{Im}\,p > 0$, and $\mathrm{Im}\,c > 0$. The kernel's logarithmic singularity explicitly given in Eq. (15) falls outside the integration interval in Eq. (11). The smooth behavior of the kernel leads to the ill-posed character of the inverse problem and to the necessity of its regularization [13].

We perform a further analysis for a specific set of parameters: $G_1(0) = 10C = 10^3$ mPa, $\tau = 0.01$ s, and $K = 4.67 \times 10^3$ mPa (these parameters fall into the region typical of polymer materials). The corresponding dimensionless variables (10) take the following values: $\chi_\infty = 0.0937$ and $C_* = 0.0188$. We specify the dimensionless relaxation time (9) to be $\tau_* = 200$, which, for the density $\rho \sim 10^3$ kg/m^3, corresponds to a layer of thickness $h \sim 10^{-1}$ m. Note that the dimensionless parameter τ_* increases with decreasing thickness, so that values of $\tau_* \ll 200$ can hardly occur in practice for polymer items.

It is instructive to derive some rough estimates. A measure of deviation from the classical Hooke's law is the so-called dissipation factor, i.e., the ratio of the imaginary part of the complex modulus to its real part [16]. In our model, the maximum of the dissipation factor is $0.5\gamma/\sqrt{1-\gamma}$, where $\gamma = C/G_1(0)$; this maximum is reached at the frequency $\kappa_0 = \sqrt{1-\gamma}\tau_*^{-1}$. If $\kappa \gg \kappa_0$, the layer is close to an elastic layer in its properties. For the above parameters, we have $\gamma = 0.1$ and $\kappa_0 \approx \tau_*^{-1} \ll 1$. At the same time, critical frequency (15) is comparable with unity, $\bar{\kappa} = 0.481$. Because $\bar{\kappa} \gg \kappa_0$, we can conclude that, for frequencies exceeding the critical frequency, the wave pattern appears to be almost the same as that in the case of an elastic layer with the only difference that homogeneous modes transform into weakly decaying modes.

This inference is supported by the following example. At a frequency of $\kappa = 2$, only three quasi-homogeneous modes are present; for these modes, we calculated the complex wave numbers p_m that coincide with the poles of the function $K(p)$. In the table, these wave numbers are compared with the corresponding wave numbers determined in the approximation of an elastic layer, i.e., for $C = 0$. As may be seen from the table, the imaginary additions to wave numbers do not exceed 0.03% and the real parts remain intact within the calculation error. The viscosity-induced corrections to the kernel $k(\zeta)$ (Eq. (12)) are mainly related to the attenuation of quasi-homogeneous modes. For relatively small distances $|\zeta| = |x - x'|$ such that $|\zeta||\mathrm{Im}\,p_m| < 10^{-2}$, these corrections appear to be smaller than one percent. It becomes obvious that, if we assume that the measurement error is estimated as 1% [4], we can perform the reconstruction in this region of parameters by using the elastic-layer approximation (see [10] for examples of reconstruction of model functions for $\kappa > \bar{\kappa}$). The consideration of viscosity in this parameter region should be worthwhile only for a much smaller measurement error, because the class of functions $q(x)$ that allow an adequate reconstruction enlarges very slowly with

increasing measurement accuracy. The latter conclusion can be explained in terms of singular decompositions [4, 5, 10]; namely, in view of the fast decrease of singular numbers, a decrease in input errors by 1–2 decimal digits allows, as a rule, reconstruction of at most 1–2 additional terms in the generalized Fourier expansion of the desired function.

Thus, the consideration of viscosity for $\kappa > \bar{\kappa}$ is of little interest with the exception of situations when an additional small or large parameter appears in the model. These situations are realized (i) if the distances between the points $x' \in [X_1, X_2]$ and $x \in [X_3, X_4]$ are on the order of $|\mathrm{Im}\,|\mathrm{Im}\,p_m|^{-1}$ or greater, so that the attenuation of quasi-homogeneous modes becomes apparent; (ii) if the frequency is close to the resonance frequency (see paper [18] for the theory of resonances in the case of an elastic layer). In these cases, viscosity will be an essential factor. Note that both the above situations are unfavorable for the wave field reconstruction. Indeed, different quasi-homogeneous modes are characterized by different logarithmic decrements (see table as an example), so that the modes decaying more weakly become predominant at large distances and only one mode prevails in the asymptotics, in agreement with Eq. (16). For this reason, the degeneration characteristic of the far zone (see discussion in [10]) becomes still stronger in the case under discussion. A similar degeneration occurs near the resonance frequencies, where only the resonance mode can be observed distinctly and other modes can hardly be distinguished against the background of the resonance mode, which results in a loss of information about the source (in [5] the opposite effect of improved reconstruction near the resonances was reported; however, this effect refers to the reconstruction of integral characteristics of the wave field rather than its spatial configuration).

Consider now the frequency range $\kappa \sim \tau_*^{-1}$, where dissipation becomes most apparent. Figure 1 shows the typical behavior of Green's function $k(\zeta)$ (Eq. (12)) for such frequencies (these curves and the following numerical results are obtained for the frequency $\kappa = \tau_*^{-1} = 0.005$). For $|\zeta| \gtrsim 3$, the main term of asymptotics (16) prevails and approximates function (12) with an error smaller than 1%; for these distances, the kernel approaches its degenerate form and the field reconstruction is hardly possible. Viscosity only slightly affects the real part of the function $k(\zeta)$, and its main effect consists in the appearance of the imaginary part of the kernel. The curves describing the real and imaginary parts are similar in shape (see Fig. 1); this means that traveling waves (which are absent for low frequencies in the case of an elastic layer) are weakly pronounced. Hence, the main consequence of viscosity is the above effect of retardation, i.e., the appearance of an additional common phase in the displacement function. It is obvious that this effect by no means affects the basic possibility of reconstruction. The viscosity-induced imaginary corrections to Green's function come to about 10% (as expected, these corrections are about $\gamma = 0.1$). To estimate how important these corrections are in solving the inverse problem, direct numerical experiments are required.

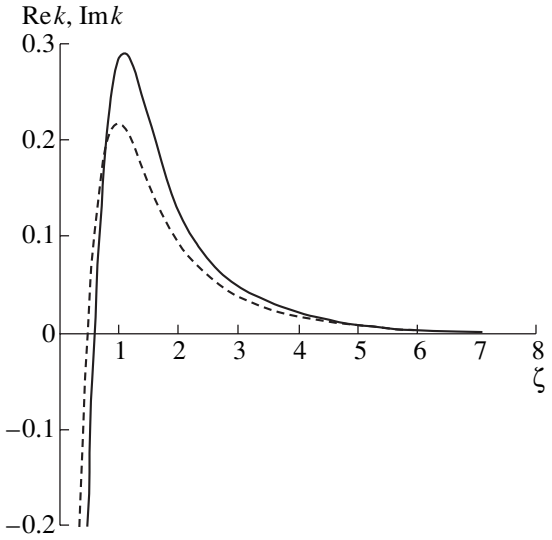

Fig. 1. Green's function $k(\zeta)$ (Eq. (12)) for $\kappa = 0.005$; the solid line shows $\mathrm{Re}\{k(\zeta)\}$, and the dashed line shows $\mathrm{Im}\{k(\zeta)\} \times 10$.

Such experiments with the reconstruction of model load functions were carried out according to the known scheme; namely, for a given original function $q(x)$, we determined the numerical solution to the direct problem by using Eqs. (11) and (12) and then used the resulting function of displacements as the initial data in the reconstruction problem. To solve integral equation (11), we used the finite-difference algorithm with the first-order stabilizer [12, 13] that was derived in the framework of the Tikhonov approach. Random errors were simulated according to the procedure used in paper [10]. We used real model original functions; in addition, as was done in [10], we passed to the modified integral equation with the kernel $\tilde{k}(\zeta) = \mathrm{Re}\{\exp(i\theta)k(\zeta)\}$ and the right-hand side $\tilde{u}(x) = \mathrm{Re}\{\exp(i\theta)u(x)\}$. For the real phase θ corresponding to an observation instant $t = \theta/\omega$, we specified a value of $\pi/4$; in this case, the real and imaginary parts of kernel (12) contribute to the kernel $\tilde{k}(x - x')$ with identical weights, which yields an objective estimate of the viscosity contribution.

Figures 2 and 3 show examples of reconstructing the fields of the load acting on the viscoelastic layer (we used model load functions of the form $q(x) = a_0 \sin(kx + b) + a_1$). These figures show the whole of the region $[X_1, X_2]$ of load application, and the solid lines show the original functions. In the figure captions, we give the values of the following parameters: the number of observation points J uniformly distributed on the segment $[X_3, X_4]$, the number of nodes n of the

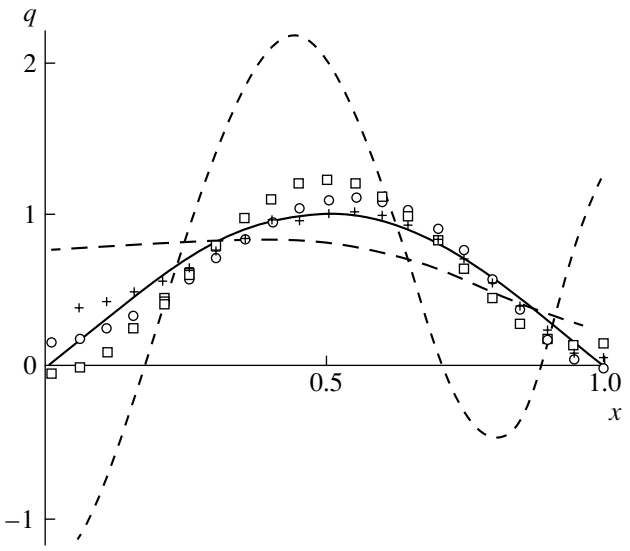

Fig. 2. Reconstruction of the model function. The parameters are as follows: $[X_3, X_4] = [1.5, 6]$; $J = 15$; $n = 21$; $\Delta = 0.03$; and $\alpha = 10^{-m}$, where $m = 6, 7, \ldots, 10$.

finite-difference mesh on the segment $[X_1, X_2]$, the relative level of random errors Δ [10], and the regularization parameter α [13]. We present here the results obtained for different parameters α to give a clear idea about the reconstruction fidelity. The two dashed lines in each of the figures correspond to the maximum and minimum values used for the parameter α (as usual, results appear unstable for very small α and smoothed for large α); the dots show the results obtained with intermediate optimum values of the regularization parameter.

According to our experience with calculations, the contact stress reconstruction at low frequencies (below critical frequency (14)) is ineffective in comparison with the case of high frequencies, at which (quasi-)homogeneous modes are present. This fact is unrelated to the presence of viscosity and is characteristic of the elastic layer as well (the interpretation of this fact requires separate research and is beyond the scope of this paper). In the absence of weakly decaying modes and for relative random errors $\Delta \sim 10^{-3}$–10^{-2}, a satisfactory quality of reconstruction can be achieved only for simple functions that have no more than one prominent extremum (see Figs. 2 and 3 and compare with the examples of reconstruction for frequencies exceeding the critical frequency [10]).

For the example of Fig. 3, we carried out calculations using two different procedures. In the first case (Fig. 3a), we solved the inverse problem by simulating the transition to the elastic-layer approximation; for this purpose, we rejected the imaginary part of the kernel $k(\zeta)$ (Eq. (12)). In the other case (Fig. 3b), we constructed the solution to the inverse problem without additional approximations. As may be seen from the curves, the attempt to neglect the viscosity-induced complex corrections results in a deterioration of images; moreover, the results appear to be less stable with respect to the value of the regularization parameter.

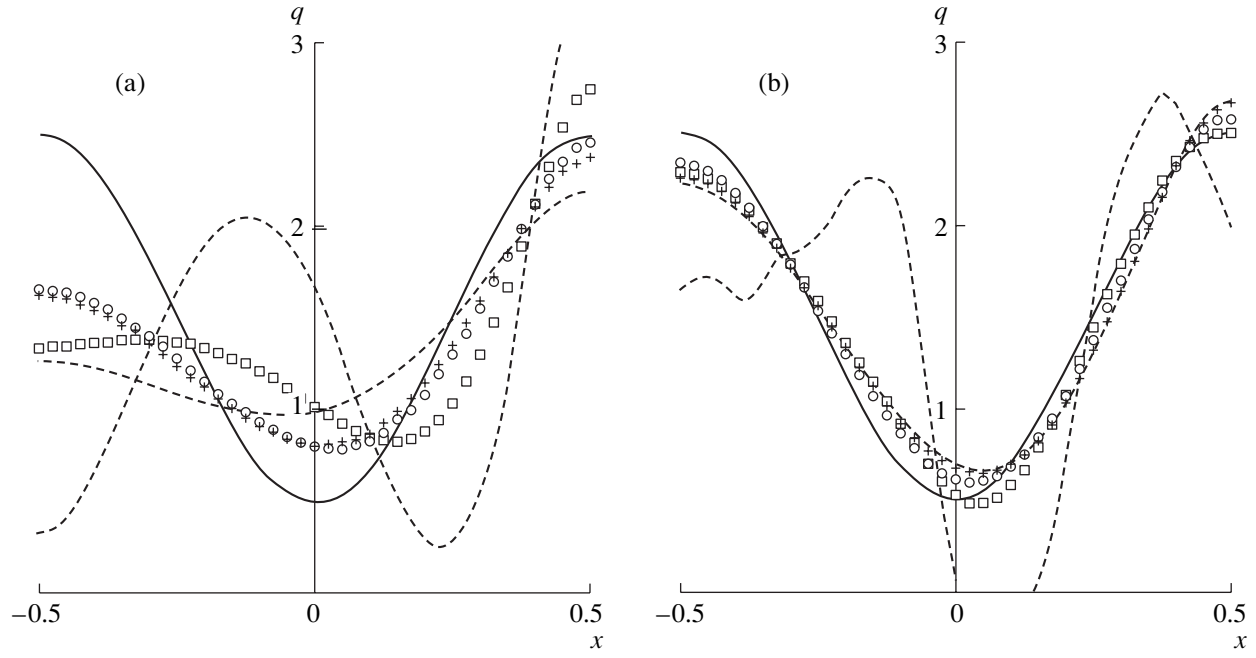

Fig. 3. Reconstruction of the model function (a) without considering the imaginary part of the kernel and (b) with allowance for the imaginary part of the kernel. The parameters are as follows: $[X_3, X_4] = [1, 3]$; $J = 21$; $n = 41$; $\Delta = 0.001$; and $\alpha = 10^{-m}$, where (a) $m = 7, 8, \ldots, 11$ and (b) $m = 9, 10, \ldots, 13$.

Thus, in the framework of the proposed model, we realized the numerical solution of the inverse boundary-value problem for stationary wave fields excited in a viscoelastic body. With the chosen parameters of the model, we successfully performed a detailed comparison with a similar model [10] developed in the approximation of the classical Hooke's law. As can be seen from our analysis, inelastic effects do not affect the efficiency of the reconstruction of a contact load, except for the natural restrictions related to the attenuation of quasi-homogeneous modes at large distances. At the same time, a successful reconstruction generally requires that viscosity-induced corrections be taken into account. First and foremost, this refers to the reconstruction of the fields at frequencies of about the inverse relaxation time and at frequencies close to resonance. The example given in this paper shows that, at least for dissipation factors of about 10^{-1} and greater, the neglect of relaxation in inverse problems is undesirable.

ACKNOWLEDGMENTS

This work was supported in part by a grant from the President of the Russian Federation in Support of Leading Scientific Schools (grant no. NSh-2113.2003.1).

REFERENCES

1. A. V. Fomin and A. K. Preĭss, Mashinovedenie, No. 1, 79 (1982).
2. A. V. Fomin, Mashinovedenie, No. 4, 67 (1982).
3. A. K. Preĭss, Mashinovedenie, No. 2, 77 (1984).
4. Yu. I. Bobrovnitskiĭ, Akust. Zh. **40**, 367 (1994) [Acoust. Phys. **40**, 331 (1994)].
5. Yu. I. Bobrovnitskiĭ, M. P. Korotkov, A. A. Kochkin, and T. M. Tomilina, Dokl. Akad. Nauk, Mekhanika, No. 2, 190 (1998).
6. S. E. S. Karlsson, J. Sound Vib. **196** (1), 59 (1996).
7. A. O. Vatul'yan, I. I. Vorovich, and A. N. Solov'ev, Prikl. Mat. Mekh. **64** (3), 373 (2000).
8. A. O. Vatul'yan and A. N. Solov'ev, Akust. Zh. **46**, 451 (2000) [Acoust. Phys. **46**, 385 (2000)].
9. A. O. Vatul'yan, Izv. Vyssh. Uchebn. Zaved., Estestv. Nauki, Severo-Kavkazskiĭ Region, 31–35 (2001).
10. A. O. Vatul'yan, V. M. Dragilev, and L. L. Dragileva, Akust. Zh. **47**, 757 (2001) [Acoust. Phys. **47**, 665 (2001)].
11. A. O. Vatul'yan and E. V. Sadchikov, in *Proceedings of V International Conference on Modern Problems of Mechanics of Continua, Rostov-on-Don, Russia, 2000* (Sev.-Kavk. Nauch. Tsentr Vysh. Shkola, Rostov-on-Don, 2000), Vol. 2, pp. 53–57.
12. A. O. Vatul'yan and A. N. Solov'ev, in *Proceedings of VIII All-Union Congress on Theoretical and Applied Mechanics, Perm, Russia, 2001* (Perm, 2001), p. 146.
13. A. N. Tikhonov and V. Ya. Arsenin, *Solutions of Ill-Posed Problems* (Nauka, Moscow, 1986; Halsted Press, New York, 1977).
14. A. N. Tikhonov, A. V. Goncharskiĭ, V. V. Stepanov, and A. G. Yagola, *Numerical Solutions of Ill-Posed Problems* (Nauka, Moscow, 1990) [in Russian].
15. A. M. Denisov, *Introduction to the Theory of Ill-Posed Problems* (Mosk. Gos. Univ., Moscow, 1994) [in Russian].
16. R. Christensen, *Theory of Viscoelasticity: An Introduction* (Academic, New York, 1971; Mir, Moscow, 1974).
17. A. Nashif, D. Jones, and J. Henderson, *Vibration Damping* (Wiley, New York, 1985; Mir, Moscow, 1988).
18. I. I. Vorovich and V. A. Babeshko, *Mixed Dynamic Problems of the Theory of Elasticity for Nonclassical Regions* (Nauka, Moscow, 1979) [in Russian].

Translated by A. Vinogradov

Acoustical Physics, Vol. 51, No. 6, 2005, pp. 644–652. Translated from Akusticheskiĭ Zhurnal, Vol. 51, No. 6, 2005, pp. 749–758.

Fluctuations of Noiselike Signals Reflected from a Rough Surface at the Output of a Correlation Receiver

E. P. Gulin

Andreev Acoustics Institute, Russian Academy of Sciences, ul. Shvernika 4, Moscow, 117036 Russia
e-mail: bvp@akin.ru

Received June 20, 2003

Abstract—The frequency and time averaging of the fluctuations that occur in the cross-correlation function of a radiated noiselike acoustic signal with the signal received after its reflection from a rough water surface is considered. The variance and temporal correlation function are calculated for the output effect of a correlation receiver for different ratios between the averaging time and the time correlation interval of fluctuations, the band width of the radiated signal, and the frequency correlation interval of the transfer function fluctuations. © *2005 Pleiades Publishing, Inc.*

In solving different problems by means of sonar monitoring (underwater observation), it is necessary to take into account the effect of random variations in the parameters of the underwater sound channel, which are caused by the dynamic processes arising at the surface and in the water column of the ocean. This effect manifests itself in the distortion of the initial information on the objects under observation. In the general case, the characteristics of signals propagating in channels with random parameters, the underwater sound channel being one of them, depend on both the properties of the initial radiation and the features of the linear stochastic filter of the medium, which determines the distortions of the initial signals. The measure of such distortions can be the cross-correlation function Q_{su} between the received signal $s(t)$ and the radiated signal $u(t)$. This function is a significant element of various algorithms for optimized processing of received signals and, in particular, characterizes the noise immunity of the coherent and incoherent reception in channels with random parameters [1–3]. Investigations showed that the decrease in the cross-correlation of radiated noiselike sonar signals with the received ones is due to both multipath sound propagation and sound scattering by random volume inhomogeneities of the refractive index, the rough sea surface, and the roughness and inhomogeneities of the sea bottom [4–9]. Note that different aspects related to investigations of the efficiency of the correlation reception of noise and noiselike sonar signals were also considered in later works, including the series of works published in recent years [10–12].

Using the known relationships of the theory of linear stochastic filters [1, 3, 13], the estimate of the output effect of a correlation receiver (a synchronous detector), after integrating over time T, can be presented as

$$\begin{aligned} Q_{su}(t_d) &= \frac{1}{T}\int_0^T s(t)u(t-t_d)dt \\ &= \frac{A_{sr}}{2\pi T}\int_0^T\int_{-\infty}^{\infty}\int_{-\infty}^{\infty} P(\omega_1, t_1)u(t_1-t_d)u(t_2) \\ &\quad\times \exp[i\omega_1(t_1-t_2)]dt_1dt_2d\omega_1, \end{aligned} \tag{1}$$

where $P(\omega_1, t_1)$ is the transfer function of the propagation channel for acoustic signals; t_d is the time delay of the reference signal which is the replica of the radiated signal delayed by the time of its propagation; and $u(t)$ and $s(t)$ are real random processes. The quantity A_{sr} is a constant factor equal to the product of the transfer coefficients of linear tracks (devices) for the formation and reception of signals, the sensitivity of the transducer in the radiation mode [14], and the sensitivity of the sound receiver. These quantities are assumed to be frequency-independent within the signal frequency band. In what follows, we set $A_{sr} = 1$. Expression (1) allows one to calculate the temporal autocorrelation function of the signal at the output of the correlation receiver: $K_Q(\Delta t, t_d) = \langle Q_{su}(t_d)Q_{su}(t_d - \Delta t)\rangle$. The angular brackets denote statistical averaging over the ensemble of random parameters of the signal propagation channel. This is sufficient for the case of deterministic signals, for example, for signals with the intrapulse modulation that follows a given law. For a noiselike signal, it is necessary to carry out an additional statistical averaging over the ensemble of the initial random signals $u(t)$. In this case, we assume that $u(t)$ is a normally distributed stationary random function with zero mean value, a variance σ_u^2, and a frequency spectrum $G_u(\omega)$. In spite of

the fact that the calculations presented below were carried out for continuous noiselike acoustic radiation, their results are applicable to pulsed signals whose duration noticeably exceeds the integration time.

The transfer function P can be represented as the sum of the mean field $\langle P\rangle$ and the fluctuations ΔP. Then, the cross-correlation function Q_{su} can be written in the form of the sum of the mathematical expectation $\langle Q_{su}\rangle$ and the fluctuation part ΔQ_{su}. The autocorrelation function (ACF) of the signal at the output of the correlation receiver can be represented as $K_Q(\Delta t, t_d) = K_{\langle Q\rangle}(\Delta t, t_d) + K_{\Delta Q}(\Delta t, t_d)$, where $K_{\langle Q\rangle}(\Delta t, t_d) = \langle Q_{su}(t_d)\rangle\langle Q_{su}(t_d - \Delta t)\rangle$ is the part of the ACF caused by the coherent field and $K_{\Delta Q}(\Delta t, t_d) = \langle \Delta Q_{su}(t_d)\Delta Q_{su}(t_d - \Delta t)\rangle$ is the temporal correlation moment of the fluctuation part of the output effect of the correlation receiver. In the case of the transfer function fluctuations described by a stationary random process, we have

$$K_{\langle Q\rangle}(\Delta t, t_d) = \frac{1}{T^2}\int_0^T\int_0^T dt_1 dt_2 \int_{-\infty}^{\infty}\int_{-\infty}^{\infty} G_u(\omega_1)G_u(\omega_2)$$
$$\times \exp(i\omega_2\Delta t)\{2\langle\tilde{P}(\omega_1)\rangle\langle\tilde{P}^*(\omega_2)\rangle$$
$$\times \exp[i(\omega_1-\omega_2)\tau_d]\exp[i(\omega_1+\omega_2)(t_1-t_2)/2] \quad (2)$$
$$\times \cos[(\omega_1+\omega_2)(t_1-t_2)/2]$$
$$+ \langle|\tilde{P}(\omega_1)|^2\rangle\exp[i(\omega_1-\omega_2)(t_1-t_2)]\}d\omega_1 d\omega_2,$$

$$K_{\Delta Q}(\Delta t, t_d) = \frac{1}{T^2}\int_0^T\int_0^T dt_1 dt_2 \int_{-\infty}^{\infty}\int_{-\infty}^{\infty} G_u(\omega_1)G_u(\omega_2)$$
$$\times \exp(i\omega_2\Delta t)\{2\tilde{K}_{\Delta P}(\omega_1, \omega_2, \Delta t)$$
$$\times \exp[i(\omega_1-\omega_2)\tau_d]\exp[i(\omega_1+\omega_2)(t_1-t_2)/2] \quad (3)$$
$$\times \cos[(\omega_1+\omega_2)(t_1-t_2)/2]$$
$$+ \tilde{K}_{\Delta P}(\omega_1, \omega_1, \Delta t)\exp[i(\omega_1-\omega_2)(t_1-t_2)]\}d\omega_1 d\omega_2,$$

where $\tilde{K}_{\Delta P}(\omega_1, \omega_2, \Delta t)$ is the frequency–time correlation moment of fluctuations of the transfer function envelope $\tilde{P} = P\exp(i\omega t_0)$ (in general case, a complex one), $\tau_d = t_d - t_0$, and t_0 is the propagation time of the signal (its coherent part). In deriving Eqs. (2) and (3), we used the property of the transfer function that $P(-\omega, t) = P^*(\omega, t)$, where the asterisk means complex conjugation, and took into account the parity of the power spectrum of the initial signal: $G_u(-\omega) = G_u(\omega)$. At $\Delta t = 0$, Eqs. (2) and (3) describe, respectively, the intensity of the coherent component, I_{Qc}, and the signal variance at the output of the correlation receiver σ_Q^2, while their sum describes the mean signal intensity $I_Q = I_{Qc} + \sigma_Q^2 = K_Q(0, t_d)$ for different time delays t_d. Let us denote by Δt_P and $\Delta\omega_P$ the time and frequency correlation scales of the transfer function fluctuations at the central frequency ω_0 of the radiated narrowband signal and by $\Delta\omega_u$, the effective bandwidth of the spectrum for this signal. In the limiting cases $\Delta t_p \ll T$ and $\Delta t_P \gg T$ (rapid and slow fluctuations), $\Delta\omega_P \gg \Delta\omega_u$ and $\Delta\omega_P \ll \Delta\omega_u$ (synchronous and selective fading according to the terminology of the statistical theory of communication [2]), one can obtain approximate estimates of the intensity of the fluctuation component (the variance σ_Q^2) and the total energy, I_Q, of the output effect of the correlation receiver. These estimates do not depend on the fluctuation nature in the signal propagation channel, the form of frequency–time correlation moment $\tilde{K}_{\Delta P}(\omega_1, \omega_2, \Delta t)$, or that of the radiated signal $C_u(\omega)$ [8]. In order to obtain the results in a wider range of parameter variations, it is necessary to specify the forms of the frequency–time correlation moment of the transfer function and the spectrum of the noiselike radiated signal.

As an example of a channel with random parameters, consider the reflection of acoustic signals from a rough sea surface. As is known, rather intense sound scattering from the rough sea surface is observed in a wide frequency range beginning from tens of hertz, which gives rise to rapid random fluctuations and a reduction of the coherence of the sound field reflected from the surface. Assume that surface displacements $\zeta(x, y, t)$ (deviations from the mean plane) are described by a random function stationary in time and homogeneous in space, normally distributed with a variance σ_ζ^2. Assume that the energy spectrum of the initial noiselike signal has the form

$$G_u(\omega) = \frac{\sigma_u^2}{\sqrt{\pi}\Delta\omega_u}\left\{\exp\left[-4\left(\frac{\omega-\omega_0}{\Delta\omega_u}\right)^2\right]\right.$$
$$\left. + \exp\left[-4\left(\frac{\omega+\omega_0}{\Delta\omega_u}\right)^2\right]\right\}, \quad (4)$$

which corresponds to the time correlation function $K_u(\Delta t) = \sigma_u^2\exp[-(\Delta\omega_u\Delta t)^2/16]\cos(\omega_0\Delta t)$. Consider first the coherent signal component at the correlation receiver output. Let us substitute the known expression for the reflected mean field (the envelope of the transfer function) into Eq. (2):

$$\langle\tilde{P}(\omega)\rangle = R_0^{-1}\exp\left(-\frac{\Phi_0^2\omega^2}{2\omega_0^2}\right), \quad (5)$$

where $R_0 = (z_s + z_r)/\sin\psi$; ψ is the grazing angle at the point of specular reflection from the mean plane; z_s and z_r are the depths of sound radiation and reception, respectively; $\Phi_0 = 2(\omega_0/c_s)\sigma_\zeta\sin\psi$ is the Rayleigh

parameter at the central frequency of the spectrum ω_0; and c_s is the sound speed. For the spectrum $G_u(\omega)$ given by Eq. (4), after some calculations, we obtain an expression containing a weighted sum of single integrals:

$$K_{\langle Q\rangle}(\Delta t, \tau_d) = \sum_{n=1}^{5} N_n J_n. \tag{6}$$

Here, the following notations are introduced:

$$J_1 = \cos(\omega_0\beta\Delta t) + \cos(\omega_0\beta\tilde{t}_0),$$

$$J_n = \frac{1}{T}\int_0^T \left(1 - \frac{\tau}{T}\right)\exp(-a_n\tau^2)$$

$$\times [\exp(-c_n\tau)\cos(b_n\tau + d_n)$$

$$+ \exp(c_n\tau)\cos(b_n\tau - d_n)]d\tau, \quad n = 2\ldots5;$$

$$\beta = (1 + 0.5\Phi_0^2\delta_\omega^2)^{-1}, \quad \delta_\omega = 0.5\Delta\omega_u/\omega_0,$$

$$\tilde{t}_0 = \Delta t + 2\tau_d, \quad N_{1-3} = N_0\exp(-h_1 - h_2),$$

$$N_0 = 0.5R_0^{-2}\sigma_u^4\beta\exp(-\Phi_0^2\beta), \tag{7}$$

$$N_{4,5} = \tilde{N}_0\exp(-h_1 - h_2), \quad h_1 = (\Delta\omega_u\beta\Delta t)^2/32,$$

$$h_2 = (\Delta\omega_u\tilde{t}_0)^2/32, \quad a_{2,3} = (\Delta\omega_u\beta)^2/8,$$

$$a_{4,5} = (\Delta\omega_u\tilde{\beta})^2/(8\beta), \quad b_2 = 2\omega_0\beta, \quad b_3 = 0,$$

$$b_4 = 2\omega_0\tilde{\beta}/\beta, \quad b_5 = \omega_0\tilde{\beta}\delta_\omega^2\Phi_0^2,$$

$$c_{2,3} = (\Delta\omega_u\beta)^2\Delta t/8, \quad c_{4,5} = (\Delta\omega_u\tilde{\beta})^2\Delta t/8,$$

$$d_2 = \omega_0\beta\Delta t, \quad d_3 = \omega_0\beta\tilde{t}_0, \quad d_{4,5} = \omega_0\tilde{\beta}\Delta t.$$

The quantities $\tilde{N}_0$ and $\tilde{\beta}$ are obtained from N_0 and β with Φ_0^2 in place of $2\Phi_0^2$.

An analysis of sum (6) shows that, for $\Delta\omega_u T \gg 1$, the first term prevails. Because $\delta_\omega < 1$, for $\Phi_0^2 \ll 1$ we have $\beta \simeq 1$, $\Delta\omega_u\beta \simeq \Delta\omega_u$, and $\omega_0\beta \simeq \omega_0$. In this case, the intensity of the coherent component of the noiselike signal is close to the mean intensity of the total reflected field and does not depend on the bandwidth $\Delta\omega_u$. The time correlation function $K_{\langle Q\rangle}(\Delta t)$ at $\tau_d = 0$, after the introduction of the delay for the signal propagation time $t_d = R_0/c_s$, coincides within a constant factor with the time correlation function of the initial signal $K_u(\Delta t)$. As the Rayleigh parameter Φ_0 increases, the effective bandwidth $\Delta\omega_u\beta$ and the central frequency $\omega_0\beta$ of the coherent component of the radiated noiselike signal decreases due to the stronger decrease in the high-frequency part of the spectrum. The intensity of the coherent field, the time correlation scale, and the period of the correlation function oscillations $K_{\langle Q\rangle}(\Delta t)$ increases as the initial signal band increases according to the expression

$$K_{\langle Q\rangle}(\Delta t) \simeq R_0^{-2}\sigma_u^4\beta\exp(-\Phi_0^2\beta)$$

$$\times \exp[-(\Delta\omega_u\beta\Delta t)^2/16]\cos(\omega_0\beta\Delta t).$$

These effects are most pronounced for $\Phi_0^2\delta_\omega^2 \gg 1$; however, in this case, the intensity of the coherent component is negligibly small compared to the mean intensity of the total field. A noticeable influence of these effects appears only in the region $\Phi_0 \simeq 1$ for a relatively wide frequency band of the initial noiselike signal.

We now turn to calculations of the correlation of the fluctuation component of the reflected signal at the output of the correlation receiver. Calculations for the frequency–time correlation moment of the transfer function fluctuations $\tilde{K}_{\Delta P}(\omega_1, \omega_2, \Delta t)$ were performed in [15–17]. The limiting cases of strong and weak fluctuations were considered for $\exp(-\Phi_\omega^2) \ll 1$ and $\Phi_\omega^2 \ll 1$, respectively, where the values of the Rayleigh parameter Φ_ω were taken for the frequency range $\omega_{\min} \le \omega \le \omega_{\max}$ occupied by the noiselike signal. According to the expressions obtained in the general case for an arbitrary frequency band, the scattered field cannot be considered as statistically homogeneous in frequency. Let us use approximate expressions suitable for the description of the transmission of relatively narrow-band signals through a linear stochastic filter caused by the scattering from a quasi-harmonic roughness of the water surface. In the small-slope approximation and for low scattering angles with respect to the specular reflection from the mean surface, in the framework of the two-dimensional model of the sea roughness, when the surface displacements depend on the single horizontal coordinate, the frequency–time correlation moment $\tilde{K}_{\Delta P}(\Delta\omega, \Delta t)$ is determined by the expression

$$\tilde{K}_{\Delta P}(\Delta\omega, \Delta t) \simeq R_0^{-2}\left(1 + i\frac{\Delta\omega}{\Delta\omega_{P1}}\right)^{-1}$$

$$\times \exp\left\{-\left(\frac{\Delta\omega}{\Delta\omega_{P2}}\right)^2 - \left(\frac{\Delta t}{\Delta t_{P0}}\right)^2\left[1 + i\left(\frac{\Delta\omega}{\Delta\omega_{P1}}\right)\right]^{-1}\right\} \tag{8}$$

in the case of strong fluctuations and by the expression

$$\tilde{K}_{\Delta P}(\Delta\omega, \Delta t) \simeq \frac{\Phi_0^2}{2R_0^2}\left[1 + i\left(\frac{\Delta\omega}{\Delta\omega_{P1}}\right)\right]^{-1/2}$$

$$\times \exp(-i\Delta\omega\Delta t_d)\left\{\exp\left[-\left(\frac{\Delta t}{\Delta t_\zeta} + \frac{\Delta\omega}{\Delta\omega_{P2}}\right)^2\right.\right.$$

$$\left.\left.\times \frac{1}{\sqrt{1 + i(\Delta\omega/\Delta\omega_{P1})}} - i\Omega_\zeta\Delta t\right]\right. \tag{9}$$

$$+\exp\left[-\left(\frac{\Delta t}{\Delta t_\zeta}-\frac{\Delta\omega}{\Delta\omega_{P2}}\right)^2\frac{1}{\sqrt{1+i(\Delta\omega/\Delta\omega_{P1})}}+i\Omega_\zeta\Delta t\right]\Bigg\},$$

in the case of weak fluctuations. Expression (8) obtained for a quasi-harmonic gravity wave on the surface of a deep basin does not depend on the form of the correlation function $\Gamma_\zeta(\rho, \Delta t)$ or the random sea spectrum $G_\zeta(\omega)$ and is determined only by the spectral moments $\overline{\Omega_\zeta^n} = 2\int_0^\infty G_\zeta(\Omega)\Omega^n d\Omega$. Expression (9) was obtained for the frequency spectrum of the random sea G_ζ corresponding to time correlation function $\Gamma_\zeta(\Delta t) = \exp[-(\Delta t/\Delta t_\zeta)^2]\cos(\Omega_\zeta\Delta t)$. The parameters $\Delta\omega_{P1}$ and $\Delta\omega_{P2}$ in Eqs. (8) and (9) have the meaning of frequency correlation scales for the transfer function fluctuations. One of them describes the decay of the frequency correlation by the power law, the second, by the exponential law. In the case of strong fluctuations, $\Delta\omega_{P1} = \omega_0^2 g^2(z_s + z_r)\sin^3\psi[\Phi_0^2\overline{\Omega_\zeta^4} z_s z_r c_s(1 - \cos^2\psi\sin^2\alpha)]^{-1}$, $\Delta\omega_{P2} = \sqrt{2}\,\omega_0/\Phi_0$, g =9.81 m/s^2, $\Delta t_{P0} = \sqrt{2}/(\sqrt{\overline{\Omega_\zeta^2}}\,\Phi_0)$ is the time correlation scale of the transfer function fluctuations at the frequency ω_0, α is the angle in the horizontal plane between the direction of surface wave propagation and the vertical plane containing the sound source and the receiver. In the case of weak fluctuations, $\Delta\omega_{P1} = 2\omega_0/[D_\alpha(l+1)l^2]$, $\Delta\omega_{P2} = 2\omega_0/(D_\alpha\Omega_\zeta\Delta t_\zeta l)$, $D_\alpha = c_s R(1 - \cos^2\psi\sin^2\alpha)/[\omega_0\sin^2\psi v^2(\Delta t_\zeta)^2]$, v is the phase speed of gravity waves on the basin surface, $R = 2z_s z_r/[(z_s + z_r)\sin\psi]$, $\Delta t_d = \Omega_\zeta\Delta t_\zeta/(2l\Delta\omega_{P2})$, $l = 1$ for a shallow basin, and $l = 2$ for a deep basin. At $l = 2$, Eq. (9) is an approximate one that is valid for a quasi-harmonic sea surface when $\Omega_\zeta\Delta t_\zeta \gg 1$ (in this case, $v \simeq g/\Omega_\zeta$). For a quasi-harmonic sea surface, $\Delta\omega_{P2}/\Delta\omega_{P1} \simeq (\Omega_\zeta\Delta t_\zeta)^{-1} \ll 1$ and, therefore, the frequency correlation decay is mainly determined by the smaller scale ($\Delta\omega_{P2}$).

With allowance for the statistical homogeneity of the frequency fluctuations of the transfer function, according to Eqs. (8) and (9), the initial integral expression (3) is reduced to the form

$$K_{\Delta Q}(\Delta t, t_d) \simeq \frac{2\sigma_u^4}{T}\int_0^T\int_{-\infty}^{\infty}\int_{-\infty}^{\infty}\left(1-\frac{\tau}{T}\right)G_u(\omega+\Omega/2)$$
$$\times G_u(\omega-\Omega/2)\exp[i(\omega-\Omega/2)\Delta t]$$
$$\times\{2\tilde{K}_{\Delta P}(\Omega,\tau)\exp(i\Omega\tau_d)\cos^2(\omega\tau)$$
$$+\tilde{K}_{\Delta P}(0,\tau)\cos(\Omega\tau)\}d\tau d\omega d\Omega. \quad (10)$$

Consider first the case of strong fluctuations. For calculating integral (10), we use the one-dimensional model of the frequency correlation function by assuming that conditions $(\Delta\omega_{P2}/\Delta\omega_{P1})^2 \ll 1$ and $\Delta\omega_{P1} \geq \Delta\omega_u$ are valid. In this case, the decay of the frequency correlation within the signal frequency band is determined by the exponential factor with the correlation scale $\Delta\omega_{P2}$. A similar model was also considered in [18]. In the framework of this model, the frequency decorrelation of acoustic field fluctuations is related to the change in wave dimensions (the number of Fresnel zones) of the scattering region along the vertical as the frequency varies [15, 19]. Substituting Eqs. (4) and (8) into Eq. (10), after calculating the integrals with respect to the variables ω and Ω, we arrive at a result that can be represented as the weighted sum of the integrals J_n coinciding in the form with integral (7):

$$K_{\Delta Q}(\Delta t, \tau_d) \simeq K_Q(\Delta t, \tau_d) = \sum_{n=1}^{6} M_n J_n. \quad (11)$$

Parameters a_n, b_n, c_n, and d_n involved in J_n, as well as the weighting coefficients M_n, in Eq. (11) take the following values:

$$a_{1,2} = 1/(\Delta t_{P0})^2, \quad a_{3-6} = (\Delta\tilde{\omega}_u)^2/8 = (\Delta\omega_u)^2/8 + a_1,$$
$$b_{1,2,4,5} = 0, \quad b_{3,6} = 2\omega_0, \quad c_{1,2} = 0,$$
$$c_{3-6} = (\Delta\omega_u)^2\Delta t/8, \quad d_{1,3,5,6} = \omega_0\Delta t,$$
$$d_{2,4} = \tilde{\omega}_0\tilde{t}, \quad \tilde{\omega}_0 = \omega_0\gamma_{up}^2, \quad \tilde{t} = 2\tau_d + \Delta t,$$
$$M_{1,3} = 0.5M_0\exp(-H_1 - H_2),$$
$$M_{2,4} = 0.5M_0\exp(-H_1 - H_2 - H_3), \quad (12)$$
$$M_{5,6} = 0.5M_0\gamma_{up}^{-1}\exp(-2H_1),$$
$$M_0 = \sigma_u^4 R_0^{-2}\gamma_{up}, \quad \gamma_{up} = [1 + 0.5(\Delta\omega_u/\Delta\omega_{P2})^2]^{-1/2},$$
$$H_1 = (\Delta\omega_u\Delta t)^2/32,$$
$$H_2 = (\Delta\omega_u\tilde{t})^2\gamma_{up}^2/32, \quad H_3 = (2\omega_0/\Delta\omega_{P2})^2\gamma_{up}^2.$$

Integrating over τ in Eq. (7), the correlation function $K_{\Delta Q}$ can be evaluated in terms of the tabulated probability integrals of the complex argument [20, 21] $w(Z) \simeq \exp(-Z^2)\left[1 + \frac{2i}{\sqrt{\pi}}\int_0^Z \exp(t^2)dt\right]$, where $Z = X + iY$. The tables are composed for the region $X > 0$, $Y > 0$. For calculating $w(Z)$ beyond this region, one can use the relationships $w(-Z) = 2\exp(-Z^2) - w(Z)$ and $w(Z^*) = 2\exp[-(Z^*)^2] - w^*(Z)$. Upon integration in Eq. (7), we obtain

$$J_n = \frac{1}{2a_nT^2}\exp(-a_nT^2)$$
$$\times[\exp(c_nT)\cos(b_nT - d_n)$$
$$+\exp(-c_nT)\cos(b_nT + d_n)] - \frac{\cos d_n}{a_nT^2}$$

$$+\frac{\sqrt{\pi}}{a_n T^2}[\exp(-X_n^2+Y_{no}^2)$$
$$\times(-Y_{no}\cos\varphi_n+X_n\sin\varphi_n+\sqrt{a_n}T\cos\varphi_n)$$
$$+(U_{no}Y_{no}+V_{no}X_n)\cos d_n$$
$$-(V_{no}Y_{no}-U_{no}X_n)\sin d_n] \qquad (13)$$
$$-\frac{\sqrt{\pi}}{2a_n T^2}\exp(-a_n T^2)$$
$$\times\{\exp(c_n T)[\cos(b_n T-d_n)(Y_{n1}U_{n1}+X_n V_{n1})$$
$$+\sin(b_n T-d_n)(X_n U_{n1}-Y_{n1}V_{n1})]$$
$$+\exp(-c_n T)[\cos(b_n T+d_n)(Y_{n2}U_{n2}+X_n V_{n2})$$
$$+\sin(b_n T+d_n)(X_n U_{n2}-Y_{n2}V_{n2})]\},$$

where

$$U_{nm}=\mathrm{Re}w(Z_{nm}),\quad V_{nm}=Jmw(Z_{nm}),$$
$$(n=1\ldots6;\ m=0,1,2),\quad \varphi_n=2Y_{no}X_n-d_n,$$
$$Z_{nm}=X_{nm}+iY_{nm},$$
$$X_{n0}=X_{n1}=X_{n2}=X_n=b_n/(2\sqrt{a_n}),$$
$$Y_{n0}=c_n/(2\sqrt{a_n}),$$
$$Y_{n1}=\sqrt{a_n}T-c_n/2\sqrt{a_n},\quad Y_{n2}=\sqrt{a_n}T+c_n/2\sqrt{a_n}.$$

A comparative analysis of the terms entering into sum (11) shows that, for narrow-band signals $(\Delta\omega_u/\omega_0)^2 \ll 1$) at the rather small interval of frequency correlation ($(\Delta\omega_{P2}/\omega_0)^2 \ll 1$) and weak restrictions that are usually satisfied in practice for composite noiselike signals ($\Delta\omega_u T \gg 1$, $\Delta\omega_u \Delta t_{P0} \gg 1$, and $|\Delta t|/T \ll 1$), the main contribution is made by the first term, $M_1 J_1$. The next term in order of magnitude is the term with the number $n = 5$. As a result, we obtain the following approximate expression for the correlation function $K_{\Delta Q}$:

$$K_{\Delta Q}(\Delta t, t_d)\simeq 0.5\sigma_u^4 R_0^{-2}\gamma_{up}\varepsilon^{-1}$$
$$\times\exp(-H_1-H_2)\cos(\omega_0\Delta t)$$
$$\times\{\sqrt{\pi}\Phi(\varepsilon)-\varepsilon^{-1}[1-\exp(-\varepsilon^2)]$$
$$+[2\sqrt{2\pi}\varepsilon\exp(H_2)](\Delta\omega_u T\gamma_{up})^{-1}\}.$$

Here, ε denotes the ratio $\varepsilon = T/\Delta t_{P0}$ and $\Phi(\varepsilon) = \frac{2}{\sqrt{\pi}}\int_0^{\varepsilon}\exp(-x^2)\,dx$ is the probability integral. Then, for small integration times T compared to the time correlation scale Δt_{P0} (the case of slow fluctuations) and a completely compensated time delay of the signal ($t_d = R_0/c_s$, $\tau_d = 0$, and $\tilde{t} = \Delta t$), we obtain

$$K_{\Delta Q}(\Delta t, R_0/c_s)\simeq 0.5\sigma_u^4 R_0^{-2}\gamma_{up}$$
$$\times\exp(-H_1-H_2)\cos(\omega_0\Delta t) \qquad (14)$$
$$\times\{1+2\sqrt{2\pi}\exp(H_2)(\Delta\omega_u T\gamma_{up})^{-1}\}.$$

Let us introduce the normalized variance of fluctuations (NVF), $\tilde{\sigma}_Q^2 = \sigma_Q^2(2R_0^2/\sigma_u^4) = K_{\Delta Q}(0, R_0/c_s)(2R_0^2/\sigma_u^4)$, which in the case of strong fluctuations is almost equal to the normalized mean intensity of the output effect of the correlation receiver $\tilde{I}_Q$. From Eq. (14), we obtain

$$\tilde{\sigma}_Q^2\simeq[1+0.5(\Delta\omega_u/\Delta\omega_{P2})^2]^{-1/2}+[2\sqrt{2\pi}/\Delta\omega_u T].$$

For $(\Delta\omega_u/\Delta\omega_{P2})^2 \ll 1$ (slow synchronous fluctuations within the signal frequency band), $\gamma_{up} \simeq 1$ and $\tilde{\sigma}_Q^2 \simeq 1 + [2\sqrt{2\pi}/\Delta\omega_u T]$. For $(\Delta\omega_u/\Delta\omega_{P2})^2 \gg 1$ (slow selective fluctuations), $\tilde{\sigma}_Q^2 \simeq (\sqrt{2}\,\Delta\omega_{P2}/\Delta\omega_u) + [2\sqrt{2\pi}/\Delta\omega_u T]$. For large integration times compared to the correlation scale Δt_{P0} (the case of rapid fluctuations), we have

$$K_{\Delta Q}\simeq 0.5\sigma_u^4 R_0^{-2}\{\varepsilon^{-1}\gamma_{up}\sqrt{\pi}\exp(-H_1-H_2)\cos(\omega_0\Delta t)$$
$$+(2\sqrt{2\pi}/\Delta\omega_u T)\exp(-H_1)\cos(\omega_0\Delta t)\}.$$

Therefore, at $(\Delta\omega_u/\Delta\omega_{P2})^2 \ll 1$, we obtain $\tilde{\sigma}_Q^2 \simeq (\sqrt{\pi}\,\Delta t_{P0}/T) + (2\sqrt{2\pi}/\Delta\omega_u T)$, whereas for $(\Delta\omega_u/\Delta\omega_{P2})^2 \gg 1 - \tilde{\sigma}_Q^2 \simeq (\sqrt{2\pi}\,\Delta\omega_{P2}\Delta t_{P0}/\Delta\omega_u T) + [\sqrt{8\pi}/\Delta\omega_u T]$. From the formulas presented above, it follows that NVF $\tilde{\sigma}_Q^2$ characterizes the extent of frequency and time averaging of fluctuations. The quantity $\tilde{\sigma}_Q^2$ is the sum of two terms. The first term strongly depends on the ratios $\Delta t_{P0}/T$ and $\Delta\omega_{P2}/\Delta\omega_u$ and determines the averaging of fluctuations caused by the scattering from the rough surface. The second term only depends on the parameters of the initial signal and the correlation processing. It is determined by the remainder of fluctuations (not completely averaged) of the initial noiselike signal. To neglect this term in the above limiting cases, it is sufficient to impose the conditions $\min(\Delta f_u, \Delta f_{P2})T \gg 1$ and $\min(\Delta f_u, \Delta f_{P2})\Delta t_{P0} \gg 1$, where $\Delta f_u = \Delta\omega_u/2\pi$, and $\Delta f_{P2} = \Delta\omega_{P2}/2\pi$. When these conditions are met, the normalizing coefficient $0.5\sigma_u^4 R_0^{-2}$ (the ratio of the true variance to the normalized one, $\sigma_Q^2/\tilde{\sigma}_Q^2$) is approximately equal to the maximum value of the variance $\sigma_{Q\max}^2$, which corresponds to the case of slow synchronous fluctuations when the averaging over frequency and time is absent. In the case of strong fluctuations at $(\Delta\omega_u/\omega_{P2})^2 \gg 1$, the frequency averaging leads to a decrease in the mean intensity of the signal at the output of the correlation receiver.

The normalized AKF of the output effect of the correlation receiver, $\Gamma_{\Delta Q} = K_{\Delta Q}/\sigma_Q^2$, for both small and large times of integration, is determined by the relationship

$$\Gamma_{\Delta Q} \simeq \exp[-(\Delta\omega_u \Delta t)^2(1+\gamma_{up}^2)/32]\cos(\omega_0 \Delta t).$$

For $(\Delta\omega_u/\Delta\omega_{P2})^2 \ll 1$, it coincides with the normalized temporal correlation function of the initial noiselike signal: $\Gamma_{\Delta Q} \simeq \Gamma_u = K_u/\sigma_u^2 = \exp[-(\Delta\omega_u \Delta t)^2/16]\cos(\omega_0 \Delta t)$. For $(\Delta\omega_u/\Delta\omega_{P2})^2 \gg 1$, $\Gamma_{\Delta Q} \simeq \exp[-(\Delta\omega_u \Delta t)^2/32]\cos(\omega_0 \Delta t)$. In this case, the frequency averaging of fluctuations leads to an increase in the time correlation scale and a narrowing of the spectrum of the noiselike signal by a factor of $\sqrt{2}$.

If, along with the signal reflected from the surface, a weakly fluctuating direct signal without any contacts with the surface is received, then, with the compensation for the time its propagation, the mean intensity of the fluctuating part of the field will additionally be weakened:

$$I_Q \simeq \sigma_Q^2 \simeq \frac{\sigma_u^4}{2R_0^2}[1+0.5(\Delta\omega_u/\Delta\omega_{P2})^2]^{-1/2} \times \exp[-(\Delta\omega_u \Delta R \gamma_{up})^2/(8c_s^2)].$$

Here, ΔR is the path difference between the direct signal and of the signal reflected from the surface.

The analytical estimates obtained are valid for composite noiselike signals and do not allow the transition to the case of monochromatic radiation. Substituting $u(t) = A_0\cos(\omega_0 t - \varphi_0)$ in Eq. (1), at $\omega_0 T \gg 1$, we arrive at the following expression for the variance of monochromatic signal fluctuations σ_{Q0}^2 at the output of the correlation receiver:

$$\sigma_{Q0}^2 \simeq I_{Q0}^2 \simeq \frac{A_0^4}{4T^2}\int_0^T\left(1-\frac{\tau}{T}\right) \times \{\mathrm{Re}\tilde{K}_p(\omega_0, \omega_0, \tau)[1+\cos(2\omega_0\tau)] + \mathrm{Re}\tilde{K}_p(\omega_0, -\omega_0, \tau)]\}d\tau.$$

Taking into account that, at $(\Delta\omega_P/\omega_0)^2 \ll 1$, we have $|\mathrm{Re}\tilde{K}_p(\omega_0, -\omega_0, \tau)| \ll |\mathrm{Re}\tilde{K}_p(\omega_0, \omega_0, \tau)|$, and, in the case of small integration times when $(T/\Delta t_{P0})^2 \ll 1$, we obtain $\sigma_{Q0}^2 \simeq I_{Q0}^2 \simeq A_0^4 R_0^{-2}/8$. For identical values of the mean square of the noiselike signal amplitude distributed by the Rayleigh law and the square of the monochromatic signal amplitude, we have $A_0^2 = 2\sigma_u^2$. With allowance for this equality, the ratio of the variance of the noiselike signal fluctuations and that of the monochromatic signal equals NVF $\tilde{\sigma}_Q^2$, which determines the extent of averaging over frequency and time of noiselike signal fluctuations.

Consider now the case of weak fluctuations. Carrying out the same transformations as for strong fluctuations, in the framework of one-dimensional model Taking into account only the exponential decay of the frequency correlation in Eq. (9),[1] we arrive at the expression $K_{\Delta Q}(\Delta t, \tau_d) = \sum_{n=1}^{9}\tilde{M}_n J_n$. The latter represents the weighted sum of nine integrals coinciding in their form with intergal (7) but with different values of parameters entering in J_n:

$$a_{1,2} = (\gamma_{up}/\Delta t_\zeta)^2, \quad a_{3-6} = (\Delta\omega_u)^2/8 + (\gamma_{up}/\Delta t_\zeta)^2,$$

$$a_{7-9} = (\Delta\tilde{\omega})^2/8 = (\Delta\omega_u)^2/8[1+8/(\Delta\omega_u \Delta t_\zeta)^2],$$

$$b_{1,2,5,6} = \tilde{\Omega}_\zeta = \Omega_\zeta - 0.25\Delta\omega_{P2}\gamma_{up}^2(\Delta\omega_u/\Delta\omega_{P2})^2(\tilde{t}/\Delta t_\zeta),$$

$$b_3 = 2\omega_0 + b_1, \quad b_4 = 2\omega_0 - b_1,$$

$$b_7 = 2\omega_0 + \Omega_\zeta, \quad b_8 = 2\omega_0 - \Omega_\zeta,$$

$$b_9 = \Omega_\zeta, \quad c_1 = 0, \quad c_2 = (4/\Delta t_\zeta)(\omega_0/\Delta\omega_{P2})\gamma_{up}^2,$$

$$c_{3,4,7-9} = (\Delta\omega_u)^2 \Delta t/8, \quad c_5 = c_2 + c_3,$$

$$c_6 = c_2 - c_3, \quad d_{1,3,4,7,8} = \omega_0 \Delta t, \quad d_{2,5,6} = \tilde{\omega}_0 \tilde{t},$$

$$d_9 = 0, \quad \tilde{\omega}_0 = \omega_0 \gamma_{up}^2,$$

$$\tilde{t} = \Delta t + 2\tau_d - \Delta t_d, \quad \Delta t_d = \Omega_\zeta \Delta t_\zeta/(l\Delta\omega_{P2}).$$

The coefficients $\tilde{M}_n$ have the following form: $\tilde{M}_1 = 0.5\tilde{M}_0\exp(-H_1 - H_2)$,

$$\tilde{M}_2 = 0.5\exp(-H_1 - H_2 - H_3) = \tilde{M}_1\exp(-H_3),$$

$$\tilde{M}_{3,4} = 0.5\tilde{M}_1, \quad \tilde{M}_{5,6} = 0.5\tilde{M}_2,$$

$$\tilde{M}_{7,8} = 0.25(\tilde{M}_0/\gamma_{up})\exp(-2H_1),$$

$$\tilde{M}_9 = 2\tilde{M}_7\cos(\omega_0 \Delta t), \quad \tilde{M}_0 = \sigma_u^4 \Phi_0^2 \gamma_{up}/R_0^2.$$

The quantities H_1, H_2, and H_3 have the same form as in the case of strong fluctuations (Eqs. (12)). As in the case of $\exp(-\Phi_0^2) \ll 1$, the integration results can be expressed in terms of the probability integrals of the complex argument (see Eq. (13)).

An analysis of the sum of integrals shows that the terms $\tilde{M}_n J_n$ with numbers $n = 7$–9 do not depend on the time delay in the channel of the reference signal t_d or the frequency correlation scale $\Delta\omega_{P2}$. They are propor-

[1] In this model, the frequency decorrelation of fluctuations is related to the shift of intensely scattering regions of the surface with a change in frequency.

tional to $(\Delta\omega_u T)^{-1}$ and characterize incompletely averaged fluctuations of the initial noiselike signal. The terms with numbers n = 3, 4, 7–9 do not depend on the ratio between the integration time T and the correlation scale of random sea Δt_ζ, the term with the number $n = 9$ being predominant in the absolute value. At $\Delta\tilde{\omega}_u T \gg 1$, this term approximately equals $\tilde{M}_9 J_9 \simeq 0.5(\Phi_0/R_0)^2\sigma_u^4 \exp(-2H_1)\cos(\omega_0\Delta t)\sqrt{8\pi}/(\Delta\tilde{\omega}_u T)$. By the assumption that the signal is narrow-band ($(\Delta\omega_u/\omega_0 \ll 1)$, we have $|\tilde{M}_n J_n| \ll |\tilde{M}_1 J_1|$ at $n = 2, 5, 6$. As a result, as in the case of strong fluctuations and with the same restrictions, we arrive at the approximate expression in the form of two terms with numbers $n = 1$ and 9. The main contribution is given by the first term $\tilde{M}_1 J_1$ while $\tilde{M}_9 J_9$ is the next term in order of magnitude with respect to $(\Delta f_u T)^{-1}$.

Consider the limiting cases on the assumption that $(\Delta f_u T)^{-1} \ll 1$. In this case, at small integration times when the condition $\tilde{\Omega}_\zeta T \ll 1$ is satisfied, we have

$$\begin{aligned} K_{\Delta Q}(\Delta t, \tau_d) &\simeq \tilde{M}_1 J_1 \simeq 0.5(\Phi_0/R_0)^2\sigma_u^4\gamma_{up} \\ &\times \cos(\omega_0\Delta t)\exp(-H_1 - H_2) \\ &= 0.5(\Phi_0/R_0)^2\sigma_u^4\gamma_{up}\cos(\omega_0\Delta t) \\ &\times \exp\{-(\Delta\omega_u)^2[\Delta t\sqrt{1+\gamma_{up}^2} \\ &+ (2\tau_d - \Delta t_d)\gamma_{up}^2/\sqrt{1+\gamma_{up}^2}]^2/32\} \\ &\times \exp[-(\Delta\omega_u\gamma_{up})^2(2\tau_d - \Delta t_d)^2/32(1+\gamma_{up}^2)]. \end{aligned} \quad (15)$$

According to Eq. (15), the position of the maximum of the AKF envelope, $K_{\Delta Q}(\Delta t)$, depends on the time delay in the reference signal channel. Only with the introduction of the delay for the arrival time of the scattered (incoherent) component of the received signal, $t_d = (R_0/c_s) + (\Delta t_d/2)$, the maximum fits the zero shift, $\Delta t = 0$. In this case, the normalized AKF, $\Gamma_{\Delta Q}(\Delta t) = K_{\Delta Q}(\Delta t)/K_{\Delta Q}(0)$, has the same form as for strong fluctuations. With the introduction of the delay for the propagation time of the coherent signal component, $t_d = R_0/c_s$, the maximum of the envelope of $\Gamma_{\Delta Q}(\Delta t)$ is shifted by $\Delta t_m = \gamma_{up}^2\Delta t_d/(1+\gamma_{up}^2)$ but the effective width of the correlation maximum remains the same as in the case of $\tau_d = \Delta t_d/2$. Note that the condition $\tilde{\Omega}_\zeta T \ll 1$, under which Eq. (15) is valid, is almost equivalent to the inequality $\Omega_\zeta T \ll 1$ for temporal delays varying within the effective width of the correlation maximum near the values $\tau_d = \Delta t_d/2$ and $\tau_d = 0$.

The expression for the NVF, which for weak fluctuations we define by the relationship $\tilde{\sigma}_Q^2 = K_{\Delta Q}(0, \tau_d)2R_0^2/\Phi_0^2\sigma_u^4$, has the form

$$\begin{aligned} \tilde{\sigma}_Q^2 &\simeq [1 + 0.5(\Delta\omega_u/\Delta\omega_{P2})^2]^{-1/2} \\ &\times \exp[-(\Delta\omega_u\gamma_{up})^2(2\tau_d - \Delta t_d)^2/32]. \end{aligned} \quad (16)$$

The power factor in Eq. (16) is equal to the maximal value of NVF, $\tilde{\sigma}_{Q\max}^2$, which corresponds to the reference signal delay, $t_d = (R_0/c_s) + (\Delta t_d/2)$. The quantity $\tilde{\sigma}_{Q\max}^2$, which characterizes the extent of frequency averaging at the maximum of the incoherent signal component, coincides with the maximum value of the NVF for the case of strong fluctuations and corresponds to the delay $t_d = R_0/c_s$. With the introduction of the delay $t_d = R_0/c_s$, the quantity $\tilde{\sigma}_Q^2$ in the case of weak fluctuations decreases due to the shift in time of the maxima of coherent and incoherent signal components at the output of the correlation receiver and becomes equal to

$$\begin{aligned} \tilde{\sigma}_Q^2 &\simeq [1 + 0.5(\Delta\omega_u/\Delta\omega_{P2})^2]^{-1/2} \\ &\times \exp[-(\Delta\omega_u\gamma_{up}\Omega_\zeta\Delta t_\zeta/l\Delta\omega_{P2})^2/32]. \end{aligned}$$

The frequency averaging at the maximum of the coherent component, i.e., at $t_d = R_0/c_s$, can also be characterized by the variation coefficient of the output effect of the correlation receiver $\eta_Q = \sigma_Q I_{Qc}^{-1/2} = \sqrt{K_Q(0,0)/I_{Qc}}$. In the limiting cases $(\Delta\omega_u/\Delta\omega_{P2})^2 \ll 1$ (synchronous fluctuations) and $(\Delta\omega_u/\Delta\omega_{P2})^2 \gg 1$ (selective fluctuations), we have $\eta_Q^2 \simeq 0.5\Phi_0^2\tilde{\sigma}_Q^2 \simeq 0.5\Phi_0^2\exp[-(\Delta\omega_u\Omega_\zeta\Delta t_\zeta/l\Delta\omega_{P2})^2/32]$ and $\eta_Q^2 \simeq 0.707\Phi_0^2(\Delta\omega_{P2}/\Delta\omega_u)\exp[-(\Omega_\zeta\Delta t_\zeta)^2/16l^2]$, respectively. In the first case, for a sufficiently small $\Delta\omega_u$, the quantity η_Q approaches the value determined by the amplitude variation coefficient of the monochromatic signal reflected from the statistically rough surface.

For large integration times (at $\varepsilon_\zeta = T/\Delta t_\zeta \geq 1$), we have

$$\begin{aligned} K_{\Delta Q}(\Delta t, \tau_d) &\simeq 0.5(\Phi_0/R_0)^2\sigma_u^4 \\ &\times \exp(-H_1 - H_2)\cos(\omega_0\Delta t) \\ &\times \{(\sqrt{\pi}\Delta t_\zeta/T)\exp[-(0.5\tilde{\Omega}_\zeta\Delta t_\zeta/\gamma_{up})^2] \\ &+ 2[1 - \exp(-\varepsilon_\zeta^2\gamma_{up}^2)]/\tilde{\Omega}_\zeta^2 T^2\}. \end{aligned} \quad (17)$$

In the intermediate region, at $\tilde{\Omega}_\zeta T \geq 1$, $(T\gamma_{up}/\Delta t_\zeta)^2 \ll 1$ (this may be at $(\Delta\omega_u/\Delta\omega_{P2})^2 \gg 1$, when $\gamma_{up}^2 \ll 1$), we have

$$K_{\Delta Q}(\Delta t, \tau_d) \simeq 0.5(\Phi_0/R_0)^2\sigma_u^4\exp(-H_1 - H_2) \times \cos(\omega_0\Delta t)\{2\gamma_{up}[1 - \cos(\tilde{\Omega}_\zeta T)]/\tilde{\Omega}_\zeta^2 T^2\}. \quad (18)$$

The form of the function $\Gamma_{\Delta Q}(\Delta t)$ is determined by the same expressions as at $\Omega_\zeta T \ll 1$, i.e., almost does not depend on the ratio between the integration time and the correlation scales of random sea, Ω_ζ and Δt_ζ. Expressions in the braces in Eqs. (17) and (18) describe the NVF of signals for $\tau_d = \Delta t_d/2$ (in this case, $\tilde{\Omega}_\zeta \equiv \Omega_\zeta$ but, in general, depending on the ratio between $\Delta\omega_u$ and $\Delta\omega_{P2}$, $\tilde{\Omega}_\zeta$ can take values in the interval $0.5\Omega_\zeta/l < \tilde{\Omega}_\zeta < \Omega_\zeta$). At $\tau_d = 0$, these expressions are acquire the factor $\exp[-(\Delta\omega_u\Delta t_d\gamma_{up})^2/32(1 + \gamma_{up}^2)]$ characterizing, as in the case of $\tilde{\Omega}_\zeta T \ll 1$, the additional smoothing of fluctuations caused by time shifts of the maxima of coherent and incoherent components. Along with averaging over frequency, averaging over time is also present in Eqs. (17) and (18).

Thus, in this paper, the variance and time correlation of fluctuations were studied for the output effect of a correlation receiver at the reflection of acoustic noiselike signals from a rough sea surface for different values of the radiation bandwidth, the scale of frequency correlation of the transfer function fluctuations, and the time delay in the reference signal channel. Calculations are carried out on the basis of the general expression obtained for arbitrary linear channels with random parameters and the expression for the frequency–time correlation moment of the transfer function fluctuations in the channel with reflections from a water surface with two-dimensional quasi-harmonic roughness. The cases of strong and weak fluctuations are considered in the framework of a single-scale model of frequency correlation. According to these calculations, under the conditions of a rapid selective fading, the fluctuations of the reflected signal at the output of the correlation receiver are substantially averaged, as compared to the case of a slow synchronous fading. Under these conditions, at comparable intensities of the coherent and incoherent components or with the predominance of the coherent component, the extension of the frequency band of the radiated signals, which promotes the averaging of fluctuations, leads to an improvement of the reception quality owing to the suppression of distortions associated with amplitude and phase fluctuations and to an increase in the signal coherence. Under the same conditions, at a low level of the coherent component (strong fluctuations), the frequency averaging of fluctuations, which increases as the signal frequency band broadens, leads to a considerable decrease in the total intensity of the output effect of the correlation receiver for the signals reflected from the sea surface and, therefore, to an energy loss, as compared to the case of synchronous slow fading, which is realized for small integration times and narrowband radiation. At the same time, in the presence of a weakly fluctuating direct signal, the suppression of the reflected signal arriving with a small delay raises the efficiency of the correlation reception. The results of the calculations presented above can be used in choosing the signal parameters matched with the propagation channel, as well as the algorithms and parameters of signal processing, in underwater monitoring systems based on the active sonar technique and in underwater sound communication in the presence of reflections from the sea surface.

A closer investigation of the frequency and time averaging of fluctuations can be performed on the basis of numerical calculations by using the expressions obtained in this paper for different ratios between the parameters of the probing signals, the parameters of the correlation processing, and the characteristics of the transfer function of the channel with reflections from the rough surface, as well as with the use of the results of calculations for a more general two-scale model of frequency correlation.

ACKNOWLEDGMENTS

This work was supported by the Russian Foundation for Basic Research, project no. 96-02-18430-a.

REFERENCES

1. I. Tolstoy and C. S. Clay, *Ocean Acoustics* (McGraw-Hill, 1966; Mir, Moscow, 1969).
2. L. M. Fink, *Theory of Discrete Communication Transmission* (Sovetskoe Radio, Moscow, 1970) [in Russian].
3. N. E. Kirillov, *Noise-Immune Data Communication through Linear Channels with Randomly Varying Parameters* (Svyaz', Moscow, 1971) [in Russian].
4. J. L. Stewart, W. B. Allen, R. M. Zarnowitz, and M. K. Brandon, J. Acoust. Soc. Am. **37**, 1079 (1965).
5. N. A. Vasil'ev and Yu. I. Tuzhilkin, Akust. Zh. **13**, 28 (1967) [Sov. Phys. Acoust. **13**, 22 (1967)].
6. É. P. Gulin, Akust. Zh. **18**, 219 (1972) [Sov. Phys. Acoust. **18**, 183 (1972)].
7. É. P. Gulin, in *Proceedings of 3rd All-Union Workshop on Statistical Hydroacoustics, Moscow, 1972* (Moscow, 1972), pp. 4–20.
8. É. P. Gulin, in *Proceedings of 8th All-Union Acoustical Conference, Moscow, 1973* (Moscow, 1973).
9. A. V. Nosov, Okeanologiya **29** (3), 415 (1989).
10. J. L. Spiesberger, J. Acoust. Soc. Am. **109**, 1997 (2001).
11. A. I. Mashoshin, Akust. Zh. **47**, 823 (2001) [Acoust. Phys. **47**, 727 (2001)].
12. V. M. Kudryashov, Akust. Zh. **48**, 375 (2002) [Acoust. Phys. **48**, 325 (2002)].

13. G. Sherman, in *Lectures on the Theory of Communication Systems*, Ed. by E. J. Bagdady (Mir, Moscow, 1964) [Russian translation].
14. R. J. Urick, *Principles of Underwater Sound* (McGraw-Hill, 1975; Sudostroenie, Leningrad, 1978).
15. É. P. Gulin, in *Proceedings of the Acoustics Institute* (Moscow, 1967), Issue II, pp. 49–70.
16. É. P. Gulin, Akust. Zh. **45**, 789 (1999) [Acoust. Phys. **45**, 711 (1999)].
17. É. P. Gulin, Izv. Vyssh. Uchebn. Zaved., Radiofiz. **13** (3), 401 (1970).
18. An. N. Venetsanopoulos and E. B. Tuteur, J. Acoust. Soc. Am. **49**, 1100 (1971).
19. V. I. Neklyudov and S. D. Chuprov, Akust. Zh. **19**, 393 (1973) [Sov. Phys. Acoust. **19**, 255 (1973)].
20. V. N. Fadeeva and N. M. Terent'ev, *Tables of Values of the Probability Integral with Respect to a Complex Argument* (GITTL, Moscow, 1954) [in Russian].
21. *Handbook of Mathematical Functions*, Ed. by M. Abramowitz and I. A. Stegun (National Bureau of Standards, Washington, 1964; Nauka, Moscow, 1979).

Translated by Yu. Lysanov

Acoustical Physics, Vol. 51, No. 6, 2005, pp. 653–663. Translated from Akusticheskiĭ Zhurnal, Vol. 51, No. 6, 2005, pp. 759–770.

Characteristics of Biot Waves Produced by a Vibration Exciter in a Fluid-Saturated Medium

Yu. M. Zaslavskiĭ

Institute of Applied Physics, Russian Academy of Sciences,
ul. Ul'yanova 46, Nizhni Novgorod, 603950 Russia
e-mail: zaslav@hydro.appl.sci-nnov.ru

Received October 7, 2004

Abstract—Results of a theoretical calculation of the directional characteristics of elastic waves excited by an oscillating point force in a fluid-saturated porous medium are presented. Based on Boit's theory and the theory of elementary acoustic sources, the wave amplitude and radiation power are calculated for two kinds of longitudinal waves and the transverse wave. An analysis of the spatial angular characteristics of elastic waves is performed for two types of rock, namely, water- and gas-saturated sandstones. The angular distributions of vibrations in the solid and liquid (gaseous) phases of the medium and the frequency dependences of the radiation power associated with each of the three types of acoustic waves are presented in graphical form. © *2005 Pleiades Publishing, Inc.*

This paper is devoted to analyzing the characteristics of longitudinal waves of the first and second kinds and the transverse waves radiated into an infinite fluid-saturated two-component porous medium under the excitation of the medium by an oscillating force applied at a certain spatial point. Among the approaches used for analyzing the acoustic wave processes in porous media and solving a number of applied problems, the Frenkel–Biot wave theory occupies an important place; in addition, this theoretical model has found further development in many investigations. As follows from the recent literature concerned with this subject [1], modifications of this theory are mostly directed toward an adequate description of the processes occurring when a seismoacoustic wave propagates in actual (characterized by complex structural and physical properties) rocks forming layers of fluid-saturated collectors and toward an explanation of the accompanying effects. These papers investigate the features related to the complication of acoustic wave processes induced by the multicomponent structure of a porous medium. At the same time, there are only a few works that develop the analysis of the efficiency of acoustic radiation by vibration sources in such media. Presumably, this occurs because of the lack of reliable data on the measurements of both fast and slow Biot waves that would be obtained from actual seismic investigations or practical works on borehole acoustics, which puts in the forefront the necessity of analyzing the conditions for the existence of the mentioned waves while the problem of wave excitation in a complex multicomponent medium is shifted to the background. However, in order to explain the absence of recent experimental data with measured seismoacoustic signals that can be identified with confidence with longitudinal Biot waves of both kinds, it is worthwhile to analyze the efficiency of their excitation by different sources in a model medium imitating fluid-saturated rocks. Of fundamental interest is the calculation of acoustic fields excited by elementary vibrators (in particular, by a dipole vibrator) similar to that carried out in [2] for the field of a pulsating source. The cited paper considered the excitation of elastic waves described by Biot's model by a monopole source in a two-phase medium. The wave amplitude and the acoustic power carried by the waves were calculated under the assumption that the pore-filling fluid is either water or gas (air), the skeleton parameters being the same in both versions of the problem. The present paper deals with a similar analysis under conditions of the same two-component medium with water or air saturation of open pores, but in the case of elastic wave radiation by a vibrator known in acoustics as a dipole source or a source of alternating force.

In addition, the enhancement of the efficiency of seismoacoustic radiation in the form of the desired waves (i.e., elastic waves of a certain required type) is an important stage in solving the problems of localization and diagnosis of producing collectors saturated with hydrocarbons, as well as the problems of an active vibration action on oil and gas pools with the aim of increasing the discharge of oil and gas wells [3].

The calculation is carried out under the assumption that the two-phase medium described by Biot's theory [4] is unbounded and is excited at a certain spatial point by an alternating force. Basically, such an analysis could be performed on the basis of modeling the operation of borehole sources, which would be in better agreement with actual conditions. However, such a statement would complicate the problem by the necessity of considering the structural features of the source

1063-7710/05/5106-0653$26.00

and the borehole; to omit this necessity, we consider the above problem in the simplest statement. We use the same idealizations as in the basic theory and take into account all the normal waves excited by the force source; each of these waves makes its own contribution to the total energy balance, and the calculation of these contributions is also part of the problem on the acoustic excitation of a porous medium. Solving this problem, we use the approach in which the force source is modeled as a rigid foreign massless sphere of a small wave size, which is embedded in the medium and can oscillate in the axial direction with a given displacement amplitude [5].

Monograph [5] includes the derivation of the formulas for the spatial distribution of elastic particle displacements and stresses in a single-phase elastic medium under the action of an alternating force source in the form of a periodically pulsating sphere whose walls are in good contact with the particles of the medium. Such a source is also known as a dipole source, and the corresponding dipole moment is determined in terms of the vector of elastic displacements of the medium **u**, which coincides with the vector of the displacements of the oscillating sphere at the sphere–medium contact boundary under the condition that the sphere radius r_0 tends to zero [5]. If this source operates in a solid or liquid medium, the dipole moment is related to the displacement vector by the following expressions: in a solid medium, $\mathbf{N}_s = \lim_{r_0 \to 0} -12\pi r_0 \mathbf{u}\,(r = r_0)/\omega^2(2/c_t^2 + 1/c_l^2)$, where c_l and c_t are the velocities of propagation of longitudinal and transverse waves and ω is the frequency of the action; in a liquid medium, $\mathbf{N}_f = \lim_{r_0 \to 0} -2\pi r_0^3 \mathbf{u}\,(r = r_0)$. In both cases, the dipole moment is related to the force acting on the medium by the expression $\mathbf{F}_{s,f} = -\rho\omega^2 \mathbf{N}_{s,f}$, where ρ is the density of the medium. In what follows, we assume that inequalities $|\mathbf{u}| \ll r_0 \ll 2\pi c_t/\omega$ hold; we also omit everywhere the temporal factor $e^{-i\omega t}$.

We start with the expressions given in the aforementioned monograph for the radial and meridional components of oscillating displacements in a conventional elastic medium driven longitudinally by axial vibrations of the sphere. In view of the fact that our medium is composed of two phases, namely, skeleton and fluid, we modified these expressions by considering the contributions of all normal modes to the oscillating displacements of particles of each fraction. Then, we can represent the spatial dependence of the total field of displacements in the form

$$\begin{aligned} u_r &= \frac{C\cos\theta}{4\pi r^3}(2 - 2ik_{l1}r - (k_{l1}r)^2)e^{ik_{l1}r} \\ &+ \frac{D\cos\theta}{4\pi r^3}(2 - 2ik_{l2}r - (k_{l2}r)^2)e^{ik_{l2}r} \\ &+ \frac{2E\cos\theta}{4\pi r^3}(ik_t r - 1)e^{ik_t r}, \end{aligned} \tag{1}$$

$$\begin{aligned} u_\theta &= -\frac{C\sin\theta}{4\pi r^3}(ik_{l1}r - 1)e^{ik_{l1}r} \\ &- \frac{D\sin\theta}{4\pi r^3}(ik_{l2}r - 1)e^{ik_{l2}r} \\ &- \frac{2E\sin\theta}{4\pi r^3}(1 - ik_t r - (k_t r)^2)e^{ik_t r}, \end{aligned} \tag{2}$$

$$\begin{aligned} v_r &= \frac{M_1 C\cos\theta}{4\pi r^3}(2 - 2ik_{l1}r - (k_{l1}r)^2)e^{ik_{l1}r} \\ &+ \frac{M_2 D\cos\theta}{4\pi r^3}(2 - 2ik_{l2}r - (k_{l2}r)^2)e^{ik_{l2}r}, \end{aligned} \tag{3}$$

where u_r and u_θ are the radial and meridional components of the oscillating displacements of the skeleton; v_r is the radial component of displacements of the fluid; indices $l1$ and $l2$ of the wave numbers and phase velocities, $k_{l1} = \omega/c_{l1}$ and $k_{l2} = \omega/c_{l2}$, correspond to the longitudinal waves of the first and second kinds (Biot waves); and index t of the wave number and phase velocity, $k_t = \omega/c_t$, corresponds to the shear (transverse) wave.

The coefficients C, D, and E are unknown, and they are to be determined in solving the problem on wave excitation. We do not draw here the component v_θ in an explicit form, because it does not appear in the boundary conditions at the source–medium contact interface in view of the slippage of the liquid fraction. However, this component is taken into account in the calculation of the total acoustic power, because it is present in the radiation field of the shear wave. It can be expressed in the form $v_\theta = M_t u_\theta$ [6]; the meaning of the quantity M_t will be explained below.

The wave numbers k_{l1}, k_{l2}, and k_t can be determined, in accordance with [4, 6], as $k_{l1}^2 = \bar{z}_1(\omega/V_\alpha)^2$, $k_{l2}^2 = \bar{z}_2(\omega/V_\alpha)^2$, and $k_t^2 = (\omega/c_t)^2 = (\omega/V_t)^2(E_r - iE_i)$, where V_t is the velocity of shear waves in the skeleton material and $\bar{z}_1$, and $\bar{z}_2$ are the roots of the dispersion equation that governs the velocities and attenuation coefficients of longitudinal waves of the first and second kinds:

$$(z - z_1)(z - z_2) - iM(z - 1) = 0. \tag{4}$$

Explicit expressions for the parameters appearing in this equation, including the quantity M and the charac-

teristic velocity of longitudinal waves V_α, as well as frequency correction functions E_r and E_i that govern the transverse wave dispersion and attenuation, will be given below.

A further analysis of acoustic radiation characteristics is preceded by the numerical solution of Eq. (4), whose roots $\bar{z}_{1,2}$ define the phase velocities and attenuation coefficients of longitudinal waves by the relationships $c_{l1,2} = V_\alpha/\mathrm{Re}(\sqrt{\bar{z}_{1,2}})$ and $\alpha_{1,2} = \omega\mathrm{Im}(\sqrt{\bar{z}_{1,2}})/V_\alpha$. The parameters z_1 and z_2 appearing in Eq. (4) are expressed as follows: $z_1 = V_\alpha^2/c_l^2$ and $z_2 = V_\alpha^2/c_f^2$, where c_l and c_f are the velocities of longitudinal waves in the materials of the skeleton and the fluid.

Biot [4] introduced a number of parameters, which include a combination of the densities of the skeleton (ρ_s) and the fluid (ρ_f) $\rho = \rho_s - \beta(\rho_s - \rho_f)$, the effective interphase density parameter ρ_α, the parameter $b = 8\mu\beta\xi/a^2$, the coefficient of fluid dynamic viscosity μ, the dimensionless porosity β, the dimensionless pore winding ξ, and the average pore radius a. In addition, Biot introduced the dimensionless density and elasticity constants (now called Biot's constants) determined in terms of the above parameters as follows:

$$\begin{cases} \gamma_{11} = \dfrac{(1-\beta)\rho_s + \rho_\alpha}{\rho_s + \beta(\rho_f - \rho_s)}, \quad \gamma_{12} = -\dfrac{\rho_\alpha}{\rho_s + \beta(\rho_f - \rho_s)}, \\ \gamma_{22} = \dfrac{\beta\rho_f + \rho_\alpha}{\rho_s + \beta(\rho_f - \rho_s)}, \end{cases} \tag{5}$$

$$\begin{cases} \sigma_{11} = \dfrac{c_l^2((1-\beta)\rho_s + \rho_\alpha)}{c_s^2((1-\beta)\rho_s + \rho_\alpha) + 2Q + c_f^2(\beta\rho_f + \rho_\alpha)} \\ \sigma_{12} = \dfrac{Q}{c_l^2((1-\beta)\rho_s + \rho_\alpha) + 2Q + c_f^2(\beta\rho_f + \rho_\alpha)} \\ \sigma_{22} = \dfrac{c_f^2(\beta\rho_f + \rho_\alpha)}{c_l^2((1-\beta)\rho_s + \rho_\alpha) + 2Q + c_f^2(\beta\rho_f + \rho_\alpha)}. \end{cases} \tag{6}$$

The squared characteristic velocity V_α^2 is expressed by the following explicit relationship:

$$V_\alpha^2 = \frac{c_l^2((1-\beta)\rho_s + \rho_\alpha) + 2Q + c_f^2(\beta\rho_f + \rho_\alpha)}{\rho_s + \beta(\rho_f - \rho_s)},$$

where Q is the interphase stiffness and parameter M in Eq. (4) is given by the formula

$$M = \frac{\varepsilon_1 + i\varepsilon_2}{\sigma_{11}\sigma_{22} - \sigma_{12}^2}.$$

Here, the functions ε_1 and ε_2 describe the deviations of the fluid flow from Poiseuille flow in the presence of vibrations of the liquid along open cylindrical channels that model the pores of the medium. These functions are related to the special function

$$F(\kappa) = \frac{1}{4}\frac{\kappa T(\kappa)}{1 + i(2/\kappa)T(\kappa)}$$

that Biot [4] introduced to correct the frequency characteristics of longitudinal waves. The quantity $T(\kappa)$ is expressed in terms of the zero-order Kelvin cylindrical function and its derivative

$$T(\kappa) = \frac{\dfrac{d}{d\kappa}(ber(0,\kappa) + ibei(0,\kappa))}{(ber(0,\kappa) + ibei(0,\kappa))};$$

the argument of these functions is $\kappa \cong 2\sqrt{f/f_c}$, and the characteristic (or critical) frequency is given by the relationship $f_c = b/2\pi\rho(\gamma_{12} + \gamma_{22})$. The aforementioned relationship is as follows:

$$\varepsilon_1 = (\gamma_{12} + \gamma_{22})\frac{f_c}{f}\mathrm{Re}(F(\kappa)),$$

$$\varepsilon_2 = (\gamma_{12} + \gamma_{22})\frac{f_c}{f}\mathrm{Im}(F(\kappa)).$$

The functions used to correct the frequency characteristics of transverse waves are also expressed in terms of the functions ε_1 and ε_2:

$$E_r = \frac{(\gamma_{11}\gamma_{22} - \gamma_{12}^2)(\gamma_{22} + \varepsilon_2) + \gamma_{22}\varepsilon_2 + \varepsilon_1^2 + \varepsilon_2^2}{(\gamma_{22} + \varepsilon_2)^2 + \varepsilon_1^2},$$

$$E_i = \frac{\varepsilon_1(\gamma_{12} + \gamma_{22})^2}{(\gamma_{22} + \varepsilon_2)^2 + \varepsilon_1^2}.$$

The frequency-dependent velocity of transverse waves is described by the relationship $c_t = V_t/\mathrm{Re}(\sqrt{E_r - iE_i})$.

The coefficients M_1 and M_2 in Eq. (3) can be derived by correlating the results obtained by Biot [4] with those of paper [6]. The corresponding expressions in terms the dimensionless constants are given by the formulas

$$\begin{aligned} M_1 &= \frac{-\gamma_{12} + \bar{z}_1\sigma_{12} - M(\sigma_{11}\sigma_{22} - \sigma_{12}^2)}{\gamma_{22} - \bar{z}_1\sigma_{22} - M(\sigma_{11}\sigma_{22} - \sigma_{12}^2)}, \\ M_2 &= \frac{-\gamma_{12} + \bar{z}_2\sigma_{12} - M(\sigma_{11}\sigma_{22} - \sigma_{12}^2)}{\gamma_{22} - \bar{z}_2\sigma_{22} - M(\sigma_{11}\sigma_{22} - \sigma_{12}^2)}. \end{aligned} \tag{7}$$

The system of equations in coefficients C, D, and E can be obtained by drawing the conditions that express the dipole forces in terms of the corresponding limiting values of the elastic displacement vectors of both fractions of the medium at the sphere boundary in the limit $r_0 \longrightarrow 0$. In the general case, an acoustic dipole applies

to the skeleton and the fluid the forces that can be represented in the form [5]

$$\mathbf{F}_s = \lim_{r_0 \to 0} 12\pi r_0 \rho \mathbf{u}(r = r_0)/(2/c_t^2 + 1/c_l^2),$$
$$\mathbf{F}_f = \lim_{r_0 \to 0} 2\pi r_0^3 \omega^2 \rho \mathbf{v}(r = r_0). \quad (8)$$

Along with the normal and tangential components of acoustic displacements, it is convenient to introduce the corresponding components of the forces acting on the medium from the part of the sphere by the relationships

$$F_{sr} = |\mathbf{F}_s|\cos\theta,$$
$$F_{s\theta} = -|\mathbf{F}_s|\sin\theta, \quad F_{fr} = |\mathbf{F}_f|\cos\theta. \quad (9)$$

Then, substituting Eqs. (1)–(3) into Eq. (8), we obtain the system of equations in coefficients C, D, and E

$$\begin{cases} F_{sr} = \dfrac{3\rho}{r_0^2(2/V_t^2 + 1/c_l^2)}\cos\theta(C + D - E), \\ F_{s\theta} = \dfrac{3\rho}{r_0^2(2/V_t^2 + 1/c_l^2)}\sin\theta(C/2 + D/2 - E), \\ F_{fr} = \omega^2\rho\cos\theta(M_1 C + M_2 D), \end{cases} \quad (10)$$

whose solution can be expressed as follows:

$$C = \frac{1}{\rho(M_1 - M_2)} \times \left[\frac{2r_0^2(2/V_t^2 + 1/c_l^2)}{3} M_2\left(\frac{F_{sr}}{\cos\theta} - \frac{F_{s\theta}}{\sin\theta}\right) - \frac{F_{fr}}{\omega^2\cos\theta}\right], \quad (11)$$

$$D = -\frac{1}{\rho(M_1 - M_2)} \times \left[\frac{2r_0^2(2/V_t^2 + 1/c_l^2)}{3} M_1\left(\frac{F_{sr}}{\cos\theta} - \frac{F_{s\theta}}{\sin\theta}\right) - \frac{F_{fr}}{\omega^2\cos\theta}\right], \quad (12)$$

$$E = \frac{r_0^2(2/V_t^2 + 1/c_l^2)}{3\rho}\left(\frac{F_{sr}}{\cos\theta} - \frac{2F_{s\theta}}{\sin\theta}\right). \quad (13)$$

Description of the field of vibrations assumes that the relationship be specified between the forces acting from the part of the dipole source on the skeleton and the fluid; physically, the most justified assumption for the medium with open pores is the assumption that the source immediately acts only on the solid skeleton: $|\mathbf{F}_s| = F$, $|\mathbf{F}_f| = 0$. The use of Eqs. (9) simplifies expressions (11)–(13) for the coefficients, reducing them to the form

$$C = \frac{2FM_2 r_0^2(2/V_t^2 + 1/c_l^2)}{3\rho(M_1 - M_2)},$$
$$D = -\frac{2FM_1 r_0^2(2/V_t^2 + 1/c_l^2)}{3\rho(M_1 - M_2)}, \quad (14)$$
$$E = \frac{Fr_0^2(2/V_t^2 + 1/c_l^2)}{2\rho}.$$

In these expressions, the factor $r_0^2(2/V_t^2 + 1/c_l^2)$ should be considered as the square of a certain inverse frequency $\varpi^{-2} = r_0^2(2/V_t^2 + 1/c_l^2)$ that depends on the parameters of the medium and the size of the source.

Substituting Eqs. (14) into Eqs. (1)–(3), we arrive at the desired expressions for the wave displacements in the far (radiation) zone:

$$u_{r1} = \frac{F\omega^2 M_2\cos\theta}{6\pi\varpi^2\rho c_{l1}^2 r(M_1 - M_2)}\exp(ik_{l1}r),$$
$$v_{r1} = \frac{F\omega^2 M_1 M_2\cos\theta}{6\pi\varpi^2\rho c_{l1}^2 r(M_1 - M_2)}\exp(ik_{l1}r) \quad (15)$$

for vibrations in the first longitudinal wave in the solid and liquid fractions and

$$u_{r2} = -\frac{F\omega^2 M_1\cos\theta}{6\pi\varpi^2\rho c_{l2}^2 r(M_1 - M_2)}\exp(ik_{l2}r),$$
$$v_{r2} = -\frac{F\omega^2 M_1 M_2\cos\theta}{6\pi\varpi^2\rho c_{l2}^2 r(M_1 - M_2)}\exp(ik_{l2}r) \quad (16)$$

for vibrations in the second longitudinal wave in the solid and liquid fractions.

Taking into account the expression for coefficient E in Eqs. (14) and the relationship between the oscillation amplitudes of transverse waves in the skeleton and the fluid,

$$v_\theta = M_t u_\theta,$$

where

$$M_t = \frac{-\gamma_{12} - M(\sigma_{11}\sigma_{22} - \sigma_{12}^2)}{\gamma_{22} - M(\sigma_{11}\sigma_{22} - \sigma_{12}^2)},$$

which can be derived by analogy with Eqs. (7), we can represent the wave displacements of each fraction in the transverse wave by the formulas

$$u_\theta = \frac{F\omega^2\sin\theta}{4\pi\varpi^2\rho c_t^2 r}\exp(ik_t r),$$
$$v_\theta = M_t\frac{F\omega^2\sin\theta}{4\pi\varpi^2\rho c_t^2 r}\exp(ik_t r). \quad (17)$$

Prior to analyzing the results of calculating the spatial angular behavior of acoustic field and radiated power, we give the values of parameters used in the subsequent calculations for rocks of two types, namely,

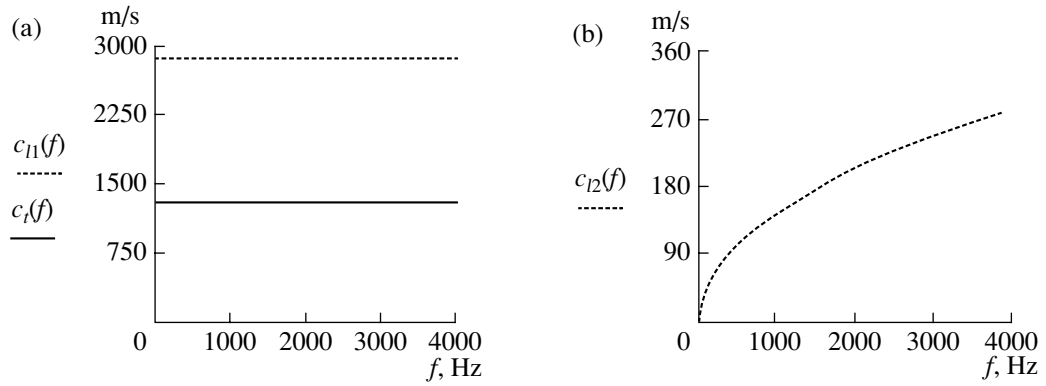

Fig. 1. Frequency dispersion of the propagation velocity of acoustic waves in water-saturated sandstone: (a) velocities of the first longitudinal, c_{l1}, and transverse, c_t, waves; (b) velocity of the second longitudinal wave c_{l2}.

for highly porous sandstone with water-filled pores in the first case and with air-filled pores in the second case. In both cases, we use the following parameters: $\xi = 1$, $\beta = 0.45$, and $\pi a^2 = 10$ D. We specify the skeleton parameters as follows: $\rho_s = 2.5$ g/cm^3, $c_l = 3$ km/s, and $V_t = 1.73$ km/s; it is clear that the use of reference data for specifying these values is not quite appropriate, because reference data correspond to the medium with pores, whose presence reduces the stiffness and the density. In contrast to this approximation, which is suitable only in the context of qualitative demonstrative analysis, the assumption that $\rho_f = 1$ g/cm^3 and $c_f = 1.5$ km/s for water taken as the fluid is fairly rigorous, because these parameters remain practically intact for the moisture filling the pores. In the case of gas-filled pores, we suggest the following values of the fluid parameters: $\rho_f = 0.001$ g/cm^3 and $c_f = 340$ m/s. As is known, in the pores of rocks located at large depths, these values can appreciably differ from the values measured under room conditions. The basic parameters being fixed, the interphase stiffness Q and interphase density ρ_α, i.e., the parameters that determine the relationship between the subsystems of the skeleton–fluid system, can be found from the relationship that holds for Biot's dimensionless stiffness and density constants: $\sigma_{11} + \sigma_{22} + 2\sigma_{12} = \gamma_{11} + \gamma_{22} + 2\gamma_{12} = 1$. As a result, we find that, in the case when the pore fluid is water, the dimensionless constants are as follows: the elasticity constants $\sigma_{11} = 0.87$, $\sigma_{12} = 0.0244$, and $\sigma_{22} = 0.0811$ and the density constants $\gamma_{11} = 0.80822$, $\gamma_{12} = -0.0548$, and $\gamma_{22} = 0.30137$. Calculating these constants, we obtained the interphase elasticity $Q = 3.75 \times 10^8$ Pa and the interphase density $\rho_\alpha = 0.1$ g/cm^3. In this case, the corresponding values of the characteristic velocity of longitudinal waves and the critical frequency are $V_\alpha = 2.893$ km/s and $f_c = 232$ kHz for this type of rock.

In the case when the pore fluid is air, the parameters determining the subsystem relationship assume the values $\rho_\alpha = 0.0001$ g/cm^3 and $Q = 6.5 \times 10^3$ Pa. In addition, we obtain new values for Biot's dimensionless constants (they are again calculated by Eqs. (5) and (6)): $\sigma_{11} = 0.9999938$, $\sigma_{12} = 5 \times 10^{-7}$, and $\sigma_{22} = 5.2 \times 10^{-6}$ for the elasticity constants and $\gamma_{11} = 0.9997455$, $\gamma_{12} = -0.0000727$, and $\gamma_{22} = 0.0003998$ for the density constants. The characteristic velocity of longitudinal waves now assumes the value $V_\alpha = 3$ km/s, and the critical frequency becomes much higher: $f_c \geq 3$ MHz.

Now, we present the frequency-dependent propagation velocities and attenuation coefficients of acoustic waves calculated with the use of Biot's model for both versions of the two-phase medium with the above-specified parameters. Our interest lies in the frequency range 0–4000 Hz, whose low-frequency part corresponds to the seismic prospecting range and whose high-frequency part is suitable for use in borehole logging measurements or borehole-to-borehole surveys. Figure 1a shows that velocities c_{l1} and c_t remain nearly constant; a rapid variation with frequency is characteristic only of the propagation velocity of the longitudinal wave of the second kind c_{l2}. As may be seen from Fig. 1b, in the frequency range of interest, its value varies from a few to three hundred meters per second. Figure 2a shows the frequency-dependent attenuation coefficients of the longitudinal wave of the first kind (α_1) and the transverse wave (α_t), and Fig. 2b shows the frequency-dependent attenuation coefficient of the longitudinal wave of the second kind α_2. The coefficients α_1 and α_t grow with frequency according to quadratic laws, the increment being somewhat higher (but quite comparable) in the case of the transverse wave. The coefficient α_2 increases according to a law close to $\sqrt{f}$ and, in the frequency range of interest, exceeds the coefficients corresponding to the first and transverse waves by at least three orders of magnitude. This is indicative of the fact that pore-wall deceleration becomes the prevailing factor in the loss mechanism, as distinct from the conventional viscous-volume losses for the two former wave types. It is obvious that the strong attenuation makes the measurement of this wave very difficult.

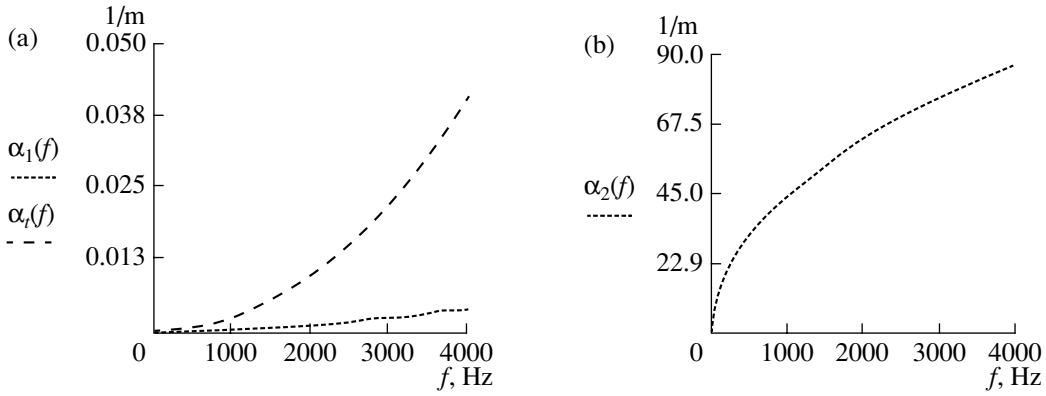

Fig. 2. Frequency-dependent attenuation coefficients of acoustic waves in water-saturated porous sandstone: (a) attenuation coefficients of the first longitudinal, α_1, and shear, α_t, waves; (b) attenuation coefficient of the second longitudinal wave α_2.

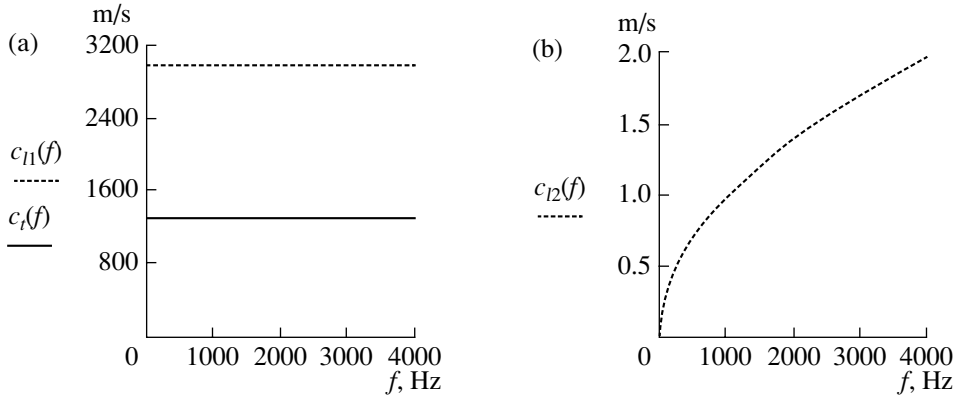

Fig. 3. Frequency dispersion of the propagation velocity of acoustic waves in gas-saturated sandstone: (a) velocities of the first longitudinal, c_{l1}, and transverse, c_t, waves; (b) velocity of the second longitudinal wave c_{l2}.

Similar results were calculated for the acoustic characteristics corresponding to another type of rock—the gas-saturated sandstone. Figure 3a shows the propagation velocities c_{l1} and c_t that appear to be approximately constant in the frequency range of our interest, and Fig. 3b shows the frequency-dependent velocity c_{l2}, which appears to be abnormally low. Figures 4a and 4b present the attenuation coefficients calculated by Biot's model; from these curves it follows that the attenuation of the second longitudinal wave appears even higher (by three orders of magnitude) than in the above case of water-saturated rock. This is indicative of the fact that the use of this wave in practice faces even greater difficulties related to the wave attenuation. At the same time, not only transverse and first longitudinal waves, but also the second wave is of interest for the diagnosis of the medium. The use of this wave for active action on oil or gas pools could be expedient in view of the fact that precisely the second wave is capable of initiating relative displacements of fractions, because the fluid vibrations relative to the skeleton walls are characterized in this wave by an appreciable phase shift (at frequencies below the critical one), while the corresponding phase shift in the first and transverse waves is negligible. As calculations show, sources of the dipole type efficiently excite these waves, which favorably distinguishes dipole sources from monopole sources, and the analysis of powers radiated in different types of waves additionally supports this conclusion. In particular, the results of calculations offer a possibility to analyze the total energy balance and compare the relative contributions of different types of acoustic waves excited by dipole and monopole sources in a two-phase medium.

Consider the acoustic characteristics of the dipole source that are calculated by Eqs. (15)–(17). In the calculations, we used the data on wave velocities in both types of rock.

Adverting first to the water-saturated sandstone, we consider Fig. 5a, which shows the directional patterns of the first longitudinal wave (one curve for skeleton vibrations u_{r1} and the other for fluid vibrations v_{r1}) in the source plane, the angular coordinate of the observation point being measured with respect to the direction of the force vector. In the calculations of the angular

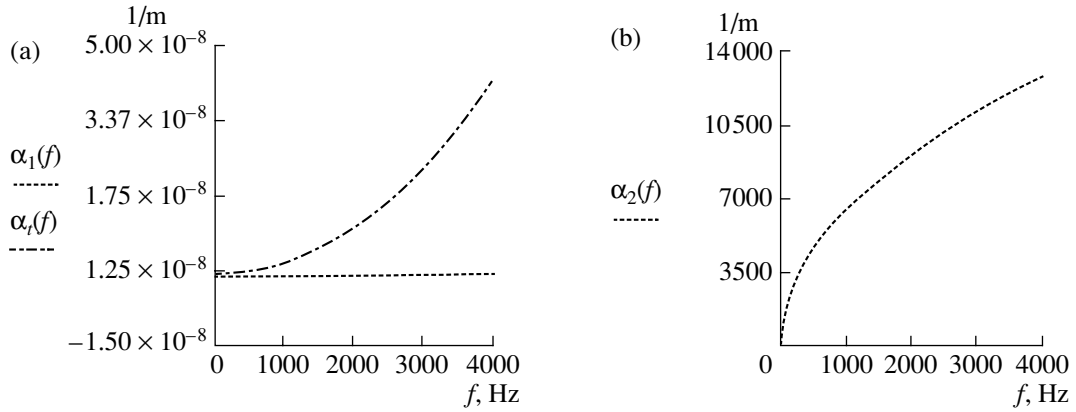

Fig. 4. Frequency-dependent attenuation coefficients of acoustic waves in gas-saturated sandstone: (a) attenuation coefficients of the first longitudinal, α_1, and shear, α_t, waves; (b) attenuation coefficient of the second longitudinal wave α_2.

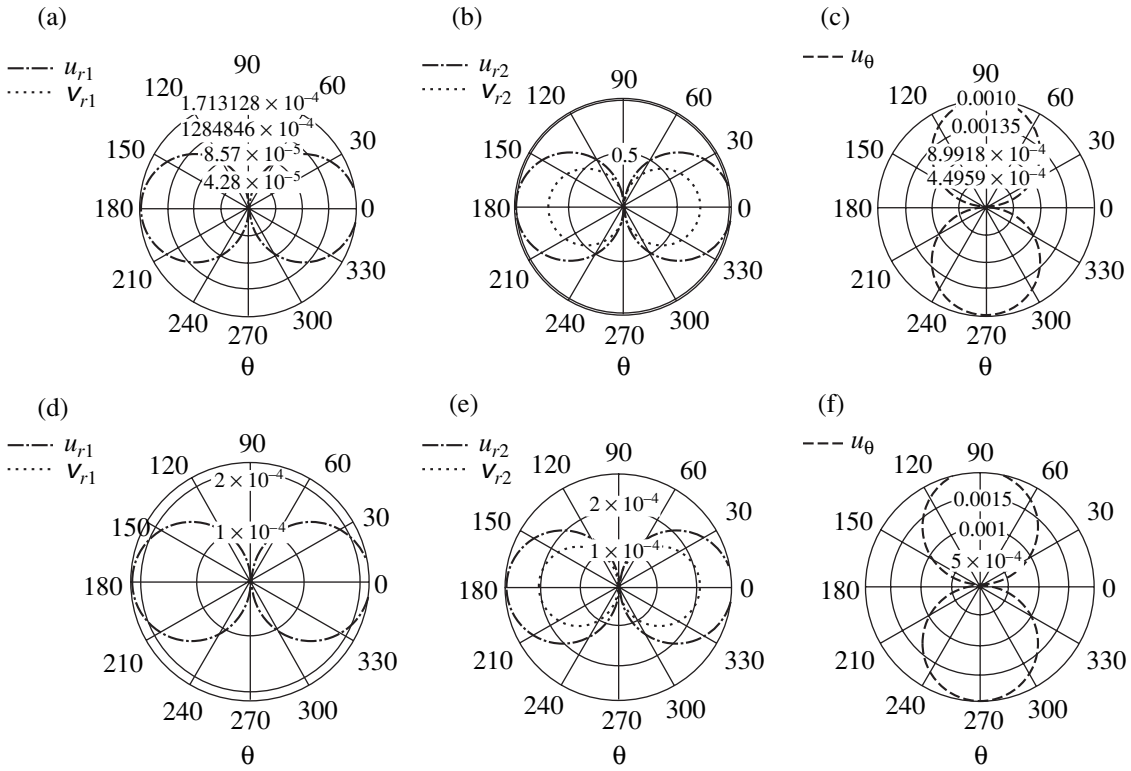

Fig. 5. Directional patterns of acoustic waves (radial components for the longitudinal waves and meridional component for the transverse wave) at a frequency $f = 100$ Hz; the amplitudes are normalized by $\max u_{r2}$ in water-saturated sandstone). Water-saturated sandstone: (a) first longitudinal wave in the skeleton, u_{r1}, and in the fluid, v_{r1}; (b) second longitudinal wave in the skeleton, u_{r2}, and in the fluid, v_{r2}; (c) transverse wave in the skeleton, u_θ. Gas-saturated sandstone: (d) first longitudinal wave in the skeleton, u_{r1}, and in the fluid, v_{r1}; (e) second longitudinal wave in the skeleton, u_{r2}, and in the fluid, v_{r2}; (f) transverse wave in the skeleton, u_θ.

and frequency characteristics, we normalized the data by the maximal amplitude of skeleton vibrations u_{r2} in the longitudinal wave of the second kind in water-saturated sandstone (see the circular pattern in Fig. 5b), so that the levels of vibrations in other waves were measured relative to this maximal amplitude. Amplitudes u_{r1} and v_{r1} calculated at a frequency of 100 Hz are quite close to each other. As regards the amplitudes u_{r2} and v_{r2}, we have drastically different (by more than three orders of magnitude) levels of vibrations in favor of the wave of the second kind. Unlike the vibrations in longitudinal waves, the angular distribution of skeleton vibrations in the transverse wave u_θ (see Fig. 5c) is described by the function $\sin\theta$, and the vibration ampli-

tude exceeds the corresponding amplitude in the longitudinal wave of the first kind by a factor of about ten. The spatial distribution of fluid vibrations v_θ in this wave coincides with that of skeleton vibrations u_θ; for this reason, we present no such curve, though the amplitude of these vibrations is somewhat different.

One can expect that this excess of the second longitudinal wave over other waves in level is caused not only by the specificity of the dipole source action but also by the reduced velocity of this wave in the medium. Nevertheless, in the case of excitation of the medium by a monopole source, there is an inverse ratio between the levels of the longitudinal waves [2]. Because of the more efficient generation and higher degree of attenuation of the second waves, the decision about the possibility of experimental measurements and practicability of these waves requires a further analysis of wave characteristics.

The circular patterns in Figs. 5d–5f show the calculated directional patterns of waves generated by the same source in gas-saturated rock. The angular behavior of each of the waves coincides with that of the corresponding wave considered earlier, and the levels of the transverse and first longitudinal waves are nearly the same as in the case of water-saturated sandstone. However, the level of the second longitudinal wave increases in this case by 80 dB. Because the attenuation coefficient of acoustic waves of this type in the gas-saturated medium also increases by orders of magnitude and far exceeds the attenuation coefficient in the water-saturated medium (see Fig. 4b), a discussion of other wave characteristics will be instructive for understanding the whole picture.

In particular, it is of interest to consider the frequency-dependent amplitude of waves generated by the dipole source in the water- or gas-saturated porous medium and received at a certain reference distance from the source (for example, at a distance of 1 m in the direction of the maximum of the directional pattern for each wave). Figures 6a–6d show the calculated wave amplitudes in the frequency range 0–4 kHz for both medium types (as earlier, we normalize all the data by the maximal amplitude of wave u_{r2} for the water-saturated sandstone). Comparing these characteristics, we should mention the weak frequency dependence of the skeleton and fluid vibrations in the first longitudinal and transverse waves (see curves in Figs. 6a and 6c); in addition, the amplitude of vibrations in the transverse wave is an order of magnitude greater than the amplitude of the first longitudinal wave. Figures 6b and 6d show a similar dependence for the second longitudinal wave in the skeleton and the fluid in both water- and gas-saturated media. Unlike the previous curves (Figs. 6a, 6c), this dependence shows that the generated wave amplitude rapidly decreases with frequency. In addition, these data support the relationships illustrated in Fig. 5; namely, the level of the second wave radiated into the water-saturated sandstone exceeds the levels of the first and shear waves by at least three orders of magnitude and, when this wave is radiated into the gas-saturated sandstone, it exceeds the level of other waves by another three orders of magnitude up to ultrasonic frequencies.

In parallel with the displacement wave field, the total acoustic power carried by the first and second longitudinal and transverse waves is also an informative characteristic. The wave energy balance is an integral characteristic that is important for the optimum choice of the wave type used for sounding fluid-saturated rocks. We calculated the powers of each of the three waves described by Eqs. (15)–(17) according to the following final expressions (also used for calculating the frequency-dependent curves):

$$W_1 = \frac{F^2\omega^6}{54\pi\rho c_{l1}^3\varpi^4}\frac{|M_2|^2(1+|M_1|^2)}{|M_1-M_2|^2}, \tag{18}$$

$$W_2 = \frac{F^2\omega^6}{54\pi\rho c_{l2}^3\varpi^4}\frac{|M_1|^2(1+|M_2|^2)}{|M_1-M_2|^2}, \tag{19}$$

$$W_s = \frac{F^2\omega^6(1+|M_t|^2)}{24\pi\rho c_t^3\varpi^4}, \tag{20}$$

where $W_{1,2,s}$ are the acoustic powers of the first and second longitudinal waves and the transverse wave, respectively.

Consider the powers calculated by Eqs. (18)–(20) at $F = 1$ N and $\varpi = 2\pi 4000$ s^{-1}. The curves in Figs. 7a–7c show the frequency-dependent acoustic power carried by the first and second longitudinal waves and the transverse wave excited in water-saturated sandstone. The curves in Figs. 7d–7f show similar dependences for gas-saturated sandstone. One can see that the power of each type of wave increases with frequency according to approximately similar laws, the power of transverse waves exceeding the power of the first longitudinal waves by a factor of approximately 30 for all frequencies in both media. The frequency-dependent power of the second longitudinal wave is given in Figs. 7b and 7e for water- and gas-saturated sandstone, respectively. In the case of the water-saturated medium, the average level of this power exceeds the power level of other wave types by two orders of magnitude, and this excess increases to seven orders of magnitude in the case of the gas-saturated medium. Such proportions in the wave energy balance are indicative of the fact that the energy of the source is mainly spent for exciting the second longitudinal wave, though this fact cannot ensure the predominance of this kind of wave for all distances because of the acoustic energy dissipation. In order to take into account the above data on the acoustic wave attenuation, one must consider the joint effect of the wave attenuation and the dipole source excitation efficiency, whose competition determines the amplitudes of acoustic fields for different distances.

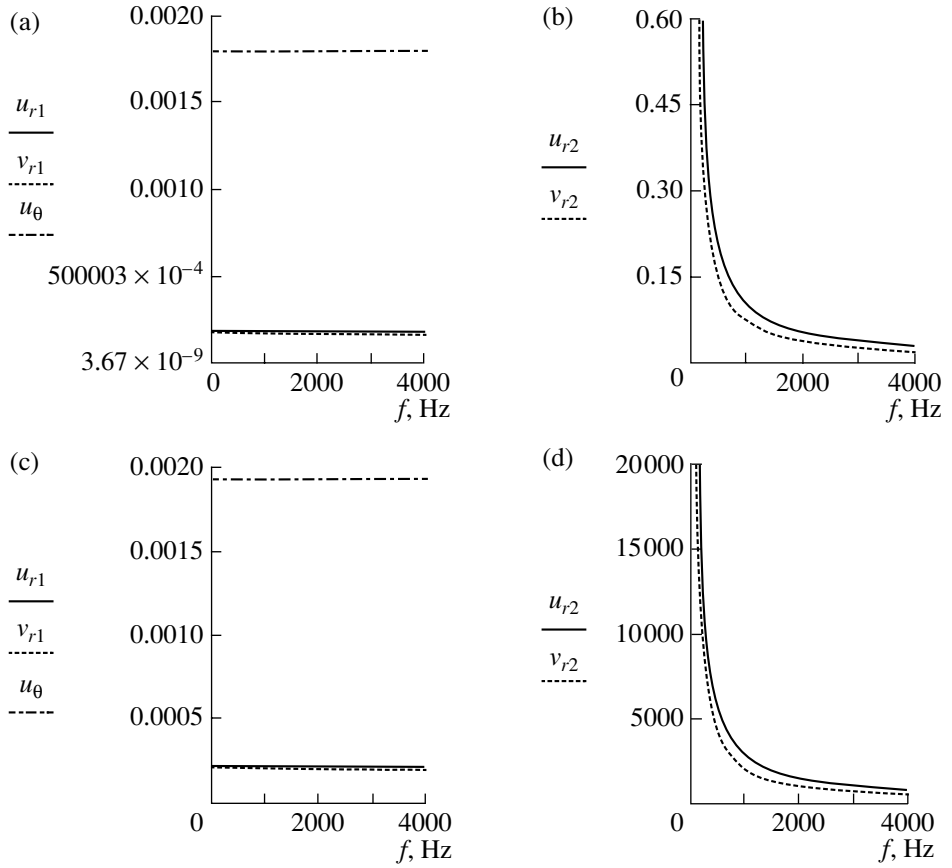

Fig. 6. Frequency-dependent amplitude of waves in the directions of the maxima of their directional patterns (the amplitudes are normalized by $\max u_{r2}$ in water-saturated sandstone). Water-saturated sandstone: (a) first longitudinal wave in the skeleton, u_{r1}, and the fluid, v_{r1}, and the transverse wave in the skeleton, u_θ; (b) second longitudinal wave in the skeleton, u_{r2}, and the fluid, v_{r2}. Gas-saturated sandstone: (c) first longitudinal wave in the skeleton, u_{r1}, and the fluid, v_{r1}, and the transverse wave in the skeleton, u_θ; (d) second longitudinal wave in the skeleton, u_{r2}, and the fluid, v_{r2}.

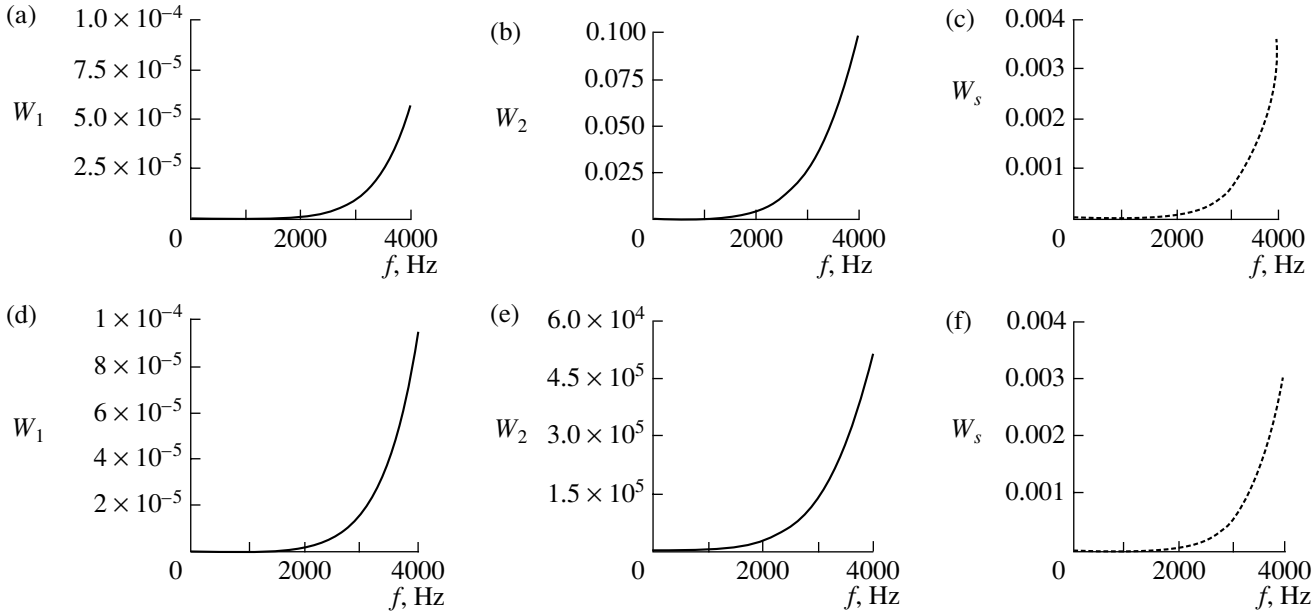

Fig. 7. Frequency-dependent acoustic radiation power (dimensionless units). Water-saturated sandstone: power versus frequency for the (a) first longitudinal wave, W_1, (b) second longitudinal wave, W_2, and (c) transverse wave, W_s. Gas-saturated sandstone: power versus frequency for the (d) first longitudinal wave, W_1, (e) second longitudinal wave, W_2, and (f) transverse wave, W_s.

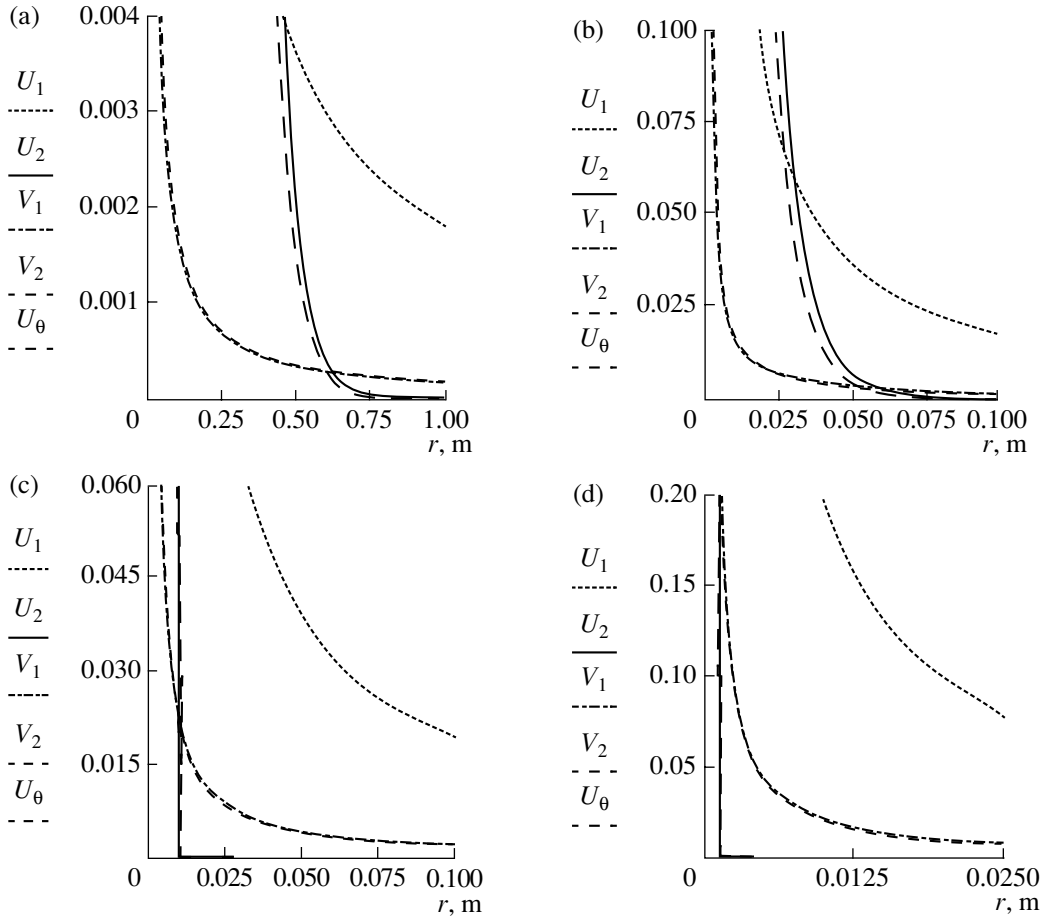

Fig. 8. Distance-dependent amplitude of acoustic waves propagating in the skeleton and the fluid of the (a, b) water-saturated and (c, d) gas-saturated sandstones at frequencies of (a, c) 100 Hz and (b, d) 4 kHz. Notation: U_1 is the first longitudinal wave in the skeleton, V_1 is the first longitudinal wave in the fluid, U_2 is the second longitudinal wave in the skeleton, V_2 is the second longitudinal wave in the fluid, and U_θ is the transverse wave in the skeleton.

Consider now the results that show the law of the wave level decay in water- and gas-saturated media. Figure 8 shows the levels of acoustic waves propagating in the skeleton and the fluid. The curves in Figs. 8a and 8b are calculated for water-saturated sandstone and correspond to acoustic waves with frequencies of 100 Hz and 4 kHz, respectively (the latter frequency imitates the range of acoustic borehole logging operations). Figures 8c and 8d show the curves calculated for waves of the same frequencies, 100 Hz and 4 kHz, in gas-saturated sandstone. We emphasize that the amplitudes given in these figures take into account only the field of radiation, although we use distances from the source that are comparable with the wavelength of the second longitudinal wave (and smaller than the wavelength of the first longitudinal and transverse waves) for both 100-Hz and 4-kHz frequencies, which means that nonwave terms can noticeably contribute to the total level of vibrations for these distances. Therefore, the curves in Fig. 8 are no more than an illustration of the distance-dependent relationship between the levels of acoustic vibrations (due to the divergence and dissipation) of different waves without taking into account the near fields. These curves clearly show that the amplitude of the second longitudinal wave (propagating in both skeleton and fluid) decays with distance faster than the first longitudinal and transverse waves. The region where the amplitude of the second longitudinal wave exceeds the amplitudes of other waves is limited to distances comparable with the wavelength of this wave, which means that it certainly falls in the near-field region of the shear and first longitudinal waves. Therefore, difficulties may arise in detecting this wave against the background of other waves. Incidentally, we note that the use of a piston vibrator instead of the point source considered here can considerably reduce the contribution of nonwave terms, which were ignored in constructing the plots. Nevertheless, the interval of distances where the amplitude of the second wave exceeds the amplitudes of other waves in each of the plots of Fig. 8 represents the distance range (though relatively small) where this wave can be received in principle. For example, in the case of water-saturated sandstone, this interval is 0.5 m at a frequency of 100 Hz and only

2.5 cm at a frequency of 4 kHz. Comparing these results with similar results obtained in [2], one can see that we obtained a situation opposite to that in the medium driven by a monopole source. In the latter case, there is no region where the second longitudinal wave prevails and its selection against the background of the first longitudinal and shear waves requires special techniques and special measuring instruments.

Thus, using numerical calculations, we demonstrated the fundamental possibility of measuring both Boit waves (the first and second longitudinal waves) in actual rocks (water- and gas-saturated sandstones). In low- and middle-frequency ranges, there exists a certain region of distances from the dipole acoustic source where vibrations in the form of the second longitudinal wave prevail in amplitude over other waves, which is impossible in the case of a monopole acoustic source. This inference argues in favor of the necessity to solve the problem on acoustic wave excitation by an oscillating force source. It is quite possible that a similar result can be obtained for other, more complex types of vibrators. The numerical calculations performed above also explain the difficulties that may hinder obtaining reliable experimental data on the second longitudinal waves from seismoacoustic signals measured under the conditions of actual borehole observations or seismic surveys. In addition, the results obtained may be useful for evaluating the possibilities of using both types of vibrators considered above, as well as newly designed modern vibrators that ensure an effective acoustic action on oil pools and improve the accuracy of localization of the fluid-saturated regions against the background of other rocks.

ACKNOWLEDGMENTS

I am grateful to A.S. Zykov for the assistance in numerical calculations. This work was supported by the Russian Foundation for Basic Research, project no. 05-02-16874.

REFERENCES

1. *Proceedings of the 2nd Biot Conference on Poromechanics, Grenoble, France, 2002* (Grenoble, 2002).
2. Yu. M. Zaslavskiĭ, in *Year-book of the Russian Acoustical Society 2003: Acoustics of Inhomogeneous Media*, Ed. by S. A. Rybak (Moscow, 2003), pp. 67–76 [in Russian].
3. G. A. Maksimov and A. V. Radchenko, in *Year-book of the Russian Acoustical Society: Acoustics of Inhomogeneous Media*, Ed. by S. A. Rybak (Moscow, 2003), pp. 37–53 [in Russian].
4. M. A. Biot, J. Acoust. Soc. Am. **28** (2), 179 (1956).
5. M. A. Isakovich, *General Acoustics* (Nauka, Moscow, 1984) [in Russian].
6. L. Ya. Kosachevskiĭ, Prikl. Mat. Mekh. **23** (6), 1115 (1959).

Translated by A. Vinogradov

Acoustical Physics, Vol. 51, No. 6, 2005, pp. 664–670. Translated from Akusticheskiĭ Zhurnal, Vol. 51, No. 6, 2005, pp. 771–777.

On the Vertical Structure of the Sound Field in a Canonical Waveguide at Long Ranges

V. A. Zverev and G. K. Ivanova

Institute of Applied Physics, Russian Academy of Sciences,
ul. Ul'yanova 46, Nizhni Novgorod, 603950 Russia
e-mail: ivg@hydro.appl.sci-nnov.ru

Received April 12, 2004

Abstract—The geometrical-acoustics approach is used to calculate the vertical structure of the sound field in an oceanic waveguide. The profile of the sound speed is specified to be canonical and range-independent along a 1000-km propagation path. A monochromatic sound source lies on the waveguide axis. It is shown that, at long distances from the source, the sound field formed by the water-path rays is mainly concentrated in the caustics, the number of which is determined by the number of the overlapping ray cycles at a given distance. A method for estimating the amplitude of the sound field produced by individual rays is proposed. The amplitudes obtained are used to calculate the total sound field along the vertical. A possible cause of the chaotic distribution of ray coordinates is considered. This cause may consist in the arbitrary choice of the number of rays and their departure angles without taking into account the discrete character of one of the variables. This mechanism of ray chaos formation furnishes an explanation for the fact that the chaos obtained in calculations is mainly associated with the flat rays. © *2005 Pleiades Publishing, Inc.*

An important problem of ocean acoustics is the study of long-range sound propagation. The urgency of this problem is particularly determined by the development of the methods of ocean tomography. In [1–3], experiments on superlong-range propagation of pulsed signals are described, and the data obtained are interpreted using calculations based on different theoretical models, both with and without taking into account the fluctuations in the medium. In computations, the ray-theory representation of the sound field prevails. The ray trajectories are calculated by solving the Hamilton–Jacobi equations that are derived from the wave equation in view of the analogy between a material particle trajectory and a ray path.

The authors of the cited publications argue that, in the vertical plane, the ray chaos is formed at long ranges both in the presence of the fluctuations in the medium (caused by internal waves, for instance) and in the absence of any disturbances. The major part of [3] consists in a study of the ray chaos, which is considered to be a consequence of the Hamiltonian structure of the ray equations. According to such considerations, the strongest chaos corresponds to the near-axis flat rays. In this case, multimicropaths appear that hinder the separation of individual sound pulses. For the arrivals of steep rays, multimicropaths are few in number and the characteristic features of the undisturbed time structure of the sound field persists in the vertical plane, though on the background of the ray chaos. The difference in the chaos of flat and steep rays is explained in [3] by the fact that the ray chaos in these utmost angular ranges of the rays obey different statistical descriptions. However, no mechanism linking the statistical description and the chaos is considered in [3]. Therefore, the problem arises to study the origin of the ray chaos by numerical computations in view of the structure of the wave field and to elucidate the origin of the observed relation between the characteristics of the chaos and the ray parameters. In [4], the vertical structure of the sound field is calculated for a natural underwater sound channel (USC) at a long distance (1500 km) from the source. By using the methods of geometrical acoustics, a highly ordered structure of the vertical coordinates of rays and the vertical projections of their wave numbers is obtained with no traces of ray chaos. However, the conditions of sound propagation in [4] differ from those in [1–3]. According to [4], the sound source was located at the near-surface maximum of the sound speed. Hence, the sound field was formed by a relatively small group of rays whose lower turning points were at a depth where the sound speed was greater than that at the near-surface maximum. As a result, a large group of channel rays fell out of the consideration.

The objective of this work is to use the canonical waveguide as an example for calculating the vertical distribution of the sound field produced by a number of rays that is sufficient for the ray chaos to be formed. For this purpose, the calculation is performed for a long distance (1000 km) from a source positioned at the channel axis.

The calculations show that the sound field at long ranges in the canonical waveguide is mainly concentrated at the caustics, whose number is proportional to the number of the overlapping ray cycles at the distance

1063-7710/05/5106-0664$26.00

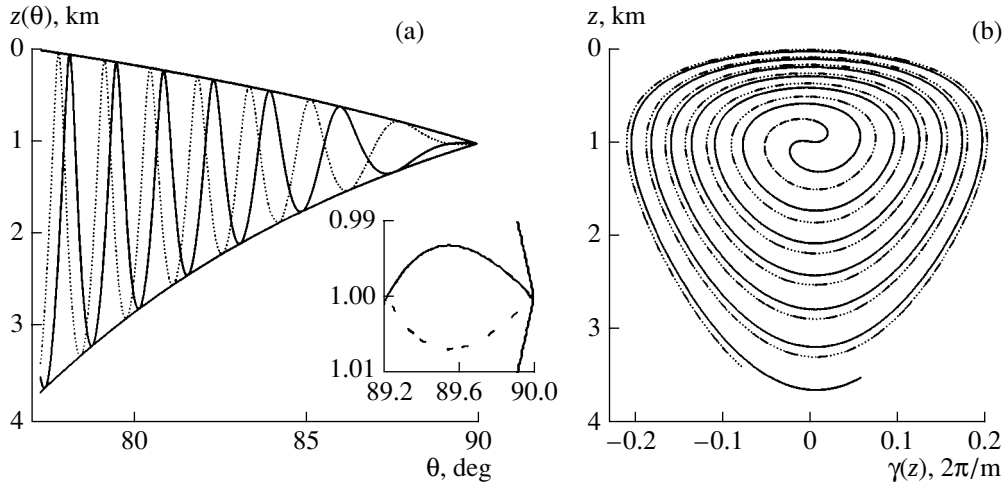

Fig. 1. Vertical structure of the sound field for the rays leaving the source towards the surface (the solid curves) and the bottom (the dashed curves): (a) the distribution of the ray coordinates in the departure angle, $z(\theta)$; (b) the projections of the wave numbers onto the z axis, $\gamma(z)$.

in question. The field amplitude in the caustics is much higher than between them. Note that the presence of a number of caustics in the vertical field structure at long ranges can be experimentally verified.

The vertical structure of the sound field was calculated for the canonical model of the USC, which is fairly close to the actual profiles of the sound speed in some ocean regions [7]. A monochromatic sound source with a frequency of 233.6 Hz was positioned at the channel axis lying at the depth $z_0 = 1$ km; the waveguide thickness was 4 km. Only pure water rays were considered. By using the method described in [4], the following characteristics were computed: the angular distribution (AD) of the vertical coordinates of the rays and the vertical projections of their wave numbers (PWN) as functions of the departure angle. The dependences obtained were used to calculate the total sound field produced by individual rays at all depths.

One of the main results of the calculations is the determination of the role of the function $z(\theta)$ (Fig. 1) that represents the AD of the rays at the maximal distance $x_c = 1000$ km from the source, where θ is the departure angle relative to the z axis (the vertical). Here and in the following figures, the solid and dashed curves correspond to the rays leaving the source towards the surface and the bottom, respectively. The lines that envelop the $z(\theta)$ curves from above and from below carry important information about the sound field: they show the depths of the turning points of the rays near the surface and the bottom. The inset in Fig. 1a shows the functions $z(\theta)$ near $\theta = 90°$ on an enlarged scale. The oscillating form of the AD is caused by the dependence of the length of the ray cycles on the departure angle. The rays leaving the source at θ close to 90° produce 24 full cycles at the distance x_c; those with $\theta \sim 77.3°$ produce 17 cycles. The difference between the numbers of cycles produced by the rays with maximal and minimal cycle lengths is 7. The latter number coincides with the number of oscillations of the $z(\theta)$ curves shown in Fig. 1a (with allowance for the curves in the inset).

The following features of the AD are most important. All the maxima and minima of both curves are the caustics rather than the turning points, seemingly because of the closeness of all the extrema, except for those shown in the box, to the turning points. Each curve exhibits 14 caustics. The caustics shown in the box differ from the others in that they are caused by the existence of the minimum in the cycle length as a function of the departure angle near $\theta = 90°$. The centers of these caustics are far from the turning points, which are shown as the two lines in the box. According to the figure, these caustics are much wider than the others: their angular width $\Delta\theta$ is about 0.8°. In the vicinity of these caustics, a great number of rays (that is, the major portion of the sound field energy) are concentrated. The remaining caustics correspond to a monotonic variation of the cycle length and have smaller angular widths.

Another important characteristic of the wave field is the projection of the wave numbers (PWN) on the z axis as a function of the departure angle. Let us denote them as $\gamma(\theta)$. They are also of an oscillating nature similar to that of the AD $z(\theta)$. The dependence of the PWN on the depth of the ray arrivals at a given distance is of most interest. This function, $\gamma(z)$, is obtained from $\gamma(\theta)$ with the use of the AD by eliminating the departure angle. The functions $\gamma(z)$ are shown in Fig. 1b, again for the two groups of rays leaving the source towards the surface and the bottom. It is assumed that $\gamma(z) > 0$ if the rays are directed to the bottom and $\gamma(z) < 0$ if they are directed to the surface. In contrast to Fig. 1a, the turning points are pronounced in Fig. 1b; at these points, $\gamma(z) = 0$. The caustics are hardly visible. Their positions are

close to those of the turning points, and $\gamma(z)$ is close to zero at all the caustics.

Note that the curves given in [1] differ from those shown in Fig. 1b by a constant factor that is equal to the cyclic frequency. It seems that this difference prevented the authors of [1] from noticing the physical meaning of the curves.

Let us consider the characteristic features of the vertical structure of the sound field at long distances from the source by using Figs. 1a and 1b. The vertical coordinates of the rays, the AD, and the PWN exhibit a strictly ordered character. The curves obtained are very informative, without calculating the sound field itself, because they determine the depths of ray concentration (the caustics), the number of rays arriving at all depths, and the possible set of spatial frequencies for the rays along the z axis. Along the vertical, a great number of caustics are formed, and this number is proportional to the number of the overlapping cycles. At the distance x_c, 28 caustics are present. The calculation of the AD and the PWN at the distance $x = 3250$ km, which is considered in [2, 3], leads to a similar picture. The only difference consists in the number of caustics: this number is increased by a factor of approximately 3. The PWN, $\gamma(z)$, strongly depends on the depth. This fact leads to a nonlinear depth dependence of the phase of the total sound field produced by the rays in the vertical plane. The areas where the values of $\gamma(z)$ can be assumed to be constant are near the channel axis, and their sizes are no greater than 200 m.

The calculation of the sound field in the vertical plane was carried out with the use of the functions $z(\theta)$ and $\gamma(z)$. The field was calculated as a sum of the fields produced by the rays arriving at the given horizon z. The sound field of each ray has its own amplitude. We propose the following technique for the calculations.

Suppose that the amplitude of the field produced by an individual ray is equal to the ratio of its angular width, which is supposed to remain constant in the course of propagation, to the depth interval Δz occupied by this ray at the distance x_c from the source: $\Delta\theta/\Delta z$. The quantity $\Delta\theta$ can be considered as the difference between the departure angles of the adjacent or close rays, and Δz is the difference in the depths at which these rays arrive. The angular width $\Delta\theta$ of the ray depends on the departure angle: according to Snell's law, $\Delta\theta$ decreases as θ decreases. The quantity Δz is a function of z and characterizes the density of the rays along the vertical; it is determined from the AD $z(\theta)$. Instead of calculating the additional rays, we used interpolation to fill the domains of $z(\theta)$ to which the calculated rays do not arrive. The purpose of this procedure was to obtain equal intervals Δz between the adjacent rays. In our case, this interval is equal to that of sampling along the z axis. The interpolation allowed us to calculate the amplitudes of both individual fields and the total field for a greater number of rays than that initially chosen. In the vicinity of the caustics, many rays have the same coordinates in depth but different departure angles, i.e., $\Delta z = 0$. The reason is that a narrower sampling window is required for these rays to be resolved in the z direction. In such a situation, the value of Δz was specified to be equal to the sampling interval, that is, to the least vertical spacing of the rays for the calculation parameters used. This approximation leads to a decrease in the ray amplitudes in the vicinity of caustics. Such a decrease is the main inaccuracy in the proposed technique of calculating the amplitudes of the sound fields corresponding to individual rays. In our case, the ray amplitude was calculated by averaging over two sampling intervals. In [8], the number of rays used in averaging was not constant: it was chosen in such a way that Δz was not lower than the sampling interval. This method leads to overestimation of the amplitudes at caustics.

The distribution of the ray amplitudes is shown in Fig. 2a as a function of the departure angle. The notations are the same as in Fig. 1. The maxima of the ray amplitudes are at the centers of the caustics. The amplitudes at the initial near-axis caustics, which are the broadest ones, are equal for the rays leaving the source towards the surface and the bottom. At the centers of the caustics, the amplitudes smoothly decrease as the departure angle decreases. The real part of the total sound field is shown in Fig. 2b. Here, all the caustics are pronounced. The two central caustics that are symmetric about the waveguide axis merge on the scale used in Fig. 2b. Although a great number of rays are summed in the gaps between the caustics, the amplitude produced by these rays is much lower than that at the caustics. Figure 2b leads to a conclusion that the caustics predominate in the vertical distribution of the sound field at long ranges.

Some recent works ([1–3], for instance) concentrate on the calculations of the arrival times of the pulses and their coordinates along the z axis. In addition to the calculation of $z(\theta)$, we also calculated the time of sound propagation along the ray trajectories. Figures 3a and 3b show the coordinates of rays along the vertical, $z(\theta)$, as functions of the travel time for the corresponding rays. In Fig. 3b, the depths of arrivals of the near-axis rays are shown as functions of time on an enlarged scale. It can be seen that the arrival times are regular in the case at hand. The points of inflection are those of the caustics. According to Fig. 3a, there are few points at which the travel times coincide for different trajectories. One can find a depth at which pulses arriving in sequence can be well resolved if the width of the pulses is lower than the time interval between them. The longest travel times correspond to the near-axis flat rays whose departure angles are close to 90°. The difference in the travel times is smaller for the flat rays than for the steep ones. Figure 3b shows the travel times for the rays in the vicinity of the three initial near-axis caustics; here, the caustics nearest to the axis are represented by a single point. The travel times for these caustics are

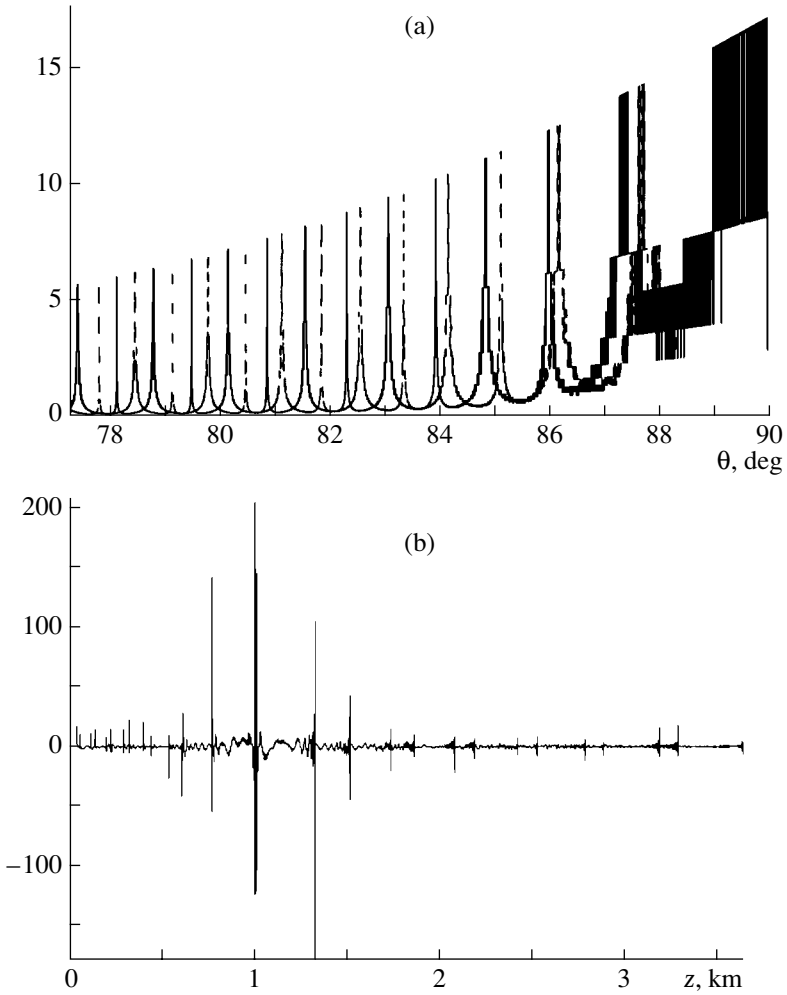

Fig. 2. Sound field of the water-path rays: (a) the sound field amplitude versus the departure angle; (b) the amplitude of the real part of the total sound field along the vertical.

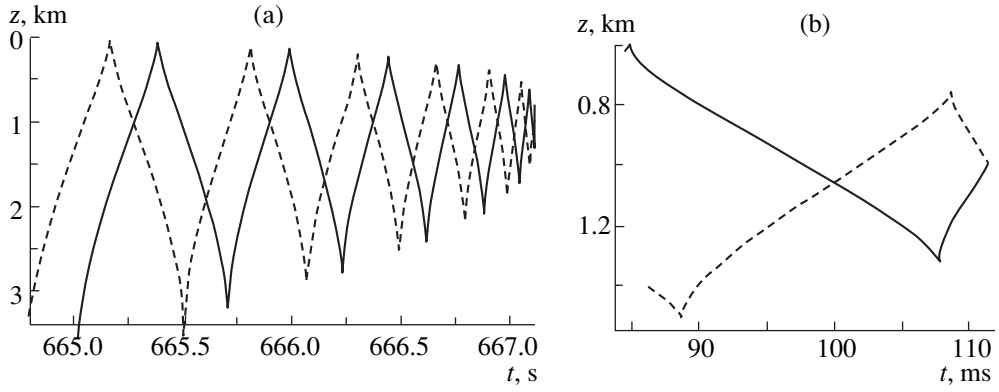

Fig. 3. Relation between the vertical coordinate of the rays and their travel times (a) for all water-path rays and (b) for the near-axis rays (on an enlarged scale).

equal to the time of sound propagation along the waveguide axis to an accuracy of 0.05 ms. The interval between the initial symmetric caustics and the second caustic does no exceed 5 ms. These caustics are spaced by more than 200 m in the vertical. The difference in the travel times of the pulses should be compared with $1/\Delta f$, where Δf is the expected frequency bandwidth of the source determined by the sound absorption in the

ocean. If we specify $\Delta f \sim 100$ Hz, the duration of the sound pulse should be no smaller than 10 ms. Usually, in the experiments on long-range sound propagation in the ocean, the duration of the pulses is 10–30 ms. Hence, between the first and second caustics, the near-axis rays can be resolved in their travel times if the duration of the pulses is about 1 ms or less, which can not likely be realized because of the sound absorption. However, the lack of ability to separate the overlapping pulses propagating over close rays is no reason to argue that these rays are chaotic.

Let us now consider one of the main tasks of this work: the analysis of the possible origin of the ray chaos. Note that the chaos is observed in numerical calculations that have their own specific features, in particular, the discreteness of the data representation. As reported earlier [9], the discreteness of the data influences the accuracy of calculating the diffraction of the wave field. Let us consider the role of the discreteness in the formation of the ray chaos. If we show that the origin of the chaos lies in the calculation errors caused by the discretization, this statement will be true for [2, 3] as well, at least until one proves that the discreteness of data representation in [2, 3] does not lead to calculation errors.

In our paper, the discrete coordinate is the depth z, which is specified with the step Δz. Rays that are close in their departure angles are commonly treated as different if the depths of their turning points are different. Hence, the number of rays (the number of discrete values of departure angles) should not exceed the number of points in depth, from the waveguide axis to its most distant boundary. Let us denote the latter number as N. If calculations involve rays whose number is greater than N, some of the rays will have the same depths of their turning points. By definition, these rays are the same, although they have different vertical coordinates because of their different departure angles. This difference is just what causes the ray chaos. These rays are redundant or phantom rays. Another origin of the chaos is the arbitrary choice of the ray departure angle. Let us consider rays that differ by $\Delta\theta$ in their departure angles and by Δz in the depths of their turning points. From Snell's law, we can obtain the approximate relation of the step $\Delta\theta$ in the departure angle to the quantities Δz, θ, and $c(z)$:

$$\left|\frac{\Delta\theta}{\Delta z}\right| = \left|\frac{\tan(\theta)}{\Delta z}\right|\left|\frac{\Delta c}{c(z)}\right|. \quad (1)$$

According to Eq. (1), the angular step $\Delta\theta$ depends on the departure angle θ and the interval Δz. If Δz is constant, $\Delta\theta$ decreases as the departure angle decreases. If one chooses a constant angular step ($\Delta\theta$ = const), the turning points of individual rays may occur between the discrete depth points, which leads to errors in calculating the AD, the PWN, and the travel times for the ray trajectories because of the inaccuracy in determining the depth of the turning points. Therefore, the ray departure angle should be chosen so that its turning point coincides with some of the discrete points of the z axis. Another important feature of the ray structure follows from Eq. (1). The angular density $\Delta\theta/\Delta z$ of the rays decreases as the departure angle θ decreases. Hence, a conclusion can be drawn that the greatest density of the rays can be observed near the waveguide axis for flat rays. This conclusion has been repeatedly confirmed by experiments and calculations. Let us illustrate the aforementioned statements by calculation.

Figure 4a shows the AD calculated for rays whose number exceeds the admissible one (N) by a factor of 2.3. The rays involved in the calculation were those leaving the source towards the bottom at a constant step in angle. Comparison with the similar curve of Fig. 1a, which corresponds to the optimal number of rays and the choice of the departure angle matched with the position of the turning point, shows that the general character of the curve persists for the excessive number of rays. The reason is that the relation between the departure angle and the turning point is violated for none of the rays except those turning at the depths between the adjacent discrete points. The coordinates of the rays whose departure angles were matched with the turning points remained unchanged. The greatest number of phantom rays corresponds to the near-axis region (flat rays), because, according to Eq. (1), the highest density of rays occurs in this region. The greatest angular interval separating the adjacent rays corresponds to the vicinity of the waveguide axis: it may contain several phantom rays. In the region of steep rays with smaller values of θ, the number of phantom rays between the adjacent rays decreases or is even equal to zero. In this case, the matched angular step $\Delta\theta$ decreases by a factor of about 3 from the beginning to the end of the angular range. Figure 4b illustrates the calculation, in which the matching between the departure angle and the turning points is completely excluded. The number of rays taken for the calculation was N. Figure 4b corresponds to a constant step in the departure angle. Here, one can see no regular structure similar to that observed in Figs. 1a and 4a. The greatest number of points is also concentrated near the USC axis and corresponds to departure angles close to 90°. The reason for such a concentration is the same as above. The PWN, which is not shown in the figure, is also chaotic in this case.

However, the depth dependence of the travel time along the ray (Fig. 4c) retains its basic structure, as in Figs. 3a and 3b, in spite of the apparent chaos in the AD, $z(\theta)$. The explanation of such stability of the travel time with respect to the unmatched departure angles may consist in the fact that, in calculating $z(\theta)$, the accuracy of computing the horizontal coordinate of the trajectory is much lower that in the case of travel-time calculations. Note that the chaos illustrated in Figs. 4a–4c and obtained by the incorrect calculations does not

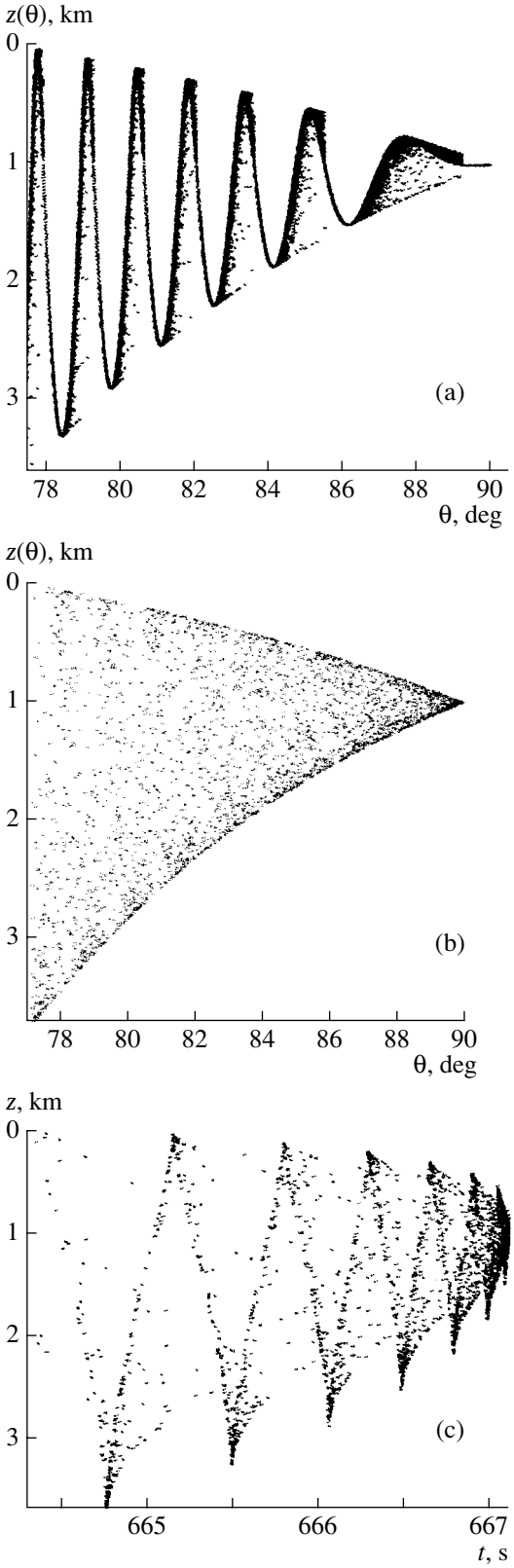

Fig. 4. Angular distribution of the ray coordinates $z(\theta)$ (a) for the excessive number of rays and (b) for the departure angles unmatched with the turning points at a constant angular step; (c) the dependence of the travel time along the rays on the arrival depth for the departure angles unmatched with the turning points at a constant angular step.

differ from that presented in [1, 3] for the case of the sound speed fluctuations along the path. Hence, the fact that the chaos shown in [1, 3] is caused by the fluctuations rather than by the discreteness of calculation has to be verified.

In [1, 3], the differential equations of the ray trajectories were solved by the Runge–Kutta method. This method implies a constant-step sampling of the horizontal coordinate (the distance to the source), and the angular step is also constant. Note that the main problem of this method is the need to specify the sound speed at all depths passed by the rays. Therefore, the ray chaos can be caused by the violation of the main property of the ray trajectories, namely, the equality of the sound speed at the upper and lower turning points. This condition can be satisfied only approximately, the accuracy of the approximation being different for different trajectories. The effect of the violation is that the upper and lower parts of the trajectories may belong to different but close rays. This fact was also mentioned in [3]: the authors reported the appearance of multimicrotrajectories of new rays near the main ones and interpreted them as the proper rays. The greatest number of new rays corresponds to the near-axis region, near the flat rays. This feature is quite understandable: the gradient of the sound speed is small in the near-axis region, and, hence, the difference in the values of $c(z)$ is also small at the turning points of the adjacent rays, which favors the splitting of the trajectories.

The results obtained from the calculation of the vertical structure of the sound field in the canonical waveguide can be summarized as follows. At long ranges from the source positioned at the waveguide axis, the ray coordinates and the spatial frequencies along the vertical, as calculated in the framework of the ray theory, are described by regular functions of the angles at which the rays leave the source. These regular dependences have an obvious physical explanation. At long ranges, the sound field along the vertical is mainly determined by groups of rays that form the caustics, within which the major portion of the signal energy is concentrated. The remaining rays produce an acoustic background, whose amplitude is much smaller than the field amplitude at the caustics. It is precisely the caustics that create the regular and predictable structure of the sound field at long ranges. This conclusion is drawn from the calculations and can be verified by experiments on long-range sound propagation with vertically extended antenna arrays.

ACKNOWLEDGMENTS

This work was supported by the grant from the President of Russian Federation no. NSh-1641.2003.2.

REFERENCES

1. J. Simmen, S. M. Flatte, and G.-Yu. Wang, J. Acoust. Soc. Am. **102**, 239 (1997).

2. P. F. Worcester and B. Cornuelle, J. Acoust. Soc. Am. **105**, 3185 (1999).
3. F. J. Beron-Vera, M. G. Brown, J. A. Colosi, *et al.*, J. Acoust. Soc. Am. **114**, 1226 (2003).
4. V. A. Zverev and G. K. Ivanova, Akust. Zh. **49**, 632 (2003) [Acoust. Phys. **49**, 535 (2003)].
5. V. A. Zverev, V. P. Ivanov, and G. K. Ivanova, in *Proceedings of 9th Workshop by Acad. L.M. Brekhovskikh, Moscow, 2002* (GEOS, Moscow, 2002), p. 128.
6. I. N. Didenkulov, V. A. Zverev, V. P. Ivanov, and G. K. Ivanova, Akust. Zh. **50**, 783 (2004) [Acoust. Phys. **50**, 677 (2004)].
7. *Sound Transmission through a Fluctuating Ocean*, Ed. by S. M. Flatte (Cambridge Univ. Press, Cambridge, 1979; Mir, Moscow, 1982).
8. V. A. Zverev and G. K. Ivanova, in *Proceedings of 10th Workshop by Acad. L. M. Brekhovskikh, Moscow, 2004* (GEOS, Moscow, 2004), p. 86.
9. V. A. Zverev, Akust. Zh. **45**, 74 (1999) [Acoust. Phys. **45**, 65 (1999)].

Translated by E. Kopyl

Acoustical Physics, Vol. 51, No. 6, 2005, pp. 671–679. Translated from Akusticheskiĭ Zhurnal, Vol. 51, No. 6, 2005, pp. 778–786.

Properties of a Magnetic-Fluid Membrane

Yu. Yu. Kameneva, G. V. Karpova, V. V. Kovarda, O. V. Lobova, and V. M. Polunin

Kursk State Technical University, ul. 50 Let Oktyabrya 94, Kursk, 305040 Russia

e-mail: Polunin_VM@hotbox.ru

Received April 5, 2004

Abstract—Experimental results concerning the influence of both the parameters of magnetic fluid and the conditions of vibration excitation on the elastic, electrodynamic, and kinetic properties of a breaking magnetic-fluid membrane are presented. The mechanism of the sound excitation in the air cavity due to the closure of the magnetic-fluid membrane is discussed. © *2005 Pleiades Publishing, Inc.*

INTRODUCTION

The possibility of using a magnetic fluid (MF) as a source of ultrasonic vibrations was studied in [1–7]. In these publications, an MF was considered as a continuous compressible medium characterized by a strong magnetic susceptibility. Some recent publications [8–10] described vibratory systems with controlled magnetic-fluid sealants. In particular, in [9–11], a vibratory system with an inert magnetic-fluid element that was spring-loaded by a gas cavity and a pondermotive elasticity was investigated. Such a system can be considered as a magnetic-fluid membrane (MFM).

An MFM has the form of a magnetic colloid drop that plugs the cross section of a glass tube under the stabilizing effect of an inhomogeneous magnetic field produced by a coaxial ring magnet [12]. If the tube has a bottom, the MFM isolates the air cavity lying below it. In this case, the MF functions as an incompressible medium and properties such as its magnetic controllability of the free surface, fluidity, and inertness become important [12, 13]. Unlike conventional fluid films, an MFM is capable of self-recovery. The breakage–recovery of the MFM is accompanied by the generation of decaying acoustic and electromagnetic pulses [10, 11].

Studies of the physical properties of MFMs are of interest from both theoretical and applied points of view. In particular, it is of interest to consider the possibility of using an MFM as a metering valve for a controlled gas supply to a reactor with a corresponding indication in the form of acoustic and electromagnetic pulses. Such a device could be used in certain chemical, physical-biological, and pharmaceutical technologies.

In this paper, we report the experimental study of the effect of the MF parameters and vibration excitation conditions on the elastic (the pondermotive and gas elasticities, the vibration frequency, and the critical pressure drop), electrodynamic (the initial amplitude of the generated electromagnetic pulse, the dynamical range, and the sensitivity), and kinetic (the gas flow velocity in the membrane hole, the lifetime of the hole, the displacement of the membrane, and the mass of gas passed) properties of an MFM. We also discuss the mechanism of sound excitation in the air resonator at the instant of membrane closure.

ELASTIC AND ELECTRODYNAMIC PROPERTIES

Since the pondermotive elasticity of an MFM strongly depends on the strength and degree of inhomogeneity of magnetic field [12, 14], we performed both experimental and theoretical studies of the magnetic field produced by the ring magnet included in the experimental setup.

The thin line in Fig. 1 approximates the results of measuring the magnetic field strength along the axis with a Hall-type teslameter. The abscissa axis represents the distance from the center in ring-magnet half-thickness units.

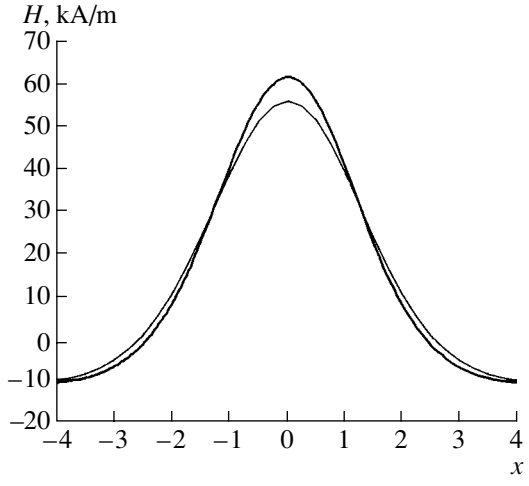

Fig. 1. Magnetic field strength versus the coordinate of the corresponding point on the axis.

1063-7710/05/5106-0671$26.00 © 2005 Pleiades Publishing, Inc.

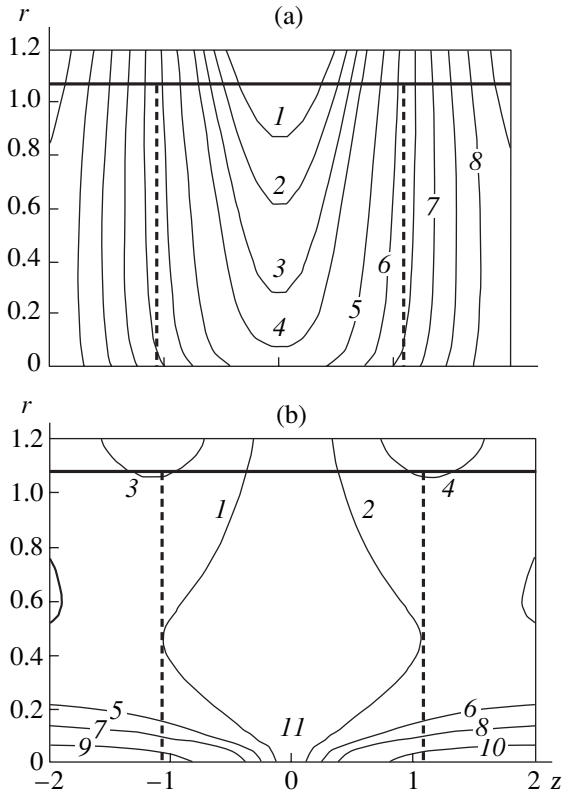

Fig. 2. (a) Isolines of the axial projection of magnetic induction: (*1*) 90, (*2*) 86, (*3*) 81, (*4*) 77, (*5*) 68, (*6*) 60, (*7*) 42, and (*8*) 25 mT. (b) Isolines of the radial projection of magnetic induction: (*1*) –3, (*2*) 3, (*3*) –7, (*4*) 7, (*5*) –7, (*6*) 7, (*7*) –10, (*8*) 10, (*9*) –23, (*10*) 23, and (*11*) 0 mT.

The theoretical analysis of the magnetic field was performed on the basis of the model, according to which the ring magnet possesses a volume-constant magnetization M oriented along its axis. Then, the magnetic induction components are determined by the formula $\mathbf{B} = -\text{grad}\psi$, where the scalar potential has the form

$$\psi = -\frac{M}{2\pi}\left(\int_{R_1}^{R_2} K(k_1)\frac{k_1 q}{\sqrt{qr}}dq - \int_{R_1}^{R_2} K(k_2)\frac{k_2 q}{\sqrt{qr}}dq\right).$$

Here, $k_1 = 2\sqrt{qr/((q+r)^2 + (z-l)^2)}$, $k_2 = 2\sqrt{qr/((q+r)^2 + (z+l)^2)}$, R_1, and R_2 are the inner and outer radii of the magnet, l is its half-width, and $K(k)$ is an elliptical integral of the first kind.

The magnitude of magnetization was determined from the magnetic induction measured at the center of the magnet. The outer and inner radii of the magnet divided by its half-thickness are equal to 5.78 and 2.19, respectively.

The thick line in Fig. 1 shows the value obtained in the framework of the given model for H_z averaged over the cross section of the tube. The difference between the average data and the results of measurements along the axis does not exceed 8.5%.

Figures 2a and 2b show the isolines of the axial H_z and radial H_r components of magnetic field. The dashed lines show the contour of the MFM, and the solid horizontal line bounds the magnetic field region enclosed inside the tube.

The data obtained suggest the following conclusions: (i) the magnetic field within the contour of the drop is predominantly directed along the axis of the ring magnet; i.e., the axial field component H_z predominates; (ii) the field is approximately uniform over the cross section of the tube, and the gradient of the field strength has a predominant axial component $G = \partial H_z/\partial z$; (iii) in the radial direction, H_z slightly increases; (iv) in the plane $z = 0$, the radial field component H_r is absent and shows a tendency to increase in the vicinity of the axis. The presence of a relatively small radial component of magnetic field near the axis and a relatively small radial gradient of the axial component favors the flow of the fluid to the maximum field region. As a result, the free surface of the membrane acquires a biconcave-lens shape [9, 10]. At the center, on both sides of the membrane, one can see small peaks caused by the instability of the MF surface in a transverse field that exceeds some threshold strength value [15, 16]. According to our estimates, the volume fraction of these peaks is less than 0.5% of the membrane volume [10].

The expression for the coefficient of pondermotive elasticity was obtained in [9, 10] in the framework of the model in which the magnetic field was symmetric with respect to the maximum strength surface and the equilibrium position of the MFM coincided with this surface. However, in a more general case, the magnetic field can be asymmetric and the center of mass of the membrane can be displaced from the maximum field region. Such a situation occurs, e.g., in MF sealants at a certain configuration of the poles in the presence of a pressure drop [17].

The weakly-magnetic medium approximation adopted in [9–11] and the aforementioned geometrical features of magnetic field in the region of the membrane can be used to calculate the coefficient of pondermotive elasticity in the case under study according to the simple scheme shown in Fig. 3.

Inside a tube *1* with a cross section S, an MF plug *2* of height b is present. Because of the pressure difference between the gas cavities *3*, the center of mass of the plug is shifted to the point with the coordinate $z = a$.

A small displacement of the center of mass by δz should lead to an increase in the plug volume by $S\delta z$ at the point with the coordinate $z = \frac{b}{2} + a$ and to a decrease in its volume by the same value at the point $z = -\frac{b}{2} + a$. The appearance (disappearance) of the virtual MF disk *4*

in the vicinity of the upper and lower free surfaces of the MF drop gives rise to a perturbation of the pondermotive force:

$$\delta f_1 = \mu_0 S\left(M_z\frac{\partial H_z}{\partial z}\right)_{z=\frac{b}{2}+a}\delta z - \mu_0 S\left(M_z\frac{\partial H_z}{\partial z}\right)_{z=-\frac{b}{2}+a}\delta z. \quad (1)$$

In addition, at the upper and lower free surfaces of the plug, the normal component of magnetic field exhibits a discontinuity, which gives rise to a magnetic pressure force. The perturbation of this force can be represented as [12]

$$\delta f_2 = -\mu_0 S\left[\left(M_z\frac{\partial M_z}{\partial z}\right)_{z=-\frac{b}{2}+a} - \left(M_z\frac{\partial M_z}{\partial z}\right)_{z=\frac{b}{2}+a}\right]\delta z.$$

Using the expression $M_z = \chi H$, where χ is the local magnetic susceptibility, we obtain

$$\delta f_2 = -\mu_0 S\left[\left(\chi M_z\frac{\partial H_z}{\partial z}\right)_{z=-\frac{b}{2}+a} - \left(\chi M_z\frac{\partial H_z}{\partial z}\right)_{z=\frac{b}{2}+a}\right]\delta z. \quad (2)$$

With Eqs. (1) and (2) taken into account, the formula for the restoring pondermotive force takes the form

$$\delta f_p = \mu_0 S\left\{\left[(1+\chi)M_z\frac{\partial H_z}{\partial z}\right]_{z=\frac{b}{2}+a} - \left[(1+\chi)M_z\frac{\partial H_z}{\partial z}\right]_{z=-\frac{b}{2}+a}\right\}\delta z.$$

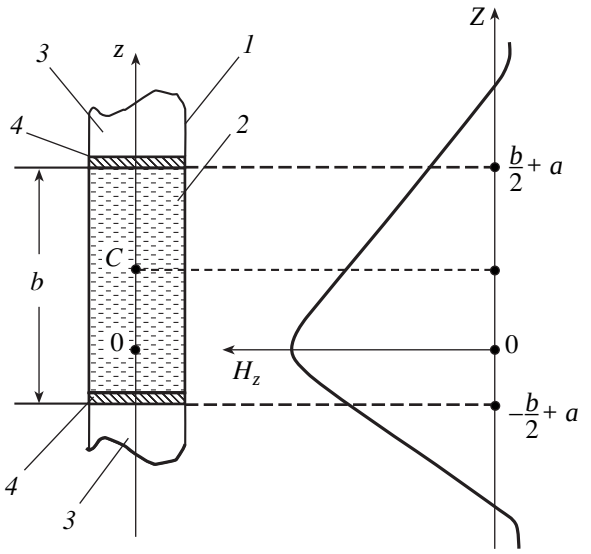

Fig. 3. Scheme used for calculations.

The coefficient of elasticity of the vibratory system, k, is the sum of the coefficient of pondermotive elasticity $k_p \equiv \delta f_p/\delta z$ and the coefficient of elasticity of the gas cavity k_g [11]:

$$k = \rho_g c^2\frac{S^2}{V_0} + \mu_0 S\left\{\left[(1+\chi)M_z\frac{\partial H_z}{\partial z}\right]_{z=-\frac{b}{2}+a} - \left[(1+\chi)M_z\frac{\partial H_z}{\partial z}\right]_{z=\frac{b}{2}+a}\right\}, \quad (3)$$

where ρ_g and c are the density of gas and the sound velocity in it and V_0 is the volume of the isolated gas cavity. The vibration frequency ν of the system is calculated by the formula

$$\nu = \frac{1}{2\pi}\sqrt{\frac{\rho_g c^2 S}{\rho b V_0} + \frac{\mu_0}{\rho b}\left\{\left[(1+\chi)M_z\frac{\partial H_z}{\partial z}\right]_{z=-\frac{b}{2}+a} - \left[(1+\chi)M_z\frac{\partial H_z}{\partial z}\right]_{z=\frac{b}{2}+a}\right\}}, \quad (4)$$

where ρ is the density of the MF.

When the magnetic field is symmetric about the plane $z = 0$ and $a = 0$, the expression for k_p is reduced to the form [9, 10]

$$k_p = 2\mu_0 S M_z\left(\frac{\partial H_z}{\partial z} + \chi\frac{\partial H_z}{\partial z}\right)_{z=-\frac{b}{2}}. \quad (5)$$

From the methodological point of view, one of the key points is the presence of a linear dependence of the emf induced in the inductance coil positioned inside the ring magnet on the displacement of the center of the MFM with respect to the equilibrium position, i.e., the determination of the limits of the dynamical range. To determine the aforementioned dependence, an experiment was carried out with an MFM described in [11]. In this experiment, the MFM plugs the cross section of a tube that is the neck of a glass flask with a volume of 0.5 l. The inner diameter of the neck is 16.5 mm.

When the flask is shifted upwards by Δz above the stand and fixed in this position, the membrane is shifted from the equilibrium position by δz, so that

$$\delta z = \frac{k_g}{k_g + k_p}\Delta z.$$

When the flask abruptly returns to the initial position, the membrane proves to be shifted from the equi-

Table 1

Sample	ρ, kg/m^3	η_s, Pa s	M_s, kA/m	χ
MF-1	1294	3.2×10^{-3}	52 ± 1	6.2
MF-2	1499	8.1×10^{-3}	60 ± 1	7.5
MF-3	1424	–	43 ± 1	5.0

librium position by δz because of its inertia, which leads to the development of a vibratory process. At the instant when the plug passes through the equilibrium position, the maximum emf is reached: ε_m. The abrupt motion of the flask occurs under the impact of a falling body with a mass of 125 g. The induced signal is supplied to the input of an oscilloscope operating in external synchronization mode. The oscillogram is photographed by a digital video camera and entered in a computer where it is processed an analyzed with the Corel Draw program. This method of obtaining and processing the results of vibration frequency measurements provides a confidence interval of 5% with a confidence level of 0.95.

We used MFs common to mechanical engineering: colloid solutions of single-domain particles of Fe_3O_4 magnetite in kerosene (MF-1 and MF-2) and in silicon organics (MF-3) [17]. The physical parameters of magnetic colloids are given in Table 1: ρ is the density of the MF, χ is the initial magnetic susceptibility, and η_s is the static shear viscosity of the colloid. These parameters were determined by standard methods [12, 17].

The fluid was introduced into the neck of the flask by a syringe, which was weighted with MF before and after the introduction of the drop.

As a result of the measurements, we determined

—the dynamical range for the MFMs (at $T = 24 \pm 0.5$°C, the dependences $\varepsilon_m(\Delta z)$ obtained for the MFMs on the basis of MF-1 and MF-2 are approximated by segments of a straight line in the intervals 0–4.5 mm and 0–3.5 mm, respectively, with the confidence level of approximation being 0.99 and 0.98, respectively);

—the sensitivity of the device to displacement, β, which is determined as the tangent of the slope angle of the approximated straight line;

—the amplitude of the first vibration, ε_{m0}, at $\Delta z = 0$, this vibration being a consequence of the pressure produced by the flask on the damping cotton pad and the excitation of elastic vibrations of the flask walls at the instant of impact.

Table 2 presents the values of β and ε_{m0} obtained from the experiments with different fall distances of the load, h'.

For the MFM consisting of the more concentrated colloid MF-2, the parameter β is almost twice as large as that in the case of MF-1. This result can presumably be explained by the negative role of viscous forces, which lead to a decrease in the amplitude of initial membrane displacement from the equilibrium position at the instant of impact. The small increase in β with increasing distance of fall h', which is more pronounced for MF-1, is presumably caused by the inertial properties of the membrane. A considerable increase in β should be obtained under the condition $k_g \gg k_p$, and this can be achieved by reducing the volume of the isolated gas cavity V_0.

The calculation of the vibration frequency of the MFM is in good agreement with experimental data [9, 10]. In the present study, we performed a direct experiment on determining the parameter k_p by the added-cavity method. The essence of this method is as follows. The vibration frequency is sequentially measured with the tube open on one end, ν_1, and with the tube closed on both ends, ν_2. When the tube is open on one end, the MFM is string-loaded with the elasticity of the isolated gas cavity and the pondermotive elasticity. When the tube is closed on both ends, the MFM is loaded with the two aforementioned elasticities and the elasticity of the added gas cavity. The coefficient k_p is calculated by the formula

$$k_p = \frac{\pi^2 \rho_g c^2 d^4}{16 V_{ac}} \left[\frac{1}{n^2 - 1} - \frac{V_{ac}}{V_0} \right],$$

where V_{ac} is the volume of the added cavity and $n \equiv \nu_2/\nu_1$.

Let us compare the results of calculating k_p by Eq. (5), $(k_p)_{\text{theor}}$, and the experimental results obtained by the aforementioned method, $(k_p)_{\text{exp}}$. In the experiments, the MFM is placed in a cylindrical neck of a glass flask. The added cavity is formed by applying a ground stopper. From preliminary measurements of the field dependence of the magnetization of magnetic colloids, we obtained the data necessary for calculating $(k_p)_{\text{theor}}$.

For the MF-1 membrane, we obtained $b = 1.68$ cm, $M = 34.5$ kA/m, $G = 4.6 \times 10^6$ A/m^2, $\chi = 0.25$, and $(k_p)_{\text{theor}} = 100$ N/m. From the measurements by the

Table 2

Colloid	h', mm	β, mV/mm	ε_{m0}, mV	Colloid	h', mm	β, mV/mm	ε_{m0}, mV
MF-1	9.0	4.6	0.5	MF-2	10.8	2.5	0.7
	14.6	4.9	0.5		20.3	2.6	0.5
	19.4	5.3	0.5				

added cavity method, we obtained h_{ac} = 4.64 cm, ν_1 = 24 Hz, ν_2 = 68 Hz, and $(k_p)_{exp}$ = 98 N/m.

For the MF-2 membrane: b = 2 cm, M = 42 kA/m, $G = 4.6 \times 10^6$ A/m^2, χ = 0.4, h_{ac} = 6.3 cm, n = 1.9, $(k_p)_{theor}$ = 136 N/m, and $(k_p)_{exp}$ = 137 N/m.

Taking into account the estimated character of the model calculations and the errors inherent in the adopted method of measurements, we should expect a difference between $(k_p)_{theor}$ and $(k_p)_{exp}$ of about ten percent. Presumably, in the case under study, the good agreement between the calculated and measured values of k_p is partially caused by the mutual compensation of errors in the determination of individual parameters.

The model theory makes it possible to predict qualitatively the behavior of the elasticity and vibration frequency of the MFM as functions of the displacement of its equilibrium position. For example, from Eqs. (3) and (4), it follows that, by virtue of the symmetry of magnetic field with respect to the plane z = 0 (Fig. 1), a displacement of the membrane should not lead to considerable changes in the magnetic elasticity and vibration frequency. However, as the free surface of the membrane approaches the maximum-field plane, we obtain $\partial H_z/\partial z \longrightarrow 0$ and, hence, the values of k_p and ν also decrease. This position of the MFM is critical [12, 17], because a further increase in the pressure drop leads to its breakage.

The above conclusions of the model theory were experimentally tested with MF-1 and MF-2 colloids. The MF covers the cross section of the neck of a flask. The use of a flask with a large volume in the MFM system allows us to obtain a considerable predominance of the pondermotive elasticity over the elasticity of the gas cavity. The displacement of the equilibrium position of the membrane is obtained by raising the ring magnet, which is rigidly bound to the kinematic unit of a cathetometer, to a height Δz measured with an accuracy of 0.01 mm. The vibrations are excited by a mechanical shock in the vertical direction.

As a result, it was found that

—at $\Delta z \le 30$ mm, the dependence $\nu(\Delta z)$ has virtually the same form of a segment of a straight line parallel to the abscissa axis for both colloids (the prediction of the model theory is confirmed in this part of the experiment);

—in both cases, several 0.5-mm steps of magnet displacement before the breakage of the membrane, the vibrations acquire strongly pronounced nonlinear properties: the oscillograms of damped vibrations first become saw-toothed; then, the second harmonic appears; and, finally, the vibration frequency is doubled.

Thus, the conclusion of the model theory concerning the sharp drop of the vibration frequency near the critical position of the MFM could not be confirmed or disproved in our experiments because of the strong nonlinearity of the vibratory process. Therefore, the model theory based on the applicability of Hooke's law should be extended with allowance for the actual nonlinearity of the expression for the restoring force in the vicinity of membrane breakage.

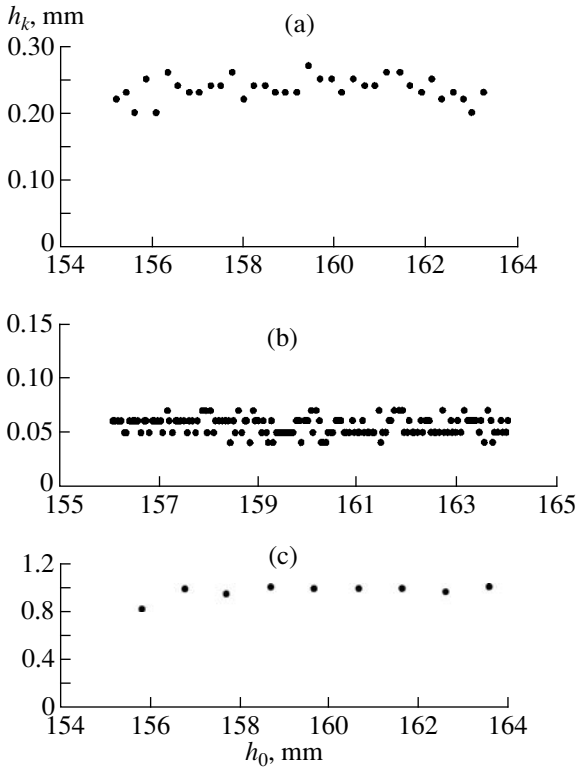

Fig. 4. Dependence $h_k(h_0)$ for the MFMs on the basis of (a) MF-1, (b) MF-2, and (c) MF-3.

KINETIC PROPERTIES

Let us consider the results of measuring the critical pressure drop P_k causing the breakage of the MFM. To form the MFM, in this case we used a glass tube with a flat bottom, a length of 350 mm, and an inner diameter of 13.5 mm. To eliminate the reactive oscillatory motion of the tube, the latter was rigidly fixed in a massive brass holder. In part of the experiments, the membrane formation was realized through the "self-trapping" of a portion of MF by the ring magnet moved from the bottom of the tube to a height h_0 above the fluid level. The pressure drop in the isolated gas cavity was obtained by the displacement of the ring magnet along the tube with an accuracy of 0.01 mm.

Figures 4a–4c represent the results of measuring h_k (h_k is the distance between two sequential breakings of the membrane) as a function of the height h_0 of the air column isolated by the fluid for the MF-1, MF-2, and MF-3 colloids, respectively. Presumably, the scatter in the values of h_k could be reduced by taking additional measures for the vibration, acoustic, and thermal insulation of the MFM.

Table 3

	h_0, mm	$\overline{h_k}$, mm	P_c, kPa	Δm, mg	ε_{m1}, mV	k_g, N/m	k_p, N/m	h_d, mm	v_g, m/s	τ, ms
MF-1	161	0.24	0.078	0.042	6.6	135	145	0.12	17.5	2.40
	177	0.25	0.076	0.045	6.0	123	145	0.12	17.0	2.60
	194	0.26	0.075	0.045	6.0	112	145	0.11	16.5	2.70
	204	0.26	0.074	0.046	5.9	106	145	0.11	16.4	2.80
MF-2	90	0.06	0.027	0.010	4.8	242	166	0.04	27.2	0.36
	164	0.06	0.021	0.010	3.5	132	166	0.03	23.6	0.42
	181	0.05	0.016	0.009	3.0	120	166	0.02	22.8	0.40
MF-3	150	0.97	0.280	0.17	7.5	144	107	0.55	26.4	6.40
	161	0.96	0.260	0.17	7.3	135	107	0.54	25.7	6.50
	170	1.03	0.280	0.18	8.2	127	107	0.56	25.6	6.90
	181	1.05	0.270	0.19	6.8	120	107	0.56	25.1	7.30

By averaging over a great number of experimental data (no less than 50 for MF-1 and 150 for MF-2) in a narrow interval of magnetic head displacement from h_0 to $h_0 + \Delta h$ ($\Delta h \approx 1$ cm) for several different values of the air column height h_0, we obtained the average value of $\overline{h_k}$ and determined the law governing the increase in $\overline{h_k}$ with increasing h_0. The corresponding data are presented in Table 3.

The breakage of the MFM is not observed when the magnetic head moves in the reverse direction within the region of a certain width 2Γ. Thus, Γ is the cathetometer-measured distance between the initial equilibrium position and the first displaced equilibrium position. For MF-1, MF-2, and MF-3, we obtained: $\Gamma_1 = 1.77$, $\Gamma_2 = 3.04$, and $\Gamma_3 = 4.53$ mm.

Figure 5 shows the thermodynamic process as a function $P(z)$ under the assumption that the magnetic head moves slowly upwards along a tube of constant cross section.

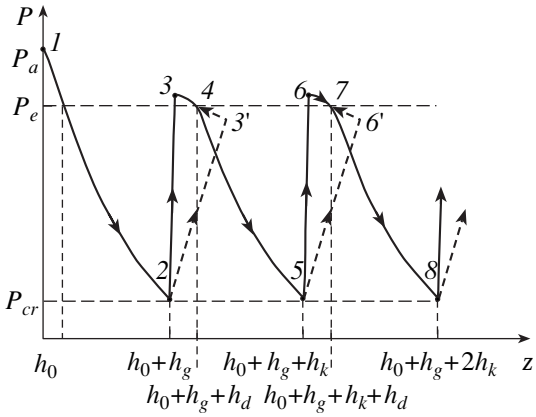

Fig. 5. Thermodynamical process in the gas cavity.

Regions *1–2*, *4–5*, and *7–8* correspond to the isothermal expansion of the gas cavity (by a hyperbola). The displacement h_k between two breakings of the MFM, which is measured by the cathetometer, consists of the increment of the gas cavity height h_g' and the displacement of the membrane h_d, which are related as $h_g'/h_d = k_p/k_g$. The calculated values of k_p, k_g, and h_d are presented in Table 3.

The critical pressure drop $P_{c1} = P_a - P_{cr}$, which causes the breakage of the membrane when it is displaced from the initial equilibrium position ($z = h_0$), is determined from the relation

$$P_{c1} = \frac{\gamma P_a \Gamma}{h_0 + \gamma\Gamma},$$

where $\gamma \equiv \dfrac{k_p}{k_p + k_g}$.

For the samples of MF-1, MF-2, and MF-3, the values of P_{c1} are as follows: $P_{c1} = 0.57$, 1.04, and 1.24 kPa, respectively.

In states *2*, *5*, and *8*, the continuity of the membrane fails and a hole appears in its central part. Under the effect of the pressure difference, air passes through this hole, which results in a jumplike pressure increase. At this stage of the process, the membrane is shifted towards the equilibrium position, i.e., in the direction of ∇H. This leads, on the one hand, to a certain increase in the gas cavity volume and, on the other hand, to conditions favorable for the closure of the cavity.

Within the period when the hole is present in the membrane (the lifetime of the hole τ), the state of the gas in the gas cavity may vary according to one of the two variants of the transition to the new state with an equilibrium pressure P_e, each of them leading to the excitation of free vibrations of the MFM.

The first variant (*2–3*, *5–6*, etc.) is characterized as follows: the displacement of the membrane is very small because of its inertness and because of the "rigid" connection of the process of self-recovery of continuity with the topography of the magnetic field, while the pressure increase in the cavity is caused by adiabatic air flow through the hole. One can also assume that, by the instant of full recovery of the membrane continuity, the gas flow velocity is maximum and the pressure on the walls of the hole is minimum.

In the second variant (*2–3'*, *5–6'*, etc.; the dashed lines in Fig. 5), within the time τ, the membrane passes through the equilibrium position and, by the instant of closure (points *3'* and *6'*), it stops and then moves toward the equilibrium position. This situation is theoretically possible if no rigid connection exists between the continuity of the membrane and the topography of magnetic field while the process of deceleration of the membrane and closure of its hole is mainly determined by the gas-dynamic effect of the increasing gas flow drag with increasing gas flow velocity.

Upon the termination of the damped vibrations and the establishment of thermodynamic equilibrium, the gas in the cavity proves to be in a state corresponding to points *4* and *7* in Fig. 5. As the magnet is raised further, the breakage of the membrane occurs at a smaller pressure increase in the gas cavity. The expression for calculating the critical pressure drop for the subsequent membrane breakings, $P_c \equiv P_e - P_{cr}$, has the form

$$P_c = P_a \frac{h_0 \gamma h_k}{(h_0 + \gamma\Gamma - \gamma h_k)(h_0 + \gamma\Gamma + h_k)}.$$

For $h_0 \gg \gamma(\Gamma - h_k)$ and $h_0 \gg \gamma\Gamma + h_k$, we have $P_k \cong P_a \gamma h_k / h_0$.

The results of calculating the parameter P_c with the use of the values of $\overline{h_k}$ are shown in Table 3.

These data confirm the physically predictable result that P_c is independent of the height h_0 of the isolated gas cavity. A slight decrease in P_c with height h_0 is observed for the MFM on the basis of MF-2. It is related to the decrease in the mass of the membrane because of the loss of its part remaining on the inner surface of the tube, which is confirmed by visual observations.

The MFM made of the MF-1 colloid, which is characterized by a lower concentration of magnetic phase and, hence, lower values of M_s and χ than those characterizing the MF-2 colloid, exhibits a much higher value of the critical pressure drop P_c (for the parameter P_{c1}, there is an inverse ratio). This seems to be unexpected at first glance. We believe that the physical origin of this result lies in the "more rigid" connection of the membrane continuity with the topography of magnetic field in the case of the membrane made of the MF with the higher value of χ. The recovery of its continuity occurs at a smaller displacement in the direction of ∇H, within a shorter time interval, and at a relatively small velocity of displacement.

In the framework of the assumed thermodynamic process (Fig. 5), the mass of the gas portion passing through the MFM can be calculated by the formula

$$\Delta m = \frac{\mu P_e \pi d^2 \overline{h_k}}{4RT},$$

where μ is the molar mass of the gas, R is the universal gas constant, and T is the absolute temperature. Taking the air parameters $\mu = 30$ kg/kmol, $P_e \cong 10^5$ Pa, $d = 13.6$ mm, and $T = 298$ K, we obtain

$$\Delta m = 1.76 \times 10^{-4} \overline{h_k}.$$

Table 3 presents the values of Δm for the MFMs under investigation. The minimum value $\Delta m_{\min} = 0.009$ mg belongs to the MFM on the basis of MF-2, and the maximum value $\Delta m_{\max} = 0.17$ mg characterizes the MFM on the basis of MF-3. Varying the amount of colloid introduced in the MFM, one can slightly extend the range of values of Δm. For example, a considerable decrease in Δm is obtained by reducing to a minimum the amount of MF-2 in the membrane. In this case, in the absence of special measures for thermal stabilization and vibration and sound insulation, the breakage–recovery process in the MFM becomes uncontrolled.

To estimate the velocity of the air flow through the hole, v_g, we use the relation between the pressure drop at the hole, ΔP_g, and the velocity at the point of maximum compression of the flow, v_g, [18]:

$$\Delta P_g = \frac{1}{2} \rho_g v_g^2 \xi \left(\frac{\sigma}{S}\right),$$

where σ is the area of the hole and ξ is the hydraulic drag coefficient, which depends on the area of the hole and on the Reynolds number. Using the results of [18], for the case of $\sigma \ll S$, we take $\xi = \xi_0 = 2.9$. Then, we can write

$$v_g = \sqrt{\frac{2\Delta P_g}{\rho_g \xi_0}}.$$

Taking into account that the pressure drop is

$$\Delta P_g = P_a - \frac{P_e - P_{cr}}{2} = \frac{\gamma P_a}{2}\left[\frac{\Gamma - h_k}{h_0 + \gamma(\Gamma - h_k)} + \frac{\Gamma}{h_0 + \gamma\Gamma}\right] \approx \frac{\gamma\Gamma}{h_0} P_a,$$

we obtain

$$v_g \approx \sqrt{\frac{2\gamma P_a \Gamma}{\rho_g \xi_0 h_0}}.$$

The lifetime of the hole, τ, can be estimated by the formula

$$\tau = \frac{\Delta m}{\rho_g \sigma v_g}.$$

In our experiments, we did not perform any direct measurements of σ, but, according to visual observations, the diameter of the hole was within 1–3 mm. To estimate τ from above, we use the minimum value of the diameter. In Table 3, we present the kinetic parameters, v_g and τ, for the MFMs under study.

Thus, the proposed approach allows one to experimentally estimate the following kinetic parameters of the MFM: the displacement of the membrane, h_d; the mass of the passed gas portion, m; the velocity of the air flow through the hole in the membrane, v_g; and the lifetime of the hole, τ.

The lifetime of the hole proved to be smaller than the period of membrane vibrations [10, 11], which suggests that the first variant of transition of the MFM to the equilibrium state (Fig. 5) is more probable. An argument in favor of this conclusion is the fact that the formula for the increase in the potential energy of the vibratory system at the instant of membrane breakage,

$$\Delta E_p = 0.5(k_p h_d^2 = k_g h_g'^2),$$

yields a value as small as 2×10^{-6} J (for the experiment with MF-1), whereas the kinetic energy calculated from the average velocity of the membrane displacement (according to the second variant) is

$$E_k \geq \frac{\pi \rho d^2 b h_d^2}{4\tau^2} \approx 2.6 \times 10^{-5} \text{ J}.$$

VIBRATION EXCITATION IN THE AIR CAVITY

If the membrane is at rest at the instant of its closure, the hydraulic impact of the air flow on the obstacle gives rise to a set of sound waves in the upper open part of the tube. These waves are described by the expression [19]

$$\delta P = -\frac{4u_0 \rho_g c}{\pi} \sum_{n=1}^{n=\infty} \frac{\cos k_n z}{2n-1} \sin \omega_n t,$$

where k_n is the wave number of the nth harmonic and u_0 is the velocity of the air flow in the tube at the instant of closure. For the fundamental harmonic (a quarter-wavelength tube), we have

$$\delta P_1 = -\frac{4}{\pi} u_0 \rho_g c \cos \frac{\pi z}{2L} \sin \frac{\pi c}{2L} t,$$

where L is the length of the open part of the tube. The pressure acting on the membrane ($z = 0$) is expressed as

$$\delta P_1 = -\frac{4}{\pi} u_0 \rho_g c \sin \frac{\pi c}{2L} t.$$

The relations between the parameters of the vibratory systems under consideration determine the character of membrane oscillations [20]. In particular, beats are possible with a frequency equal to the difference between the frequencies of initial oscillations, i.e., the frequency detuning:

$$\Omega = |\omega_1 - \omega_2|.$$

The above considerations do not contradict the results of our experiments with a tube 51 cm in length and 1.35 cm in diameter for the MF-2 colloid with b = 1.5 cm. The oscillograms exhibited clearly pronounced beats at a fundamental frequency of about 170 Hz when the magnetic head approached the bottom of the tube ($h_0 \approx$ 1–0.5 cm). The beats occurred twice: first, due to the excess over the frequency of acoustic vibrations of the air column, and, second, due to the excess over the frequency of membrane vibrations; between these two regions, the oscillogram has the form of "classical" damped oscillations. When the head moved in the backward direction, the beats also appeared, but, in this case, the frequency detuning occurred in the reverse order.

As was noted above, a membrane on the basis of MF-2 is characterized by small values of displacement and velocity of displacement at the instant of closure. In this respect, compared to other membranes, it fits better the Rayleigh conditions of vibration excitation in an air cavity [19].

REFERENCES

1. B. B. Cary and F. H. Fenlon, J. Acoust. Soc. Am. **45**, 1210 (1969).
2. V. M. Polunin, Akust. Zh. **24**, 100 (1978) [Sov. Phys. Acoust. **24**, 52 (1978)].
3. V. M. Polunin, Magn. Gidrodin., No. 1, 141 (1978).
4. A. R. Baev and P. P. Prokhorenko, Dokl. Akad. Nauk BSSR **22** (3), 242 (1978).
5. P. S. Dubbelday, IEEE Trans. Magn. **16** (2), 372 (1980).
6. V. G. Bashtovoĭ and M. S. Krakov, Magn. Gidrodin., No. 4, 3 (1979).
7. V. M. Polunin, Akust. Zh. **28**, 541 (1982) [Sov. Phys. Acoust. **28**, 318 (1982)].
8. B. R. Mace, R. W. Jones, and N. R. Harland, J. Acoust. Soc. Am. **109**, 1417 (2001).
9. G. V. Karpova, O. V. Lobova, E. B. Postnikov, *et al.*, in *Proceedings of 11th Session of Russian Acoustical Society, Moscow, 2001* (Moscow, 2001), Vol. 2, p. 203.
10. G. V. Karpova, O. V. Lobova, V. M. Polunin, *et al.*, Magnetohydrodynamics **38** (4), 385 (2002).
11. G. V. Karpova, O. V. Lobova, V. M. Paukov, *et al.*, Akust. Zh. **48**, 364 (2002) [Acoust. Phys. **48**, 305 (2002)].
12. R. E. Rosensweig, *Ferrohydrodynamics* (Univ. Press, Cambridge, 1985).
13. É. Ya. Blum, M. M. Maĭorov, and A. O. Tsebers, *Magnetic Fluids* (Zinatne, Riga, 1989) [in Russian].

14. V. G. Bashtovoĭ, B. M. Berkovskiĭ, and A. N. Vislovich, *Introduction to Thermomechanics of Magnetic Fluids* (IVTAN, Moscow, 1985) [in Russian].
15. M. D. Cowley and R. E. Rosensweig, J. Fluid Mech. **89** (4), 671 (1967).
16. A. O. Tsebers, in *Hydrodynamics and Thermal Physics of Magnetic Fluids* (Salaspils, 1980), pp. 127–134 [in Russian].
17. D. V. Orlov, Yu. O. Mikhalev, and N. K. Myshkin, in *Magnetic Fluids in Mechanical Engineering*, Ed. by D. V. Orlov and V. V. Podgorkov (Mashinostroenie, Moscow, 1993) [in Russian].
18. P. S. Landa and O. V. Rudenko, Akust. Zh. **35**, 855 (1989) [Sov. Phys. Acoust. **35**, 497 (1989)].
19. J. W. S. Rayleigh, *The Theory of Sound*, 2nd ed. (Macmillan, London, 1896; Gostekhizdat, Moscow, 1955).
20. O. V. Rudenko and A. V. Shanin, in *Physical and Nonlinear Acoustics: Proceedings of the Seminar of Professor Krasil'nikov's Scientific School, Moscow, 2002* (Moscow, 2002), p. 31.

Translated by E. Golyamina

Acoustical Physics, Vol. 51, No. 6, 2005, pp. 680–687. Translated from Akusticheskiĭ Zhurnal, Vol. 51, No. 6, 2005, pp. 787–794.

Heart Sounds as a Result of Acoustic Dipole Radiation of Heart Valves

S. G. Kasoev

General Physics Institute, Russian Academy of Sciences, ul. Vavilova 38, Moscow, 117942 Russia

e-mail: serg@kapella.gpi.ru

Received March 9, 2004

Abstract—Heart sounds are associated with impulses of force acting on heart valves at the moment they close under the action of blood-pressure difference. A unified model for all the valves represents this impulse as an acoustic dipole. The near pressure field of this dipole creates a distribution of the normal velocity on the breast surface with features typical of auscultation practice: a pronounced localization of heart sound audibility areas, an individual area for each of the valves, and a noncoincidence of these areas with the projections of the valves onto the breast surface. In the framework of the dipole theory, the optimum size of the stethoscope's bell is found and the spectrum of the heart sounds is estimated. The estimates are compared with the measured spectrum. © *2005 Pleiades Publishing, Inc.*

Auscultation of heart sounds with a stethoscope is the most widespread method of the original study of heart activity. Sounds produced by the heart are conventionally divided into heart sounds and cardiac murmur. The fundamental heart sounds are produced at the beginning of the main phases of cardiac contraction, systole (contraction of the myocardium and pushing of the blood out to arteries) and diastole (relaxation of the myocardium and filling of ventricles with blood) and are designated as the first and second heart sounds, respectively (Fig. 1).

The first sound is produced at the moment of closure of the heart valves between the atria and ventricles: the left (mitral) and right (tricuspid) ones. Normally, the duration of the first sound is about 150 ms and the pressure amplitude (in the stethoscope's bell) is about 3 Pa [1]. In spite of the seemingly clear connection between the first sound and the oscillations of the atrioventricular valves, the origin of the first sound is not yet considered to be ultimately ascertained. This uncertainty arose under the influence of such scholars of authority as Rushmer, who considered the first sound to result from oscillations of the muscular tunic as a whole in the process of deceleration of the blood flow from atria to ventricles [2], and Luisada, who considered that the first sound is produced by oscillations of the left half of the heart alone [3]. For example, Gitterman and Lewkowiz's physical model [4] considers the oscillations of the elastic spherical tunic as the main source of the first heart sound and describes the oscillations of the valves with allowance for the elastic properties of the constituting tissues as a possible complement.

There is a greater amount of certainty in understanding the second sound, which appears at the moment when the aortic and pulmonic valves between the ventricles and corresponding arteries close. It is universally recognized that the second sound is caused by the closure and further oscillations of the arterial valve [1]. The second sound lasts for 100–120 ms, its pressure amplitude (in the stethoscope's bell) is about 3 Pa, and it has a somewhat higher frequency spectrum than the first sound.

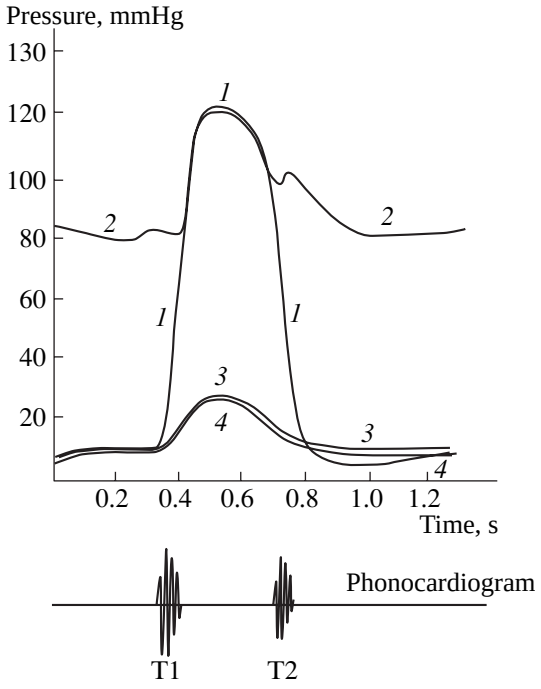

Fig. 1. Time dependences of pressure in the (*1*) left ventricle, (*2*) right ventricle, (*3*) aorta, and (*4*) pulmonary artery [9, 11]. The plot at the bottom is a phonocardiogram of the first T1 and second T2 sounds.

1063-7710/05/5106-0680$26.00 © 2005 Pleiades Publishing, Inc.

Thus, although possible origins of the heart sounds are named and indicated in the literature, the primary mechanism of heart sound generation, in particular, that for the first sound, is as yet undetermined. Previous efforts to physically describe the phenomenon of sound generation seem to be qualitative or preliminary in character, and the results are far from solving the problem [1, 2, 4–6].

This paper proposes an original acoustic approach to formulating a physical model of heart sound formation from the generation of sounds to their reception with a stethoscope or a microphone.

It is important to note that the following facts known from auscultation practice were still beyond the scope of discussion. First, the sounds can only be heard over very small areas of the breast (variations in the intensity are noticeable with shifting the stethoscope's bell by 1–2 cm [7]). Second, in the aforementioned limited areas, only one of the sound components is heard best: the mitral, aortic, pulmonary, or tricuspid component [8]. Third, these areas of best hearing do not coincide with the projections of the corresponding valves onto the breast surface [9].

As we will show below, the proposed theory gives a clear and unique explanation of these facts.

1. GENERALIZED THEORY OF HEART VALVES

Heart valves are soft flexible shells. Under the excess pressure of backward blood flow, they take a filled shape and block the flow; under the pressure of forward flow, they lose their shape and are pushed by the blood flow to the vessel or ventricular cavity walls. All four valves are different in size, structure, and shape.

Consider the heart valves in their closed state, when they can emit sound. Because the heart valves are soft shells, they acquire their shape under the action of the pressure difference: between the artery and ventricle in the diastole and between the ventricle and atrium in the systole; the shell tension is determined by this pressure difference alone. Acting upon the valve surfaces, this pressure difference creates an external nonstationary force, under the action of which the valves execute forced and free oscillations. If the time of variation of the external force is longer than the decay time of the free oscillations, the oscillation spectrum is determined by the spectrum of the external force. Otherwise, if the action takes a short time and the Q factor of the oscillating system is high, the oscillation spectrum is determined by the eigenfrequencies of this system.

Consequently, the fundamental question concerning the choice of the valve model is determined by the valve's Q factor. If the Q factor is high, the eigenmodes of valve oscillation (i.e., the valve structure and the elastic parameters of the constituent tissues) are significant [1, 4, 5]. If the Q factor of the valves as oscillating systems is low, their motion is determined by the external force and the time dependence of this force alone is important, whereas the valve structure is of minor significance. In the latter case, the source of acoustic radiation of all four valves is described in terms of a single simple model: a time-varying external force applied to the aperture closed by a given valve.

The Q factor of a valve as an oscillating system can be directly determined only from sufficient experimental data on the heart valve oscillations, which are presently unavailable. However, indirect evidence of the valve's Q factor being small is given by the fact that the duration of the heart sounds coincides with that of the external force. That is, the duration of the sound produced by the valve itself is apparently negligibly small compared to the duration of the external force's action.

As will be shown below, a variable external force applied to the valve tissues provides a satisfactory explanation for the main acoustic features of the heart sounds.

2. A MODEL VALVE AS AN ACOUSTIC DIPOLE

The acoustic model of heart valves is based on the following two assumptions. First, from the viewpoint of propagation of longitudinal waves, the human body in the first approximation is a continuous homogeneous waterlike medium, because the density and the elastic properties of its tissues are close to uniform and the wavelengths of the heart sounds far exceed any dimension of the body (and, all the more, the dimension of any of its organs). Second, the external force is directed along the flow (the valve axis) and is a product of the pressure gradient and the cross-sectional area of the valve aperture. As an acoustic source, a force applied to a homogeneous medium can be represented by a dipole with its axis coinciding with the force vector and the dipole force being equal to the magnitude of the external force [10]. The radiation produced by this dipole is equal to the scalar product of the force vector and the gradient of the monopole field:

$$p = \mathbf{F} \cdot \nabla\left(\frac{\exp(ikr)}{4\pi r}\right) = \mathbf{F} \cdot \mathbf{q}(r), \qquad (1)$$

where p is the sound pressure, $\mathbf{F}$ is the vector of the external force, k is the wave number, r is the length of the position vector of the observation point, and ∇ is the Hamiltonian.

Thus, as an acoustic source, any heart valve can be represented by a dipole located at a small (in terms of the wavelength of its own radiation) distance under the body–air boundary. Consequently, the problem of sound radiation by the heart valves is reduced to the determination of the normal velocity field at a perfectly soft boundary lying in the near field of a dipole.

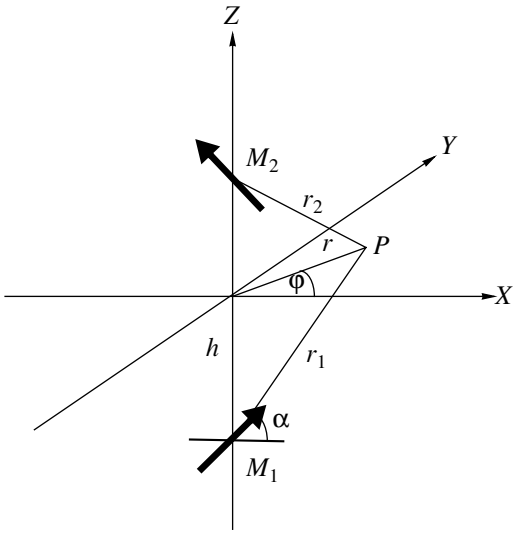

Fig. 2. Spatial position of the real dipole M_1 and its image M_2 with respect to the boundary *XY*; *P* is the observation point.

3. THE NEAR FIELD OF A DIPOLE IN THE VICINITY OF A PERFECTLY SOFT PLANE BOUNDARY

In the first approximation, the body–air boundary can be considered to be plane. The field near this boundary can be represented as a superposition of the fields produced by two dipoles: the given dipole and its mirror image with an oppositely directed axis [10], because the images of the monopoles forming the dipole change their sign at a soft boundary. Consider a rectangular coordinate system (Fig. 2) such that its *XY* plane coincides with the boundary and the dipole axis lies in the *XZ* plane and makes an angle α with the *X* axis.

The normal velocity of the boundary can be found using the Euler equation, from the pressure fields of the real dipole and its mirror image:

$$V_n = \frac{\partial}{\partial z}(\mathbf{M}_1 \cdot \mathbf{q}(r_1) + \mathbf{M}_2 \cdot \mathbf{q}(r_2)), \quad z = 0, \qquad (2)$$

where $\mathbf{M}_1$ and $\mathbf{M}_2$ are the dipole moments related to the dipole force through the general expression $\mathbf{M} = 1/\rho\int \mathbf{F}\,dt$, r_1 and r_2 are the distances between dipole centers and the observation point (Fig. 2), and ρ is the density of the medium.

Let the depth of the dipole under the boundary be *h*, the distance from the dipole projection onto the boundary to the observation point *P* along the boundary be *r*, and the angle between the projection of the dipole axis onto the boundary and direction to the observation point be φ. Then, after some algebra (see the appendix), the following general expression for the normal velocity of the boundary can be obtained:

$$V_n = \frac{M}{2\pi}\exp(ikR)\frac{h^2}{R^5}$$
$$\times\left\{(3 - 3ikR - k^2R^2)(\xi\cos\alpha\cos\varphi + \sin\alpha)\right. \qquad (3)$$
$$\left. + \frac{R^2}{h^2}\sin\alpha(ikR - 1)\right\},$$

where $R = \sqrt{r^2 + h^2}$, and $\xi = r/h$.

In the near-field region $kR \ll 1$, expression (3) can be considerably simplified:

$$V_n \approx \frac{M}{2\pi h^3(\sqrt{1 + \xi^2})^5} \qquad (4)$$
$$\times(3\xi\cos\alpha\cos\varphi + 2\sin\alpha - \xi^2\sin\alpha).$$

Formula (4) is the basis for the subsequent estimates. The distributions of the normal velocity amplitude V_n over the boundary for different angles α between the dipole axis and the boundary are plotted in Fig. 3.

Consider a dipole that is normal to the boundary (curve *4* in Fig. 3). In this case, the amplitude of the normal velocity at the boundary is independent of the angle and gradually decreases as the inverse cube of the distance from the projection of the dipole onto the boundary to the observation point:

$$V_n \approx \frac{M}{2\pi h^3}\frac{2 - \xi^2}{(\sqrt{1 + \xi^2})^5}. \qquad (5)$$

This case does not agree with the actual valve positions, in which the valve axes are almost parallel to the breast surface, as shown in Fig. 4 borrowed from [9].

Consider the case of a dipole parallel to the boundary (Fig. 3, curve *1*). The distribution of the normal velocity at the boundary is described by a cosine function:

$$V_n \approx \frac{3M}{2\pi h^3}\frac{\xi}{(\sqrt{1 + \xi^2})^5}\cos\varphi. \qquad (6)$$

In addition, the normal velocity is zero above the dipole and maximum at two symmetric points positioned at equal distances $r \approx h/2$ from the projection of the dipole onto the boundary along the direction parallel to the dipole axis. The normal velocity amplitude decreases with distance from the maxima as the fourth power of distance from the dipole projection onto the boundary; i.e., the maxima are sharp.

Thus, formula (6) gives a complete qualitative explanation for, first, the pronounced localization of the places on the breast where the heart sounds are distinctly audible, second, the displacement of these

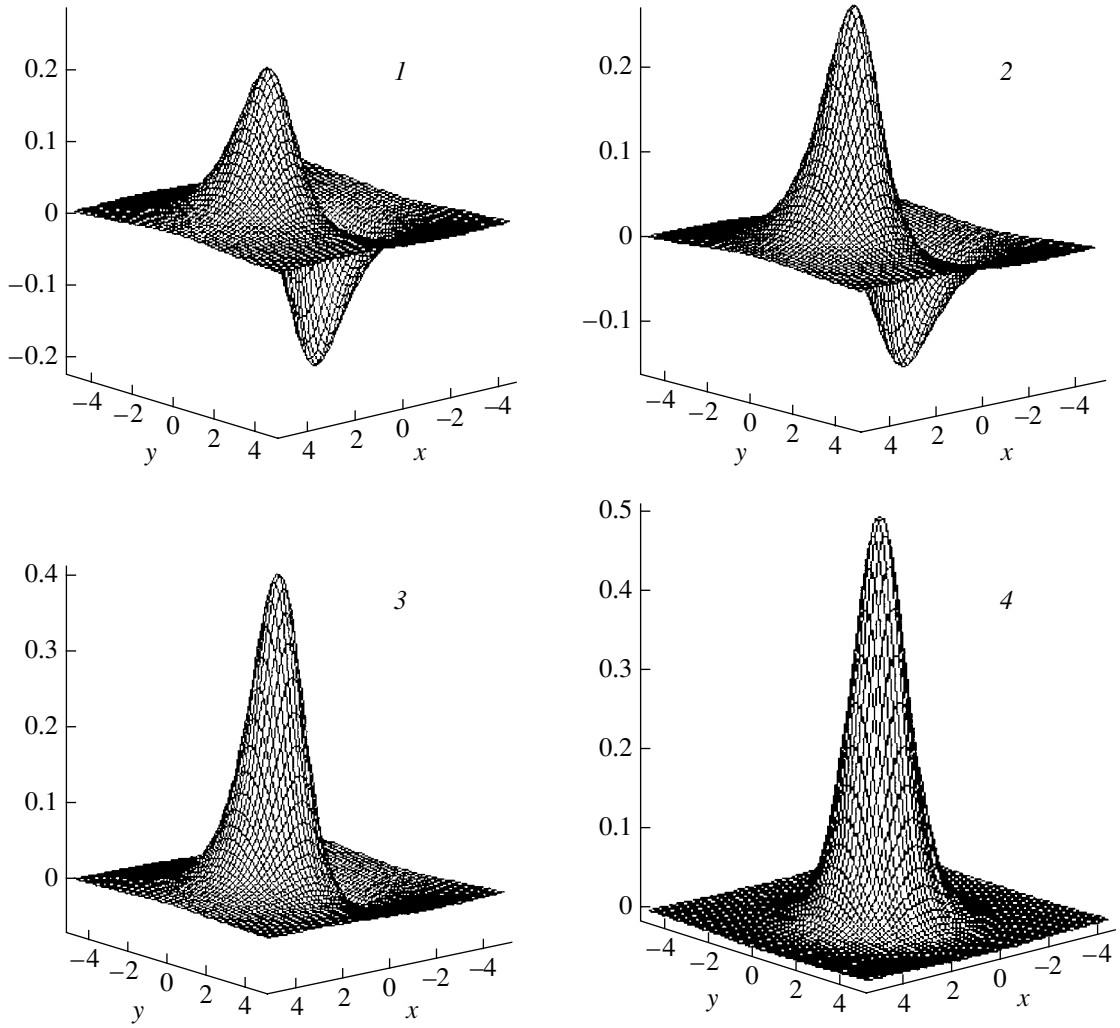

Fig. 3. Amplitude distribution of the normal velocity of the boundary for the dipole inclined at α = (*1*) 0°, (*2*) 30°, (*3*) 45°, and (*4*) 90°.

places from projections of the valves onto the breast surface, and, third, the difference in the positions of these places for different valves. The best audibility areas are schematically shown in Fig. 4 together with the heart valves. As can be seen from this figure, in accordance with Eq. (6), the best audibility areas lie on the valve axes and are displaced along these axes by certain distances, which are different for different valves, because the depths of the valves and their inclinations relative to the breast's surface are different.

4. THE PHYSICAL MODEL OF THE STETHOSCOPE

To correctly compare the results of the model valve description, we must allow for the transfer properties of the heart's sound receivers, because Eqs. (4) and (6) refer to a point velocity receiver located on the breast's surface. Actually, the receiver of heart sounds may be a stethoscope or an air or contact microphone. All of these receivers contact the breast over a limited contact area.

Let us begin with the contact microphone, which is actually a detector of normal acceleration, or an accelerometer.

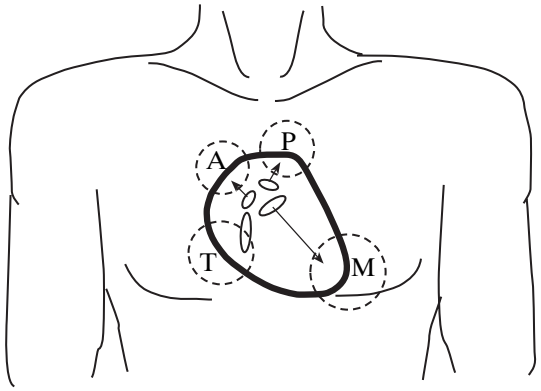

Fig. 4. Schematic representation of the heart valve positions and the best-audibility areas for heart sounds of the (A) aortic, (P) pulmonary, (M) mitral, and (T) tricuspid valves [9].

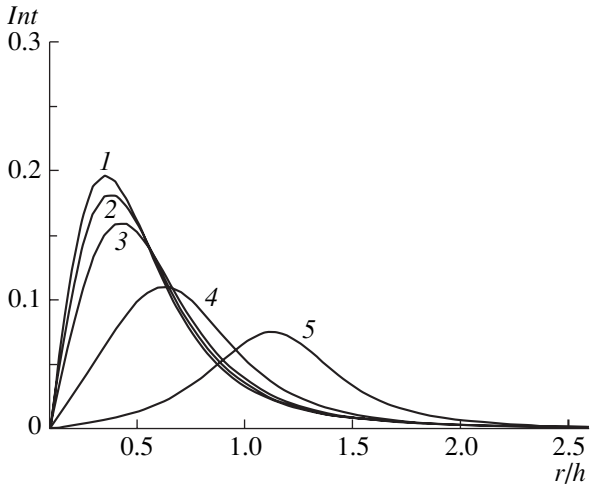

Fig. 5. Ratio of the surface integral in Eq. (9) to the area of the stethoscope's bell versus the distance along the dipole axis from the bell center to the projection of the valve onto the boundary (the distance is normalized by the depth of the valve) for different ratios of the bell radius to the valve depth: (*1*) 0.1, (*2*) 0.3, (*3*) 0.5, (*4*) 1.0, and (*5*) 2.0.

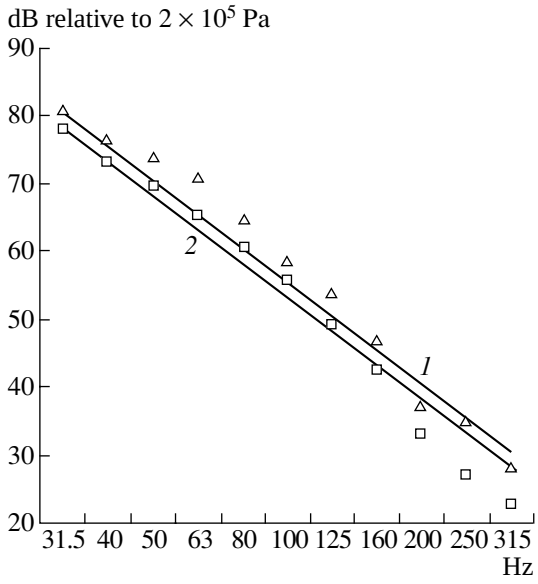

Fig. 6. Heart sound spectra measured in one-third-octave bands for the (triangles) first and (squares) second sounds and the corresponding calculations for the (*1*) mitral and (*2*) aortic valves.

Only a small part of the data on heart sounds reported in the literature refer to measurements with this kind of receiver, which hampers its comparison with the theory. However, this receiver offers certain advantages worthy of note. In fact, as follows from Eq. (6), the normal acceleration is proportional to the dipole force or to the driving force:

$$a \approx \frac{3\mathbf{F}}{2\pi h^3}\frac{\xi}{(\sqrt{1+\xi^2})^5}\cos\varphi. \tag{7}$$

This means that the output signal of a perfect contact microphone directly gives the driving force spectrum.

An air microphone, such as a stethoscope, has a bell-shaped cavity, which, being applied to the breast surface, forms a closed air-filled cavity. Normal displacements of the breast surface cause pressure oscillations in this cavity, which are detected by the microphone or by ear in the case of the stethoscope's bell. Since these receivers are identical, we consider a stethoscope with given parameters: the cross-sectional area of the bell opening and the total internal volume, which includes the internal volume of the bell and the guiding pipes. Assuming that the air compression in the internal space of the stethoscope under the action of a small displacement of the breast surface is adiabatic, in the first approximation we obtain the following expression for the sound pressure in the stethoscope:

$$p_s = \gamma\frac{P_a S}{U}\int_{-\infty}^{t} V_n dt, \tag{8}$$

where γ is the adiabatic index, U is the internal volume of the stethoscope, S is the area of the bell opening, and P_a is the atmospheric pressure.

Substituting expression (6) for the normal velocity into the time integral in Eq. (8), we obtain the sound pressure in the stethoscope as a function of the external force that acts upon the valve:

$$\begin{aligned} p_s &= \frac{3\gamma}{2\pi}\frac{P_a}{Uh^3}\int_{-\infty}^{t} M(t)dt\iint_0^S \frac{\xi(x,y)\cos\varphi\,dxdy}{(\sqrt{1+\xi^2})^5} \\ &= \mathrm{Int}\frac{3\gamma}{2\pi}\frac{P_a S}{Uh^3}\int_{-\infty}^{t} M(t)dt. \end{aligned} \tag{9}$$

The ratio Int of the surface integral in Eq. (9) to the area of the stethoscope's bell is plotted in Fig. 5 versus the distance along the dipole axis from the bell center to the projection of the valve onto the boundary (the distance is normalized by the depth of the valve) for five values of the ratio of the bell opening radius to the valve depth. As can be seen from this figure, the greater the bell radius, the more the pronounced the audibility maximum of each valve is shifted along its axis and displaced from the projection of the valve, because, when the relative bell radius is greater than 0.3, the effect of the symmetric antiphase region (Fig. 3) disappears only when the shift is equal to the bell radius. This theoretical result is in good qualitative agreement with the aforementioned experimental facts known from auscultation practice [7–9].

As can be seen from Fig. 5, at a given valve depth and a given internal volume of the stethoscope, the sig-

nal reaches its maximum at a particular radius of the bell opening (no more than 0.3 of the valve depth), and the auscultation signal decreases with a further increase in the bell size. This behavior is explained by the pronounced localization of the normal surface displacements produced by the valve oscillations and by their dipole character. Therefore, to achieve the maximum heart sound loudness, real stethoscope designs use an empirical bell diameter of 2–3 cm, which, according to the above physical model, corresponds to realistic valve depths of 5–9 cm. As is known, fetoscopes use greater aperture diameters of 5–6 cm, because a fetus's heart valves are at a longer distance from the surface of a mother's body.

5. THE MODEL SPECTRUM OF THE DIPOLE FORCE

Let us show that the dipole model of a valve predicts not only the true spatial characteristics of acoustic fields produced by the valves with localization of auscultation areas observed in practice but also the true levels and spectra of radiation.

The analysis of classical plots [9, 11] of simultaneous pressure variation in auricles, ventricles, and arteries (Fig. 1) shows that, first, these pressures increase fast in the left part of the heart and the pressure differences are substantial, and, second, all variations are continuous; i.e., the curves are everywhere smooth in the mathematical sense. For clarity, we consider the process of closure of the mitral valve. It can be concluded from Fig. 1 that the first sound begins when the pressure in the left ventricle starts rising, and it ends when the aortic valve opens. It is therefore natural to model the pressure behavior in time by the following exponential function:

$$p = P_0 \exp(\beta t), \quad t \le 0, \quad p = 0, \quad t > 0, \qquad (10)$$

where P_0 is the blood pressure amplitude for each of the valves and β is the characteristic frequency of pressure variation.

The characteristic time intervals, reciprocal of β, are equal to the interval of the isometric contraction (0.02–0.04 s) for the mitral and tricuspid valves and to the interval of sharp pressure drop in the ventricle (0.02–0.04 s) for the aortic and pulmonary valves.

The spectrum of the variable pressure difference that acts upon the valves and is described by Eq. (10) can be calculated through the Fourier transform:

$$G_p(\omega) = P_0 \frac{1}{\beta + i\omega}, \qquad (11)$$

where $\omega = 2\pi f$ is the circular frequency.

The magnitude of spectrum (11) decreases in inverse proportion to frequency; that is, above the frequency $\omega = \beta$, the spectrum of the driving force falls off at a rate of 6 dB/octave. Such a spectrum slope must also characterize the response of a perfect accelerometer to the heart sounds.

For the air microphone and the stethoscope, the signal spectrum is steeper: its magnitude varies in inverse proportion to the cube of frequency, or at a rate of 18 dB/octave. Indeed, the double integral with respect to time in Eq. (9) gives rise to an additional factor, the squared frequency, in the denominator. Precisely this kind of frequency spectrum was reported for the heart sounds in the literature [7, 8] and was measured by the author of this paper (experimental points in Fig. 6).

Thus, the heart sound spectrum is in good agreement with that predicted by the model.

Let us use Eqs. (9)–(11) to calculate the sound pressure created by the heart valves in the stethoscope's bell. We use the initial data on the pressure exerted on the valves and the data on the valve cross sections borrowed from the literature [2, 9, 11] and summarized in the table. The right-hand column of the table contains the data on the amplitudes of the heart sounds (data for the tricuspid valve are absent) from [1].

Table

Heart valve	Pressure on the valve (kPa)	Valve cross section (cm^2)	Dipole force (N)	Sound pressure (Pa)
Aortic	12	0.9	1	2.9–3.3
Mitral	9	1.6	1.4	2.6–2.8
Pulmonary	2	0.8	0.16	1.5–1.8
Tricuspid	3	2.9	0.87	–

The solid lines in Fig. 6 show the three-octave spectra of the first (mitral valve, upper curve) and second (aortic valve, lower curve) sounds recorded with a stethoscope, as calculated from the dipole model. Figure 6 also shows the experimental points obtained by the author for the mitral (triangles) and aortic (squares) valves. As shown in Fig. 6, the calculated sound pressure in the stethoscope's bell is close to the experimental values. According to the table, the proportions between the pressure amplitudes of sound radiation from different valves are primarily determined by the differences in the driving forces. Therefore, the radiation of the tricuspid and, especially, pulmonary valves contributes little to the first and second sounds, which is well known from the auscultation practice.

CONCLUSIONS

The dipole model of heart sound generation described in this paper is in good agreement with experimental data on the spatial, spectral, and amplitude characteristics of the acoustic field of the heart. The following conclusions can be drawn from the analysis presented above:

(i) The heart sounds are generated by the oscillations of closed heart valves under the action of the time-varying pressure difference upon the valve, whereas the free oscillations of healthy valves contribute little to the heart sound generation because of the low Q factor of the valves. The physical model of heart sound generation is the same for all the four valves: the external force (the product of the aperture cross section of the closed valve by the pressure gradient) applied to a homogeneous waterlike medium, which, as an acoustic source, can be represented by a dipole with its axis being parallel to the force.

(ii) The dipole model of the heart sound generation is the only model that explains the localization of audibility areas for each valve and associates the positions of these areas relative to the valves with the orientation of the valve (dipole) axis and with the valve (dipole) distance from the breast surface.

(iii) The dipole model of heart sound generation provides a good agreement between theoretical and experimental data on the heart sound levels and spectra, which allows one to uniquely relate the heart sound parameters to the time behavior of the pressure gradient at the valve and to the cross-sectional area of the valve's aperture.

(iv) The dipole model can be used to calculate the heart sound pressure perceived through the stethoscope as a function of stethoscope parameters (the internal volume and the cross-sectional area of the bell) and spatial parameters (the position of the bell on the breast relative to the valve and the valve's orientation and depth under the brest surface).

(v) For a given valve depth, the optimum size of the stethoscope's bell is determined. The empirically established difference in the stethoscope and fetoscope bell diameters is shown to be dictated by the difference in the depths of the auscultated valves.

This paper contains only the main experimental results, which corroborate the dipole theory of the heart valve radiation. A further application of the theory to explaining particular facts of auscultation and phonocardiographic examinations requires a dedicated paper.

APPENDIX

Let us introduce the notations

$$r_1 = \sqrt{(x^2 + y^2 + h^2 + 2hz + z^2)},$$

$$r_2 = \sqrt{(x^2 + y^2 + h^2 - 2hz + z^2)}.$$

Then, formula (2) takes the form

$$V_n = \frac{1}{4\pi}\frac{\partial}{\partial z}\bigg|_{z=0}\Bigg(M\cos\alpha\frac{\partial}{\partial x}\frac{\exp(ikr_1)}{r_1} - M\cos\alpha\frac{\partial}{\partial x}\frac{\exp(ikr_2)}{r_2} + M\sin\alpha\frac{\partial}{\partial z}\frac{\exp(ikr_1)}{r_1} + M\sin\alpha\frac{\partial}{\partial z}\frac{\exp(ikr_2)}{r_2}\Bigg) = \frac{M}{4\pi}\frac{\partial}{\partial z}\bigg|_{z=0}$$

$$\times(W_1\cos\alpha - W_2\cos\alpha + W_3\sin\alpha + W_4\sin\alpha),$$

where $W_1 = \dfrac{(ikr_1 - 1)x}{2r_1^3}\exp(ikr_1)$, $W_2 = \dfrac{(ikr_2 - 1)x}{2r_2^3}\times$ $\exp(ikr_2)$, $W_3 = \dfrac{(ikr_1 - 1)(h+z)}{r_1^3}\exp(ikr_1)$, and $W_4 = \dfrac{(ikr_{21} - 1)(-h+z)}{r_2^3}\exp(ikr_2)$.

The differentiation of expressions for W_j with respect to z yields

$$\frac{\partial}{\partial z}W_1 = \frac{\exp(ikr_1)}{r_1^5}x(h+z)(3 - 3ikr_1 - k^2r_1^2),$$

$$\frac{\partial}{\partial z}W_2 = \frac{\exp(ikr_2)}{r_2^5}x(-h+z)(3 - 3ikr_2 - k^2r_2^2),$$

$$\frac{\partial}{\partial z}W_3 = \frac{\exp(ikr_1)}{r_1^5}$$

$$\times((h+z)^2(3 - 3ikr_1 - k^2r_1^2) + 4ikr_1^3 - r_1^2),$$

$$\frac{\partial}{\partial z}W_4 = \frac{\exp(ikr_2)}{r_2^5}$$

$$\times((-h+z)^2(3 - 3ikr_2 - k^2r_2^2) + 4ikr_2^3 - r_2^2).$$

The substitution of these expressions into formula (2) at $z = 0$ gives formula (3) for the normal velocity of the boundary:

$$V_n = \frac{M}{2\pi}\exp(ikR)\frac{h^2}{R^5}$$

$$\times\Bigg\{(3 - 3ikR - k^2R^2)(\xi\cos\alpha\cos\varphi + \sin\alpha) + \frac{R^2}{h^2}\sin\alpha(ikR - 1)\Bigg\},$$

where $R = \sqrt{r^2 + h^2}$ and $\xi = r/h$.

REFERENCES

1. P. D. Stein, *A Physical and Physiological Basis for the Interpretation of Cardiac Auscltation* (Futur, New York, 1981).
2. R. F. Rashmer, *Dynamics of the Cardiovascular System* (Meditsina, Moscow, 1981) [in Russian].
3. A. A. Luisada, *The Sound of Normal Heart* (Warren H. Green, St. Lois, 1972).

4. M. Gitterman and M. Lewkowiz, *Towards Diagnostic Interpretation of Phonocardiology*, Vol. 6 of *Advances in Cardiovascular Physics*, Ed. by D. N. Ghista and L. Mihoczy (Karger, Basel, 1989).
5. V. P. Glotov, R. A. Vadov, and P. A. Kolobaeva, Akust. Zh. **50**, 712 (2004) [Acoust. Phys. **50**, 614 (2004)].
6. F. F. Tetenev, *Physical Methods of Investigation in the Clinic of Internal Diseases* (Tomskiĭ Gos. Univ., Tomsk, 2001) [in Russian].
7. K. Holldack and D. Wolf, *Atlas und Kurzgefasstes Lehrbuch der Phonokardiographie und Verwandter Untersuchungsmethoden* (Thieme, Stutgart, 1956; Meditsina, Moscow, 1964).
8. A. A. Luisada and F. Portaluppi, *The Heart Sounds. New Facts and the Clinical Implications* (Praeger, New York, 1982).
9. E. Van Vollenhoven, N. Suzumura, D. N. Ghista, *et al.*, *Phonocardiography: Analyses of Instrumentation, and Vibration of Heart Structure to Determine Their Constitutive Properties*, Vol. 5 of *Advances in Cardiovascular Physics*, Ed. by D. N. Ghista *et al.* (Karger, Basel, 1983).
10. M. A. Isakovich, *General Acoustics* (Nauka, Moscow, 1973) [in Russian].
11. C. G. Caro, T. J. Pedley, R. C. Schroter, and W. A. Seed, *The Mechanics of the Circulation* (Oxford Univ. Press, London, 1978; Mir, Moscow, 1981).

Translated by A. Khzmalyan

Acoustical Physics, Vol. 51, No. 6, 2005, pp. 688–694. Translated from Akusticheskiĭ Zhurnal, Vol. 51, No. 6, 2005, pp. 795–801.

Deformation of a Homeotropic Nematic Liquid Crystal Layer at Oblique Incidence of an Ultrasonic Wave

E. N. Kozhevnikov

Samara State University, ul. Akademika Pavlova 1, Samara, 443011 Russia

e-mail: kozhev@ssu.samara.ru

Received April 12, 2004

Abstract—The change of orientation of a nematic liquid crystal layer and the associated optical effect under an obliquely incident ultrasonic wave are considered. The theoretical analysis is performed under the assumption that the acoustic flows caused by convective stress in the boundary layers are responsible for the orientation effects in the nematic liquid crystal layer. An analytical description of the acoustooptic effect is developed for low ultrasonic frequencies, and for high frequencies, a numerical calculation is performed. It is demonstrated that the theoretical results agree both qualitatively and quantitatively with experimental data. The hypothesis that the effect produced by ultrasound on nematic liquid crystals is caused by the relatively strong elastic anisotropy of these crystals is analyzed. © *2005 Pleiades Publishing, Inc.*

The sensitivity of the orientational structure of liquid crystal layers to ultrasonic action determines the prospects for the use of these objects in the visualization of sound fields and, in particular, in the development of acoustic flaw detectors on their basis. These prospects stimulate the long-term interest in studying the effect of sound upon the structure of liquid crystals from both experimental and theoretical points of view (for example, see [1, 2]). The optical effects in liquid crystals are caused by the reorientation of crystal molecules in the sound field. In theoretical publications, various mechanisms of the effect of sound on a nematic liquid crystal have been suggested: parametric instability [3]; threshold action caused by the second-order viscosities [4]; anisotropy of sound absorption, which, according to Prigozhin's principle, must lead to the alignment of long nematic molecules in the direction of acoustic wave propagation [5]; and acoustic flows, in which viscous moments rotate the molecules of the crystal [6–8]. I support the point of view that the reorientation of molecules occurs in the acoustic flows that arise due to the convective stress in the boundary layers, whose thickness is on the order of the viscous wavelength. This point of view is confirmed by the qualitative agreement of theoretical calculations, which were performed for different geometries of sound action, with experimental data and also by the agreement within order of magnitude between the theoretical and experimental values of ultrasonic intensity at which the effect is observed (see reviews [1, 2]). At the same time, the absence of detailed information on the parameters of the liquid crystal cells used in the experiments often prevents the numerical comparison of the theory with experimental data and the verification of the assumption concerning the responsibility of acoustic flows for crystal reorientation. This situation leads to the appearance of new hypotheses explaining the sound effect on the nematic liquid crystal structure.

A recent paper [9] gives the most complete information on the parameters of the liquid crystal cell, which provides the opportunity to conduct a numerical (not on the order of magnitude) comparison of the theoretical pattern with experimental results. This paper considers the translucence of a nematic liquid crystal layer immersed in water in the case of the oblique incidence of an ultrasonic wave upon it. The paper gives the thicknesses of the nematic liquid crystal layers and the boundary plates and also their densities and the velocities of longitudinal waves in the plates. The authors conventionally evaluate the degree of molecule reorientation according to the change of the optical properties (saturation) of the layer. They suggest a new theoretical explanation for the observed phenomenon on the basis of the anisotropy of the elastic properties of the nematic.

Let us again consider the acoustooptic effect in a layer of a normally oriented nematic liquid crystal at the oblique incidence of an ultrasonic wave upon it and perform a numerical comparison of theoretical results with the experimental data given in [9]. The theoretical explanation of the effect that was suggested in [9] is discussed in the final part of the paper.

The analysis of the effect is carried out as follows. Under the assumption that the motion of the boundaries of the nematic liquid crystal layer are preset, we determine the wave field in the layer. Retaining the terms quadratic in the velocities in the hydrodynamic equations, we determine the velocities of the stationary flow, and, according to the rotation angle of molecules in the flow, we determine the optical effect. The motion of the boundaries of a nematic liquid crystal layer in the case

1063-7710/05/5106-0688$26.00

of the incidence of an ultrasonic wave on the cell is determined at high frequencies by numerical calculation using a computer and at low frequencies, analytically.

We restrict our calculations to the sound frequencies ω at which the viscous wavelength in the layer is much smaller than the layer thickness h:

$$\lambda_\eta \ll h. \tag{1}$$

Describing the longitudinal waves, we ignore the viscous stress compared to the elastic one ($\eta\omega \ll \rho c^2$). In the calculation of the wave field in the layer, the viscous effects are taken into account only by the presence of viscous waves propagating from the layer boundaries along the normal. The dynamic viscosity in these waves is equal to $\eta = (\alpha_4 + \alpha_5 - \alpha_2\gamma_2/\gamma_1)/2$, where α_k are the Leslie viscosity coefficients and $\gamma_1 = \alpha_3 - \alpha_2$, $\gamma_2 = \alpha_3 + \alpha_2$ [10, 11].

Let us direct the z axis along the normal to the layer and choose the origin of coordinates at the lower boundary of the layer. Let the x axis be directed along the layer in the plane of the ultrasonic wave incidence. In this case, the acoustic oscillations of particles, the stationary flow, and the molecule rotation occur in the (xz) plane.

Let us preset the oscillation velocities of the boundaries of the nematic liquid crystal layer, v_x and v_z, in the form

$$v_\kappa\big|_{z=\beta} = v_0 v_{\kappa\beta}\exp(-i\omega t + ik_x x). \tag{2}$$

Here, v_0 is the amplitude of particle velocity in the wave incident upon the liquid crystal cell, the index $\kappa = x, z$ determines the velocity component, the index $\beta = 0$, h indicates the layer boundary, $k_x = \omega/c\sin\theta$ is the x component of the wave number in the ultrasonic wave incident upon the layer, c is the sound velocity in the liquid, and θ is the angle of incidence. The coefficients $v_{\kappa\beta}$ are complex:

$$v_{\kappa\beta} = v_{\kappa\beta 1} + iv_{\kappa\beta 2}.$$

The solution to the wave equation of the liquid motion in the layer

$$\rho\frac{\partial^2\mathbf{v}}{\partial t^2} + \eta\,\mathrm{curlcurl}\frac{\partial\mathbf{v}}{\partial t} - c^2\Delta\mathbf{v} = 0$$

with the boundary conditions given by Eq. (2) has the form

$$v_x = v_0\mathrm{Re}\left\{\frac{\exp\{i(k_x x - \omega t)\}}{\sin kh}\right.$$

$$\times\{i\tan\theta[v_{z0}\cos(k(h-z)) - v_{zh}\cos kh]$$

$$+ e^{(i-1)qz}[v_{x0}\sin kh - i\tan\theta(v_{z0}\cos kh - v_{zh})]$$

$$\left.+ e^{(i-1)q(h-z)}[v_{xh}\sin kh - i\tan\theta(v_{z0} - v_{zh}\cos kh)]\}\right\}, \tag{3}$$

$$v_z = v_0\mathrm{Re}\left\{\frac{\exp\{i(k_x x - \omega t)\}}{\sin kh}\right.$$

$$\left.\times[v_{zh}\sin kz + v_{z0}\sin(k(h-z))]\right\},$$

where $k = \omega/c\cos\theta$ and $q = \sqrt{\rho\omega/\eta}$ is the wave number in the viscous wave propagating along the axis of the nematic crystal.

The convective stress arising in the wave field in the nematic liquid crystal layer gives rise to stationary flows, and the viscous moments in the flows cause the rotation of the crystal molecules through the angle φ, both the liquid motion and the molecule rotation occurring in the plane of sound incidence. We will discuss the sound effect upon the nematic liquid crystal layer according to the translucence of the layer positioned between crossed polarizers. The degree of the effect will be determined by the optical transparency M, which is maximal at the orientation of crossed polarizers at 45° with respect to the rotation plane of nematic liquid crystal molecules. In this case, this quantity acquires the form [12]

$$M = \sin^2\left\{\frac{1}{2}\Delta n k_0\int_0^h \sin^2\varphi\,dz\right\}. \tag{4}$$

Here, Δn is the optical anisotropy of the nematic crystal and k_0 is the wave number of light in the ordinary wave. The intensities of the sound effect at which the rotation angle of molecules remains small, $\varphi \ll 1$, are of practical significance. For small values of φ, we assume that, in Eq. (4), we have $\sin\varphi \approx \varphi$ and linearize the equations of hydrodynamics for the nematic liquid crystal with respect to φ.

The determination of the transparency of the layer is reduced to the determination of the rotation angle of molecules φ. Taking into account the fact that the time-average quantities in the case under consideration do not depend on x, we obtain (following [10, 11]) the equations for the velocity of the stationary flow, v_x, and the angle φ in the form

$$\eta_2\frac{d^3 v_{2x}}{dz^3} = \rho\frac{d^2}{dz^2}\overline{(v_x v_z)} + (*),$$

$$K_{33}\frac{d^2\varphi}{dz^2} \approx \alpha_2\frac{dv_{2x}}{dz} + (*). \tag{5}$$

Here $\eta_2 = (\alpha_4 + \alpha_5 - \alpha_2)/2$; the overbar means averaging over time; $(*)$ are terms of the form $\alpha(d^2/dz^2)\overline{(\theta\nabla v)}$ and $\alpha(d^2/dz^2)\overline{(v\nabla\theta)}$, which provide a small contribution to the solution of the equation; and K_{33} is Frank's elastic constant.

Solving system of equations (5) with zero boundary conditions for the angle $\theta_2|_{z=0,h} = 0$ and velocity $v_{2x}|_{z=0,h} = 0$ under the condition that the flow is closed, $\int_0^h v_{2x}dz = 0$, we determine φ as

$$\varphi_2 = \frac{\rho v_0^2 \alpha_2 h}{2q\eta_2 K_{33}} \times\left\{Q\frac{z}{h} + (S-2Q)\left(\frac{z}{h}\right)^2 + (Q-S)\left(\frac{z}{h}\right)^3\right\}, \quad (6)$$

where Q and S are parameters independent of v_0:

$$Q = v_{x02}v_{z01} - v_{x01}v_{z02} - v_{x01}v_{z01} - v_{x02}v_{z02} + \frac{\tan\theta}{\sin kh}(v_{zh1}v_{z01} + v_{zh2}v_{z02} + v_{zh2}v_{z01} - v_{zh1}v_{z02}) - \tan\theta\cot kh(v_{z01}^2 + v_{z02}^2),$$

$$S = v_{xh2}v_{zh2} + v_{xh1}v_{zh1} + v_{xh1}v_{zh2} - v_{xh2}v_{zh1} + \frac{\tan\theta}{\sin kh}(v_{zh1}v_{z01} + v_{zh2}v_{z02} + v_{zh1}v_{z02} - v_{zh2}v_{z01}) - \tan\theta\cot kh(v_{zh1}^2 + v_{zh2}^2).$$

Substituting the angle φ from Eq. (6) into Eq. (4) for the transparency and integrating φ^2 over z, we obtain

$$M = \sin^2[B\Lambda J^2], \quad (7)$$

where

$$B = \frac{\Delta n k_0 \alpha_2^2 h^3}{32c^2 K_{33}^2 q^2 \eta_2^2},$$

$J = \rho v_0^2 c$ is the sound intensity in the wave incident upon the layer; and Λ is the dimensionless parameter determined by the characteristics of the cell, the angle θ, and the frequency ω through the coefficients Q and S:

$$\Lambda = \frac{1}{105}Q^2 + \frac{1}{70}QS + \frac{1}{105}S^2.$$

Thus, the optical properties of the liquid crystal cell are determined by the acoustic field formed in the liquid crystal layer at the incidence of the ultrasonic wave on the cell. To calculate this field, we consider a typical liquid crystal cell in which the layer of a normally oriented nematic crystal is placed between two transparent substrates with thicknesses H_1 and H_2. We assume that the cell is completely immersed in water and a sound wave is incident upon it at an angle θ from the side of the first plate (H_1). We assume that the boundary plates are made of identical materials with the density ρ_g and the velocities of longitudinal and transverse waves c_l and c_t. We also assume the values of the density ρ and the sound velocity c in water and in the liquid crystal to be identical.

To determine the coefficients $v_{\alpha\beta}$ and, hence, the optical effect, we consider the wave problem on the transmission of a sound wave through the liquid–solid plate–liquid–solid plate–liquid multilayer system. Let us introduce (for the wave transmission through the liquid crystal cell) the scalar potentials of velocity in the sound waves propagating in the liquid and in the longitudinal waves propagating in the boundary plates:

$$\Phi_k = \Phi_0\exp(ik_x x - i\omega t)\begin{cases} e^{ikz} + Re^{-ikz} \\ a_1e^{ik_l z} + b_1e^{-ik_l z} \\ d_1e^{ikz} + d_2e^{-ikz} \\ a_2e^{ik_l z} + b_2e^{-ik_l z} \\ De^{-ikz} \end{cases}$$

and the vector potentials of velocity in the shear waves propagating in the boundary plates:

$$A_{1,2} = \Phi_0(r_{1,2}e^{ik_t z} + s_{1,2}e^{-ik_t z})\exp(ik_x x - i\omega t).$$

Here, Φ_0 is the amplitude of the scalar potential in the wave incident upon the layer; R and D are the coefficients of reflection and transmission of the sound wave; $k_l = \sqrt{k_{l0}^2 - k_x^2}$ and $k_t = \sqrt{k_{t0}^2 - k_x^2}$ are the z projections of wave numbers of the longitudinal and shear waves in the boundary plates, respectively; $k_{t0} = \omega/c_t$; and $k_{l0} = \omega/c_l$.

The coefficients involved in the potentials are determined from the boundary conditions, which include the equality of the normal velocities v_z of the liquid and the solid plate and the equality of the normal stresses in the solid and the pressure in the liquid. Ignoring the viscous stresses in the liquid in comparison with the shear ones in the solid plates (their ratio is equal to $\rho\omega/\rho_g c_t^2 \ll 1$), we represent the equations for the coefficients in the form

$$a_1e^{-ik_lH_1} - b_1e^{ik_lH_1} = \frac{k(1-R)}{k_l\kappa},$$

$$a_1e^{-ik_lH_1} + b_1e^{ik_lH_1} + \xi_t(r_1e^{-ik_lH_1} - s_1e^{ik_lH_1}) = \frac{\rho(1+R)}{\rho_g\kappa},$$

$$r_1e^{-ik_tH_1} + s_1e^{ik_tH_1} - \xi_l(a_1e^{-ik_lH_1} - b_1e^{ik_lH_1}) = 0,$$

$$a_1 - b_1 = \frac{k}{k_l\kappa}(d_1 - d_2),$$

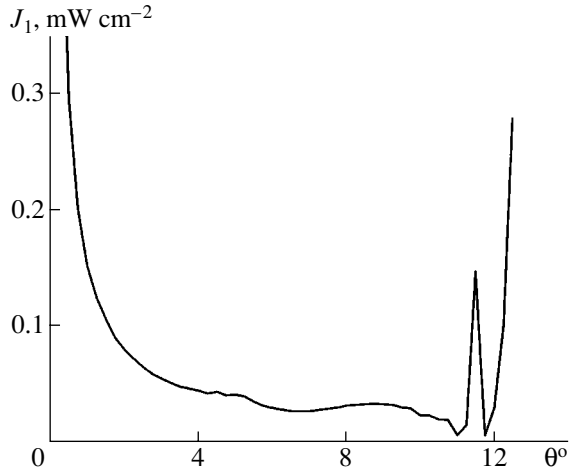

Fig. 1. Ultrasonic intensity J_1 versus the angle of incidence θ.

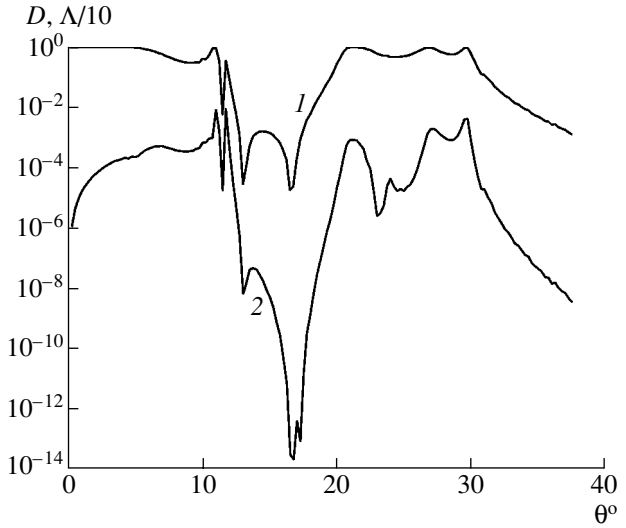

Fig. 2. (*1*) Acoustic and (*2*) optical transparencies of the layer versus the angle of sound incidence.

$$
\begin{aligned}
a_1 + b_1 + \xi_t(r_1 - s_1) &= \frac{\rho}{\rho_g \kappa}(d_1 + d_2),\\
r_1 + s_1 - \xi_l(a_1 - b_1) &= 0,\\
a_2 - b_2 &= \frac{k}{k_l \kappa}(d_1 e^{ikh} - d_2 e^{-ikh}),\\
a_2 + b_2 + \xi_t(r_2 - s_2) &= \frac{\rho}{\rho_g \kappa}(d_1 e^{ikh} - d_2 e^{-ikh}),\\
r_2 + s_2 - \xi_l(a_2 - b_2) &= 0,\\
a_2 e^{ik_l H_2} - b_2 e^{-ik_l H_2} &= \frac{k}{k_l \kappa} D,\\
a_2 e^{ik_l H_2} + b_2 e^{-ik_l H_2} + \xi_t(r_2 e^{ik_t H_2} - s_2 e^{-ik_t H_2}) &= \frac{\rho}{\rho_g \kappa} D,\\
r_2 e^{ik_t H_2} + s_2 e^{-ik_t H_2} - \xi_l(a_2 e^{ik_l H_2} - b_2 e^{-ik_l H_2}) &= 0.
\end{aligned}
\tag{8}
$$

Here, we have introduced the notations $\xi_l = 2k_x k_l/(k_{t0} - 2k_x^2)$, $\xi_t = 2k_x k_t/(k_{t0} - 2k_x^2)$, and $\kappa = k_{t0}^2/(k_{t0}^2 - 2k_x^2)$.

Let us analyze the results of calculation. At low sound intensities, the dependence of the transparency of the nematic liquid crystal layer on the intensity of the sound wave is determined by the relation $M \sim J^4 \sim v_0^8$. However, in a real experiment, a nematic liquid crystal layer has a finite "background" transparency and the comparison of calculation with experimental data at small values of J is difficult. Therefore, we compare theoretical and experimental results in the sound intensity J_1 at which the optical transparency reaches its first maximum:

$$J_1 = \left(\frac{\pi}{2B\Lambda}\right)^{1/2}.$$

The analytical description of the acoustic wave field in a liquid crystal layer is cumbersome in the general case and does not lead to physically illustrative results. Therefore, in the case of arbitrary cell parameters, frequencies, and angles of sound incidence, the wave field in the liquid crystal layer is determined by the numerical solution to system of equations (8). Thus, the coefficients $v_{\alpha\beta}$, the optical transparency of the layer M, and the intensity J_1 are determined.

In the numerical calculation, we take the sound frequency f and the cell parameters to be equal to the corresponding values given in [9]: $f = 3.3 \times 10^6$ Hz, $H_1 = H_2 = 0.09$ cm, $h = 0.015$ cm, $c = 1.5 \times 10^5$ cm s^{-1}, $c_l = 6 \times 10^5$ cm s^{-1}, $\rho = 1$ g cm^{-3}, and $\rho_g = 2.5$ g cm^{-3}. We assume that the velocity of shear waves in the boundary plates, which is not given by the authors of [9], to be equal to $c_t = 3.6 \times 10^5$ cm s^{-1}, i.e., to the velocity in crown glass [13]. We take the viscosity coefficients for the liquid crystal and Frank's elastic constant to identical to those for a typical MBBA liquid crystal [10]: $\alpha_4 = 0.83$ P, $\alpha_2 = -0.78$ P, $\alpha_5 = 0.46$ P, $\alpha_6 = -0.34$ P, $\alpha_3 = -0.01$ P, and $K_{33} = 0.7 \times 10^{-6}$ dyn.

The results of calculation are given in Figs. 1 and 2. The intensity J_1 as a function of the angle of sound incidence is plotted in Fig. 1. At angles $\theta < 11°$, the intensity J_1 and, therefore, the layer transparency are characterized by a smooth dependence on θ. The singularity in the curve $J_1 = J_1(\theta)$ at $\theta \approx 11°$ corresponds to the total reflection of longitudinal waves at the solid–liquid boundary. As the angle of incidence grows further, the smooth dependence of J_1 on θ vanishes. In the case of the incidence angle $\theta = 8°$, the theoretical value of the intensity J_1 is equal to 31 mW cm^{-2}. This value almost coincides with the experimental value of $J_1 \approx 30$ mW cm^{-2} given in [9] for the same conditions for one of the liquid

crystal mixtures (5SV) and is somewhat smaller than the value of J_1 = 40 mW cm^{-2} indicated in the same paper for another mixture.

In the case of small angles of sound wave incidence, when the relations $k_l H_\alpha \theta^2/2 \ll 1$ and $kh\theta^2/2 \ll 1$ are valid, the acoustic field in the system is determined from the solution of the problem on the transmission of a sound wave incident normally upon a nematic liquid crystal cell, and the coefficients $v_{z\beta}$ do not depend on the angle θ. The boundary velocities $v_{x\beta}$ are determined from the condition of zero shear stress in the boundary plates. For the coefficients $v_{x\beta}$, we have $v_{x\beta} \sim k_x/k \sim \theta$. In this case, $Q, S \sim \theta$, and $\Lambda \sim \theta^2$, while the dependence of the layer transparency on the incidence angle of the sound wave is determined by the relation $M = \sin^2(\mathrm{const} J^2\theta^2)$. The dependence $J_1 \sim \theta^{-1}$ for small angles of incidence of the sound wave and the given above parameters at $\theta < 4°$ is also shown in Fig. 1.

The curves in Fig. 2 demonstrate the correlation of acoustic and optical transparencies for a nematic liquid crystal cell in a wide range of angles of sound incidence. It is necessary to note that this correlation was indicated earlier in an experiment [14] and in the theoretical analysis of the effect [8] for different parameters of the nematic liquid crystal layer.

The correlation $|D|$ and Λ in a wide range of angles of incidence and also the numerical coincidence of the values of J_1 in the theory and the experiment confirm the major prerequisite lying at the basis of the above theoretical calculation: namely, the effect of sound on a nematic liquid crystal layer in the case of an oblique incidence is caused by the acoustic flows caused by convective stresses in the boundary layers whose thickness is on the order of the viscous wavelength.

Let us separately consider the saturation of a nematic liquid crystal cell at low sound frequencies and small angles of sound incidence by assuming that the inequalities

$$k_{l0}H_\alpha < k_{t0}H_\alpha < 1, \quad kh < 1, \qquad \theta \ll 1, \quad k_x \approx k\theta \ll k_{t0} \tag{9}$$

are valid and by limiting the frequencies from below by Eq. (1), as before.

In this case, the solution to the system of Eqs. (8) has a simple analytical form, which yields the following expressions for the coefficients $v_{\alpha\beta}$:

$$v_{x0} \approx -\frac{(\nu^2-2)\rho}{\nu^2\rho_g}\theta,$$

$$v_{xh} \approx -\frac{[1-\nu-\nu^2+m(1+\nu))]\rho}{\nu^2\rho_g}\theta e^{ikh},$$

$$v_{z0} \approx \left[1 + i\left(\frac{m^2+1}{2m}k_l H_1 + \frac{m^2-1}{2m}k_l H_2 e^{2ikh}\right)\right],$$

$$v_{zh} \approx \left[1 + i\left(\frac{m^2+1}{2m}k_l H_1 + \frac{m^2-1}{2m}k_l H_2\right)\right]e^{2ikh},$$

where $\nu = c_l/c_t$ and $m = \rho_g k/\rho k_l$ is the ratio of the impedances of longitudinal waves in the plate and the liquid; in the case of normal incidence of ultrasound, m is equal to the ratio of acoustic resistances: $m = \rho_g c_l/\rho c$.

The parameter Λ at low frequencies is determined by the expression

$$\Lambda \approx \frac{1}{210}\frac{\rho^2}{\rho_g^2}\frac{[2+\nu^2(\rho_g/\rho-1)]^2}{\nu^4} \times \left[1 - \frac{m^2+1}{2m}\frac{\nu^2-2}{2+\nu^2(\rho_g/\rho-1)}k_l H_1 + \frac{m^2-1}{2m}\frac{2+\nu^2(2\rho_g/\rho-1)}{2+\nu^2(\rho_g/\rho-1)}k_l H_2\right]\theta^2, \tag{10}$$

and, at identical thicknesses of the boundary plates $H_1 = H_2 = H$, it takes on the form

$$\Lambda \approx \frac{1}{210}\frac{\rho^2}{\rho_g^2}\frac{[\nu^2(1-\rho_g/\rho)-2]^2}{\nu^4} \times \left\{1 + k_l H\frac{m^2[(\rho_g/\rho-1)\nu^2+2] - \rho_g/\rho\nu^2}{m[(\rho_g/\rho-1)\nu^2+2]}\right\}\theta^2. \tag{11}$$

For small values of the layer thickness, when $k_l H_{1,2} < [\nu^2(\rho_g/\rho-1)+2]/[m(\nu^2-2)]$, we obtain

$$M = \sin^2\left[J^2\frac{B}{210}\frac{\rho^2}{\rho_g^2}\frac{[\nu^2(1-\rho_g/\rho)-2]^2}{\nu^4}\right].$$

In this case, the longitudinal (mass) impedance of the boundaries vanishes and the nematic liquid crystal cell becomes almost transparent for the sound waves; the appearance of flows and, hence, the layer saturation can be explained only by the difference in the shear impedances of the boundary plates and the liquid and does not depend on the values of H_1 and H_2. If the thickness of the plates increases, the mass impedance of the layer boundaries grows linearly in H_1 and H_2, which leads to the variation of the velocities v_z in the liquid crystal layer and a linear dependence of the parameter Λ on H_1 and H_2. For real values of the parameters $\nu \approx 2$, $m \approx 10$, and $\rho_g/\rho \approx 2.5$, the fractional coefficients multiplying $k_l H_1$ and $k_l H_2$ in Eq. (10) are positive. Thus, the increase of the thickness H_1 reduces (and the increase of the second plate thickness H_2 enhances) the optical transparency of the nematic liquid crystal layer. In the case of equal values of $H_1 = H_2 = H$, as H increases, the value of Λ (Eq. (11)) and the optical transparency grow.

The thickness of the nematic liquid crystal layer is absent in the expression for Λ at low frequencies.

In the range of frequencies satisfying the inequality

$$1 > k_l H_1 > \frac{\nu^2(\rho_g/\rho - 1) + 2}{m(\nu^2 - 2)},$$

we have $\Lambda \sim k_l \sim \omega$. In this case, the layer transparency does not depend on the sound frequency, and its dependence on the thickness of the nematic liquid crystal layer, sound intensity, and incidence angle is determined by the relation $M = \sin^2(\mathrm{const} h^3 J^2 \theta^2)$, while the constant at different thicknesses of the boundary plates is proportional to H.

The dependence of the optical effect on the sound frequency and the thickness of the boundary plates in the frequency range determined by Eqs. (1) and (9) is illustrated in Fig. 3, where the values of the product $J_1\theta$ are plotted as functions of frequency for the layer parameters indicated above and the thicknesses of the boundary plates $H_1 = H_2 = 0.05$, 0.1, and 0.5 cm.

In conclusion, let us consider the theory of the acousto-optic effect at oblique incidence of ultrasound, which was proposed in [9]. The authors treat the effect as a consequence of the elastic anisotropy of the nematic liquid crystal by introducing it through additional terms in the free energy of the nematic:

$$\delta g = \{u_1 n_i n_j \partial_i \partial_j \rho + u_2[(\mathbf{n}\nabla)\rho]^2\}. \qquad (12)$$

Here, u_k are certain coefficients.

If the sound wave propagates in the crystal, the averaging of the second term in Eq. (12) over the period of oscillations contributes to the energy in proportion to the intensity of the sound wave. This contribution depends on the angle between the directions of wave propagation and molecule orientation β:

$$\delta g' = \frac{1}{2} u_2 (\Delta\rho)^2 (\mathbf{kn})^2 = \frac{1}{2}\frac{u_2 \rho J}{c^3}\cos^2\beta.$$

Variation of the energy $\delta g'$ over the angle β leads to the moments $\delta\Gamma$ rotating the crystal molecules,

$$\delta\Gamma = \frac{u_2 \rho k^2 J \sin(2\beta)}{c^3},$$

and, as a consequence, to the layer saturation with the transparency M_e in the form

$$M_e = \sin^2\{L J^2 \sin^2(2\beta)\}, \qquad (13)$$

where

$$L = \frac{u_2^2 \Delta n \rho^2 k_0 k^4 h^5}{240 c^6 K_{33}^2}.$$

In [9], only a qualitative agreement of the theory predicting the dependence $M_e = \sin^2[\mathrm{const} J^2]$ with experimental data is noted.

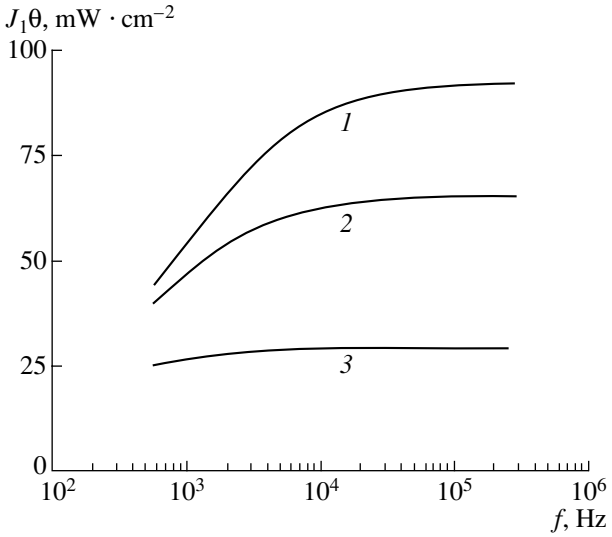

Fig. 3. Ultrasonic intensity J_1 versus the frequency of the sound wave f for H = (*1*) 0.05, (*2*) 0.1, and (*3*) 0.5 cm.

Let us analyze the provisions lying at the basis of the theoretical construction [9]. Variation of the liquid density is connected with the displacement of liquid particles $\mathbf{U}$: $\Delta\rho = -\rho\,\mathrm{div}\,\mathbf{U}$. Let us represent the additional term containing u_2 in the energy given by Eq. (12) in terms of the displacement:

$$\delta g' = u_2 \rho^2 [n_\alpha \partial_\alpha \partial_i U_i]^2. \qquad (14)$$

The elastic energy given by Eq. (14) leads to additional mass forces and changes the form of the equation for elastic waves in the liquid crystal:

$$\partial_t^2 U_i - c^2 \partial_i \partial_k U_k - 2u_2 \rho n_\alpha n_\beta \partial_\alpha \partial_\beta \partial_i \partial_k U_k = 0.$$

The propagation velocity of such waves depends on the angle β between the propagation direction of waves and the crystal orientation. A simple calculation leads to the following expression for the velocity of sound waves $c(\beta)$:

$$c(\beta) = c\frac{\omega\tau\cos\beta}{\sqrt{2(\sqrt{1 + \omega^2\tau^2\cos^2\beta} - 1)}}. \qquad (15)$$

Here, $\tau = \sqrt{8u_2\rho/c^4}$ is a certain characteristic time arising in the calculation and c is the sound velocity obtained without taking into account the anisotropy of elasticity.

Equation (15) predicts the dispersion of velocity with a value depending on the propagation direction of the sound wave. If the wave propagates perpendicularly to the crystal axis ($\beta = \pi/2$), the dispersion is absent: $c(\pi/2) = c$. In the case of the propagation along the crystal axis ($\beta = 0$), the wave must be subjected to a considerable dispersion: at low frequencies, when $\omega\tau \ll 1$, we have $c(0) = c$, and at high frequencies, when $\omega\tau \gg 1$, we

have $c(0) \approx c\sqrt{\omega\tau/2}$. Let us determine the time τ by preliminarily finding the coefficient u_2. The intensity of the sound wave in the nematic liquid crystal layer J is determined by the intensity J_0 of the wave incident on the cell and by the acoustic transparency of the layer $|D|$: $J = J_0|D|^2$. Equating J_1 involved in Eq. (13),

$$J_1 = \sqrt{\frac{\pi}{2L|D|^2\sin^2(2\beta)}},$$

to the experimental value $J_1 = 30$ mW cm^{-2} given in [9] for the angle of ultrasound incidence equal to 8° and using the value $|D| = 0.36$ determined by numerical calculation, we obtain $u_2 = 6.25 \times 10^5$ cm^7 g^{-1} s^{-2}. The time τ in this case is equal to $\tau = 3.3 \times 10^{-8}$ s. At the frequencies $f > 10$ MHz, the velocity of sound propagating along the crystal axis must increase with frequency according to the law $c(0) \sim \omega^{1/2}$; the anisotropy of sound velocity must also increase analogously. At the frequency $f = 7$ MHz, the sound velocity $c(0)$ and the relative anisotropy of velocity determined according to Eq. (15) must be equal to $c(0) \approx 2c$ and $\Delta c/c = c(0)/c - 1 = 1$. In reality, the sound velocity in a crystal exhibits only a small dispersion and a small anisotropy. The relative dispersion jump of velocity $Dc = c(\omega = \infty)/c(\omega = 0) - 1$ in a nematic crystal, which is maximal near the point of orientation melting, does not exceed the value $Dc = 0.15$, and the relative anisotropy does not exceed the value $\Delta c/c = 10^{-2}$ [1, 2]. Thus, the assumption that the relatively strong anisotropy of elasticity in a nematic liquid crystal may be responsible for orientation effects under the action of sound on a nematic crystal, which was put forward in [9], does not agree with reality and is inconsistent.

REFERENCES

1. A. P. Kapustin and O. A. Kapustina, *Acoustics of Liquid Crystals* (Nauka, Moscow, 1986) [in Russian].
2. D. Demus, in *Physical Properties of Liquid Crystals* (Wiley, Berlin, 2000), pp. 447–466.
3. I. A. Chaban, Akust. Zh. **25**, 124 (1979) [Sov. Phys. Acoust. **25**, 67 (1979)].
4. W. Helfrich, Phys. Rev. Lett. **29** (24), 1583 (1972).
5. J.-L. Dion, J. Appl. Phys. **50** (4), 2965 (1979).
6. K. Miyano and Y. R. Shen, Appl. Phys. Lett. **28** (9), 473 (1976).
7. S. Candau, A. Ferre, A. Petters, *et al.*, Mol. Cryst. Liq. Cryst. **61**, 7 (1980).
8. E. I. Zhukovskaya, E. N. Kozhevnikov, and V. M. Podol'skiĭ, Zh. Éksp. Teor. Fiz. **83** (1), 207 (1982) [Sov. Phys. JETP **56** (1), 113 (1982)].
9. J. V. Selinger, M. S. Spector, V. A. Greanya, *et al.*, Phys. Rev. **E66**, 051708 (2002).
10. M. J. Stephen and J. P. Straley, Rev. Mod. Phys. **46** (4), 617 (1974).
11. P. de Gennes, *The Physics of Liquid Crystals* (Clarendon, Oxford, 1974; Mir, Moscow, 1977).
12. L. D. Landau and E. M. Lifshitz, *Course of Theoretical Physics*, Vol. 8: *Electrodynamics of Continuous Media* (Nauka, Moscow, 1982; Pergamon, New York, 1984).
13. *Small Encyclopedia: Ultrasound*, Ed. by I. P. Golyamina (Sov. Éntsiklopediya, Moscow, 1979) [in Russian].
14. J. N. Perbet and M. Hareng, Rev. Phys. Appl. **14**, 569 (1979).

Translated by M. Lyamshev

Acoustical Physics, Vol. 51, No. 6, 2005, pp. 695–704. Translated from Akusticheskiĭ Zhurnal, Vol. 51, No. 6, 2005, pp. 802–812.

Measurement of Acoustic Power in Studying Cavitation Processes

I. M. Margulis and M. A. Margulis

Andreev Acoustics Institute, Russian Academy of Sciences, ul. Shvernika 4, Moscow, 117036 Russia

e-mail: margulis@akin.ru

Received February 9, 2004

Abstract—A comparative calorimetric method for measuring the acoustic power generated by a sound source under cavitation conditions and the power absorbed by a liquid with bubbles is developed. The conditions under which the whole of the generated power is absorbed by the liquid with bubbles are determined experimentally. An instrument for power calibration of sound sources operating under cavitation conditions is designed. The instrument is found to provide a high measurement accuracy (3% or better). The requirements on the dimensions of the vessel and on the volume of the liquid in which the sound source operates are formulated to make the power generated under cavitation conditions independent of these parameters. For the first time, it is shown experimentally (by the example of the reaction of nitric oxide formation under the action of sound) that, if these conditions are satisfied and the sound intensity exceeds the threshold intensity, the rate of a number of sonochemical reactions is proportional to the sound intensity in the range from 1.7 to at least 47 W/cm^2. It is shown that the dependence of the rate of cavitation processes on the sound intensity with a maximum at 8.6 W/cm^2 and a sharp decrease in the rate with a further intensity increase is determined by the fact that the measured quantity was the electric power at the transducer rather than the acoustic one. © *2005 Pleiades Publishing, Inc.*

The measurement of acoustic power generated by a source of ultrasound and the power absorbed in a volume of liquid under cavitation conditions [1, 2] is an urgent and important problem of acoustics, which was not solved until recently, although cavitation had been studied for many decades [1, 3, 4]. The existing methods of measuring the radiated and absorbed power under cavitation conditions (they are considered below) can be used, at best, only for qualitative estimates [1, 2]. However, the measurement of acoustic power under cavitation is of great scientific and applied interest for studying the efficiency of sonochemical processes, sonoluminescence [1, 4–6], erosion, emulsification, and ultrasonic cleaning, for the calibration of ultrasonic equipment, in research, in studying and scaling cavitation processes, etc. Recent investigations show that cavitation may arise in cells *in vivo*. Therefore, in developing and applying the therapeutic and diagnostic equipment in medicine [1, 7, 8], it is necessary to take into account the influence of cavitation and perform the dosimetry of acoustic energy absorbed by a living body. Because of the uncertainty in the radiated and absorbed acoustic powers under cavitation conditions, the experimental results obtained by different researchers are incomparable. The lack of a reliable method for measuring the acoustic power makes it impossible to solve many scientific problems, for instance, to determine the dependence of the rate of a sonochemical reaction on the frequency of ultrasonic waves or to optimize various production processes accompanied by fully developed cavitation.

It is fairly easy to measure the electric energy delivered to a transducer, but this quantity cannot characterize the energy of the cavitation process. According to current concepts, in chemical and physicochemical processes accompanying cavitation, only the absorbed acoustic energy can be active [1, 9]. This condition is consistent with the Grotthuss–Draper law [10] for photochemical reactions, according to which only the absorbed part of luminous energy can be chemically active. Therefore, the rates of cavitation processes should be related to the absorbed acoustic power. The radiated power is the main energy characteristic of ultrasonic instruments used in their calibration [9]. However, in the majority of experimental works, even in the recent ones, the difference between these powers, as far as we know, was not discussed.

In this paper, a new method (a comparative calorimetric method) is presented, which makes it possible to measure quantitatively the acoustic power radiated by a sound source under cavitation conditions, as well as the power absorbed by a liquid with bubbles. In addition, the paper reports the experimental results obtained with this method.

At present, the following main methods of determining or estimating the acoustic power radiated by a source of ultrasound under cavitation are known [1, 2]:

(i) The determination of the radiated power by measuring the vibration amplitude of a waveguide using a

1063-7710/05/5106-0695$26.00 © 2005 Pleiades Publishing, Inc.

vibration meter [1, 2, 11]. Under cavitation conditions, this method leads to erroneous results [1, 9], because the appearance of cavitation bubbles sharply reduces the acoustic impedance ($\rho_L c_L$), where ρ_L is the density of the medium and c_L is the sound speed. This decrease in ($\rho_L c_L$) results from an abrupt decrease in the sound speed in a cavitating liquid: c_L can even become much smaller than the sound speed in gas [12–14]. The reason for the decrease in c_L is that the liquid–bubble system has a compressibility nearly equal to the compressibility of gas and a density almost equal to that of a liquid [12]. The sound speed in cavitating water can decrease by two orders of magnitude compared to the sound speed c_0 in pure water (1500 m/s) and reach a value of 15–50 m/s or less [13, 14]. Under cavitation, the acoustic impedance of the medium changes considerably and randomly in space and time; there is also a substantial dispersion of the sound speed [14]. In addition, following this method, one usually measures only the amplitude of the waveguide face [1, 2, 11], and the measurement of the vibration amplitude in other directions presents a cumbersome and difficult problem. We can mention, however, that the solution of this problem makes no sense, because the measurement error, due to the variation of c_L over a wide range, is large.

(ii) Calculation of acoustic intensity by the well-known formula [2, 11]

$$I = k(f)U^2(\rho_L c_L), \tag{1}$$

where the conversion coefficient $k(f)$ depends on the type of the transducer and is taken to be constant for the whole line of transducers, U is the voltage at the transducer, and f is the frequency of ultrasonic waves. The coefficient k is undefinable (because the value of the acoustic power is unknown) and, in addition, it can change in a wide range for every specific transducer and depending on the conditions of the experiment [1].

(iii) The use of a piezoelectric or magnetostrictive sensor or a thermoelectric method [2, 11] based on the sound absorption and the heating of a calibrated "sticky drop" gives relative parameters at one point [1].

(iv) Optical measurements (the interferometric, or semishadow, method based on the measurement of the index of refraction) [2, 11] require a particular configuration of acoustic parameters and the form of the vessel for performing the measurements, and, in addition, they are inapplicable under the conditions of fully developed cavitation. Under cavitation, the distribution of acoustic parameters in the liquid is random and, obviously, these methods are inapplicable for measuring the ultrasonic wave power in solving conventional scientific and technological problems [1].

(v) The measurement of radiation pressure [2, 11] (for example, using a balance) after the appearance of cavitation in the liquid leads to erroneous results [1, 2]. Such results are caused by the numerous reflections of ultrasonic waves and by the additional pressure produced by shock waves and jet streams created by cavitation bubbles. The measurement of radiation pressure requires the absence of cavitation, liquid degassing, mounting of acoustic screens, employing focused radiators, etc. [2, 11]. The measurement of ultrasonic power in small volumes of liquid is quite a difficult task. Moreover, the necessity of producing an acoustic field of a certain configuration restricts the applicability of this method, because the distribution of acoustic parameters in the liquid is random.

Methods (ii)–(v) require the exact determination of the value of $\rho_L c_L$; hence, they have the same fundamental disadvantage as method (i) [1]. All five methods are relative. Thus, until recently, there were no reliable methods for determining the radiated acoustic power under cavitation conditions, and the above-mentioned methods are suitable only for making an estimate.

For measuring the acoustic power absorbed by a cavitating volume of liquid, at present, an ordinary calorimetric method is used most often [1, 2]. According to this method, the increase in the liquid temperature ΔT_{US} under the action of ultrasound is measured over a sufficiently long period of time t_{US} (5–30 min, so that the heating ΔT_{US} reaches 5–20°C). The absorbed power is calculated by the relation

$$W_{US} = c_v m \Delta T_{US}/t_{US}, \tag{2}$$

where c_v is the specific heat of water and m is the mass of water. However, this method has the following essential disadvantages [1, 9]:

(a) In principle, it is impossible to eliminate the considerable heat transfer through the waveguide; usually, the heat transfer through the vessel walls is also large.

(b) The difference between the heat capacity of the liquid $c_v m$ and the heat capacity of the liquid–waveguide–vessel–thermometer system C_{sys} is considerable (sometimes these quantities may differ several times).

(c) As a rule, in these measurements a mixer is not used, because it is supposed that ultrasound itself is an efficient mixer. However, the experiments [9] showed that mixing is necessary in the calorimetric measurements and, without mixing, the temperature distribution in the liquid is highly inhomogeneous.

(d) The experiments [9] showed that, if the time of action of ultrasound t_{US} exceeds 40–90 s (depending on the specific type of the waveguide and the efficiency of the transducer), the heat has enough time to be transferred from the acoustic transducer to the cavitating liquid through the waveguide (usually made of metal).

Consequently, using an ordinary calorimetric method, some intermediate value between the electric power at the transducer and the absorbed acoustic power is measured approximately; the errors introduced by the heat transfer, the difference in the heat capacities, etc., are practically undefinable [1, 9].

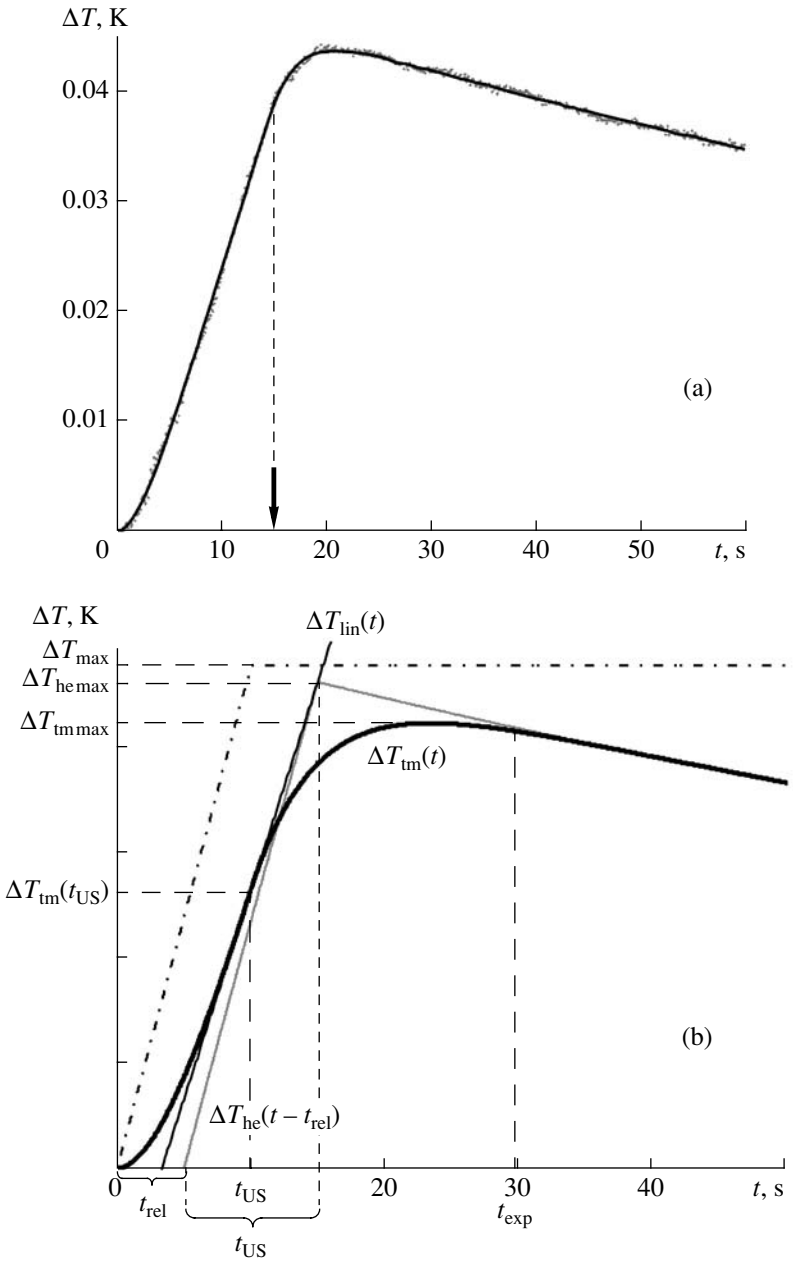

Fig. 1. (a) Comparison of the typical experimental dependence $\Delta T_{US}(t)$ under the action of ultrasound and the theoretical dependence $\Delta T_{tm}(t)$ calculated by Eqs. (8) and (9). Experimental conditions: the liquid volume is 600 ml, t_{US} = 14.7 s (the instant of termination of the ultrasound is shown by an arrow ↓), and W_{US} = 11.9 W. Parameters of the calculation are $\alpha = 0.0063\ s^{-1}$ and t_{rel} = 1.7 s. (b) Diagram illustrating the calculation of ΔT_{max} from the curve $\Delta T_{tm}(t)$ approximating the experimental data. Parameters of the calculation are t_{US} = 10 s, t_{rel} = 5 s (for clarity, t_{rel} is shown on an enlarged scale), $\alpha = 0.0067$, and, according to Eq. (10), t_{exp} = 29.6 s. The dot-and-dash line shows the dependence of the temperature rise on time for $\alpha = 0$ and $t_{rel} = 0$.

The method proposed in [15] for determining the absorbed acoustic power from the initial part of the curve of the temperature rise with time, beginning from the instant the ultrasound is turned on, eliminates the influence of the heat transfer on the temperature rise. However, the drawbacks indicated in items (b)–(d) persist [1, 9]. An additional error appears, which is connected with the inertia of the liquid–waveguide–vessel–thermometer system, since, at the initial instant, the derivative of the temperature rise measured with a thermometer with respect to time is equal to zero (see, for example, the initial part of the curve $\Delta T_{US}(t)$ in Fig. 1a). Consequently, the error in measuring the acoustic power using this method turns out to be considerable [1, 9].

1. THE COMPARATIVE CALORIMETRIC METHOD

A comparative calorimetric method for measuring the acoustic power in cavitation conditions was proposed in paper [16], and later, in [9, 17], it was considerably improved. The essence of this method is as follows. First, a source of ultrasound is turned on for a short time t_{US} and the change in temperature with time $\Delta T_{US}(t)$ is recorded by using a thermoprobe (Fig. 1a). Then, after cooling, a heater is turned on and the change in temperature is recorded again. By changing the power delivered by the heater, the similarity of the run of the curves $\Delta T_{US}(t)$ is achieved. In this case, the power, lost by the heater is considered to be the equivalent of the acoustic power absorbed in the volume of the liquid under study.

Let us consider the change in the temperature of the liquid with time if a sound source (or a heater) is turned on at the instant $t = 0$ and turned off at $t = t_{US}$ (Fig. 1a). To a high accuracy, the spatial distribution of temperature in the liquid can be considered to be homogeneous, because an efficient mixer is used (the stirring is assumed to be efficient if an increase in the mixer velocity does not change the measured value of acoustic power). For a small change in temperature, the heat transfer is proportional to its increase, and the change in temperature obeys the following set of equations [9, 17]:

$$d(\Delta T_{he})/dt = W/C_{sys} - \alpha \Delta T_{he}, \quad (t \le t_{US}) \tag{3}$$

$$d(\Delta T_{he})/dt = -\alpha \Delta T_{he}, \quad (t > t_{US}) \tag{4}$$

with the initial condition $\Delta T_{he}(0) = 0$. In these equations, W is the acoustic (or heat) power, C_{sys} is the heat capacity of the liquid–waveguide–vessel–thermometer system, and α is a constant characterizing the intensity of the heat transfer.

The solution to the set of equations (3), (4) can be written as [9, 17]

$$\Delta T_{he}(t) = \frac{Wt}{C_{sys}}\left(\frac{1 - \exp(-\alpha t)}{\alpha t}\right), \quad (t \le t_{US}) \tag{5}$$

$$\Delta T_{he}(t) = \frac{Wt_{US}}{C_{sys}}\left(\frac{1 - \exp(-\alpha t_{US})}{\alpha t_{US}}\right) \times \exp(-\alpha(t - t_{US})), \quad (t > t_{SU}). \tag{6}$$

Since the system is inertial, the thermoprobe measures the liquid temperature with a lag, which is characterized by the relaxation time t_{rel}; i.e., the thermoprobe output is determined by the equation

$$d(\Delta T_{tm})/dt = (\Delta T_{he} - \Delta T_{tm})/t_{rel} \tag{7}$$

with the initial condition $T_{tm}(0) = 0$. The solution to Eq. (7) can be written as

$$\Delta T_{tm}(t) = \frac{W}{C_{sys}(1 - \alpha t_{rel})} \times \left(\frac{1 - \exp(-\alpha t)}{\alpha} - t_{rel}(1 - \exp(-t/t_{rel}))\right), \quad (t \le t_{US}) \tag{8}$$

$$\Delta T_{tm}(t) = \frac{W}{C_{sys}(1 - \alpha t_{rel})} \times \left[\frac{1 - \exp(-\alpha t_{US})}{\alpha \exp(\alpha(t - t_{US}))} - t_{rel}\left(1 - \exp\left(-\frac{t_{US}}{T_{rel}}\right)\right)\exp\left(-\frac{t - t_{US}}{t_{rel}}\right)\right], \quad (t \ge t_{US}). \tag{9}$$

According to Fig. 1a, the measured experimental dependence $\Delta T_{US}(t)$ is approximated by the curve $\Delta T_{tm}(t)$ to a very high accuracy. The further theoretical analysis is aimed at the determination of the algorithm allowing us, by using the measured dependences $\Delta T_{US}(t)$ approximated by the curves $\Delta T_{tm}(t)$, to compare quantitatively the thermal powers from two different heat sources operating during the same time t_{US} with a constant heat capacity of the system C_{sys} but with different times of thermal inertia t_{rel} and different conditions of heat transfer (parameter α). It should be noted that the parameter α and the time t_{US} are determined from the experiment to a very high accuracy; the accuracy of determining t_{rel} is not high. We will find the time t_{exp}, beginning from which the difference between the curve ΔT_{tm} and curve $\Delta T_{US}(t)$ displaced along the time axis by the magnitude t_{rel} do not exceed the given accuracy K. From formula (9), it follows that the inertia of the thermoprobe influences the result of temperature measurement if the time is less than

$$t_{exp} = t_{US} + \frac{t_{rel}}{1 - \alpha t_{rel}} \ln\left[\frac{\alpha t_{rel}}{K}\frac{1 - \exp(-t_{US}/t_{rel})}{1 - \exp(-\alpha t_{US})}\right] \quad (t \le t_{US}). \tag{10}$$

For instance, for $K = 0.003$, $t_{US} = 10$ s, $t_{rel} = 2$ s, and $\alpha < 0.1$, we have $t_{exp} \sim 20$ s, and for $t_{rel} = 5$ s and $\alpha < 0.03$, we have $t_{exp} \sim 30$ s. Thus, the approximation of the curve $\Delta T_{tm}(t)$ by an exponent is correct for $t > t_{exp}$.

It seems that the parameter by which it is possible to compare the absorbed powers using the curves $\Delta T_{tm}(t)$

is the measured maximal temperature. Equating the derivative $d(\Delta T_{tm})/dt$ to zero, we have

$$\Delta T_{tm\,max} = \frac{W}{C_{sys}}\left(\frac{1-\exp(-\alpha t_{US})}{\alpha}\right) \times\left(\frac{1-\exp(-\alpha t_{US})}{1-\exp(-t_{US}/t_{rel})}\right)^{\alpha t_{rel}/(1-\alpha t_{rel})}. \quad (11)$$

From this expression it is seen that $\Delta T_{tm\,max}$ strongly and in a complicated way depends on t_{rel} and α and, consequently, it cannot be an appropriate parameter for comparing the curves $\Delta T_{tm}(t)$.

The analysis performed above shows that an alternative algorithm is needed. On the basis of the experimental curve approximated by Eqs. (8) and (9), it is possible to calculate or determine from the plot the tangent to it at the instant when the source of ultrasound (or the heater) is turned off (Fig. 1b). The equation of the tangent $\Delta T_{lin}(t)$ to the curve $\Delta T_{tm}(t)$ at the point t_{US} can be written as

$$\Delta T_{lin}(t) = a(t - t_{US}) + \Delta T_{tm}(t_{US}), \quad (12)$$

where a is the derivative of the temperature rise with respect to time at the moment the source of ultrasound is turned off:

$$a = \left.\frac{d(\Delta T_{tm})}{dt}\right|_{t=t_{US}} = \frac{W(\exp(-\alpha t_{US}) - \exp(-t_{US}/t_{rel}))}{C_{sys}(1-\alpha t_{rel})}. \quad (13)$$

It is easy to show that the straight line $\Delta T_{lin}(t)$ and the curves $\Delta T_{he}(t)$ (Eqs. (5) and (6)) displaced along the t axis by the time t_{rel} have a common point of intersection at the instant $(t_{rel} + t_{US})$ (see Fig. 1b) characterized by the temperature

$$\Delta T_{he\,max} = \frac{W t_{US}}{C_{sys}}\left(\frac{1-\exp(-\alpha t_{US})}{\alpha t_{US}}\right). \quad (14)$$

The quantity $\Delta T_{he\,max}$ determined in this way does not depend on t_{rel} (note that t_{rel} may be even greater than the time of operation of the source of ultrasound t_{US}). From this expression, we can obtain the maximal temperature to which the liquid would be heated without heat transfer to the environment:

$$\Delta T_{max} = \frac{W t_{US}}{C_{sys}} = \Delta T_{he\,max}/\left(\frac{1-\exp(-\alpha t_{US})}{\alpha t_{US}}\right). \quad (15)$$

The calculated ΔT_{max} does not depend either on the intensity of the heat exchange or on the relaxation time. Hence, ΔT_{max} can be used as a quantitative criterion for comparing the curves $\Delta T_{tm}(t)$ under different conditions of heat transfer and with different times of relaxation t_{rel}. This fact was supported by experiments [9]. Thus, the ratio $\Delta T_{US\,max}/\Delta T_{H\,max}$ calculated from the experimental dependences $\Delta T_{US}(t)$ and $\Delta T_{H}(t)$ is the quantitative measure of the ratio of the absorbed powers (here, $\Delta T_{US}(t)$ and $\Delta T_{H}(t)$ are the temperature rises produced by the source of ultrasound and the heater) [9, 17].

The analysis of these solutions made it possible to determine the conditions most favorable for performing the measurements [9, 17]:

—a smallness of the temperature rise (no greater than 0.1–0.4 K),

—a short time of operation of the sound source (the experiments showed that t_{US} should lie in the range 5–15 s), and

—an efficient stirring of the liquid; in the experiments described below, t_{rel} did not exceed 1–2 s.

The absorbed acoustic power was measured as follows. First, the variation of the temperature of the liquid with time under the action of sound, $\Delta T_{US}(t)$, is recorded, and then, by using a computer with an A/D converter, the approximation is performed and $\Delta T_{US\,max}$ is calculated. The selection of the heater power is carried out by a special program with a computer operating in real time in such a way that $\Delta T_{US\,max}/\Delta T_{H\,max} \approx 1$. The process is performed in one or several successive approximations, depending on the required accuracy. The value of the heater power at the first step has no effect on the final accuracy and only determines the number of iterations. The operation time of the heater is taken to be equal to t_{US}, and the power is calculated as

$$W_{H1set} = c_v m \Delta T_{US\,max}/t_{US}. \quad (16)$$

Then, the temperature variation with time, $\Delta T_{H1}(t)$, is recorded and ΔT_{H1max} is calculated in the same way as $\Delta T_{US\,max}$. From the measured current I_e and voltage U_e at the heater, the actually released thermal power $W_{H1real} = (\int I_e U_e dt)/t_{US}$ is determined to a high accuracy, with the difference between W_{H1real} and W_{H1set} not exceeding 3%. At the second step, the measurement of $\Delta T_{H2}(t)$ is performed similarly to $\Delta T_{H1}(t)$. The heating time is taken to be equal to t_{US}, and the heater power is

$$W_{H2set} = W_{H1real}\Delta T_{US\,max}/\Delta T_{H1max}. \quad (17)$$

By measuring the current I_e and the voltage U_e at the heater, W_{H2real} is determined to a high accuracy. The computed temperature rise ΔT_{H2max} turns out to be much closer to $\Delta T_{US\,max}$ than ΔT_{H1max}, and the absorbed acoustic power is found by the formula

$$W_{US} = W_{H2real}\Delta T_{US\,max}/\Delta T_{H2max}. \quad (18)$$

Note that it is possible to conduct several refining measurements, taking every time the operation time of the heater equal to t_{US} and the power at the ith step equal to

$$W_{H(i)set} = W_{H(i-1)real}\Delta T_{US\,max}/\Delta T_{H(i-1)max}. \quad (19)$$

However, our experiments showed that the required accuracy of 3% is achieved after two iterations.

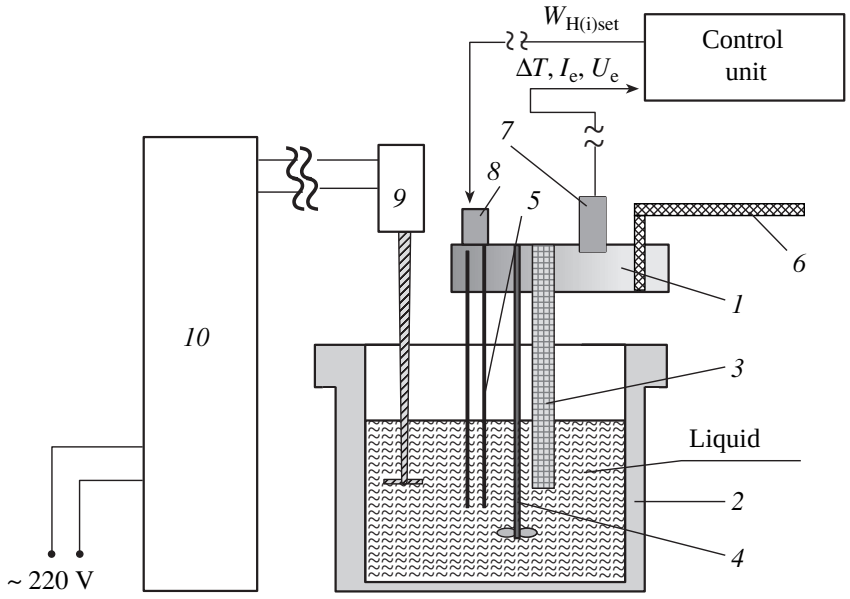

Fig. 2. Experimental setup for measuring the absorbed and radiated acoustic powers under cavitation conditions: cover *1* for mounting parts *3–8*, body *2*, thermoprobe *3*, mixer *4*, wire of the heater *5*, device *6* for fastening the cover to a stand, electric connector *7*, and power connector *8*. The setup measures the power of a sound source consisting of an ultrasonic transducer *9* and an ultrasonic generator *10*.

A typical example of the temperature variation with time under the action of ultrasound and the heater at the first and second (refining) calibrations is shown in Fig. 1b. In the measurements, we determined to a high accuracy the operation time of the sound source and the current value of the temperature rise (with an accuracy of 0.005 s and 0.0005 K, respectively). The total time of measurements did not exceed 8 min, because three curves $\Delta T_{US}(t)$, $\Delta T_{H1}(t)$, and $\Delta_{H2}(t)$ were recorded, every curve for two minutes.

For measuring the absorbed and radiated acoustic power, we used a setup schematically shown in Fig. 2. It consists of a calorimetric tank filled with insonified liquid; a sensor unit, which comprises a mixer, a coil heater, and sensors (a sensor of the liquid temperature and sensors of the heater current and voltage); and a control unit, which comprises a power supply module and a computer with an A/D converter for data acquisition. The sensor unit measures the liquid temperature rise in the calorimetric tank and the heat released by electric coil *5* of the heater (from the measured current I_e and voltage U_e); these data are passed to the control unit. The control unit assigns the electric power $W_{H(i)set}$ that will be released by the heater, controls the process of measuring the absorbed acoustic power according to the algorithm described above, and provides the power supply for the whole setup. By using the computer, the interactive mode of operation is performed and the results are displayed. All the measurements, approximation, calculations, and other operations are carried out automatically in real time. On the basis of this setup, the ARM-1 system was developed and the 3% accuracy was achieved in the acoustic power measurements.

The specific conditions under which practically the whole of the radiated power is absorbed in the volume of the cavitating liquid were determined experimentally (see below, Subsection 2.2). In this case, by measuring the absorbed power, we can also find the radiated acoustic power [9, 17].

The comparative calorimetric method has the following advantages over the known methods described above [9]:

—Unlike the acoustic methods (i)–(v), it is not necessary to know exactly the impedance of the liquid with bubbles, the conversion coefficient of the radiator, etc.; the measurements are conducted independently of the type of the radiator and the ultrasonic frequency; the proposed method is an absolute one.

—In contrast to the ordinary calorimetric method, it is not necessary to eliminate the heat transfer, because the heat transfer does not affect the accuracy in comparative measurements; the measurements do not depend on the heat capacity of the liquid–waveguide–vessel–thermometer system; because of the short time of operation of the source of ultrasound, the heat has no time to be transferred from the transducer to the liquid, i.e., the measured quantity is precisely the absorbed acoustic power.

2. EXPERIMENTAL RESULTS OBTAINED USING THE COMPARATIVE CALORIMETRIC METHOD

In the experiments, four different sound sources were employed. The first source is an ultrasonic generator with a magnetostrictive transducer, which is connected to a steel waveguide with the length $\lambda/2$, a face diameter of 15 mm, and a resonance frequency of 21.2 kHz (instrument 1). The second source is a generator with a piezoelectric transducer, which is connected to a titanium waveguide with the length λ, a face diameter of 80 mm, and a resonance frequency of 41.0 kHz (instrument 2). We also used the following ultrasonic tanks: the first tank with one piezoelectric transducer of frequency 20.2 kHz (instrument 3) and the second tank with two piezoelectric transducers of frequency 23.0 kHz (instrument 4). The measurements were carried out in four different metal vessels. The first vessel has a cylindrical form of circular cross section 60 mm in diameter and 100 mm in height. The second vessel has a cylindrical form of circular cross section 150 mm in diameter and 120 mm in height. The third vessel has the form of a parallelepiped with a square cross section of 90×90 mm and a height of 105 mm. In the experiments, distilled water at a temperature of 19–21°C was used.

2.1. Comparison of the Absorbed and Radiated Ultrasonic Powers

At the beginning, we assumed that, under the experimental conditions, the radiated acoustic power should be much greater than the absorbed power. However, the experiments did not confirm this assumption. In our previous experiments [9, 17], we determined the conditions under which practically the whole of the radiated acoustic power is absorbed in the volume of a cavitating liquid. In this case, by measuring the absorbed power, we can also determine the radiated acoustic power.

We performed the measurements with instrument 1 at four fixed values of acoustic power, 4.1 ± 0.2, 15.3 ± 0.5, 28.3 ± 0.8, and 45.8 ± 1 W, and with instrument 2 at a fixed power of 13 ± 0.3 W (these values of acoustic power corresponded to the conditions of fully developed cavitation). The waveguide was submerged to a depth of 12 ± 1 mm, and the measurements were carried out in vessels 1 and 3. The liquid volume was always equal to 400 cm^3. Similar measurements were performed with ultrasonic tanks 3 and 4 at fixed power values of 53 ± 1.5 and 65.3 ± 1.5 W, and the liquid volume was 500 and 1500 cm^3, respectively. Introducing an efficient sound absorber made of fibrous polymeric material into the system, we obtained the same acoustic power as without the sound absorber (within the accuracy of the experiment, 3%). The absorber was introduced in such a way that the form of the cavitation cloud remained unaffected. The experimental results can be explained by the fact that, in the absence of efficient absorbers, ultrasonic waves are reflected from the liquid–gas or solid wall–gas boundaries and are almost completely absorbed by the liquid with bubbles.

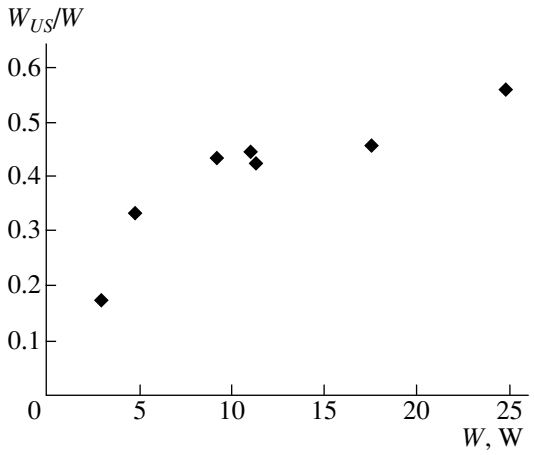

Fig. 3. Dependence of the ratio of the absorbed power W_{US} to the radiated acoustic power W on the radiated acoustic power W.

At present, a popular method of studying sonochemical processes is based on introducing the ultrasound into the system through a sound-transparent bottom to avoid the influence of the contact of the radiator material with the insonified liquid on the process under study (see, for example, [18]). It is believed that, under cavitation conditions, the whole of the introduced ultrasonic energy is absorbed by the liquid volume in the vessel. We decided to verify this assumption. We used a cylindrical vessel with a circular cross section of 60 mm in diameter and a height of 100 mm, the bottom of which was made of a sound-transparent lavsan film. The sound source was an ultrasonic tank (instrument 3). The measurements were carried out in two steps. First, the radiated acoustic power was measured (for this purpose, the power absorbed in the water filling the ultrasonic tank was measured). After this, into the liquid filling the ultrasonic tank, a vessel with a sound-transparent bottom was submerged just above the radiator, at a distance of about 3 mm, and the power absorbed in the vessel was measured. Figure 3 shows the ratio of the power absorbed in the vessel to the power radiated by the ultrasonic tank as a function of the power radiated by the ultrasonic tank. It is seen that, in a wide range of intensities, only ~40% of the radiated power is absorbed, but at a low radiated power, the share of the absorbed power in the vessel with a sound-transparent bottom considerably decreases.

Such a great difference between the radiated and absorbed acoustic powers can be explained by the fact that the sound-transparent film not only allows the sound to pass into the vessel but, according to the reciprocity principle, also permits the sound waves to escape from the vessel. Apparently, the absence of sound-transparent walls is a necessary condition for the

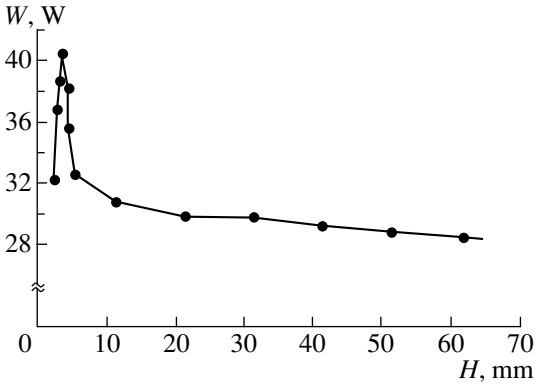

Fig. 4. Dependence of the acoustic power W (the absorbed and radiated powers coincide) on the distance H between the waveguide face and the bottom of the vessel.

whole of the radiated power to be absorbed by the liquid with bubbles.

Thus, using the described procedure, it is possible to measure not only the absorbed power but also the radiated acoustic power [9]. When using a vessel with a sound-transparent bottom, a portion of the radiated power can escape from the liquid volume. In this case, it is possible to measure only the absorbed acoustic power and then, using a vessel without sound-transparent elements through which sound can leave the system, to measure the radiated power.

2.2. Dependence of the Radiated and Absorbed Powers on the Geometrical Parameters of the Vessel–Liquid–Radiator System

Usually it is assumed that the radiated and corresponding absorbed acoustic powers under cavitation conditions strongly depend on the liquid volume and geometrical parameters of the vessel in which the measurements are performed, as well as on the depth of submergence of the sound radiator. This opinion is based on the results obtained from studying a liquid by the methods of linear acoustics, when the radiated power depends on the acoustic impedance of the system and, consequently, on the boundary conditions for the radiator, vessel, and liquid. However, experimental studies of this problem with a cavitating liquid are practically absent because of the uncertainty in the acoustic power.

For determining the dependence of the acoustic power on the vessel geometry and the liquid volume, we performed the measurements using instrument 1 at four fixed values of acoustic power: 4.1 ± 0.2, 15.3 ± 0.5, 28.3 ± 1, and 45.8 ± 1.8 W, for a waveguide submergence depth of 12 ± 0.5 mm. The measurements were conducted in vessels 1–3 for various liquid volumes (250 and 350 cm^3 in the first vessel, 650 and 1000 cm^3 in the second vessel, and 1000 and 1350 cm^3 in the third vessel). In the experiment, the conditions formulated in the previous section, under which the whole of the radiated acoustic power was absorbed by the liquid with bubbles, were met. The geometrical dimensions were chosen to be considerably greater than the characteristic size of the cavitation cloud (the height and width of the cavitation cloud usually varied from 20 to 60 mm). In spite of the various forms of vessels and various volumes of insonified liquid, in every case we obtained the same acoustic power. A similar absence of dependence of the radiated and absorbed acoustic powers on the liquid volume was obtained with ultrasonic tanks 3 and 4 for various liquid volumes (400 and 600 cm^3 for ultrasonic tank 3 and 800, 1200, and 1600 cm^3 for tank 4).

The dependence of the acoustic power W (the absorbed and radiated powers coincide) on the distance H between the waveguide face and the vessel bottom was studied with the use of instrument 1 and vessel 3 [9]. The volume of distilled water was 500 cm^3, the distance between the vessel bottom and the water surface varied from 0.5 to 81 mm, and the submergence depth of the waveguide was measured accurate to 0.5 mm. The results obtained are presented in Fig. 4 (to reveal the effect, the power scale in the plot has a break). The initial slight increase in the acoustic power with a decrease in H can be explained by the increase in the radiating (lateral) surface of the waveguide, whereas the boundary conditions for the waveguide face remain practically invariable. With a further slight decrease in H (less than 5 mm), a sharp increase in the acoustic power is observed, which can be explained by a drastic change in the boundary conditions near the waveguide face when H becomes on the order of the height of the cavitation cloud. The maximum of the acoustic power delivered by the radiator was observed for $H = 5$ mm (Fig. 4). The origin of this increase in the acoustic power (by approximately 50%) is not quite clear; however, we believe that it will be determined in the near future and the observed effect will find practical application. Note that the possibility of revealing this effect appeared only after the development of an exact method of measurement of acoustic power under cavitation conditions. Thus, the radiated and absorbed powers under conditions of fully developed cavitation, to a first approximation, do not depend on the liquid volume or the geometrical parameters of the vessel in which the measurements are carried out if the following conditions are satisfied [9]:

(a) the characteristic dimensions of the vessel are considerably greater than the characteristic dimensions of the cavitation cloud;

(b) the distance between the waveguide face and the vessel bottom is much greater than the height of the cavitation cloud; and

(c) the whole of the radiated acoustic power is absorbed by the liquid with cavitation bubbles.

3. DEPENDENCE OF THE RATE OF CAVITATION PROCESSES ON THE ACOUSTIC POWER

Until recently, it was generally accepted that the dependence of the rate w_{cav} of a number of cavitation processes (erosion, emulsification, dispersion, as well as sonoluminescence (SL) and sonochemical reactions) on the sound intensity I is as follows [1, 3, 4, 19, 20]: until the intensity I is below the threshold intensity I_{thr}, the rate w_{cav}, naturally, equals zero; after I_{thr} is exceeded, the rate w_{cav} increases first proportional to $(I - I_{thr})^2$ [1] and then linearly. In a number of papers, the presence of a maximum in the dependence $w_{cav}(I)$ at $I = I_{cr}$ is indicated: for the rate of sonochemical reactions [20, 21], the SL flux [20], the erosion activity [3, 19, 20], etc. For $I > I_{cr}$, the rate of these high-energy processes sharply decreases.

According to the conclusions made by Rozenberg and Sirotyuk [3, 19], with a considerable increase in p_m, the maximal radius R_m increases and a bubble does not have enough time to collapse within one half-period of oscillations. Equating the Rayleigh time of bubble compression to half the oscillation period and taking into account that the tensile stress is equal to $2^{-0.5}p_m$ [19], we obtain

$$p_{mcr} \cong 3 \times 2^{0.5}(0.915)^{-2} p_h \approx 5.1 p_h, \qquad (20)$$

which corresponds to the critical intensity I_{cr} = 8.6 W/cm^2.

Being capable of measuring the ultrasonic power under cavitation conditions with a high accuracy, we decided to verify the dependence of the rate of sonochemical reaction on the intensity, including the range of $I > I_{cr}$. We studied the dependence of the rate of a typical sonochemical reaction, namely, the formation of nitric oxides and corresponding ions NO_2^- in distilled water in contact with air, on the intensity of ultrasound [9]. This reaction is best suited for such experiments for a number of reasons: (a) a purified water without any additions, which may change its physicochemical parameters, undergoes sonolysis; (b) the reaction proceeds only under the action of ultrasound or under the conditions of a low-temperature plasma, in the absence of thermal and redox reactions; (c) the reaction rate is insensitive to possible microimpurities, i.e., the reaction products are sufficiently tolerant to catalytic or thermal actions; and (4) the corresponding analytical procedures provide for a high accuracy [1].

The measurement of ultrasonic power was performed by using the setup shown in Fig. 2 and an ultrasonic generator *1* with a frequency of 20 kHz. The water volume was 100 cm^3, a flask with twice-distilled water was enclosed in a thermostat maintained at a temperature T_∞ within 19.5–20.5°C. The quantity of the resulting NO_2^- was measured by the calorimetric method [1].

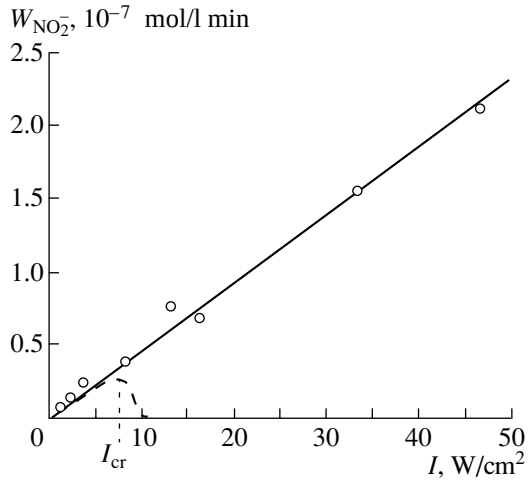

Fig. 5. Dependence of the rate $W_{NO_2^-}$ on the ultrasonic intensity I. The dashed line shows the previously reported character of the dependence of the rate w_{cav} of various cavitation processes (erosion, emulsification, dispersion, as well as SL and sonochemical reactions) on the sound intensity [3, 19–21], where I_{cr} is determined from Eq. (20).

At first, the dependence of the NO_2^- concentration on the time t_{US} of operation of the source of ultrasound was determined for various intensities I. At the initial period of time, the increase in NO_2^- at a constant rate $W_{NO_2^-}$ was observed; then, the rate $W_{NO_2^-}$ decreased and, at large times of sonolysis, a stationary concentration of NO_2^- of about 3.5 μmol/l was formed regardless of the sound intensity. This limit is determined by the initial quantity of N_2 in the air dissolved in water and by the rate of degassing, which agrees well with reported experimental data [1].

To eliminate the influence of the degassing on the dependence of $W_{NO_2^-}$ on I, we determined the rate $W_{NO_2^-}$ from the initial part of the curves $[NO_2^-](t_{US})$; i.e., the rate of the synthesis of NO_2^- at high intensities was determined for rather small times of sonolysis (on the order of 10–30 s). As a result, we obtained a linear dependence $W_{NO_2^-}(I)$, shown in Fig. 5 [9]. Since the least measured acoustic power in our experiments was 3 W and the diameter of the waveguide face was equal to 15 mm, the least measured intensity was 1.7 W/cm^2, which is considerably greater than the threshold (~0.03 W/cm^2 [1, 22]). Therefore, these experiments do not yet make it possible to determine the value of the

cavitation threshold and the dependence $W_{NO_2^-}(I)$ near the threshold with sufficient accuracy.

At the same time, the maximal measured acoustic power of 75 W corresponds to $I = 47$ W/cm^2, which is six times as great as the value of I_{cr} calculated from Eq. (20). The experimental results obtained for the dependence $W_{NO_2^-}(I)$ allow us to conclude that no sharp decrease occurs in the rate of formation of NO_2^-, i.e., there is no maximum in the rate and, in a wide range of ultrasonic intensities, the dependence $W_{NO_2^-}(I)$ is linear.

The previously reported experimental dependence of the rate of the cavitation process w_{cav} on the intensity with a maximum at I_{cr} and a subsequent drop in the rate with increasing I is presumably determined by the fact that the quantity measured in those experiments was the square of the voltage U at the transducer rather than the acoustic power, and the "acoustic power" shown in Fig. 5 is actually the quantity proportional to U^2. Although the efficiency of the transducer operating under cavitation conditions was undefinable, in [3, 4, 19] it was assumed to be constant and equal to the efficiency measured under subcavitation conditions. In addition, the experiments were conducted at a constant sound frequency f (i.e., the sound source, apparently, was not tuned to resonance), although, even with a slight change in f, the efficiency of the transducer changes considerably and becomes unknown.

Thus, the extremum observed earlier in the dependence $w_{cav}(I)$ for $I > I_{cr}$ proves to be an instrumental effect.

ACKNOWLEDGMENTS

We thank S.A. Rybak, S.N. Skorodumov, and A.N. Svadkovskiĭ for discussions and helpful advice. This work was supported by the Russian Foundation for Basic Research (project nos. 02-02-16397A and 03-02-16232) and by the grant NSh-1176-2003-2.

REFERENCES

1. M. A. Margulis, *Sonochemistry and Cavitation* (Gordon and Breach, London, 1995).
2. A. E. Kolesnikov, *Ultrasonic Measurements* (Izd. Standartov, Moscow, 1970) [in Russian].
3. L. D. Rozenberg, in *High-Intensity Ultrasonic Fields*, Ed. by L. D. Rozenberg (Nauka, Moscow, 1968; Plenum, New York, 1971).
4. *Sonochemistry and Sonoluminescence*, Ed. by L. A. Crum, T. J. Mason, J. L. Reisse, and K. S. Suslick (Kluwer, 1999).
5. T. V. Gordeĭchuk, Yu. T. Didenko, and S. P. Pugach, Akust. Zh. **42**, 274 (1996) [Acoust. Phys. **42**, 240 (1996)].
6. Yu. T. Didenko, Akust. Zh. **43**, 252 (1997) [Acoust. Phys. **43**, 215 (1997)].
7. M. R. Bailey, V. A. Khokhlova, O. A. Sapozhnikov, *et al.*, Akust. Zh. **49**, 437 (2003) [Acoust. Phys. **49**, 369 (2003)].
8. E. A. Filonenko and V. A. Khokhlova, Akust. Zh. **47**, 541 (2001) [Acoust. Phys. **47**, 468 (2001)].
9. M. A. Margulis and I. M. Margulis, Zh. Fiz. Khim. **77** (7), 1318 (2003).
10. N. J. Turro, *Molecular Photochemistry* (W. A. Benjamin, New York, 1965; Mir, Moscow, 1967).
11. L. Bergmann, *Ultrasonics* (Bell, London, 1938; Inostrannaya Literatura, Moscow, 1957).
12. G. K. Betchelor, in *Proceedings of International Symposium on Modern Problems and Methods of Hydromechanics, Tard, Poland, 1967* (Tard, 1967).
13. L. J. Campbell and A. S. Pitcher, in *Proceedings of Symposium of Admiralty Research Laboratory, Middlesex, 1954* (Middlesex, 1954).
14. V. E. Nakoryakov, B. G. Pokusaev, and I. R. Shreĭber, *Wave Dynamics of Gas–Liquid and Vapor–Liquid Media* (Energoatomizdat, Moscow, 1990) [in Russian].
15. T. J. Mason, J. P. Lorimer, and D. M. Bates, Ultrasonics **30** (1), 40 (1992).
16. M. A. Margulis and A. M. Mal'tsev, Zh. Fiz. Khim. **43** (4), 1055 (1969).
17. M. A. Margulis and I. M. Margulis, in *Proceedings of the 3rd Conference on Applications of Power Ultrasound in Physical and Chemical Processing, Paris, 2001* (Paris, 2001), p. 209.
18. S. Koda, T. Kimura, T. Kondo, and H. Mitome, Ultrason. Sonochem. **10** (3), 149 (2003).
19. M. G. Sirotyuk, in *High-Intensity Ultrasonic Fields*, Ed. by L. D. Rozenberg (Nauka, Moscow, 1968; Plenum, New York, 1971).
20. H. G. Flynn, in *Physical Acoustics: Principles and Methods*, Ed. by W. P. Mason (Academic, New York, 1964; Mir, Moscow, 1967), Vol. 1b.
21. T. J. Mason, J. P. Lorimer, and T. Cuthbert, in *Proceedings of Ultrasonic International Conference, UI-89, Spain, Madrid, 1989* (Madrid, 1989), p. 1279.
22. M. A. Margulis and L. M. Grundel', Zh. Fiz. Khim. **55**, 687 (1981).

Translated by A. Svechnikov

Acoustical Physics, Vol. 51, No. 6, 2005, pp. 705–712. Translated from Akusticheskiĭ Zhurnal, Vol. 51, No. 6, 2005, pp. 813–821.

Dynamics of a Bubble Cluster in an Acoustic Field

É. Sh. Nasibullaeva and I. Sh. Akhatov

Institute of Mechanics, Ufa Scientific Center, Russian Academy of Sciences, pr. Oktyabrya 71, Ufa, 450054 Bashkortostan, Russia

e-mail: elvira@anrb.ru

Received May 26, 2004

Abstract—A mathematical model describing the dynamics of clustered gas bubbles under the effect of an acoustic field is presented. The proposed model is used as the basis for an analytical study of small bubble oscillations in monodisperse and polydisperse clusters and for a numerical study of nonlinear bubble oscillations under high-amplitude external pressures. The following effects are found to occur in a polydisperse cluster: a synchronization of the collapse phases of bubbles with different radii and a collapse intensification for bubbles of one size in the presence of bubbles of another size. These effects are explained by the interaction between bubbles of different radii in the cluster. © *2005 Pleiades Publishing, Inc.*

INTRODUCTION

Cavitation in a liquid is accompanied by the formation of bubble clusters. The dynamic processes that occur in these clusters determine many phenomena observed in physics, chemistry, and biology, and also find practical application in engineering.

Up to the present time, most attention has been concentrated on studying the dynamics of a single bubble. This is primarily related to the discovery of single-bubble sonoluminescence [1, 2] and to the possibility of tracing the motion of the surface of a single bubble with high-speed photography [3, 4]. Direct experimental studies of the bubble dynamics in bubble clusters (clouds) are fairly complicated from the technical point of view [5–9]. Therefore, the mathematical modeling of the bubble dynamics in a cluster plays an important role. The existing theoretical approaches to this problem can be divided into two groups.

In the first group, a cluster was considered as a bubbly liquid, for which the models described in theoretical publications [10–12] were used. In [13–16], the collapse of a bubble cloud caused by ultrasonic cavitation was studied both theoretically and experimentally. In these publications, the following idea was put forward: the cavities in a cluster collapse sequentially from the boundary of the cluster toward its center, and this process is accompanied by a pressure growth toward the center of the cloud because of the energy transfer from collapsing cavities to the neighboring noncollapsing ones. The model proposed in [13, 15] and used in [16] does not include the dynamics of an individual bubble and gives infinite values of pressure and collapse rate at the center of the cluster. In [14], the dynamics of a bubble was modeled by solving the Rayleigh–Plesset equation. In [5], an experimental study of a bubble cluster formed in a liquid layer between a source of ultrasound and a sample under investigation was described. It was found that the bubble fluctuations are virtually synchronous throughout the whole zone of interest. The interaction of a passive cloud of identical spherical bubbles with a shock wave was considered in [17]. It was shown that the cluster is able to absorb the energy of such an external disturbance, amplify this disturbance, and reradiate it in the form of an acoustic signal. Many of the publications concerned with this group of investigations were devoted to studying the linearized dynamics of a bubble cloud. For example, in [18], oscillations of a spherical cluster containing identical bubbles were studied under the assumption that viscosity, compressibility of the liquid, and surface tension of bubbles were absent. The theoretical consideration was based on the linearized equations of a uniform flow of a bubbly mixture, which were taken from [19]. It was shown that the eigenfrequency of a bubble cloud is much lower than the eigenfrequency of an individual bubble. The same problem was considered in [20, 21], but with allowances made for all the dissipative mechanisms. In studying the motion of a bubble cluster near a vibrating wall [22, 23], the bubble dynamics was taken into account by solving the Rayleigh–Plesset equation, which was expanded in a Fourier series to the second-order terms in the bubble radius. The results obtained in [20–23] are similar to those obtained in [18]. An experimental study of the cavitation region formed in a liquid under the effect of an ultrasonic generator was reported in [24]. In the latter paper, the theoretical description of the cavitation mode was based on the use of the averaged equations for the sound wave propagation through a bubbly medium while the interaction between the bubbles was considered as a size-averaged radiation interaction between two bubbles. Thus, the models proposed in the first group of publications make it possible to study the dynamics of a bubble cloud as an individual object but do not allow one to study in detail the dynamics of an individual bubble in a cluster and to consider

1063-7710/05/5106-0705$26.00 © 2005 Pleiades Publishing, Inc.

the interaction between bubbles of different radii within the cluster.

The second group includes the publications that focus on the interaction between bubbles. In [25], equations describing the translational motions and radius variations of a finite set of bubbles moving in a hydrostatic field were analytically derived. The cited paper was purely theoretical, and the derived equations were not applied to specific problems. Collective fluctuations of a finite number of bubbles, which may occur in a liquid near a gas source or after the separation of a large bubble into several smaller bubbles, were considered in [26]. The theory of gas bubble oscillations was developed with the use of the multiscale expansion method for the case of a liquid without dissipative mechanisms and for a polytropic gas. This approach required time-consuming computations with complete equations, and, therefore, averaging in the region of rapid bubble oscillations was used. Such a limitation prevents a detailed study of the bubble behavior in the cluster. The dynamics of a cluster containing a small number of bubbles was numerically studied in [27] with the use of the three-dimensional boundary-element method. The results were compared with those obtained analytically from an asymptotic expansion. It was assumed that the bubbles experience axisymmetric deformations so that the symmetry axis passes through the bubble under observation and the center of the cluster. In [28], the dynamics of the cluster was studied by representing the bubble surface as a series expansion in spherical harmonics. The result proved to be similar to the results reported in [18, 20–23] for the eigenfrequencies of a cluster and a single bubble. A cluster consisting of two or three bubbles lying on a straight line or at the corners of an equilateral triangle was considered in [29]. In the analysis, all the oscillation modes of the bubbles and the interaction between the bubbles were taken into account. It was shown that, as a result of the interaction between the bubbles, the resonance frequency of the cluster was shifted toward lower frequencies. All the methods proposed in [25–29] for solving the problem of interest dealt with only small numbers of bubbles arranged in specific configurations.

Therefore, it seems to be necessary to construct a mathematical model that makes it possible (i) to study the dynamics of a bubble cluster as a whole, as an individual object; (ii) to study the dynamics of individual bubbles within the cluster; (iii) to take into account the presence of bubbles with different radii in the cluster and their interaction; and (iv) to study the dynamics of bubble clusters under external actions, in particular, under the effect of an acoustic field.

STATEMENT OF THE PROBLEM AND THE MATHEMATICAL MODEL OF A BUBBLE CLUSTER

In this paper, we study a set of many bubbles performing oscillations within a finite volume of an unbounded, weakly compressible, viscous liquid under a periodic external pressure. In this case, we can separate a spherical region with bubbles, i.e., a bubble cluster. Thus, the cluster can be considered as a large spherical drop containing both liquid and a set of microbubbles. The problem is modeled under the following assumptions: first, the size R of the cluster is small compared to the sound wavelength λ ($R \ll \lambda$), and the concentration of bubbles in the cluster is also small (i.e., the condition of nonoverlapping scattering cross sections is satisfied [30]: $\sigma^{1/2} \ll l$, where σ is the scattering cross section and l is the average distance between the bubbles), which allows us to consider the pressure inside the cluster to be uniform; second, the gas bubbles are subjected to adiabatic compression and perform spherically symmetric radial motions; and third, heat- and mass-transfer processes are absent in the gas bubble–liquid system.

In the general case, when bubbles with n different radii are present in the cluster (the case of a polydisperse cluster), the dispersed phase falls into n fractions, each of them being characterized by its own bubble radius (a_{0k} for the kth fraction). Then, the radial motions of the conventional cluster boundary and the bubble boundaries can be described by the Rayleigh–Plesset equations with allowance for the acoustic radiation [31, 32]. The equations for the cluster and for the bubbles in the cluster have the form

$$R\ddot{R} + \frac{3}{2}\dot{R}^2 = \frac{p_c - p_I}{\rho_l} + \frac{R}{\rho_l C_l}\frac{d}{dt}[p_c - p_I], \tag{1}$$

$$a_k\ddot{a}_k + \frac{3}{2}\dot{a}_k^2 = \frac{p_{ak} - p_c}{\rho_l} + \frac{a_k}{\rho_l C_l}\frac{d}{dt}[p_{ak} - p_c], \quad k = \overline{1, n}, \tag{2}$$

respectively. Here, $R = R(t)$ is the cluster radius, $a_k = a_k(t)$ is the bubble radius in the kth fraction, $p_c = p_c(t)$ is the liquid pressure in the cluster, p_I is the liquid pressure at infinity, p_{ak} is the gas pressure at the bubble wall in the kth fraction, ρ_l is the density of the liquid, C_l is the sound velocity in the liquid, and t is time. The dot over a variable means the derivative with respect to time. Equations (1) and (2) are written under the assumption that the velocities of the interfaces are small compared to the sound velocity in the liquid; i.e., Eqs. (1) and (2) are valid for small Mach numbers.

Equations (1) and (2) are completed by the conservation law for the liquid volume in the cluster:

$$\sum_{k=1}^{n} N_k a_k^2 \dot{a}_k = R^2\dot{R}, \tag{3}$$

where N_k is the number of bubbles in the kth fraction.

In view of the second assumption specified above, the pressure in a bubble is determined by the formula

$$p_{ak} = \left(p_0 + \frac{2\sigma}{a_{0k}}\right)\left(\frac{a_k}{a_{0k}}\right)^{-3\gamma} - \frac{4\mu\dot{a}_k}{a_k} - \frac{2\sigma}{a_k}, \quad k = \overline{1, n}, \tag{4}$$

where p_0 is the initial pressure in the liquid, σ is the surface tension, μ is the viscosity of the liquid, and γ is the adiabatic index. The pressure variation in the liquid at infinity obeys the periodic law

$$p_I = p_0 - \Delta P \sin(\omega t), \tag{5}$$

where ΔP is the external pressure amplitude and ω is the angular frequency.

When the concentration of bubbles in the cluster is sufficiently high (about 1% or higher), the energy dissipation due to the acoustic radiation from the cluster to the surrounding liquid predominates over the energy dissipation from bubbles inside the cluster [33]. Then, the liquid in the cluster can be considered as an incompressible one and, instead of Eqs. (2), we can use the Rayleigh equations to determine the radii of the bubbles:

$$a_k\ddot{a}_k + \frac{3}{2}\dot{a}_k^2 = \frac{p_{ak} - p_c}{\rho_l}, \quad k = \overline{1, n}. \tag{6}$$

If it is necessary to take into account the pressure distribution around the bubbles, it is possible to use the cell method [34]. According to this method, each bubble of the kth fraction is placed at the center of a spherical cell of radius r_{bk}, which is determined by the formula

$$r_{bk} = \frac{a_k}{\alpha^{1/3}} \quad (k = \overline{1, n}), \quad \alpha = \frac{\sum_{j=1}^{n} N_j a_j^3}{R^3}.$$

Then, the Rayleigh equation with corrections to the pressure distribution around the bubbles in the cluster takes the form [35]

$$\left(1 - \frac{a_k}{r_{bk}}\right)a_k\ddot{a}_k + \left(\frac{3}{2} - \frac{2a_k}{r_{bk}} + \frac{a_k^4}{2r_{bk}^4}\right)\dot{a}_k^2 = \frac{p_{ak} - p_c}{\rho_l}, \quad k = \overline{1, n}. \tag{7}$$

This equation was derived under the assumption that the pressure at the outer boundary of a cell is equal to p_c.

Note that, at $n = 1$, $N = 1$, and $R \longrightarrow a$, the bubble cluster model given by Eqs. (1), (3)–(5), and (7) is reduced to the single-bubble model [10].

By virtue of the first assumption and the condition that the concentration of bubbles in the cluster is relatively high, the corrections appearing in Eq. (7) do not noticeably affect the dynamics of bubbles in the cluster. Therefore, below, we consider Eq. (6).

SMALL OSCILLATIONS OF BUBBLES IN THE CLUSTER

In [32], small oscillations of bubbles were studied and an amplitude–frequency characteristic was obtained for the case of a monodisperse cluster (a cluster with bubbles of one size, $n = 1$). In this section, we consider the case of a polydisperse cluster.

For each fraction of bubbles, the amplitude–frequency characteristic is expressed by the formula

$$\left|\frac{\tilde{A}_{a_k}}{\tilde{A}_{p_I}}\right| = \sqrt{x_k^2 + y_k^2}, \quad (k = \overline{1, n}), \tag{8}$$

where $\tilde{A}_{a_k} = A_{a_k}/a_{0k}$, $\tilde{A}_{p_I} = A_{p_I}/p_0$, and A_{a_k} and A_{p_I} are the amplitudes of deviations from the equilibrium values of the corresponding functions. In Eq. (8), the unknowns x_k and y_k are the solutions to the set of linear equations

$$\begin{cases} d_k x_k - e_k y_k + \sum_{j=1, j\neq k}^{n} (f_j x_j - g_j y_j) = -(1 + \theta^2) \\ e_k x_k + d_k y_k + \sum_{j=1, j\neq k}^{n} (g_j x_j + f_j y_j) = 0 \end{cases} \quad (k = \overline{1, n}) \tag{9}$$

with real coefficients expressed as

$$d_k = \Gamma_k - \theta^2((\alpha_{1k} + \alpha_{2k})C_d^2 - \Gamma_k) - \theta^4\alpha_{1k}C_d^2,$$

$$e_k = \theta C_d^2\mu_d + \theta^3(C_d\mu_d + \alpha_{2k}C_d^2),$$

$$f_k = -\theta^2\alpha_{2k}C_d^2, \quad g_k = \theta^3\alpha_{2k}C_d^2.$$

Here, the following dimensionless quantities were introduced: $\Gamma_k = 3\gamma + 2\sigma(3\gamma - 1)/(a_{0k}p_0)$, $\theta = \omega R_0/C_l$, $\alpha_{1k} = a_{0k}^2/R_0^2$, $\alpha_{2k} = N_k a_{0k}^3/R_0^3$, $C_d = C_l\sqrt{\rho_l/p_0}$, $\mu_d = 4\mu/(p_0 t_0)$, and $t_0 = R_0\sqrt{\rho_l/p_0}$. The quantities α_{1k} and α_{2k} represent the ratio of the surface area of a bubble from the kth fraction to that of the cluster and the concentration of the bubbles of the kth fraction in the cluster at the initial time, respectively.

For the case of a monodisperse cluster without any energy dissipation due to viscosity or acoustic radiation, the following expression was obtained for the eigenfrequency of a bubble:

$$\omega_c^2 = \frac{3\gamma p_0 + \frac{2\sigma}{a_0}(3\gamma - 1)}{\rho_l a_0^2(1 + \alpha_2/\alpha_1 - \alpha_2^{1/3})} < \omega_M^2. \tag{10}$$

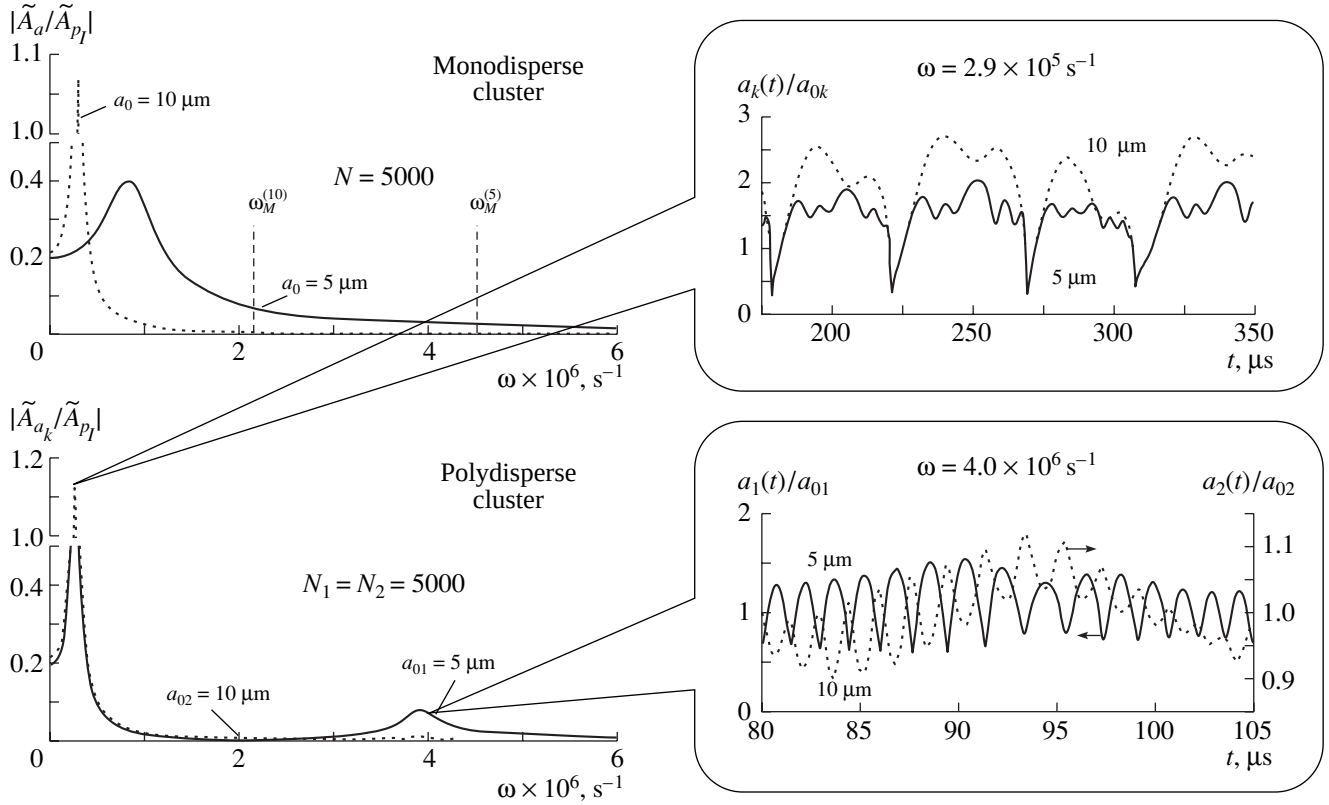

Fig. 1. Amplitude–frequency characteristics for two monodisperse clusters (top left) and a polydisperse cluster with $n = 2$ (bottom left); the patterns of bubble oscillations in the two-fraction cluster in the main resonance region (top right) and in the secondary resonance region (bottom right). The vertical dotted lines indicate the values of Minnaert frequencies $\omega_M^{(5)}$ and $\omega_M^{(10)}$ for single bubbles with initial radii of 5 and 10 μm, respectively.

Here and below, in expressions for the case of $n = 1$, we omit the subscripts indicating the fraction number. In formula (10), ω_M is the frequency of free oscillations of a single bubble in an unbounded liquid (the Minnaert frequency). In the case of a low concentration of bubbles in the cluster ($\alpha_2 \ll 1$), Eq. (10) takes the form

$$\omega_c^2 = \frac{3\gamma p_0 + \dfrac{2\sigma}{a_0}(3\gamma - 1)}{\rho_l a_0^2 (1 + N a_0/R_0)}. \qquad (11)$$

Introducing the effective parameters a_{eff} and σ_{eff} as

$$a_{eff} = a_0\sqrt{1 + N a_0/R_0}, \quad \sigma_{eff} = \sigma\sqrt{1 + N a_0/R_0},$$

we represent Eq. (11) in the form

$$\omega_c^2 = \frac{3\gamma p_0 + \dfrac{2\sigma_{eff}}{a_{eff}}(3\gamma - 1)}{\rho_l a_{eff}^2}.$$

Thus, when the concentration of bubbles is low, the eigenfrequency of the bubbles of radius a_0 with the surface tension σ in a monodisperse cluster is equal to the eigenfrequency of a single bubble of radius a_{eff} with the surface tension σ_{eff}.

Figure 1 (the left plots) represents the amplitude–frequency characteristics calculated from Eqs. (8) and (9) for two monodisperse clusters (the upper plot) and a polydisperse cluster (a two-fraction cluster with $n = 2$) (the lower plot). The values of the physical parameters that were used for calculation correspond to the parameters of water and air: $\rho_l = 10^3$ kg/m^3, $C_l = 1500$ m/s, $p_0 = 10^5$ Pa, $\sigma = 0.073$ N/m, $\mu = 10^{-3}$ Pa s, and $\gamma = 1.4$. The value of the initial radius of the cluster was taken to be $R_0 = 10^{-3}$ m. For a two-fraction cluster, in addition to the main resonance observed at a low frequency, a secondary resonance appears at higher frequencies. In Fig. 1 (the right plots), the patterns of nonlinear bubble oscillations in an acoustic field (at $\Delta P = 5 \times 10^5$ Pa) in the vicinities of these two resonances are demonstrated. One can see that, in the region of the main resonance, the bubbles of the two fractions oscillate in phase (at $\omega = 2.9 \times 10^5$ s^{-1}), and in the region of the secondary resonance, they oscillate in antiphase: the expansion period of the bubbles belonging to the first group coin-

cides with the compression period of the bubbles belonging the second group (at $\omega = 4 \times 10^6$ s^{-1}).

From set of equations (1) and (3)–(6) we eliminate all types of kinetic energy dissipation and consider the free oscillations of bubbles in a two-fraction cluster ($n = 2$). Then, the given set of equations will represent a particular case of the equations describing small oscillations of a conservative system with two degrees of freedom around its equilibrium position [36]:

$$\begin{cases} B_1\ddot{Z}_1 + H\ddot{Z}_2 + b_1 Z_1 + hZ_2 = 0, \\ H\ddot{Z}_1 + B_2\ddot{Z}_2 + hZ_1 + b_2 Z_2 = 0. \end{cases}$$

For the problem under consideration, we have

$$Z_1 = \Delta a_1(t), \quad Z_2 = \Delta a_2(t),$$

$$B_1 = \left(1 + N_1\frac{a_{01}}{R_0}\right)\frac{N_1 a_{01}^3}{R_0},$$

$$B_2 = \left(1 + N_2\frac{a_{02}}{R_0}\right)\frac{N_2 a_{02}^3}{R_0}, \quad H = \frac{N_1 N_2 a_{01}^2 a_{02}^2}{R_0^2},$$

$$b_1 = \frac{N_1 a_{01}}{\rho_l R_0}\left(3\gamma p_0 + \frac{2\sigma}{a_{01}}(3\gamma - 1)\right),$$

$$b_2 = \frac{N_2 a_{02}}{\rho_l R_0}\left(3\gamma p_0 + \frac{2\sigma}{a_{02}}(3\gamma - 1)\right), \quad h = 0.$$

The normal frequencies for the given system are expressed by the formula

$$\omega_{1,2}^2 = \frac{\beta_1^2 + \beta_2^2 \pm \sqrt{(\beta_1^2 + \beta_2^2)^2 - 4\chi\beta_1^2\beta_2^2}}{2\chi}, \qquad (12)$$

where $\chi = 1 - H^2/B_1B_2$, $\beta_1 = \sqrt{b_1/B_1}$, and $\beta_2 = \sqrt{b_2/B_2}$. The quantities β_1 and β_2 determine the frequencies in the partial coordinate system, i.e., in the system where one of the coordinates is assumed to be equal to zero. These frequencies are determined as

$$\beta_k^2 = \frac{3\gamma p_0 + \dfrac{2\sigma}{a_{0k}}(3\gamma - 1)}{\rho_l a_{0k}^2(1 + N_k a_{0k}/R_0)}, \quad k = 1, 2.$$

The latter expression determines eigenfrequencies (11) of the bubbles with the initial radii a_{01} (at $k = 1$) or a_{02} (at $k = 2$) in a monodisperse cluster.

Note that formula (12) is typical of the theory of coupled oscillators. If we consider the bubbles in different fractions as coupled oscillators, this formula will express the splitting and shift of the eigenfrequencies of bubble oscillations. If we consider other types of interaction between the bubbles, for example, Bjerknes forces [37], in the linear approximation we obtain an expression similar to Eq. (12) but with another value of the coupling coefficient χ.

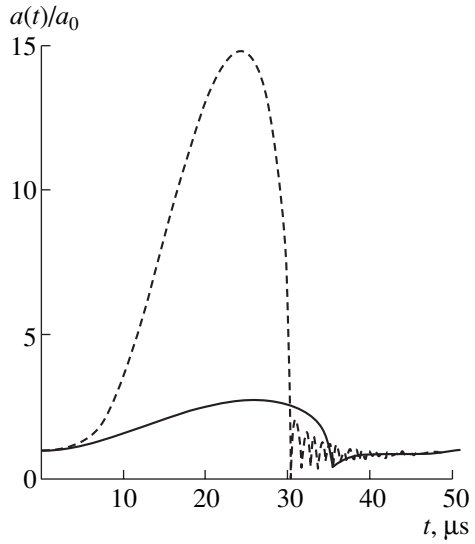

Fig. 2. Oscillations of a single bubble (the dashed line) and a bubble in a monodisperse cluster (the solid line) with the same initial bubble radius $a_0 = 5$ μm within the period of the acoustic field at $P = 1.5 \times 10^5$ Pa. The number of bubbles in the cluster is $N = 10^4$.

For the two-fraction cluster illustrated in Fig. 1, the relative errors in the resonance (normal) frequencies calculated according to Eq. (12) and Eqs. (8), (9) do not exceed 1%. Thus, viscosity and acoustic radiation produce no noticeable effect on the eigenfrequencies of bubbles.

Note that, for the two-fraction cluster under consideration, the coupling coefficient $H/\sqrt{B_1B_2} \approx 0.94$ is comparable to the quantity $|\beta_1^2 - \beta_2^2|/(\beta_1\beta_2) \approx 2.6$, which means that (see [36]) the interaction between the bubbles belonging to different fractions within the cluster is fairly strong. Hence, the interaction between the bubbles considerably affects the dynamics of the bubble cluster and cannot be ignored.

NONLINEAR BUBBLE OSCILLATIONS IN A CLUSTER

To analyze the nonlinear oscillations of bubbles in a cluster, we performed numerical calculations for the set of equations (1), (3–6) by using the Runge–Kutta method based on the Dorman–Prince formulas with an automatic step selection [38].

A comparison between the dynamics of a single bubble and that of a bubble in a monodisperse cluster is represented in Fig. 2. One can see that the bubble oscillations in a monodisperse cluster differ in character from single-bubble oscillations: for a bubble in a cluster, the oscillation amplitude and the depth of collapse are smaller than those of a single bubble. This means that, unlike a single bubble, a bubble in a cluster may experience external pressures with high amplitudes.

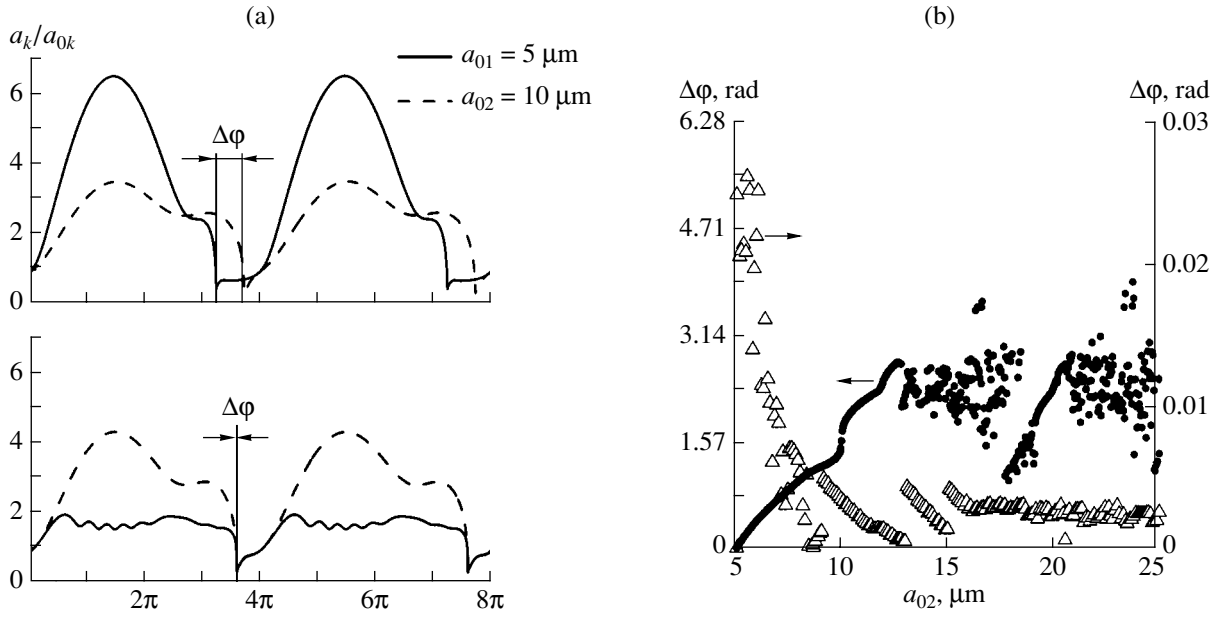

Fig. 3. Comparison of bubble oscillations in two monodisperse clusters and in a two-fraction cluster at $\Delta P = 5 \times 10^5$ Pa, $\omega = 2\pi \times$ 20 kHz, and $N = 10^4$ ($N_1 = N_2 = N/2$): (a) the dependence of the bubble radius on time and (b) the difference between the maximum compression phases (a_{01} = 5 μm is fixed and a_{02} varies).

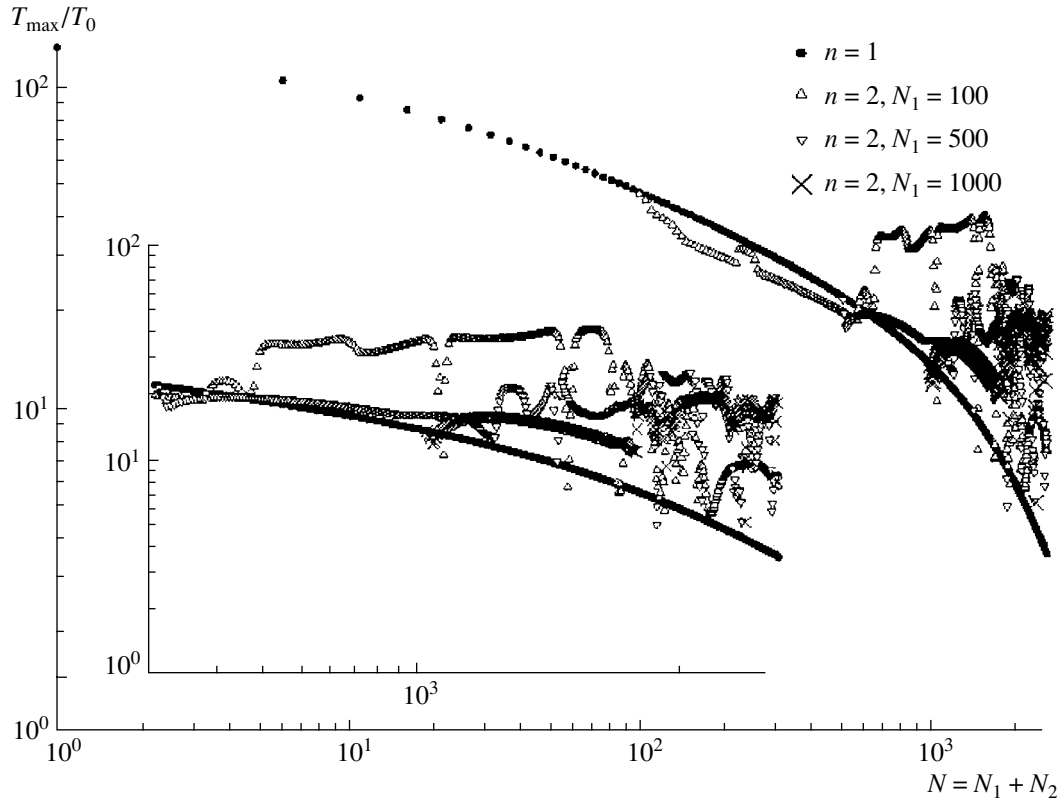

Fig. 4. Maximum temperature in a bubble with the initial radius a_{01} = 5 μm versus the total number of bubbles in the cluster at $\Delta P = 5 \times 10^5$ Pa. For the case of $n = 2$: N_1 is fixed and N_2 varies; a_{02} = 10 μm.

Therefore, one can conclude that sonoluminescence in a cluster should be of lower intensity than single-bubble sonoluminescence. Experimental studies of multibubble sonoluminescence [8, 9] showed that, after a certain threshold, an increase in the ultrasonic power leads to the formation of small bubble clusters, which results in a drastic decrease in the sonoluminescence intensity.

We also studied the effect of polydispersity on the bubble dynamics in a cluster. The effect of synchronization of the collapse phases for bubbles in a polydisperse cluster is represented in Fig. 3. From Fig. 3a, one can see that, in two separate monodisperse clusters with different initial bubble radii (a_{01} = 5 μm and a_{02} = 10 μm), the maximum compression of the bubbles occurs at different instants of time. However, when these bubbles are placed into one cluster (which is now two-fraction), their compression occurs in phase irrespective of their size. One can see that, in this case, the oscillation amplitude of a bubble from the first fraction has become smaller, whereas the oscillation amplitude of a bubble from the second fraction has become greater. This can be explained by the energy transfer between the bubbles of different radii [36]: bubbles of the first fraction give part of their energy to the bubbles of the second fraction. Figure 3b shows the difference between the maximum compression phases of bubbles with different initial radii as a function of the initial bubble radius characterizing the second fraction. The phase difference was calculated by the formula

$$\Delta\varphi = \varphi_1^{(\mathrm{col})} - \varphi_2^{(\mathrm{col})}; \quad \varphi_k^{(\mathrm{col})} = \omega t_k^{(\mathrm{col})}, \quad k = 1, 2,$$

where $t_k^{(\mathrm{col})}$ is the instant at which a bubble with the initial radius a_{0k} reaches its minimum size. For two monodisperse clusters, the difference between the collapse phases is represented by dots (the left-hand ordinate axis), and for a two-fraction cluster, by triangles (the right-hand ordinate axis). The synchronization (autophasing) effect in a system consisting of two or three cavities was experimentally investigated in [39]. In a system of two cavities that were initially excited so as to oscillate in antiphase, a subsequent synchronization of oscillation phases was observed. Note that, in most cases, the experiments revealed two resonances, the first of which produced a stronger effect on the system than the second. This pattern agrees well with Fig. 1, which refers to a multitude of bubbles of two different sizes rather than to two cavities.

Figure 4 displays the effect of a bubble collapse intensification due to the energy transfer between the fractions. Namely, with the introduction of some bubbles of one radius into a cluster containing bubbles of another radius, one obtains a deeper collapse of the latter bubbles. This result agrees well with the experiment [6]: it was found that, in a cluster with bubbles of two different radii, the smaller bubbles in the presence of greater bubbles exhibit a stronger collapse. The experimental result was also explained by the energy transfer.

CONCLUSIONS

The analytical study of small bubble oscillations on the basis of the bubble cluster model proposed in this paper showed that the eigenfrequency of bubble oscillations in a monodisperse cluster is lower than the eigenfrequency of a single bubble with the same initial radius. It was found that small oscillations of a two-fraction cluster can be considered as oscillations of a linear conservative system with two degrees of freedom. This explains the presence of the secondary resonance in addition to the main resonance in a two-fraction cluster. In the region of the main resonance, bubbles of different fractions oscillate in phase, whereas in the region of the secondary resonance, in antiphase. The kinetic energy dissipation due to viscosity and acoustic radiation does not noticeably affect the behavior of the system.

The numerical analysis of nonlinear bubble oscillations in a cluster showed that, unlike a single bubble, a bubble in a cluster may experience sound pressures of relatively high amplitudes. For a polydisperse cluster, the following effects are revealed: a synchronization of the collapse phases of bubbles with different radii and a collapse intensification for bubbles of one size in the presence of bubbles of another size. The latter effect is a result of the energy transfer between bubbles of different radii.

ACKNOWLEDGMENTS

This work was supported by the INCO Copernicus Foundation (European Commission, DG-XII Science, Research and Development Contract IC15-CT98-0141), the Ministry of Science of Russian Federation, and the Academy of Sciences of Bashkortostan. We are grateful to Academician R.I. Nigmatullin for useful discussions.

REFERENCES

1. B. P. Barber and S. J. Putterman, Nature (London) **352**, 318 (1991).
2. D. F. Gaitan, C. C. Crum, C. C. Church, and R. A. Roy, J. Acoust. Soc. Am. **91**, 3166 (1992).
3. B. P. Barber, C. C. Wu, P. H. Roberts, *et al.*, Phys. Rev. Lett. **72**, 1380 (1994).
4. C. C. Crum, Phys. Today **9**, 22 (1994).
5. V. K. Kedrinskiĭ, *Hydrodynamics of Explosion: Experiment and Models* (Sib. Otd. Ross. Akad. Nauk, Novosibirsk, 2000) [in Russian].
6. D. V. Voronin, G. N. Sankin, V. S. Teslenko, *et al.*, Prikl. Mekh. Tekh. Fiz. **44** (1), 22 (2003).
7. S. W. Yoon, L. A. Crum, A. Prosperetti, and N. Q. Lu, J. Acoust. Soc. Am. **89**, 700 (1991).
8. S. Hatanaka, K. Yasui, T. Kozuka, *et al.*, Ultrasonics **40**, 655 (2002).
9. H. Mitome, in *Proceedings of World Congress on Ultrasonics, WCU, Paris, 2003* (Paris, 2003), pp. 585–589.

10. R. I. Nigmatullin, *Dynamics of Multiphase Media* (Nauka, Moscow, 1987) [in Russian].
11. V. E. Nakoryakov, B. G. Pokusaev, and I. R. Shreĭber, *Wave Propagation in Gas–Liquid and Vapor–Liquid Media* (Inst. Tekh. Fiz., Novosibirsk, 1983) [in Russian].
12. L. Wijngaarden, J. Fluid Mech. **33**, 465 (1968).
13. J. Hansson and K. A. Morch, J. Appl. Phys. **51** (9), 4651 (1980).
14. I. Hansson, V. K. Kedrinskii, and K. A. Morch, J. Phys. D: Appl. Phys. **15**, 1725 (1982).
15. K. A. Morch, Appl. Sci. Res. **38**, 313 (1982).
16. P. M. Kanthale, P. R. Gogate, A. B. Pandit, and A. M. Wilhelm, Ultrason. Sonochem. **10**, 181 (2003).
17. V. K. Kedrinskiĭ, Yu. I. Shokin, V. A. Vshivkov, *et al.*, Dokl. Akad. Nauk **381** (6), 773 (2001) [Dokl. Phys. **46** (12), 856 (2001)].
18. R. Omta, J. Acoust. Soc. Am. **82**, 1018 (1987).
19. A. Biesheuvel and L. Wijngaarden, J. Fluid Mech. **148**, 301 (1984).
20. L. D' Agostino and C. E. Brennen, J. Acoust. Soc. Am. **84**, 2126 (1988).
21. L. D' Agostino and C. E. Brennen, J. Fluid Mech. **199**, 155 (1989).
22. S. Kumar and C. E. Brennen, J. Acoust. Soc. Am. **89**, 707 (1991).
23. S. Kumar and C. E. Brennen, J. Fluid Mech. **253**, 565 (1993).
24. V. N. Alekseev, V. G. Andreev, G. A. Romanenko, and S. A. Rybak, Akust. Zh. **47**, 442 (2001) [Acoust. Phys. **47**, 376 (2001)].
25. O. V. Voinov and A. M. Golovin, Mekh. Zhidk. Gaza, No. 3, 117 (1970).
26. G. L. Chahine and R. Duraiswami, J. Fluids Eng. **114**, 680 (1992).
27. J. F. Scott, J. Fluid Mech. **113**, 487 (1981).
28. H. Takahira, T. Akamatsu, and S. Fujikawa, JSME Int. J., Ser. B **37** (2), 297 (1994).
29. N. C. Skaropoulos, H. D. Yagridou, and D. P. Chrissoulidis, J. Acoust. Soc. Am. **113**, 3001 (2003).
30. L. L. Foldy, Phys. Rev. **67** (3-4), 107 (1945).
31. A. Prosperetti and A. Lezzi, J. Fluid Mech. **168**, 457 (1986).
32. R. I. Nigmatullin, I. Sh. Akhatov, and N. K. Vakhitova, Dokl. Akad. Nauk **348** (6), 768 (1996) [Phys. Dokl. **41** (6), 276 (1996)].
33. R. I. Nigmatullin, I. Sh. Akhatov, N. K. Vakhitova, and É. Sh. Nasibullaeva, Vestn. Bell. Gos. Univ., No. 2, 12 (1999).
34. R. I. Nigmatullin, *Foundations of Mechanics of Heterogeneous Media* (Nauka, Moscow, 1978) [in Russian].
35. R. I. Nigmatullin, I. Sh. Akhatov, N. K. Vakhitova, and E. Sh. Nasibullayeva, in *Nonlinear Acoustics at the Turn of Millenium*, Vol. 524 of *AIP Conference Proceedings*, p. 455 (Melville, 2000).
36. L. I. Mandel'shtam, *Lectures on the Theory of Oscillations* (Nauka, Moscow, 1972) [in Russian].
37. V. N. Alekseev and V. P. Yushin, Akust. Zh. **32**, 748 (1986) [Sov. Phys. Acoust. **32**, 469 (1986)].
38. E. Hairer, S. Norsett, and G. Wanner, *Solving Ordinary Differential Equations*, Vol. 1: *Nonstiff Problems* (Springer, Berlin, 1987; Mir, Moscow, 1990).
39. V. V. Bredikhin, Yu. A. Kobelev, and N. I. Vasilenko, J. Acoust. Soc. Am. **103**, 1775 (1998).

Translated by E. Golyamina

Acoustical Physics, Vol. 51, No. 6, 2005, pp. 713–718. From Akusticheskiĭ Zhurnal, Vol. 51, No. 6, 2005, pp. 822–828.

The Propagation of a Nonlinear Sound Wave in an Unconsolidated Granular Medium[1]

K. A. Naugolnykh[1] and I. B. Esipov[2]

[1] *University of Colorado, Cires, Environmental Technology Laboratory (Zeltech), USA*
e-mail: Konstantin.Naugolnykh@noaa.gov
[2] *Andreev Acoustics Institute, Moscow, Russia*
e-mail: ibesipov@akin.ru

Received March 11, 2005

Abstract—The propagation of a high-intensity sound wave in an unconsolidated medium is considered. Dissipation effects are taken into account on the basis of Buckingham's theory of a relaxation mechanism of sound attenuation in a saturated sediment. The nonlinear evolution equation for the relaxing medium is obtained, and the solutions of this equation are analyzed. The second-harmonic generation in such a medium decays, as does the linear sound wave of the same frequency. The stationary weak shock profile has a specific form due to relaxation effects. © *2005 Pleiades Publishing, Inc.*

INTRODUCTION

The evolution of a high-intensity sound wave is determined mainly by nonlinear and dissipative effects. If an initially sinusoidal wave is intense, the steepness of the wave fronts increases, resulting in the occurrence of a discontinuity in each period of the wave. On the other hand, the influence of dissipative processes tends to smooth the wave profile, diminishing the gradients of velocity and temperature. Consequently, during the propagation of an intense wave, its profile is formed as a result of the balance of nonlinear and dissipative effects. Wave propagation in a nonlinear medium with viscosity and thermal conductivity leading to square-law attenuation was considered both theoretically and experimentally (see, e.g., [1]). Later, Buckingham [2] developed the theory of sound propagation in a medium with a memory, where instantaneous stress is followed by a decrease in stress level with increasing time in accordance with the equation of relaxation. This medium can be considered as a model of saturated marine sediments [3]. The wave equation in this case includes a new dissipation term representing internal losses arising from interparticle contacts. The attenuation coefficient of sound according to this theory would scale with the first power of frequency. Marine sediments usually have the specific linear frequency dependence of the coefficient of sound attenuation [4, 5]. A power-law frequency dependence of the attenuation is also found in many biological tissues [6]. The balance of nonlinearity and dissipation in such a medium has specific features observed in the experiment discussed in [7], some of which are considered in the present paper.

[1] The text was submitted by the authors in English.

EVOLUTION EQUATION

A unified theory of sound propagation in saturated marine sediments is developed on the basis of a linear wave equation that includes a new dissipation term representing internal losses arising from interparticle contacts. An unconsolidated sediment is considered as a two-phase medium consisting of mineral particles and seawater but possessing no rigid frame. The internal losses are determined by grain–grain contacts. The analysis is based on a one-dimensional linear wave equation in which intergranular dissipation is represented by a loss term that takes into account the hysteresis, or memory, of granular media. The effect of the memory on the wave equation is accommodated by setting the frictional stress equal to a temporal convolution between the particle velocity and the material memory function $h(t)$ [2]:

$$\frac{\partial^2\varphi}{\partial x^2} - \frac{1}{c_0^2}\frac{\partial^2\varphi}{\partial t^2} + \frac{b}{\rho_0 c_0^2}\frac{\partial^3}{\partial t\partial x^2}[h(t)\otimes\varphi(t)] = 0, \quad (1)$$

where c_0 is the sound speed in a medium in the absence of grain–grain losses. The losses can be expressed in terms of the bulk properties of the two materials—mineral grain and seawater [2]—and ρ_0 is the equilibrium density of the medium. The material response function $h(t)$ can be chosen to be [3]

$$h(t) = u(t)t_0^{-1}\left(1 + \frac{t}{t_0}\right)^{-n}. \quad (2)$$

Here, $u(t)$ is the step function that ensures that the response of the medium is causal, and t_0 and n are the material parameters; t_0 actually has a sense of the time of relaxation. The dissipation coefficients $b = 4/3\eta_f + \zeta_f$

1063-7710/05/5106-0713$26.00 © 2005 Pleiades Publishing, Inc.

and η_f, ζ_f correspond to the intergranular friction of the medium, and the term $h(t) \otimes \varphi(t)$ is a temporal convolution. The dissipation term in Eq. (1) is similar to that of a hydrodynamic equation having the derivative $\partial^2/\partial x^2$, but the operand, instead of being the particle velocity, is the convolution of particle velocity with the impulse response function of the material $h(t)$. If $h(t)$ is a Dirac delta function, the convolution term reduces to the particle velocity.

Consider the propagation of a wave in one direction, which allows for the transformation of Eq. (1) into a first-order equation.

The wave equation operator can be presented as a product of the two operators:

$$\frac{\partial^2\varphi}{\partial x^2} - \frac{1}{c_0^2}\frac{\partial^2\varphi}{\partial t^2} = \left(\frac{\partial}{\partial x} - \frac{1}{c_0}\frac{\partial}{\partial t}\right)\left(\frac{\partial}{\partial x} + \frac{1}{c_0}\frac{\partial}{\partial t}\right)\varphi. \quad (3)$$

For a wave moving in a positive direction x in a perfect medium,

$$-\frac{1}{c_0}\frac{\partial\varphi}{\partial t} = \frac{\partial\varphi}{\partial x}, \quad (4)$$

so, in a medium with weak dissipation, one can use

$$\frac{\partial\varphi}{\partial x} - \frac{1}{c_0}\frac{\partial\varphi}{\partial t} \simeq 2\frac{\partial\varphi}{\partial x}, \quad (5)$$

and, after integration of Eq. (1) with respect to x, one obtains

$$\frac{\partial\varphi}{\partial x} + \frac{1}{c_0}\frac{\partial\varphi}{\partial t} + \frac{b}{2\rho_0 c_0^2}\frac{\partial^2}{\partial t\partial x}[h(t) \otimes \varphi(t)] = 0. \quad (6)$$

Changing the variables

$$x \longrightarrow x', \quad t - x/c_0 = \tau,$$
$$\frac{\partial}{\partial t} = \frac{\partial}{\partial\tau}, \quad \frac{\partial}{\partial x} = -c_0^{-1}\frac{\partial}{\partial\tau} + \frac{\partial}{\partial x'}, \quad (7)$$

one obtains

$$\frac{\partial\varphi}{\partial x'} = \frac{b}{2\rho_0 c_0^3}\frac{\partial^2}{\partial\tau^2}[h(\tau) \otimes \varphi(\tau)] = 0. \quad (8)$$

Accounting for nonlinear effects leads to an additional term in evolution equation (8) [1]:

$$\frac{\partial\varphi}{\partial x'} - \frac{\epsilon}{2c_0^3}\left(\frac{\partial\varphi}{\partial\tau}\right)^2 - \frac{b}{2\rho_0 c_0^3}\frac{\partial^2}{\partial\tau^2}[h(\tau) \otimes \varphi(\tau)] = 0. \quad (9)$$

If one transforms the nonlinear term using the equation

$$-\frac{1}{c_0}\frac{\partial}{\partial\tau} = \frac{\partial}{\partial x'}, \quad (10)$$

one obtains

$$\frac{\partial\varphi}{\partial x'} - \frac{\epsilon}{2c_0}\left(\frac{\partial\varphi}{\partial x'}\right)^2 - \frac{b}{2\rho_0 c_0^3}\frac{\partial^2}{\partial\tau^2}[h(\tau) \otimes \varphi(\tau)] = 0. \quad (11)$$

To obtain the equation in terms of particle velocity v, we make the substitution $v = \partial\varphi/\partial x'$, and differentiate over x' in the nonlinear term; then, we return back to $\partial/\partial\tau$

$$\frac{\partial v}{\partial x'} - \frac{\epsilon}{2c_0^2}\frac{\partial v^2}{\partial\tau} - \frac{b}{2\rho_0 c_0^3}\frac{\partial^3}{\partial\tau^2\partial x'}[h(\tau) \otimes \varphi(\tau)] = 0, \quad (12)$$

or

$$\frac{\partial v}{\partial x'} - \frac{\epsilon}{c_0^2}v\frac{\partial v}{\partial\tau} = \frac{b}{2\rho_0 c_0^3}\frac{\partial^3}{\partial\tau^2\partial x'}[h(\tau) \otimes \varphi(\tau)] \quad (13)$$

the evolution equation of a nonlinear wave in the relaxing medium.

A stationary wave, in particular, the stationary shock profile, is governed by the equation

$$-\frac{\epsilon}{2c_0^2}\frac{\partial v^2}{\partial\tau} - \frac{b}{2\rho_0 c_0^3}\frac{\partial^3}{\partial\tau^2\partial x'}[h(\tau) \otimes \varphi(\tau)] = 0, \quad (14)$$

which corresponds to the balance condition of nonlinear and dissipative processes.

PROPAGATION OF A LINEAR PLANE WAVE

Let us now consider linear plane wave propagation in an unconsolidated granular medium. The presence of a relaxation process in the medium leads to specific attenuation of a sound wave propagating in it, due to developing irreversible effects. The evolution equation can be used to obtain sound-wave attenuation in the relaxing medium in a simple way similar to that derived by Buckingham [2] on the basis of the wave equation. A proper wave equation could be in the form

$$\frac{\partial\varphi}{\partial x} + \frac{1}{c_0}\frac{\partial\varphi}{\partial t} + \frac{b}{2\rho_0 c_0^2}\frac{\partial^2}{\partial t\partial x}[h(t) \otimes \varphi(t)] = -S\delta(t)\delta(x), \quad (15)$$

where S is the strength of an impulsive source. The standard method of solving a linear inhomogeneous equation is to apply the Fourier transform.

The Fourier transform with respect to time is

$$\left[1 + i\omega\frac{b}{2\rho_0 c_0^2}H(i\omega)\right]\frac{\partial\Phi}{\partial x} - ik_0\Phi(i\omega) = S\delta(x),$$
$$k_0 = \frac{\omega}{c_0}, \quad (16)$$

$\Phi(i\omega)$ and $H(i\omega)$ are the Fourier transforms of φ, and $h(t)$. Convolution reduces this to a product of $H(i\omega)\dfrac{\partial\Phi}{\partial x}$. A second Fourier transform with respect to x leads to the algebraic equation

$$\left\{-ik_0 - \left[1 + i\omega\frac{b}{2\rho_0 c_0^2}H(i\omega)\right]is\right\}\Phi_s = -S, \quad (17)$$

where Φ_s is the Fourier transform of Φ with respect to x, so that $\Phi(i\omega, x) = \int \Phi_s e^{-isx} ds$. It follows that

$$\Phi_s = \frac{S}{is\left[1 + \frac{i\omega b}{2\rho_0 c_0^2}H(i\omega)\right] + ik_0} = \frac{S}{isq + ik_0} = \frac{S}{iq\left(s + \frac{k_0}{q}\right)}. \quad (18)$$

Here,

$$q = 1 + \frac{i\omega b}{2\rho_0 c_0^2}H(i\omega), \quad (19)$$

and

$$H(i\omega) = \int_{-\infty}^{\infty} h(t)\exp(-i\omega t)dt = t_0^{n-1}\int_0^{\infty} t^{-n}\exp(-i\omega t)dt = \frac{\Gamma(1-n)}{(i\omega t_0)^{1-n}}, \quad (20)$$

where $\Gamma(1 - n)$ is the gamma function.

Now, by substituting Eqs. (20) into Eq. (19), the function q can be expressed as

$$q = 1 + (i\omega t_0)^n \chi_f, \quad \chi_f = \frac{b\Gamma(1-n)}{2\rho_0 c_0^2 t_0}. \quad (21)$$

An inverse transform over the wave number s leads to the equation

$$\Phi(i\omega, x) = \frac{S}{2\pi i q}\int_{-\infty}^{\infty}\left(s + \frac{k_0}{q}\right)^{-1}\exp(isx)ds = \frac{S}{2\pi i q}\int_{-\infty}^{\infty}\frac{e^{isx}ds}{\left(s + \frac{k_0}{q}\right)} = \frac{S}{q}\exp\left(-\frac{ik_0}{q}x\right). \quad (22)$$

The residue is $s_0 = -k_0/q$, and the equation $\oint f(z)dz = 2\pi i a(z_0)$ is used; $a(z_0)$ is the coefficient of the term $(1/z - z_0)$ in the Loran expansion. Then, after substitution into Eq. (21), one obtains

$$\Phi(i\omega, x) = \frac{S}{1 + (i\omega t_0)^n \chi_f}\exp\left(-i\frac{\omega|x|}{c_0(1 + (i\omega t_0)^n \chi_f)}\right), \quad (23)$$

$$\Phi(i\omega, x) = \frac{S}{1 + (i\omega t_0)^n \chi_f}\exp\left\{-\frac{i\omega|x|}{c_0 \mathrm{Re}(1 + (i\omega t_0)^n \chi_f)} - \frac{i\omega|x|}{c_p}\left[-\frac{c_p}{c_0}\mathrm{Im}\frac{1}{1 + (i\omega t_0)^n \chi_f}\right]\right\}. \quad (24)$$

The result obtained is convenient to present in terms of a complex wave number. Indeed, introducing

$$c_p = c_0 \mathrm{Re}(1 + (i\omega t_0)^n \chi_f), \quad \text{and} \quad \beta = -\frac{c_p}{c_0}\mathrm{Im}\frac{1}{1 + (i\omega t_0)^n \chi_f}, \quad (25)$$

the result obtained can be presented as

$$k = \frac{\omega}{c_p}(1 - j\beta). \quad (26)$$

Then, one can use the following representation:

$$\Phi(i\omega, x) = e^{-i\omega x/c_p}e^{-\beta\omega x/c_p}. \quad (27)$$

In the particular case where $n \ll 1$, the expressions for β and c_p can be approximated. Following [2], one obtains

$$c_p \approx c_0\sqrt{1 + \chi_f}\left[1 + \frac{2\beta_p}{\pi}\ln(|\omega|t_0)\right], \quad (28)$$

and

$$\beta \approx \beta_p \mathrm{sgn}(\omega), \quad (29)$$

where

$$\beta_p = \frac{n\pi\chi_f}{4(1 + \chi_f)}. \quad (30)$$

In most circumstances, the dispersion is weak, and one has

$$c_p \approx c_0\sqrt{1 + \chi_f}. \quad (31)$$

Since the loss tangent β_p and the phase speed c_p are independent of frequency, the attenuation coefficient is a linear function of frequency ω,

$$\alpha_p = \frac{\omega\beta_p}{c_p} = \frac{\omega n\pi\chi_f}{4(1 + \chi_f)^{3.2}}, \quad (32)$$

and the associated dispersion is expressed by Eq. (31).

These results of the relaxation theory are consistent with the observed geoacoustic properties of many unconsolidated marine sediments. In particular, the attenuation coefficient of a sound wave propagating in such a medium is proportional to the first power of frequency. As an example, our previous data can be offered [7]. Sound attenuation in water-saturated unconsolidated marine sediment was measured using a wide-band laser-generated sound pulse. The signal was registered before and after propagation through a sam-

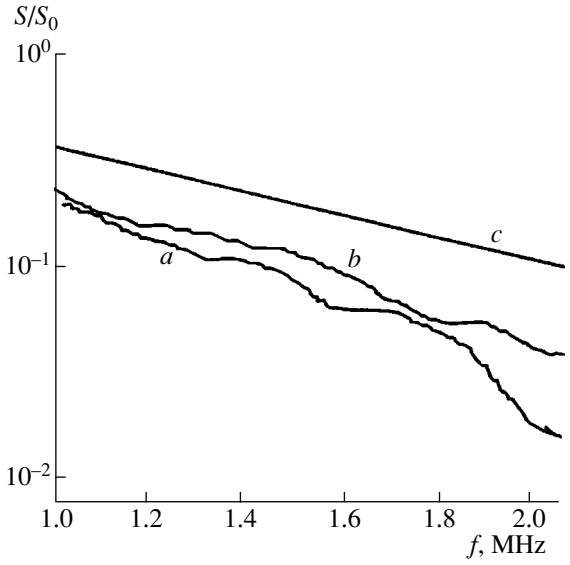

Fig. 1. Transient performance for the sample of crust. Low-amplitude sound pulse (*a*), high-intensity sound pulse (*b*), and theoretical curve (*c*).

ple of water-saturated cobalt–manganese crust (CMC). The measured spectral transient performance is represented in Fig. 1 (curves *a* and *b*). The sample of crust used in the experiment has a grainy structure with a granule diameter d of (1–5) $\times 10^2$ μm; for such a medium, the coefficient $\beta = 0.015$ [2], so, in accordance with Eq. (30), $\alpha_p = 10^{-7}\omega$ cm^{-1}. A corresponding theoretical transfer function is presented in Fig. 1 (curve *c*). The comparison of experimental and theoretical curves indicate that the attenuation of sound in an unconsolidated water-saturated medium depends linearly on the frequency [7], in accordance with the theory of relaxation-mechanism attenuation [2].

NONLINEAR WAVE IN A MEDIUM WITH RELAXATION

The evolution of an initially sinusoidal wave during propagation may be treated as a variation of its spectral composition. The growth of high-frequency harmonics in the course of plane sinusoidal wave propagation in a viscous heat-conductive medium has been considered in many papers, such as [8]. The generation of harmonics of a high-intensity wave propagating in a medium with relaxation that is modeled as an unconsolidated medium can be considered using the method of successive approximations in application to evolution equation (13).

Let us seek the solution as a sum:

$$\varphi = \varphi_1 + \varphi_2 \ldots \tag{33}$$

The boundary condition can be chosen as

$$\varphi_1 = \varphi e^{i\omega_1 t}, \quad \varphi_2 = 0, \quad x = 0. \tag{34}$$

Then, the first-order (linear) equation, according to Eq. (9), is

$$\frac{\partial \varphi}{\partial x'} - \frac{b}{2\rho_0 c_0^3}\frac{\partial^2}{\partial \tau^2}[h(\tau) \otimes \varphi(\tau)] = 0. \tag{35}$$

The solution of this equation can be represented as

$$\varphi_1 = \varphi_{10} e^{-\alpha_p x'} e^{i\omega_1 \tau}. \tag{36}$$

The second-order equation is

$$\frac{\partial \varphi}{\partial x'} - \frac{b}{2\rho_0 c_0^3}\frac{\partial^2}{\partial \tau^2}[h(\tau) \otimes \varphi(\tau)] = \frac{\epsilon}{2c_0^3}\left(\frac{\partial \varphi_1}{\partial \tau}\right)^2 = N\varphi_{10}^2 e^{-i2\omega_1 x'/c_p} e^{-2\alpha_p x'} e^{i2\omega_1 \tau}, \tag{37}$$

$$N = \frac{\epsilon}{2c_0^3}. \tag{38}$$

The Fourier transform with respect to t and x' gives

$$\left\{-ik_0 - \left[1 + i\omega\frac{b}{2\rho_0 c_0^2}H(i\omega)\right]is\right\}\Phi_s = -NS_t S_x, \tag{39}$$

where Φ_s is the Fourier transform with respect to x' for φ and $S_t S_x$ are the Fourier transforms of $(\partial\varphi_{11}/\partial\tau)^2$. Here, we are taking into account the dependence of τ on both the time t and spatial variable x according to Eq. (7). After the inverse transform with respect to x', the equation for $\varphi_2(i\omega\tau)$ reads

$$\varphi_2(i\omega\tau) = \varphi_{20} e^{-i2\omega x' x/c_p} e^{-2\alpha_p x'} e^{i2\omega_1 \tau}, \tag{40}$$

the second harmonic of a wave propagating in a relaxing medium attenuates as a small-intensity (linear) wave of the same frequency, unlike the case of conventional attenuation due to viscous effects. Indeed, in that case, the coefficient of absorption of the second harmonic is twice, rather than four times, the absorption coefficient for the first harmonic and, therefore, increases linearly rather than as the square of the frequency [8].

STATIONARY WEAK SHOCK-WAVE PROFILE

The important characteristic of the medium is the weak shock-wave stationary profile that indicates the balance of nonlinear and dissipative effects. A comparison of the stationary shock-wave profile to the initial profile of the problem under consideration allows us to predict the evolution of the initial profile and to choose the proper approximations. Indeed, if the initial profile is smooth and has a scale of thickness larger than the stationary wave thickness, it will become steeper in the process of propagation under the action of nonlinear effects, and the dissipative effects can be neglected in

this case. In contrast, the thin—in comparison to the stationary front—initial profile will be smoothed during the process of propagation as a result of the action of dissipative effects; nonlinear effects are negligible in this case.

Consider first the weak shock-wave profile in a conventional viscous medium. If $h(\tau) = \delta(\tau)$, the dissipative term of Eq. (14) is

$$\frac{b}{2\rho_0 c_0^3}\frac{\partial^3}{\partial\tau\partial x'}[h(\tau)\otimes\varphi(\tau)] = \frac{b}{2\rho_0 c_0^3}\frac{\partial^2 v}{\partial\tau^2} \sim \frac{b}{2\rho_0 c_0^3}\frac{v}{\tau^2}, \quad (41)$$

so an estimate can be made of the balance of nonlinear and dissipative effects as follows, using Eq. (14):

$$\frac{\epsilon v^2}{2c_0^2\tau} \sim \frac{b}{2\rho_0 c_0^3}\frac{v}{\tau^2}. \quad (42)$$

The estimate of the shock front duration τ_f is

$$\tau_f \sim \frac{b}{2\epsilon v\rho_0 c_0} \simeq \frac{\mu}{\epsilon v c_0}, \quad \mu = \frac{b}{\rho_0}, \quad (43)$$

where μ is the kinematic viscosity and the shock front thickness l_f, in agreement with Lighthill [9], is

$$l_f = c_0\tau_f = \frac{\mu}{\epsilon v}. \quad (44)$$

To obtain the solution for the shock-wave profile, we introduce dimensionless variables into Eq. (14):

$$V(x') = v/v_0, \quad \zeta = \tau/t_0, \quad \xi = t/t_0, \quad (45)$$

where t_0 and v_0 are the new scales of time and velocity.

By choosing these new scales of time and velocity, the dimensionless multiplier $\epsilon v_0\rho_0 c_0 t_0/b$ can be taken to be unity, so, after one integration, the final equation appears as

$$-\frac{\partial V^2}{\partial\zeta} = \frac{\partial^2}{\partial\zeta^2}\int_0^\infty\left(\frac{1}{\xi}\right)^n V(c_0\xi-\zeta)d\xi. \quad (46)$$

We consider first the nonrelaxing limit, when

$$h(\tau) = \delta(\tau). \quad (47)$$

In this case, the integral transforms into

$$\int_0^\infty\left(\frac{1}{\xi}\right)^n V(\xi-\zeta)d\xi = \int_0^\infty\delta(\xi)V(c_0\xi-\zeta)d\xi = V(\zeta), \quad (48)$$

so one get the equation

$$-\frac{\partial V^2}{\partial\zeta} = \frac{\partial^2}{\partial\zeta^2}V(\zeta). \quad (49)$$

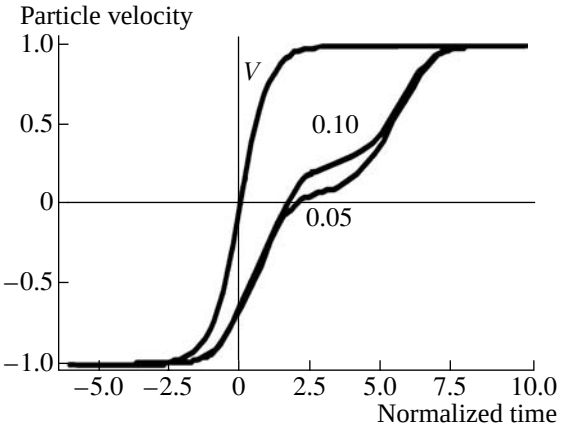

Fig. 2. Stationary shock-wave profiles. The curve labeled *V* corresponds to water; the curves marked as 0.10 and 0.05 correspond to an unconsolidated medium with a memory index of $n = 0.1$ and $n = 0.05$.

The first integral is

$$V^2 = -\frac{\partial V}{\partial\zeta} + 1, \quad (50)$$

where the constant of integration is chosen to be equal to unity. This equation has a solution, namely, $V = \tanh\zeta$. Indeed,

$$-\frac{\partial V}{\partial\zeta} = -\frac{\partial\tanh\zeta}{\partial\zeta} = -\frac{1}{\cosh^2\zeta} = \tanh^2\zeta - 1. \quad (51)$$

Substitution of this result into the previous equation indicates that $\tanh\zeta$ provides a solution.

Therefore, for a nonrelaxing medium, the shock-wave profile is governed by the hyperbolic tangents. For a medium with relaxation, Eq. (46) is solved numerically for a range of τ and a memory index n. The smaller the value of n, the longer the memory of the material. For marine sediments, previous experiments have given a wide spectrum of memory index n in the range 0.05–0.30 [4, 5].

Shock-wave profiles formed in an unconsolidated medium with a memory index of $n = 0.1$ and $n = 0.05$ are obtained by numerical solution of Eq. (46) and are presented in Fig. 2. For comparison, a shock-wave profile in water, where the dissipation is determined by viscosity and heat conductivity, is represented by the curve labeled *V*. It is seen that the relaxation effects lead to a change in the profile structure and, as a result of dispersion, cause it to shift.

Notice that the dimensionless argument $\zeta = \tau/t_0$ is normalized to the relaxation time τ, so that the dimensional shock front thickness is proportional to the relax-

ation time of the material. The profile structure varies as the material constant n changes.

CONCLUSIONS

The nonlinear theory of high-intensity sound propagation in unconsolidated granular materials is developed on the basis of Buckingham's [2] relaxing theory of sound propagation in a medium with grain–grain interactions. A nonlinear evolution equation is obtained, and a model equation for the plane wave case is derived. The generation of harmonics upon plane wave propagation is considered, and the specific features of this effect in a medium with relaxation are discussed. The structure of a stationary weak shock-wave profile in unconsolidated materials is obtained by numerical solution of the evolution equation.

ACKNOWLEDGMENTS

The authors thank Prof. S.A. Rybak for many fruitful discussions and useful remarks. This research was supported by the Russian Foundation for Basic Research (project no. 05-02-17500).

REFERENCES

1. K. Naugolnykh and L. Ostrovsky, *Nonlinear Wave Processes in Acoustics* (Cambridge Univ. Press, Cambridge, 1998).
2. M. J. Buckingham, J. Acoust. Soc. Am. **102**, 2579 (1997).
3. M. J. Buckingham, J. Acoust. Soc. Am. **108**, 2796 (2000).
4. E. L. Hamilton, Geophysics **37**, 620 (1972).
5. M. D. Richardson, in *Ocean Seismo-Acoustics*, Ed. by T. Akal and J. M. Berkson (Plenum, New York, 1986), pp. 527–536.
6. S. S. Kashcheeva, O. A. Sapozhnikov, V. A. Khokhlova, *et al.*, Akust. Zh. **46**, 211 (2000) [Acoust. Phys. **46**, 170 (2000)].
7. K. A. Naugolnykh, S. V. Egerev, I. B. Esipov, and K. A. Matveev, J. Acoust. Soc. Am. **106**, 3135 (1999).
8. K. A. Naugolnykh, in *High Intensity Ultrasonic Fields*, Ed. by L. Rosenberg (Plenum, New York, 1971).
9. M. J. Lighthill, *Surveys in Mechanics*, Ed. by G. K. Batchelor and R. M. Davies (Cambridge Univ. Press, Cambridge, 1956).

Acoustical Physics, Vol. 51, No. 6, 2005, pp. 719–721. Translated from Akusticheskiĭ Zhurnal, Vol. 51, No. 6, 2005, pp. 829–832.

SHORT COMMUNICATIONS

Damping of a Piezoelectric Plate and the Use of an Electric Circuit to Obtain a Short Acoustic Pulse

S. I. Konovalov and A. G. Kuz'menko

St. Petersburg State Electrotechnical University, ul. Prof. Popova 5, St. Petersburg, 197376 Russia

e-mail: root@post.etu.spb.ru

Received September 15, 2004

The possibility of generating a short acoustic pulse is one of the main requirements imposed on the equipment that is used in medical acoustic diagnostics and introscopy. This requirement stems from the need to minimize the dead space and increase the resolution. Therefore, considerable attention has been drawn to the development of transducers capable of generating and receiving such signals. At present, the theory of operation of piezoelectric transducers in a pulsed mode is rather well understood. However, the literature often lacks specific estimates of the pulse durations and amplitudes in relation to various parameters characterizing the transducers (the degree of damping of the active element, the wave thickness of contact layers, the parameters of correcting circuits, etc.). A number of our previous works were devoted to studying these problems [1–6]. As a load, we used a liquid (water). Of certain interest is the consideration of similar problems for the case when the transducer is loaded with a solid medium, for instance, a metal. It should be noted that, in this case, for providing a reliable acoustic contact, it is necessary to use a contact layer, which adversely affects the matching between the transducer and the medium, as compared to the case without a liquid layer, i.e., the case of an ideal acoustic contact. The latter is possible in rare cases, upon a very thorough treatment of contacting surfaces. This leads to the requirement to minimize the thickness of the contact layer, which is often a difficult task. A possible way out is to provide conditions of operation of the piezoelectric transducer under which the generated acoustic pulse remains sufficiently short in the widest possible range of wave thicknesses of the contact layer. This can be achieved, for instance, by using various degrees of damping of the active element or by connecting the plate input with an electric, for example, *RL* load.

The objective of the present study is to obtain comparative estimates of amplitudes and durations of pulses produced by a piezoelectric plate in a solid medium with the use of the two above-mentioned methods of reducing the duration of the generated pulse in a wide range of wave thicknesses of the contact layer. The statement of the problem is illustrated in Fig. 1. Figure 1a shows a piezoelectric plate with a damper on its rear side, and this plate is loaded with a solid medium through a contact layer. Figure 1b shows a similar plate with an *RL* circuit connected in series to its input (on the rear side, the plate borders the air). In both cases, Z_p, Z_c, and Z_l are the acoustic impedances of the piezoelectric plate, contact layer, and acoustic load, respectively. The acoustic impedance of the damper is Z_d. We assume that the area of all the layers, including the contact surface of the medium, which represents the acoustic load, is the same and equals S. Then, $Z_p = \rho_p c_p S$, $Z_c = \rho_c c_c S$, $Z_l = \rho_l c_l S$, and $Z_d = \rho_d c_d S$. As an active material, we choose the TsTSNV-1 ceramics. We denote the electric voltage exciting the piezoelectric plate by $U(t)$. The problem consists in the determination of the particle velocity v at the boundary between the contact layer and the metal for the given pulse of the exciting voltage $U(t)$ for the both variants shown in Fig. 1. As before [1–6], we assume that the plate is excited by a voltage pulse representing a half-period of

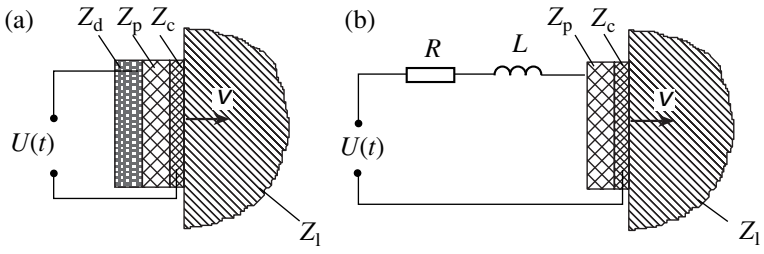

Fig. 1. Statement of the problem.

1063-7710/05/5106-0719$26.00

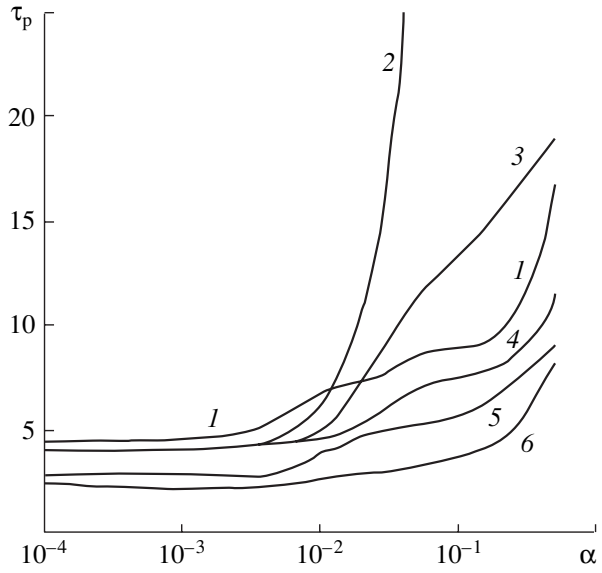

Fig. 2. Dependences of the pulse duration on the wave thickness of the contact layer.

a sinusoid at the antiresonance frequency of the piezoelectric plate. We introduce the parameter α, which allows us to characterize the wave thickness of the contact layer: $\alpha = x_c/x_p$, where x_c and x_p are the wave thicknesses of the contact layer and piezoceramics, respectively. In addition to the listed parameters, we introduce the parameters characterizing the system shown in Fig. 1b:

$$\omega_{el} = 1/\sqrt{LC_0}; \quad n = \omega_{el}/\omega_0; \quad Q = \omega_0 L/R,$$

where C_0 is the capacitance of the repressed piezoelectric plate and ω_0 is the antiresonance frequency of the plate. The physical meaning of the introduced parameters is as follows: ω_{el} is the resonance frequency of the oscillatory circuit formed by the inductance L and the proper capacitance C_0 of the piezoelectric plate, n is the relative resonance frequency of the oscillatory circuit, and Q has the meaning of the quality factor of the oscillatory circuit. In the same manner as was done in previous works, it is possible to determine the shape of the generated pulse of particle velocity $v(t)$. For this purpose, for either variant shown in Fig. 1, by considering the equivalent electric circuit of the radiator that is loaded through the contact layer with a metal, it is possible to determine the frequency response of the piezoelectric radiator. Then, finding the spectral function of the exciting pulse, we use the Fourier transform to determine the form of the time dependence of the acoustic pulse. The result of solving the problem is the determination of the values of the specific acoustic impedances z_d (for the case shown in Fig. 1a), at which the pulse is sufficiently short with an acceptable value of its maximal amplitude, and the values of the parameters Q and n (for the case shown in Fig. 1b) corresponding to the minimal durations of the generated pulses. As in previous papers, the pulse duration is taken to be the time interval from the beginning of the pulse to the instant when the particle velocity amplitude decreases to one-tenth of its maximal value. For convenience, we introduce the dimensionless time $\tau = t/(T_0/2)$, where T_0 is the period of oscillations at the frequency ω_0. This makes it possible to measure the duration of the generated pulses from the number of half-periods of oscillations at the fundamental frequency of the piezoelectric plate. The results of calculations are presented below.

Figure 2 shows a family of curves representing the dependence of the duration of the generated pulse of particle velocity τ_p on the wave thickness of the contact layer α. As a layer material, we chose water. The acoustic load is steel. Curve *1* characterizes the dependence $\tau_p(\alpha)$ for the case when the plate input is loaded with the *RL* circuit, the parameters of which, as a result of searching through numerous variants of calculations, are taken to be optimal, i.e., providing the minimal pulse duration for the chosen materials. It is worth noting that, for the whole range of variation of the parameter α, which is presented in Fig. 2, these values are constant ($n_{opt} = 1.1$ and $Q_{opt} = 2.5$). The other curves correspond to the cases of various degrees of plate damping. Curve *2* characterizes the dependence $\tau_p(\alpha)$ for $z_d = 0$, curve *3*, for $z_d = 5 \times 10^6$, curve *4*, for $z_d = 10 \times 10^6$, curve *5*, for $z_d = 15 \times 10^6$ Pa s/m, and curve *6* refers to the case when the specific acoustic impedances of the damper and the piezoceramics are equal ($z_d = z_p$). From the comparison of curves *1*, *2*, and *3*, it follows that the use of correctly chosen parameters of the electric load allows one to expand the range of variation of the contact layer thicknesses, within which no pronounced increase occurs in the duration of the generated acoustic pulse, as compared to the results achieved with relatively low degrees of damping (up to the values of z_d approximately corresponding to $(5–7) \times 10^6$ Pa s/m). It is seen that, for the indicated values of z_d, for α close to 0, the value of τ_p is about 4–5 half-periods (curves *2* and *3*), which is very close to the values of τ_p obtained with the use of an electrical circuit for $\alpha \approx 0$ (curve *1*). The increase in α to 0.05 leads to a substantial increase in τ_p. For the case of $z_d = 0$ (curve *2*), $\tau_p > 25$, and for the case of $z_d = 5 \times 10^6$ Pa s/m (curve *3*), the pulse duration is $\tau_p \approx 11$. When using an electric load, even for $\alpha = 0.1$, $\tau_p \approx 9$ (curve *1*), and with a further increase in α up to 0.5, although there is an increase in the pulse duration, it is not as pronounced as in the cases characterized by curves *2* and *3*. It should be noted that, for large values of α, the use of an electric load leads to the lengthening of the trailing edge of the pulse (its "tail"); however, even in these cases, according to the chosen criterion of the estimation of the pulse duration, the latter does not exceed $\tau_p \approx (16–17)$ for $\alpha = 0.5$.

As seen from Fig. 2, the use of the increased degrees of damping of the plate (curves *4*, *5*, and *6*) makes it possible to obtained shorter pulses than those obtained using the electric circuit. Specifically, even for $\alpha = 0.5$, the pulse duration does not exceed the value of $\tau_p = 11$ (curve *4*), $\tau_p = 9$ (curve *5*), and $\tau_p = 8$ (curve *6*).

Figure 3 shows the dependences representing the change in the maximal amplitudes of particle velocity in the generated pulse, v_{max}, with parameter α. The designations of the curves are the same as in Fig. 2. The indicated maximal amplitudes are given in conventional units, which is connected with performing the calculations accurate to constant factors. It is seen that the use of the electric circuit with optimal parameters makes it possible to form signals of higher amplitude (curve *1*) than those with the use of damping. Even for $z_d = 0$ (curve *2*), the signal amplitude is about 75% of the signal amplitude obtained by using the electric load. The increase in z_d leads to an even greater difference, which is clearly seen from the comparison of curves *1* and *3–6*.

Using the results presented in Figs. 2 and 3, it is possible, by setting the required duration of the generated acoustic pulse, to find the wave thickness of the contact layer at which this duration will be retained, as well as the amplitude of the generated signal. Let us assume that it is required to generate a signal with a duration of 8 half-periods. From Fig. 2, it is seen that this can be achieved by using a water contact layer with $\alpha \approx 0.015$ for $z_d = 0$ (curve *2*), $\alpha \approx 0.023$ for $z_d = 5 \times 10^6$ Pa s/m (curve *3*), $\alpha \approx 0.035$ for the optimally chosen electric load (curve *1*), etc. From Fig. 3, it is possible to determine the maximal amplitudes of acoustic pulses, which are equal to 1.3 (from curve *2*), 0.95 (from curve *3*), and 1.25 (from curve *1*).

Thus, on the basis of a computational study, it is shown that, by connecting an electric load with optimal parameters to the input of a piezoelectric plate loaded with a metal through a water contact layer, in a wide range of wave thicknesses of this layer, it is possible to obtain a shorter acoustic pulse than that obtained using a low degree of damping ($z_d < 7 \times 10^6$ Pa s/m). With a higher degree of damping, it is possible to generate a shorter pulse than that obtained by using an electric load.

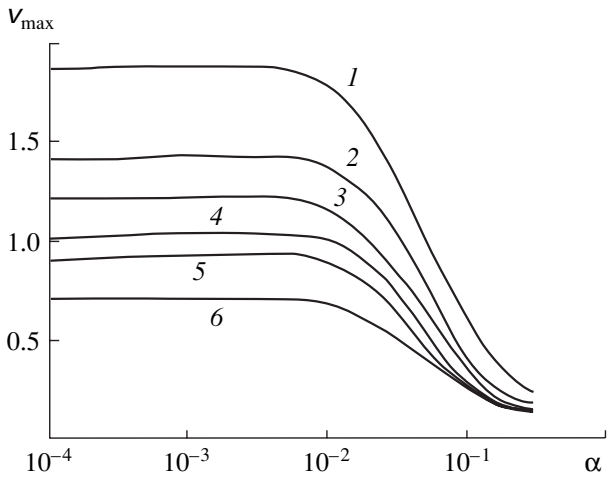

Fig. 3. Dependences of the maximal amplitude of the generated signal on the thickness of the contact layer.

REFERENCES

1. S. I. Konovalov and A. G. Kuz'menko, Akust. Zh. **44**, 119 (1998) [Acoust. Phys. **44**, 100 (1998)].
2. S. I. Konovalov and A. G. Kuz'menko, Akust. Zh. **45**, 568 (1999) [Acoust. Phys. **45**, 507 (1999)].
3. S. I. Konovalov and A. G. Kuz'menko, Akust. Zh. **47**, 856 (2001) [Acoust. Phys. **47**, 758 (2001)].
4. S. I. Konovalov, Akust. Zh. **48**, 695 (2002) [Acoust. Phys. **48**, 618 (2002)].
5. S. I. Konovalov and A. G. Kuz'menko, Akust. Zh. **49**, 852 (2003) [Acoust. Phys. **49**, 729 (2003)].
6. S. I. Konovalov and A. G. Kuz'menko, Akust. Zh. **50**, 129 (2004) [Acoust. Phys. **50**, 112 (2004)].

Translated by A. Svechnikov